

**ELECTRON SCATTERING FROM ATOMS IN THE  
GROUND STATE OR LASER-EXCITED STATES**

---

BY

YUFEI LI

A Thesis

Submitted to the Faculty of Graduate Studies  
in Partial Fulfillment of the Requirements  
for the Degree of

Doctor of Philosophy

Department of Physics  
University of Manitoba  
Winnipeg, Manitoba

© 1996



National Library  
of Canada

Acquisitions and  
Bibliographic Services Branch

395 Wellington Street  
Ottawa, Ontario  
K1A 0N4

Bibliothèque nationale  
du Canada

Direction des acquisitions et  
des services bibliographiques

395, rue Wellington  
Ottawa (Ontario)  
K1A 0N4

*Your file* *Votre référence*

*Our file* *Notre référence*

The author has granted an irrevocable non-exclusive licence allowing the National Library of Canada to reproduce, loan, distribute or sell copies of his/her thesis by any means and in any form or format, making this thesis available to interested persons.

L'auteur a accordé une licence irrévocable et non exclusive permettant à la Bibliothèque nationale du Canada de reproduire, prêter, distribuer ou vendre des copies de sa thèse de quelque manière et sous quelque forme que ce soit pour mettre des exemplaires de cette thèse à la disposition des personnes intéressées.

The author retains ownership of the copyright in his/her thesis. Neither the thesis nor substantial extracts from it may be printed or otherwise reproduced without his/her permission.

L'auteur conserve la propriété du droit d'auteur qui protège sa thèse. Ni la thèse ni des extraits substantiels de celle-ci ne doivent être imprimés ou autrement reproduits sans son autorisation.

ISBN 0-612-16186-2

Canada

Name \_\_\_\_\_

*Dissertation Abstracts International* and *Masters Abstracts International* are arranged by broad, general subject categories. Please select the one subject which most nearly describes the content of your dissertation or thesis. Enter the corresponding four-digit code in the spaces provided.

*Atomic physics*

SUBJECT TERM

0748

UMI

SUBJECT CODE

**Subject Categories**

**THE HUMANITIES AND SOCIAL SCIENCES**

**COMMUNICATIONS AND THE ARTS**

- Architecture ..... 0729
- Art History ..... 0377
- Cinema ..... 0900
- Dance ..... 0378
- Fine Arts ..... 0357
- Information Science ..... 0723
- Journalism ..... 0391
- Library Science ..... 0399
- Mass Communications ..... 0708
- Music ..... 0413
- Speech Communication ..... 0459
- Theater ..... 0465

- Psychology ..... 0525
- Reading ..... 0535
- Religious ..... 0527
- Sciences ..... 0714
- Secondary ..... 0533
- Social Sciences ..... 0534
- Sociology of ..... 0340
- Special ..... 0529
- Teacher Training ..... 0530
- Technology ..... 0710
- Tests and Measurements ..... 0288
- Vocational ..... 0747

**EDUCATION**

- General ..... 0515
- Administration ..... 0514
- Adult and Continuing ..... 0516
- Agricultural ..... 0517
- Art ..... 0273
- Bilingual and Multicultural ..... 0282
- Business ..... 0688
- Community College ..... 0275
- Curriculum and Instruction ..... 0727
- Early Childhood ..... 0518
- Elementary ..... 0524
- Finance ..... 0277
- Guidance and Counseling ..... 0519
- Health ..... 0680
- Higher ..... 0745
- History of ..... 0520
- Home Economics ..... 0278
- Industrial ..... 0521
- Language and Literature ..... 0279
- Mathematics ..... 0280
- Music ..... 0522
- Philosophy of ..... 0998
- Physical ..... 0523

**LANGUAGE, LITERATURE AND LINGUISTICS**

- Language
  - General ..... 0679
  - Ancient ..... 0289
  - Linguistics ..... 0290
  - Modern ..... 0291
- Literature
  - General ..... 0401
  - Classical ..... 0294
  - Comparative ..... 0295
  - Medieval ..... 0297
  - Modern ..... 0298
  - African ..... 0316
  - American ..... 0591
  - Asian ..... 0305
  - Canadian (English) ..... 0352
  - Canadian (French) ..... 0355
  - English ..... 0593
  - Germanic ..... 0311
  - Latin American ..... 0312
  - Middle Eastern ..... 0315
  - Romance ..... 0313
  - Slavic and East European ..... 0314

**PHILOSOPHY, RELIGION AND THEOLOGY**

- Philosophy ..... 0422
- Religion
  - General ..... 0318
  - Biblical Studies ..... 0321
  - Clergy ..... 0319
  - History of ..... 0320
  - Philosophy of ..... 0322
- Theology ..... 0469

**SOCIAL SCIENCES**

- American Studies ..... 0323
- Anthropology
  - Archaeology ..... 0324
  - Cultural ..... 0326
  - Physical ..... 0327
- Business Administration
  - General ..... 0310
  - Accounting ..... 0272
  - Banking ..... 0770
  - Management ..... 0454
  - Marketing ..... 0338
- Canadian Studies ..... 0385
- Economics
  - General ..... 0501
  - Agricultural ..... 0503
  - Commerce-Business ..... 0505
  - Finance ..... 0508
  - History ..... 0509
  - Labor ..... 0510
  - Theory ..... 0511
- Folklore ..... 0358
- Geography ..... 0366
- Gerontology ..... 0351
- History
  - General ..... 0578

- Ancient ..... 0579
- Medieval ..... 0581
- Modern ..... 0582
- Black ..... 0328
- African ..... 0331
- Asia, Australia and Oceania ..... 0332
- Canadian ..... 0334
- European ..... 0335
- Latin American ..... 0336
- Middle Eastern ..... 0333
- United States ..... 0337
- History of Science ..... 0585
- Law ..... 0398
- Political Science
  - General ..... 0615
  - International Law and Relations ..... 0616
  - Public Administration ..... 0617
- Recreation ..... 0814
- Social Work ..... 0452
- Sociology
  - General ..... 0626
  - Criminology and Penology ..... 0627
  - Demography ..... 0938
  - Ethnic and Racial Studies ..... 0631
  - Individual and Family Studies ..... 0628
  - Industrial and Labor Relations ..... 0629
  - Public and Social Welfare ..... 0630
  - Social Structure and Development ..... 0700
  - Theory and Methods ..... 0344
- Transportation ..... 0709
- Urban and Regional Planning ..... 0999
- Women's Studies ..... 0453

**THE SCIENCES AND ENGINEERING**

**BIOLOGICAL SCIENCES**

- Agriculture
  - General ..... 0473
  - Agronomy ..... 0285
  - Animal Culture and Nutrition ..... 0475
  - Animal Pathology ..... 0476
  - Food Science and Technology ..... 0359
  - Forestry and Wildlife ..... 0478
  - Plant Culture ..... 0479
  - Plant Pathology ..... 0480
  - Plant Physiology ..... 0817
  - Range Management ..... 0777
  - Wood Technology ..... 0746
- Biology
  - General ..... 0306
  - Anatomy ..... 0287
  - Biostatistics ..... 0308
  - Botany ..... 0309
  - Cell ..... 0379
  - Ecology ..... 0329
  - Entomology ..... 0353
  - Genetics ..... 0369
  - Limnology ..... 0793
  - Microbiology ..... 0410
  - Molecular ..... 0307
  - Neuroscience ..... 0317
  - Oceanography ..... 0416
  - Physiology ..... 0433
  - Radiation ..... 0821
  - Veterinary Science ..... 0778
  - Zoology ..... 0472
- Biophysics
  - General ..... 0786
  - Medical ..... 0760

- Geodesy ..... 0370
- Geology ..... 0372
- Geophysics ..... 0373
- Hydrology ..... 0388
- Mineralogy ..... 0411
- Paleobotany ..... 0345
- Paleoecology ..... 0426
- Paleontology ..... 0418
- Paleozoology ..... 0985
- Palynology ..... 0427
- Physical Geography ..... 0368
- Physical Oceanography ..... 0415

**HEALTH AND ENVIRONMENTAL SCIENCES**

- Environmental Sciences ..... 0768
- Health Sciences
  - General ..... 0566
  - Audiology ..... 0300
  - Chemotherapy ..... 0992
  - Dentistry ..... 0567
  - Education ..... 0350
  - Hospital Management ..... 0769
  - Human Development ..... 0758
  - Immunology ..... 0982
  - Medicine and Surgery ..... 0564
  - Mental Health ..... 0347
  - Nursing ..... 0569
  - Nutrition ..... 0570
  - Obstetrics and Gynecology ..... 0380
  - Occupational Health and Therapy ..... 0354
  - Ophthalmology ..... 0381
  - Pathology ..... 0571
  - Pharmacology ..... 0419
  - Pharmacy ..... 0572
  - Physical Therapy ..... 0382
  - Public Health ..... 0573
  - Radiology ..... 0574
  - Recreation ..... 0575

- Speech Pathology ..... 0460
- Toxicology ..... 0383
- Home Economics ..... 0386

**PHYSICAL SCIENCES**

- Pure Sciences
  - Chemistry
    - General ..... 0485
    - Agricultural ..... 0749
    - Analytical ..... 0486
    - Biochemistry ..... 0487
    - Inorganic ..... 0488
    - Nuclear ..... 0738
    - Organic ..... 0490
    - Pharmaceutical ..... 0491
    - Physical ..... 0494
    - Polymer ..... 0495
    - Radiation ..... 0754
  - Mathematics ..... 0405
  - Physics
    - General ..... 0605
    - Acoustics ..... 0986
    - Astronomy and Astrophysics ..... 0606
    - Atmospheric Science ..... 0608
    - Atomic ..... 0748
    - Electronics and Electricity ..... 0607
    - Elementary Particles and High Energy ..... 0798
    - Fluid and Plasma ..... 0759
    - Molecular ..... 0609
    - Nuclear ..... 0610
    - Optics ..... 0752
    - Radiation ..... 0756
    - Solid State ..... 0611
  - Statistics ..... 0463
- Applied Sciences
  - Applied Mechanics ..... 0346
  - Computer Science ..... 0984

- Engineering
  - General ..... 0537
  - Aerospace ..... 0538
  - Agricultural ..... 0539
  - Automotive ..... 0540
  - Biomedical ..... 0541
  - Chemical ..... 0542
  - Civil ..... 0543
  - Electronics and Electrical ..... 0544
  - Heat and Thermodynamics ..... 0348
  - Hydraulic ..... 0545
  - Industrial ..... 0546
  - Marine ..... 0547
  - Materials Science ..... 0794
  - Mechanical ..... 0548
  - Metallurgy ..... 0743
  - Mining ..... 0551
  - Nuclear ..... 0552
  - Packaging ..... 0549
  - Petroleum ..... 0765
  - Sanitary and Municipal ..... 0554
  - System Science ..... 0790
- Geotechnology ..... 0428
- Operations Research ..... 0796
- Plastics Technology ..... 0795
- Textile Technology ..... 0994

**PSYCHOLOGY**

- General ..... 0621
- Behavioral ..... 0384
- Clinical ..... 0622
- Developmental ..... 0620
- Experimental ..... 0623
- Industrial ..... 0624
- Personality ..... 0625
- Physiological ..... 0989
- Psychobiology ..... 0349
- Psychometrics ..... 0632
- Social ..... 0451

**EARTH SCIENCES**

- Biogeochemistry ..... 0425
- Geochemistry ..... 0996

Nom \_\_\_\_\_

Dissertation Abstracts International est organisé en catégories de sujets. Veuillez s.v.p. choisir le sujet qui décrit le mieux votre thèse et inscrivez le code numérique approprié dans l'espace réservé ci-dessous.



SUJET

CODE DE SUJET

Catégories par sujets

**HUMANITÉS ET SCIENCES SOCIALES**

**COMMUNICATIONS ET LES ARTS**

Architecture	0729
Beaux-arts	0357
Bibliothéconomie	0399
Cinéma	0900
Communication verbale	0459
Communications	0708
Danse	0378
Histoire de l'art	0377
Journalisme	0391
Musique	0413
Sciences de l'information	0723
Théâtre	0465

**ÉDUCATION**

Généralités	515
Administration	0514
Art	0273
Collèges communautaires	0275
Commerce	0688
Économie domestique	0278
Éducation permanente	0516
Éducation préscolaire	0518
Éducation sanitaire	0680
Enseignement agricole	0517
Enseignement bilingue et multiculturel	0282
Enseignement industriel	0521
Enseignement primaire	0524
Enseignement professionnel	0747
Enseignement religieux	0527
Enseignement secondaire	0533
Enseignement spécial	0529
Enseignement supérieur	0745
Évaluation	0288
Finances	0277
Formation des enseignants	0530
Histoire de l'éducation	0520
Langues et littérature	0279

Lecture	0535
Mathématiques	0280
Musique	0522
Orientalisation et consultation	0519
Philosophie de l'éducation	0998
Physique	0523
Programmes d'études et enseignement	0727
Psychologie	0525
Sciences	0714
Sciences sociales	0534
Sociologie de l'éducation	0340
Technologie	0710

**LANGUE, LITTÉRATURE ET LINGUISTIQUE**

Langues	
Généralités	0679
Anciennes	0289
Linguistique	0290
Modernes	0291
Littérature	
Généralités	0401
Anciennes	0294
Comparée	0295
Médiévale	0297
Moderne	0298
Africaine	0316
Américaine	0591
Anglaise	0593
Asiatique	0305
Canadienne (Anglaise)	0352
Canadienne (Française)	0355
Germanique	0311
Latino-américaine	0312
Moyen-orientale	0315
Romane	0313
Slave et est-européenne	0314

**PHILOSOPHIE, RELIGION ET THÉOLOGIE**

Philosophie	0422
Religion	
Généralités	0318
Clergé	0319
Études bibliques	0321
Histoire des religions	0320
Philosophie de la religion	0322
Théologie	0469

**SCIENCES SOCIALES**

Anthropologie	
Archéologie	0324
Culturelle	0326
Physique	0327
Droit	0398
Économie	
Généralités	0501
Commerce-Affaires	0505
Économie agricole	0503
Économie du travail	0510
Finances	0508
Histoire	0509
Théorie	0511
Études américaines	0323
Études canadiennes	0385
Études féministes	0453
Folklore	0358
Géographie	0366
Gérontologie	0351
Gestion des affaires	
Généralités	0310
Administration	0454
Banques	0770
Comptabilité	0272
Marketing	0338
Histoire	
Histoire générale	0578

Ancienne	0579
Médiévale	0581
Moderne	0582
Histoire des noirs	0328
Africaine	0331
Canadienne	0334
États-Unis	0337
Européenne	0335
Moyen-orientale	0333
Latino-américaine	0336
Asie, Australie et Océanie	0332
Histoire des sciences	0585
Loisirs	0814
Planification urbaine et régionale	0999
Science politique	
Généralités	0615
Administration publique	0617
Droit et relations internationales	0616
Sociologie	
Généralités	0626
Aide et bien-être social	0630
Criminologie et établissements pénitentiaires	0627
Démographie	0938
Études de l'individu et de la famille	0628
Études des relations interethniques et des relations raciales	0631
Structure et développement social	0700
Théorie et méthodes	0344
Travail et relations industrielles	0629
Transports	0709
Travail social	0452

**SCIENCES ET INGÉNIERIE**

**SCIENCES BIOLOGIQUES**

Agriculture	
Généralités	0473
Agronomie	0285
Alimentation et technologie alimentaire	0359
Culture	0479
Élevage et alimentation	0475
Exploitation des pâturages	0777
Pathologie animale	0476
Pathologie végétale	0480
Physiologie végétale	0817
Sylviculture et taune	0478
Technologie du bois	0746
Biologie	
Généralités	0306
Anatomie	0287
Biologie (Statistiques)	0308
Biologie moléculaire	0307
Botanique	0309
Cellule	0379
Écologie	0329
Entomologie	0353
Génétique	0369
Limnologie	0793
Microbiologie	0410
Neurologie	0317
Océanographie	0416
Physiologie	0433
Radiation	0821
Science vétérinaire	0778
Zoologie	0472
Biophysique	
Généralités	0786
Médicale	0760

Géologie	0372
Géophysique	0373
Hydrologie	0388
Minéralogie	0411
Océanographie physique	0415
Paléobotanique	0345
Paléocologie	0426
Paléontologie	0418
Paléozoologie	0985
Palynologie	0427

**SCIENCES DE LA SANTÉ ET DE L'ENVIRONNEMENT**

Économie domestique	0386
Sciences de l'environnement	0768
Sciences de la santé	
Généralités	0566
Administration des hôpitaux	0769
Alimentation et nutrition	0570
Audiologie	0300
Chimiothérapie	0992
Dentisterie	0567
Développement humain	0758
Enseignement	0350
Immunologie	0982
Loisirs	0575
Médecine du travail et thérapie	0354
Médecine et chirurgie	0564
Obstétrique et gynécologie	0380
Ophtalmologie	0381
Orthophonie	0460
Pathologie	0571
Pharmacie	0572
Pharmacologie	0419
Physiothérapie	0382
Radiologie	0574
Santé mentale	0347
Santé publique	0573
Soins infirmiers	0569
Toxicologie	0383

**SCIENCES PHYSIQUES**

Sciences Pures	
Chimie	
Généralités	0485
Biochimie	487
Chimie agricole	0749
Chimie analytique	0486
Chimie minérale	0488
Chimie nucléaire	0738
Chimie organique	0490
Chimie pharmaceutique	0491
Physique	0494
Polymères	0495
Radiation	0754
Mathématiques	0405
Physique	
Généralités	0605
Acoustique	0986
Astronomie et astrophysique	0606
Électromagnétique et électricité	0607
Fluides et plasma	0759
Météorologie	0608
Optique	0752
Particules (Physique nucléaire)	0798
Physique atomique	0748
Physique de l'état solide	0611
Physique moléculaire	0609
Physique nucléaire	0610
Radiation	0756
Statistiques	0463

**Sciences Appliquées Et Technologie**

Informatique	0984
Ingénierie	
Généralités	0537
Agricole	0539
Automobile	0540

Biomédicale	0541
Chaleur et thermodynamique	0348
Conditionnement (Emballage)	0549
Génie aérospatial	0538
Génie chimique	0542
Génie civil	0543
Génie électronique et électrique	0544
Génie industriel	0546
Génie mécanique	0548
Génie nucléaire	0552
Ingénierie des systèmes	0790
Mécanique navale	0547
Métallurgie	0743
Science des matériaux	0794
Technique du pétrole	0765
Technique minière	0551
Techniques sanitaires et municipales	0554
Technologie hydraulique	0545
Mécanique appliquée	0346
Géotechnologie	0428
Matériaux plastiques (Technologie)	0795
Recherche opérationnelle	0796
Textiles et tissus (Technologie)	0794

**PSYCHOLOGIE**

Généralités	0621
Personnalité	0625
Psychobiologie	0349
Psychologie clinique	0622
Psychologie du comportement	0384
Psychologie du développement	0620
Psychologie expérimentale	0623
Psychologie industrielle	0624
Psychologie physiologique	0989
Psychologie sociale	0451
Psychométrie	0632



THE UNIVERSITY OF MANITOBA  
FACULTY OF GRADUATE STUDIES  
COPYRIGHT PERMISSION

ELECTRON SCATTERING FROM ATOMS IN THE GROUND STATE  
OR LASER-EXCITED STATES

BY

YUFEI LI

A Thesis/Practicum submitted to the Faculty of Graduate Studies of the University of Manitoba in partial fulfillment of the requirements for the degree of

DOCTOR OF PHILOSOPHY

Li Yufei © 1996

Permission has been granted to the LIBRARY OF THE UNIVERSITY OF MANITOBA to lend or sell copies of this thesis/practicum, to the NATIONAL LIBRARY OF CANADA to microfilm this thesis/practicum and to lend or sell copies of the film, and to UNIVERSITY MICROFILMS INC. to publish an abstract of this thesis/practicum..

This reproduction or copy of this thesis has been made available by authority of the copyright owner solely for the purpose of private study and research, and may only be reproduced and copied as permitted by copyright laws or with express written authorization from the copyright owner.

## ABSTRACT

The inelastic electron-impact excitation of atoms can be fully characterized by electron impact coherence parameters (EICP) and the differential cross section (DCS). The investigation of these quantities can yield complete information about the excitation process in terms of a quantum physics description.

A laser-pumping technique has been employed in our superelastic scattering experiments to measure EICP for electron-impact excitation of barium and ytterbium atoms at low and intermediate impact energies, and the conventional crossed-beam method has been used in our DCS measurements on the ytterbium atom. We have applied the laser-pumping technique to measurements of i) the coherence parameters  $P_l^+$ ,  $\gamma$  and  $L_\perp^+$  for electron-impact excitation of the (...6s6p  $6^1P_1$ ) state in  $^{138}\text{Ba}$ , and ii) the  $P_1$ ,  $P_2$  and  $P_3$  parameters for excitation of the (...6s6p  $6^3P_1$ ) level in  $^{174}\text{Yb}$ . The partial differential cross sections for excitation of  $^{138}\text{Ba}$  (...6s6p  $6^1P_1$ ) state have been determined by combining available experimental results of the EICP and the DCS. We have also measured the DCS for excitation of the (...6s6p  $6^1P_1$ ) in  $^{174}\text{Yb}$  by crossed-beam method.

The comprehensive discussion has been given and comparison with available theoretical calculations has been made for experimentally measured and derived parameters.

*To the memory of my grandmother,  
Shujun Shi*

## ACKNOWLEDGMENT

I would like to thank my thesis supervisor, Dr. P. W. Zetner, for his guidance, support and encouragement over the years that I have been devoted to this research.

My special thanks should also go to Mr. G. Roy and Dr. H. Kunkel for their kindness and help through all the period of the experiment as well as to Mr. J. Lancaster, Mr. V. Zvonik and Mr. R. Hamel for their technical assistance.

Acknowledgment is extended to my colleague, P. Johnson for his helpful discussion and assistance throughout the time of my laboratory work.

This work was supported by the Natural Sciences and Engineering Research Council of Canada. I was financially sponsored by a University of Manitoba Graduate Fellowship. These supports allowed me to accomplish my research work for this thesis.

And, finally, I thank my wife and my parents for all their help and patience over the years.

# CONTENTS

<b>Chapter 1</b>	<b>Introduction</b>	1
<b>Chapter 2</b>	<b>General Theory</b>	6
2.1	Introduction	6
2.2	Concept of Coherence in the Atomic Excitation Process	8
2.3	Laser Pumping Technique	14
2.4	Discussion about Spin Effects	22
2.5	Characterization of Electron Impact Excitation by Density Matrix	25
2.6	The Measurement Quantities — Differential Cross Sections and Electron Impact Coherence parameters	27
2.7	Theoretical Prediction of EICP by First Born Approximation	41
<b>Chapter 3</b>	<b>Apparatus</b>	49
3.1	Introduction	49
3.2	General Description of the Apparatus	50
3.3	Vacuum System	54
3.4	Laser and Optical System	55
3.5	Data Collection System	68
3.6	Electron Spectrometer	76
3.7	Electron Optics	81

3.7.1	General Concept	81
3.7.2	High Resolution Electron Gun Design	87
3.7.3	High Intensity Gun	99
3.7.4	Detector	101
3.8	Metal Vapor Source	103

## **Chapter 4 Measurements of Electron Impact Coherence**

### **Parameters for Electron-Impact Excitation of $^{138}\text{Ba}$**

	<b>(...6s6p <math>^1P_1</math>)</b>	111
4.1	Introduction	111
4.2	Measurement Theory	116
4.3	Experimental Details of $P_1^+$ , $\gamma$ and $L_{\perp}^+$ Measurement	121
4.4	Data Analysis	134
	4.4.1 For $P_1^+$ and $\gamma$ Measurement	134
	4.4.2 For $L_{\perp}^+$ Measurement	138
4.5	Results and Discussion	142
4.6	Determination of PDCS for (...6s6p $6^1P_1$ ) Excitation	179
4.7	Conclusion	189

## **Chapter 5 The Studies of Electron Scattering Excitation of**

	<b><math>^{174}\text{Yb}</math></b>	192
5.1	Introduction	192
5.2	Superelastic Electron Scattering from Laser-excited $^{174}\text{Yb}(\dots 6s6p \ 6^3P_1)$	195
	5.2.1 Experimental Details	195
	5.2.2 Results and Discussions	199
5.3	DCS for Electron Impact Excitation of the (...6s6p $6^1P_1$ )	

level in Yb	210
5.3.1 Experimental Details	210
5.3.2 Data Analysis	215
5.3.3 Results and Discussion	219
5.4 Polarization Dependent Energy Loss Spectra for Electron Scattering from Laser Excited Yb	228
5.5 Conclusion	231
<b>Chapter 6 Overall Summary</b>	<b>234</b>
<b>References</b>	<b>239</b>
<b>Appendix 1 Circuit Diagrams</b>	<b>249</b>
<b>Appendix 2 Electron Optics Simulation</b>	<b>262</b>
<b>Appendix 3 Data Acquisition Programs</b>	<b>269</b>

# CHAPTER 1

## INTRODUCTION

Electron-atom collision phenomena are of fundamental importance in atomic physics and have been studied for many years. Electron scattering has become one of the most important methods for the experimental study of quantum physics. During the past two decades, progress has been made in the experimental investigation of the "fine details" of electron collisional excitation. By carrying out these types of experiments, complete information can be obtained about the excitation process in terms of a quantum physics description. Unlike the traditional electron-atom scattering experiments that could only be used to determine averaged excitation cross sections, detailed studies have been performed to characterize the shape and dynamics of atomic electron charge density distributions after electron collisional excitation. Because of the coherent nature of the excitation, such an experiment is called a "coherence and correlation measurements" of the collision process. Such efforts have resulted in a deeper understanding of the physical mechanisms of electron-atom collisional excitation phenomena.

Prior to 1971, studies of the electron-atom collision were limited to angle-averaged measurements, which determined the integral cross sections for the population of different magnetic substates of the atom by collisional excitation. The first atomic electron-photon coincidence measurement was

theoretically proposed by Macek and Jaecks in 1971 (Macek1971) followed by the article of Fano and Macek (Fano1973) which laid the foundations for this field of study. The first experimental study of such a coincidence experiment was reported in 1972 by King et al (King1972) who investigated the helium excitation at forward scattering angle. In the same year, Kleinpoppen et al performed their experiment to determine the inelastic scattering amplitudes as functions of scattering angle for electron impact excitation of helium  $2^1P$  and  $3^1P$  (Eminyan1973). The invention of the tunable cw dye laser opened a new territory for the coherence studies of electron-atom collisions and made it possible to carry out electron scattering from laser excited atoms. Hertel and Stoll were the first to use a laser pumping technique to perform the superelastic electron collisional deexcitation of atomic sodium (Hertel1974). Subsequently, Macek and Hertel demonstrated that the superelastic experiment is a time-inverse process of the inelastic electron-photon coincidence experiment and the same information can be derived from both experiments (Macek1974). A comprehensive review of the coherence studies of electron collisions by means of these two techniques and the comparison between the experimental results and available theories has been given by Andersen, Gallagher and Hertel in 1988 (Andersen1988). These authors have introduced a set of physically appealing electron impact coherence parameters to describe the shape and dynamics of the excited charge cloud distributions.

Since the pioneer effort of Hertel and Stoll, superelastic scattering experiments have played an important role in the coherence studies of atomic collisions. A large number of collision studies have been performed using this powerful tool. Among them, sodium has been studied by Scholten et al (Scholten1988), Farrell et al (Farrell1989) and Sang et al (Sang1994), Ca by

Law and Teubner (Law1993), Ba by Zetner, Li and Trajmar (Zetner1992), and Li and Zetner (Li1993, Li1994a, and Li1995a), Yb by Li and Zetner (Li1994b and Li1995b). Recent progress has been made by the Griffith University group on Rb atom (Hall1995). Superelastic scattering with spin-polarized electrons and spin-polarized laser-excited sodium atoms has been studied by Hanne et al (Hanne1982) and McClelland et al (McClelland1987).

Compared with the time consuming electron-photon coincidence techniques, laser pumping technique offers substantial advantages. The shortening of the measurement time can result in more stable performance of electronics and electron spectrometer. The convenience for the experimenter, especially in the case of metal atom studies, to prepare the atom source is essential for a practical measurement. The extremely high monochromaticity of dye laser systems allows the isolation of specific fine and hyperfine transitions belonging to specific isotopes and therefore eliminates the effects of fine and hyperfine depolarization encountered in coincidence measurements. The price one has to pay is the use of a sophisticated laser system. The number of atoms that can be measured with this technique is limited by the available laser wavelengths.

Recently, both theoretical and experimental studies have appeared in the investigation of inelastic scattering of electrons from high-Z, closed shell, two-electron atoms such as Ca, Sr, Ba, Hg and Yb. Because these atoms belong to two-electron systems, they offer a natural extension to studies which have already been extensively carried out on the helium atom. From the experimental standpoint, although metal vapor beams of these atoms can be produced quite easily, electron-photon coincidence measurements applied to these atoms are somewhat difficult, in comparison with superelastic measurements. Furthermore, the widely studied S to P transition frequencies

of these heavy atoms can be reached by available laser dye for laser pumping. Thus the superelastic-scattering technique is feasible for the investigation of electron impact excitation in these high-Z alkaline earth atoms.

On the other hand, theorists face several challenges from these heavy alkaline-earth atoms. With increasing atomic number, the electronic structure becomes more complicated. Also, electron scattering by the heavy atoms is characterized by non-negligible contributions from partial waves of high angular momentum. Due to the possible existence of a spin-dependent interactions, the relativistic approach is required for the theoretical treatments of these heavy atoms. Nevertheless, calculations of electron impact coherence parameters have been reported for Mg by Meneses, Pagan and Machado (Meneses), for Sr by Beyer et al (Beyer), for Ba by Clark et al (Clark1989), Srivastava et al (Srivastava1992) and Fabrikant (Fabrikant1985), for Yb by Clark et al (Clark) and Srivastava (Srivastava1995).

The present work concentrates on coherence studies of electron impact excitations of Ba and Yb atoms using the laser pumping technique (superelastic-scattering) without electron spin analysis. Electron impact coherence parameters characterizing atomic states excited by electron collision have been measured for different atomic levels. Some efforts have also been made on differential cross section measurements for electron impact excitation of Yb, and the determination of magnetic sublevel partial differential cross sections for electron impact excitation of Ba. Comparison has been made between experimental results and available theoretical calculations.

In Chapter 2, the general theory of coherence investigation of electron-atom scattering, superelastic scattering, and electron impact coherence parameters are discussed. Chapter 3 describes the experimental apparatus

which I helped develop and construct. The details of experiments are presented in Chapter 4 and Chapter 5. For each chapter, the specific introduction, theory and experimental arrangement are introduced, followed by results, discussion and conclusions. Finally, Chapter 6 gives the overall summary.

## CHAPTER 2

### GENERAL THEORY

#### 2.1 Introduction

In the electron-atom inelastic collision experiment, the scattered electron or emitted photon (from the spontaneous transition following the excitation) are typically detected. They carry the information about the electron-atom interaction process. In particular differential cross sections (see Section 2.6 for definition) are measured in these types of experiments for electron impact excitation. In experiments that involve the detection of scattered electrons, the measured angular differential cross section is averaged over the degenerate magnetic sublevels of the collisionally excited atom. In the experiments that involve the detection of photons, measurements of the light intensity can give the cross sections averaged over all the angles of scattering of electrons, and hence relate to the integral excitation cross section. Hence in both situations one can only get information concerning averaged quantities characterizing the collisional excitation process.

In order to obtain more detailed information about the collisional excitation process, one needs to perform experiments in which scattered electrons and the emitted photons associated with the collisional excitation

are detected correlatively. Electron-photon coincidence experiments and laser pumping superelastic-scattering experiments are the possible techniques that allow one to obtain more detailed information about the inelastic electron-atom collision.

In the case of superelastic-scattering, the target atom is pumped to an excited state by a laser beam in a certain incident direction and polarization state, and then deexcited by the electron beam. By detecting the superelastic-scattering signal as a function of the laser geometry, one can extract information about the time-inverse inelastic collisional process.

An inelastic electron collisional excitation can be described by a scattering density matrix. A minimum number of matrix elements that are related to physical observables (parameters) are required to fully characterize a specific collisional excitation. Furthermore, the spin-orbit interaction can play an important role in the excitation process for heavy atomic targets. It originates from relativistic effects in the electron-target system. The spin-orbit interaction can result in nonconservation of the total spin and couple the spin with angular orbital momenta of electrons. In this case, more parameters are required to describe the excitation.

In this chapter, we will introduce the general concept of coherent collisional excitation process and discuss the superelastic-scattering approach that can be used to investigate the time-inverse inelastic collisional excitation. We will then talk about spin-orbit effects and spin conservation in the projectile electron-atom system. We will define the electron impact coherence parameters used to characterize the inelastic electron-atom collisional excitation and discuss their physical meanings. Some theoretical approaches are also reviewed here. In this chapter we put the emphasis of our discussion on the most widely studied collisional excitation from singlet

S state to P state. Since our experimental arrangement does not provide any observation on the spin of the projectile electron, we are only interested in spin averaged observables.

## 2.2 Concept of Coherence in the Atomic Excitation Process

In the simplest process of electron impact excitation of an atom, a projectile electron with kinetic energy  $E_0$  collides with a target atom in the ground state. The electron loses kinetic energy  $\Delta E$  to excite the atom. The excited atom then spontaneously decays back to its ground state and emits a photon at polar angle  $(\theta_v, \phi_v)$  while the scattered electron travels, with kinetic energy  $E_0 - \Delta E$ , at angle  $\theta_{col}$  with respect to the incident electron direction, or otherwise called the forward scattering direction. The incident electron projectile and scattered electron projectile define the scattering plane as shown in Fig. 2.1. This scattering process can be described with expression



followed by



In this process, we are interested in the transition from an initial state  $|n_0 J_0 M_0; \vec{k}_0 m_0\rangle$  to a final state  $|n_1 J_1 M_1; \vec{k}_1 m_1\rangle$ , where each bracket represents the combined state of target atom and projectile electron, and  $J_0$  and  $J_1$  are the total electronic angular momenta of the target atom before and after the scattering,  $M_0$  and  $M_1$  are their corresponding components along the quantization axis,  $m_0$  and  $m_1$  denote the spin components of the incident and

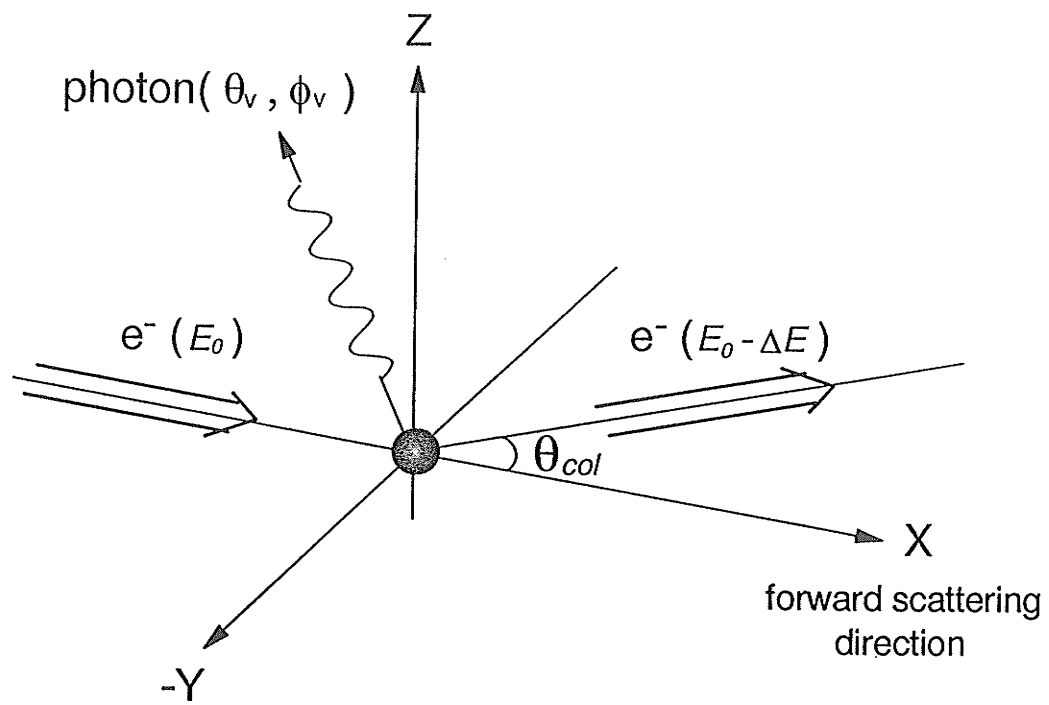


Figure 2.1. Schematic diagram of an electron impact inelastic excitation of atomic target.

outgoing electrons,  $\vec{k}_0$  and  $\vec{k}_1$  are their corresponding linear momenta, and finally  $n_0$  and  $n_1$  denote the additional quantum numbers necessary to identify the excited atomic level. If  $\Gamma_0 = (n_0, J_0, M_0, \vec{k}_0, m_0)$  and  $\Gamma_1 = (n_1, J_1, M_1, \vec{k}_1, m_1)$  are used to represent all the quantum numbers of the electron-target system before and after the collision, respectively, such a transition is described by complex scattering amplitudes

$$f(\Gamma_1 \Gamma_0) = \langle \Gamma_1 | T | \Gamma_0 \rangle \quad 2.2$$

where  $T$  is the scattering operator that depends on the interaction Hamiltonian between the projectile electron and target atom. The possible observables in this process can be expressed by density matrix elements that are the bilinear products of these scattering amplitudes

$$\rho_{\Gamma_1 \Gamma_1} = f(\Gamma_1' \Gamma_0) f^*(\Gamma_1 \Gamma_0) \quad 2.3$$

This complex density matrix contains the complete information about the collisional excitation process including the magnitude of the scattering amplitude and the phase difference between scattering amplitudes.

If the experimental arrangement does not provide any spin selection or analysis on projectile electrons and the target atoms are unpolarized in their initial state, we can average Eqn. 2.3 over initial and final spin states of the projectile electron

$$\langle f(M_1') f^*(M_1) \rangle = \frac{1}{2(2J_0 + 1)} \sum_{M_0, m_0, m_1} f(\Gamma_1' \Gamma_0) f^*(\Gamma_1 \Gamma_0) \quad 2.4$$

where the bracket represents the average over spin. We are concerned only with the dependence of the matrix elements  $\langle f(M_1')f^*(M_1) \rangle$  on atomic magnetic quantum numbers  $M_1'$  and  $M_1$ , and suppress the other quantities.

If all of the scattering density matrix elements (i.e., all scattering amplitudes  $\langle f(M_1')f^*(M_1) \rangle$ ) can be completely determined, the excitation is said to be a "fully coherent excitation process" (Bederson 1973). The experiment allowing us to measure all of these scattering amplitudes is called a "perfect scattering experiment". It gives us "complete" information about the excitation in terms of quantum mechanics. Unfortunately, only in certain cases can we obtain complete information about one particular excitation. Normally various amplitudes are averaged over some quantum number and much less detail is available. This fact is typically observed in the following two types of experiments.

In traditional electron impact experiments, the scattered electrons are detected but not the photons emitted by excited target atoms as well. In the absence of an external magnetic field, the excited states of the atoms have degenerate magnetic sublevels and these sublevels can not be separated in an electron energy spectrometer. Hence, in this type of experiment, the measured quantity is the angular differential cross section averaged over the degenerate magnetic sublevels. This corresponds to the measurement of the summation of all diagonal scattering matrix elements ( $\sum_{M_1=-J}^J \langle |f(M_1)|^2 \rangle$ ). But no information about individual diagonal and off-diagonal elements can be obtained and therefore this excitation process is incoherent.

Similarly, traditional measurements of photon yield but not of the scattered electrons as well can also provide limited information. Measurements of the light intensity and percentage polarization as a function

of the angle of emission can give the cross sections for excitation of the individual magnetic sublevels, but they are incoherently averaged over all the scattering angles of the electrons, and hence relate to the integral excitation cross section. One can not obtain the matrix element dependence on  $\vec{k}_0$  and  $\vec{k}_1$  in this type of experiment. No information about off-diagonal elements can be provided either.

The common point of these two approaches is that the excitation is performed under conditions of axial symmetry. The axis of symmetry is along the direction of the incident electron beam, and the detection of scattered electrons or emitted photons is axially symmetric along this axis. Because of the axial symmetry, all terms with  $M_1' \neq M_1$  vanish. From these types of measurements, one can only obtain terms or the sum of the terms with  $M_1' = M_1$ . On the other hand, if the excitation process has no axis of symmetry, the scattering matrix elements with  $M_1' \neq M_1$  will be nonzero in general. The parameters with  $M_1' \neq M_1$  reflect the interference between the different magnetic substates, and they can be determined only in an experiment that lacks axial symmetry.

In order to perform the coherence study of electron-atom collisions, we need to reduce the axial symmetry of the excitation. The standard method is the electron-photon coincidence experiment in which photons are detected in time coincidence with scattered electrons (Fano1973, Eminyan1974 and Blum1979). A schematic arrangement for a polarized photon- scattered electron coincident experiment is shown in Figure 2.2. The experiment involves only a selected subensemble of all the atoms excited by the electron beam. This subensemble has special properties not characteristic of the total ensemble, that is, the electron detector can only register the scattered electrons (in some selected direction and specific

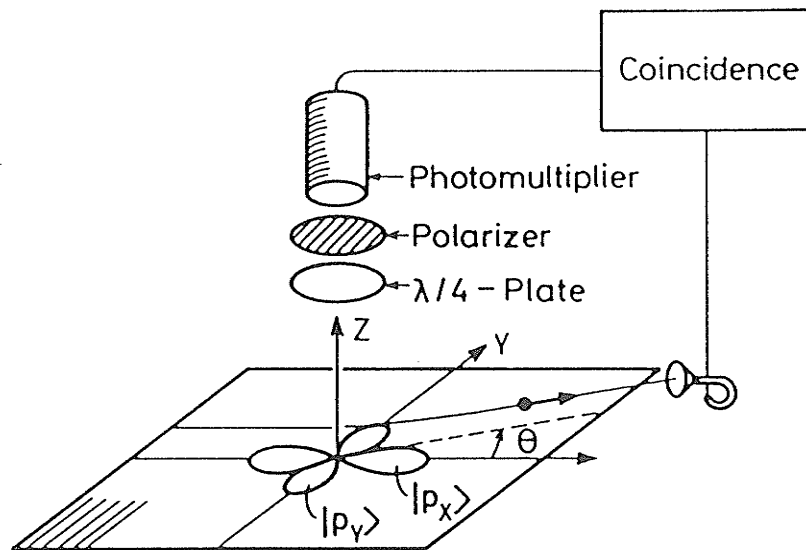
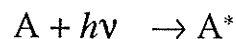


Figure 2.2. Schematic diagram of a photon-scattered electron coincidence experiment. The scattered electrons are detected in time delayed coincidence with emitted photons. Adopted from (Andersen 1982).

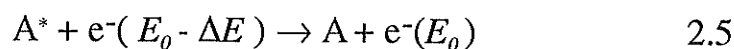
energy loss ) associated with photons admitted in some selected direction and by certain optics in front of the photomultiplier characterizing the collisional excitation event to certain atomic magnetic sublevel. The significance of this technique is that the axial symmetry is reduced to planar symmetry and the scattering matrix element with  $M_1' \neq M_1$  can be measured to determine both magnitudes and phases of scattering amplitudes. This is the deepest knowledge, also called "fine details" of the electron-impact excitation process, one can obtain in terms of a quantum physics description.

### 2.3 Laser Pumping Technique

The laser pumping technique has been used as an alternative method for coherence studies of electron impact excitation of atoms (Macek1974, Hertel1974, Hertel1977 and Fano1973). Instead of detecting inelastically scattered electrons in time coincidence with the photons emitted in a certain direction and polarization, we may prepare an atomic state by an optical pumping process with the laser beam in a given direction and polarization  $(\theta_\lambda, \phi_\lambda, pol)$  and frequency  $\nu = \Delta E/h$  prior to the collision and detect the superelastically scattered electrons which have deexcited atoms and gained energy  $\Delta E$ . The process can be expressed as:



and



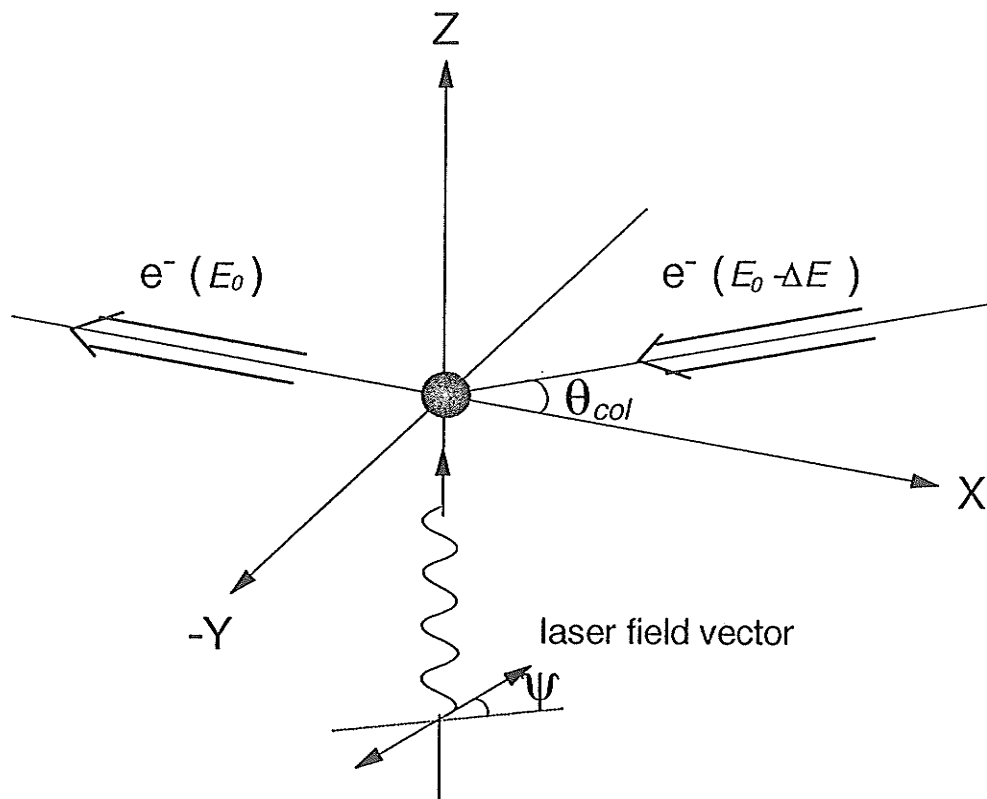


Figure 2.3. Schematic illustration of a superelastic scattering process.

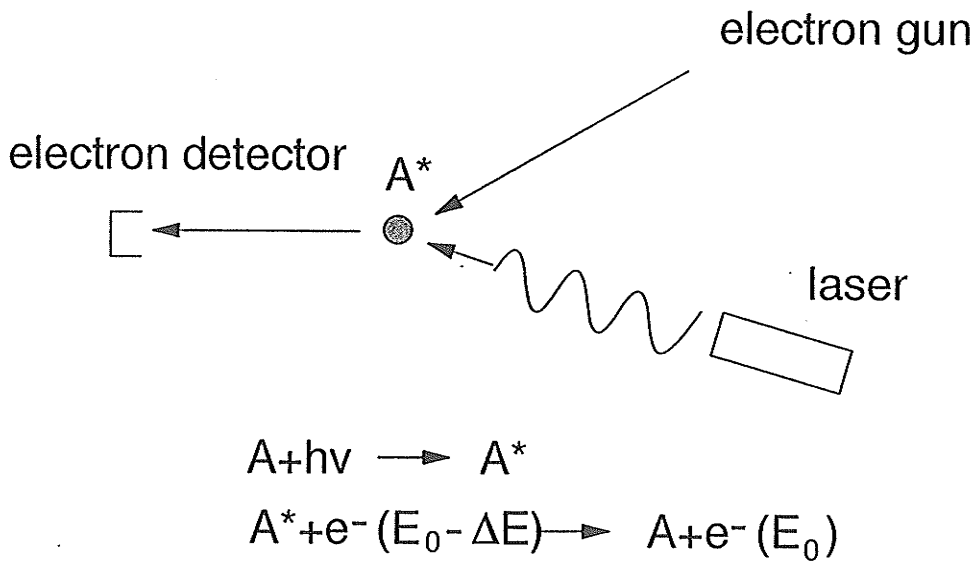
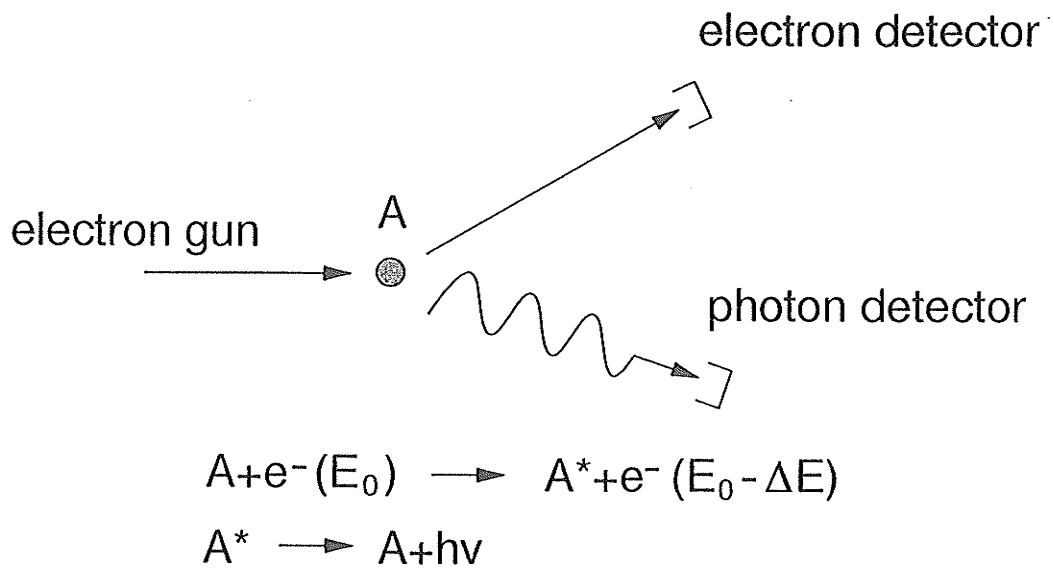


Figure 2.4. Schematic diagram of an electron-photon coincidence experiment (above) in comparison with the time-inverse superelastic-scattering experiment (below). Adopted from (Hertel1974).

Fig. 2.3 schematically illustrates the superelastic scattering process. The comparison between Fig. 2.1 and Fig. 2.3, and between Eqn. 2.1 and Eqn. 2.5 suggests that superelastic scattering is the time-reverse process of an electron-photon coincidence inelastic scattering. The correspondence of the two approaches is illustrated in Fig. 2.4.

In both cases the correlation between the scattered electrons at a well-defined scattering angle and the photon in a certain direction and polarization state is established. In the coincidence experiment this is achieved by detecting the scattered electron in time-delayed coincidence with the subsequently emitted photon from the same scattering event. In the optical pumping approach the correlation is initiated and completed by pumping the atoms to a certain substate with the laser beam at defined direction and polarization. The laser light beam in certain incident direction and polarization prepares an excited state through optical pumping. Since the incident direction and the polarization can be easily manipulated, it is possible to create all the atomic magnetic substates or a mixture of these substates by using different incident directions and polarization states of the laser light beam. In this sense, the time inverse superelastic experiment is equivalent to a coincidence experiment in principle and the same information can be obtained from either approach.

Care must be taken when we compare results from the superelastic experiment with results from a coincidence experiment or results from a theoretical calculation that is based on the inelastic process. Since superelastic scattering is the time inverse process of inelastic scattering, the coordinate axes are reversed correspondingly. Also, the kinetic energy of the incident electron  $E_0$  prior to the inelastic process corresponds to an energy  $E_0 - \Delta E$  prior to the time inverse superelastic scattering process.

Furthermore, a complication may arise due to some processes leading to the incoherent excitation, for example, interaction between the spin and orbital angular momentum of the projectile electron. Such a process always destroys coherence and transfers a pure initial state into a mixed final state. If this happens, the information we can obtain about this excitation process will be reduced somewhat.

The laser-pumping process prepares an ensemble of atoms characterized by a state that is, in general, a partially coherent mixture of the various magnetic sublevels of the excited level. This ensemble can be described by a density matrix. Macek and Hertel (Macek1974) have shown the general expression of the density matrix  $\hat{\tau}$  of the excited state generated by the laser pumping process. In the case that nuclear spin is zero and no hyperfine structure is involved, the density matrix  $\hat{\tau}$  is given by

$$\hat{\tau} = \sum_{M_1} W(M_1) |J_1 M_1\rangle \langle J_1 M_1| \quad 2.6$$

where  $W(M_j)$  is the probability that laser-excited state  $|J_1 M_1\rangle$  is prepared.

For a superelastic-scattering experiment involving unpolarized electrons in which electron spins are undetected, one can perform an incoherent average over all possible electron spin states before and after the scattering. With the above definition of  $\hat{\tau}$ , it has been shown by Macek and Hertel (Macek1974) that superelastic scattering intensity can be given in the form

$$I^s = \frac{C}{2(2J_0 + 1)} \sum_{M_0 m_0 m_1} \langle e_n(J_0 M_0, m_0 m_1) | \hat{\tau} | e_n(J_0 M_0, m_0 m_1) \rangle \quad 2.7$$

where  $C$  is a constant consisting of multiplicative factors such as detection geometry and efficiency, laser-excited atom population, incident electron flux, and the differential superelastic scattering cross section. The state vector  $|e_n(J_0 M_0 m_0 m_1)\rangle$  of the state that would be prepared by the inelastic electron collision process with well-defined initial and final electron spins and momenta appearing in Eqn 2.7 is defined by

$$|e_n(J_0 M_0 m_0 m_1)\rangle = \sum_{J_1 M_1} \bar{f}(\Gamma_1 \Gamma_0) |n J_1 M_1\rangle \quad 2.8$$

and

$$\bar{f}(\Gamma_1 \Gamma_0) = \frac{f(\Gamma_1 \Gamma_0)}{(\sum_{J_1 M_1} |f(\Gamma_1 \Gamma_0)|^2)^{1/2}}$$

where  $\bar{f}(\Gamma_1 \Gamma_0)$  is the normalized scattering amplitude for electron-impact excitation of the excited state  $|n_1 J_1 M_1\rangle$  of the atomic target from the ground state  $|n_0 J_0 M_0\rangle$  with well-defined spins and the momenta of the incident and scattered electrons.  $\Gamma_0 = (n_0, J_0, M_0, \vec{k}_0, m_0)$  and  $\Gamma_1 = (n_1, J_1, M_1, \vec{k}_1, m_1)$  refer to all the quantum numbers of the electron-target system before and after the scattering, respectively.

In order to demonstrate the physical meaning of Eqn 2.7, let us consider a simpler situation where laser pumping produces a pure P ( $J_l = 1$ ) excited state of the target atom from a  $^1S$  ( $J_0 = 0$ ) ground state

$$\hat{\tau} = |\lambda\rangle\langle\lambda| \quad 2.9$$

where  $|e\rangle = \lambda_{+1}|+1\rangle + \lambda_0|0\rangle + \lambda_{-1}|-1\rangle$  is an excited state produced by laser optical pumping.  $|i\rangle$  with  $i=+1, 0, -1$  denotes magnetic sublevels of the p-state.  $\lambda_i(\theta_\lambda, \phi_\lambda, pol)$  denotes an excitation amplitude by optical pumping which is laser polarization and direction dependent. The state

$$|e\rangle = \sum_{M=-1}^1 \bar{f}(\Gamma_1 \Gamma_0) |M\rangle \quad 2.10$$

is an excited state with  $J_l = 1$  that would be produced by inelastic electron scattering from the same ground state with specified spins and the momenta of the incident and scattered electrons. Using Eqn. 2.7, we can write the superelastic-scattering intensity

$$I^s = C \sum_{M', M=-1}^1 \lambda_{M'}^* \lambda_M \langle f(M') f^*(M) \rangle \quad 2.11$$

where we are only concerned with  $M$  and suppress other quantities in the scattering matrix  $\langle f(M') f^*(M) \rangle$ . The bracket represents the average over spins.  $\lambda_{M'}^* \lambda_M$  are well-defined for a certain setup of laser polarization and beam direction  $(\theta_\lambda, \phi_\lambda, pol)$ . By carrying out superelastic experiments with various sets of  $(\theta_\lambda, \phi_\lambda, pol)$ , in principle we can extract all scattering matrix elements  $\langle f(M') f^*(M) \rangle$  that characterize the inelastic electron impact excitation of atoms. In this way superelastic experiments carried out by laser pumping can be used to investigate the coherent excitation process by electron-atom inelastic collision.

It can be seen from Eqn. 2.7 that the superelastic-scattering intensity is proportional to the component of the laser-excited state contained in the state which would be produced by inelastic collisional excitation. A picture

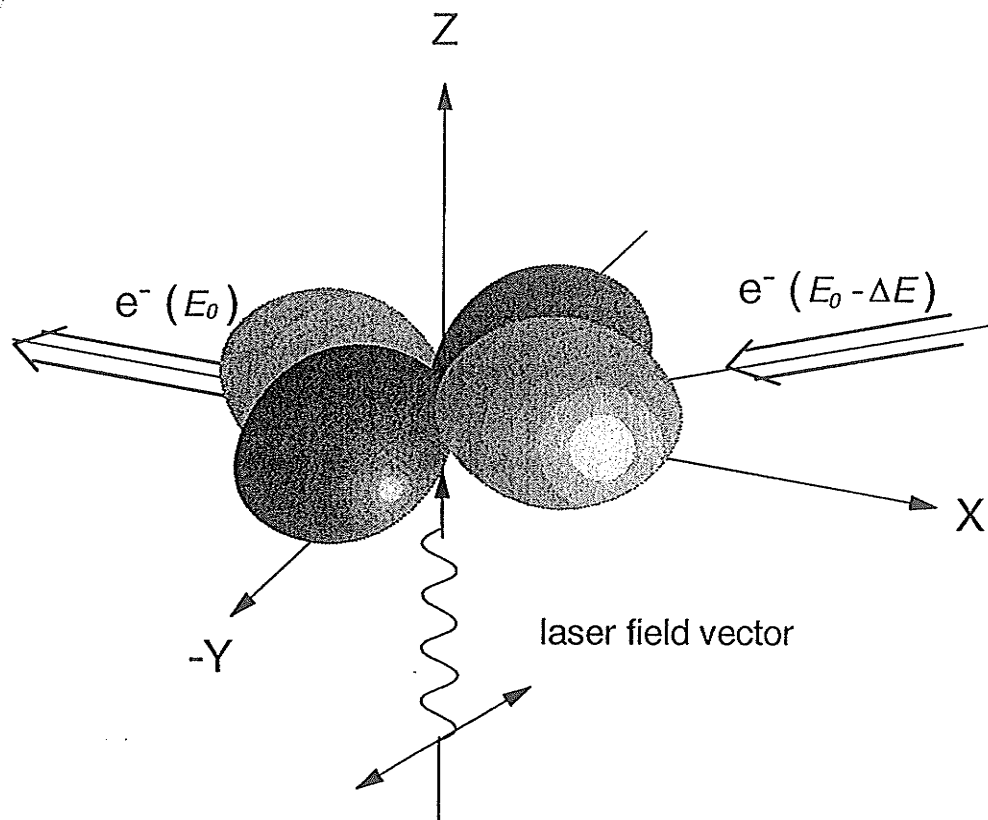


Figure 2.5. Schematic illustration of the physical meaning of Eqn. 2.7. The lighter dumbbell represents charge cloud angular distribution excited by electron collision, and the darker one is excited by a linear-polarized laser beam. The magnitude of the overlapping of these two wavefunctions is proportional to superelastic-scattering intensity.

with clear physical meaning is given in Figure 2.5. The superelastic signal intensity is determined by the overlap between the wavefunctions of the excited states produced by laser pumping and the one produced by the inelastic electron collision.

## 2.4 Discussion about Spin Effects

We are interested in the investigation of electron inelastic excitation of two-electron atoms (ground state  $^1S_0$ ). Since electron spin selection and analysis are not performed during the scattering, the fully coherent excitation corresponds to the case where the total spin ( the summation of projectile electron spin and the target electron spin) is conserved during the electron-atom interaction. In this case, the total spin is uncoupled with the atomic angular momentum and the fully detailed information about the atomic excitation process can be obtained. This is a good approximation for light atoms. But for heavier systems, where spin-orbit coupling effects can be important, this assumption may no longer be valid.

Relativistic effects are responsible for the spin-orbit coupling and can be treated by the Breit equation for small  $Z$  and by the Pauli approximation for large  $Z$  (Bethe1957). This method can be used to consider a system of two interacting electrons in an electrostatic potential due to the nucleus. Relativistic effects are represented as a perturbation expansion in the fine-structure constant  $\alpha$  about the nonrelativistic solutions to the specific problem, and the lowest-order terms retained. Among the terms that do not commute with the total spin of the system, the spin-orbit interaction, which is the coupling of the spin and orbital angular momenta of the same electron in the electrostatic field of the nucleus, is likely to be the dominant term for

low-energy electron-atom collisions. Since the spin-orbit interaction does not commute with the total spin, it is responsible for the spin-flip of the total spin. This force may affect the electron-atom excitation process in two aspects:

1) The spin of the projectile electron couples with its own orbital angular momentum under the influence of the electric field due to the atomic core if the projectile electron comes close enough to the nucleus. This interaction can result in the spin-flip of the projectile electron during collision and change the polarization of the incident electron beam. The total spin of the free electron - atom system is no longer conserved. The change of the total spin will couple with the atomic system and the atomic orbital angular momentum may be changed to maintain conservation of the total angular momentum of the free electron - atom system. Because of the spin-flip, spin-up and spin-down electrons may have different excitation amplitudes. If we do not perform spin selection and analysis in our experiment, spin-up and spin-down scattering contribute incoherently and we therefore lose some information associated with spin polarization.

2) The spin of the atomic electron couples with its own orbital angular momentum. This can affect the scattering process when electron exchange takes place. For light atoms, the spin-orbit coupling is very small in general. The basic argument for this is the so-called Percival-Seaton hypothesis (Percival 1958). The fine-structure splitting in light atoms is about  $10^{-3}$  to  $10^{-4}$  eV. Correspondingly the spin precession time due to the spin-orbit interaction is in the order of  $10^{-12}$ s. It should be compared with the collision time for an electron-scattering process, the time for the projectile electron to pass a typical diameter of the atom,  $10^{-15}$ s. These time scales are the justification of the sudden approximation. During the short collision

time, spin and orbital angular momentum of the atom are considered to be at rest because of the slow precession. As a consequence the spin-orbit interaction of the atomic electrons can be completely neglected and LS-coupling can be assumed during the collision.

On the other hand, the Percival-Seaton hypothesis can not be applied to heavy atoms due to the strong spin-orbit interaction of atomic electrons. The spin may change its orientation and spin-flip of the atomic electrons may happen. Thus LS-coupling scheme can no longer hold during the collision.

For light atoms, spin-orbit interaction does not appear and the total spin of the free electron - atom system is conserved. Therefore the reflection symmetry of the atomic wave function with respect to the scattering plane is also conserved during the collision. Only substates of the excited state that have the same reflection symmetry as the ground state can be populated. This condition results in the elimination of the substates with reflection symmetry different from the initial ground state. For heavy atoms, both mechanisms of spin-orbit interaction can cause spin nonconservation of the total spin. The assumption of conservation of reflection symmetry with respect to the scattering plane for the excited atomic wave function can not be maintained. This allows the excitation from the ground state to all possible sublevels of the excited state. We can easily conclude that if spin-orbit interaction takes place, more quantities have to be measured to completely characterize the collisional excitation process. The reader can also refer to (Walker1976) and (Hanne1988) for detailed information about spin effects.

## 2.5 Characterization of Electron Impact Excitation by Density Matrix

It has been shown that the inelastic electron impact excitation can be characterized by bilinear products of scattering amplitudes. The expression of the spin averaged scattering density matrix elements have been given in Eqn. 2.3. For the  $J = 0$  to  $J = 1$  transition, they form a  $3 \times 3$  matrix

$$\rho(J=1) = \begin{pmatrix} \langle |f(+1)|^2 \rangle & \langle f(+1)f(0)^* \rangle & \langle f(+1)f(-1)^* \rangle \\ \langle f(0)f(+1)^* \rangle & \langle |f(0)|^2 \rangle & \langle f(0)f(-1)^* \rangle \\ \langle f(-1)f(+1)^* \rangle & \langle f(-1)f(0)^* \rangle & \langle |f(-1)|^2 \rangle \end{pmatrix} \quad 2.12$$

Now we investigate how many independent density elements are needed to fully describe an excitation process. Comprehensive discussions are given in (Blum1981) and (McDaniel1991). In Eqn. 2.12, the diagonal matrix elements are real ( corresponding to the differential cross sections of three magnetic sublevels), but the off-diagonal matrix elements are complex, with two real components, namely, magnitude and phase ( corresponding to the interference terms between scattering amplitudes to various magnetic sublevels). There are in total fifteen real elements in the matrix. The number of independent elements is reduced by the hermiticity condition

$$\langle f(M')f^*(M) \rangle = (\langle f(M)f^*(M') \rangle)^* \quad 2.13$$

to nine independent elements.

In addition, the scattering plane is defined by incident electron direction  $k_0$  and outgoing electron direction  $k_f$  (see Fig. 2.1) but no direction

is defined perpendicular to the scattering plane by the geometry of the experiment, that is, the atomic subensemble under discussion can not distinguish between "up" and "down" with respect to this plane. As a result, the density matrix must be invariant under reflection with respect to the scattering plane. This symmetry condition is expressed by the relation

$$\langle f(M')f^*(M) \rangle = (-1)^{M'+M} \langle f(-M')f^*(-M) \rangle \quad 2.14$$

and the number of independent elements is reduced to five.

The number of independent elements can be further reduced if spin conservation is taken into account. In this case, all explicit spin-dependent terms have been neglected in the Hamiltonian describing the collision. Total spin and its z component are conserved during the collision. It can be shown that (Chapter 3, Blum1981)

$$\langle f(M')f^*(-M) \rangle = (-1)^M \langle f(M')f^*(M) \rangle \quad 2.15$$

and the density matrix is completely specified by four independent elements.

A smaller number of independent elements is required if initial and final atoms are spinless. In this case only one spin channel with total spin 1/2 is allowed and no spin average is necessary

$$\langle f(M')f^*(M) \rangle = f(M')f^*(M) \quad 2.16$$

A single wave function can be used to characterize the quantum state produced by the impact excitation. This corresponds to a fully coherent excitation process in which both initial and final states are pure. The number

of independent matrix elements in this special case can be further reduced to three.

In order to obtain complete information about the impact excitation process, the number of measured quantities ( or parameters) required for each particular excitation should be equal to the number of independent parameters specifying the density matrix. In general, five independent parameters are required to fully characterize the p-state excitation process if spin-orbit interaction exists. In the particular case of  $^1S_0$  to  $^1P_1$  excitation without the spin-orbit force involved, three independent parameters are needed to extract all bilinear terms  $f(M')f^*(M)$ , and eventually to extract the magnitude and phase of each scattering amplitude.

## 2.6 The Measurement Quantities - Differential Cross Sections and Electron Impact Coherence Parameters

In the last section, we have discussed the number of independent density matrix elements required to describe a collisional excitation process. Now we will define the physical observables that can be measured in scattering experiments, namely differential cross section (DCS) and electron impact coherence parameter (EICP), and give their relations to scattering amplitudes.

The DCS for a specific transition ( $\Gamma_0 \rightarrow \Gamma_1$ ) is defined as

$$DCS(\Gamma_0 \rightarrow \Gamma_1, \theta, E_0) = \sigma$$

$$= \frac{\text{scattered electron intensity}}{\text{incident electron flux} \times \text{number of target atoms}} \quad 2.17$$

where  $\theta$  is the scattering angle and  $E_0$  the kinetic energy of the incident electrons. Its dimension is  $\text{cm}^2/\text{sr}$ . The DCS represents the probability of a specific collisional excitation in a target by an incident electron with a given kinetic energy scattered to a certain scattering angle. For S to P excitation, the DCS for excitation of the various magnetic sublevels are given by the diagonal matrix elements  $\langle |f(M)|^2 \rangle$  ( $M = -1, 0, 1$ ). The trace of the density matrix gives an observable - the differential cross section

$$\sigma = \sum_{M=-1}^1 \langle |f(M)|^2 \rangle \quad 2.18$$

The physical meaning of the EICP is associated with the atomic electron charge cloud distribution of the excited state. We are interested in the atomic alignment and orientation of excited p states after the collision. Here alignment means the shape of the excited state charge cloud and its direction of alignment in space, and orientation is the angular momentum transferred to the atom during the course of the collision. Fig. 2.6 depicts the angular part of an excited P-state charge cloud distribution along with the definitions of the relative length ( $l$ ) width ( $w$ ) and height ( $h$ ) of the charge cloud. This charge cloud distribution has an alignment, i.e., its charge distribution is found in a nonisotropic shape with the expectation value of each magnetic substate  $\langle M^2 \rangle \neq \langle J^2 \rangle / 3$ . It also has an orientation, i.e., a finite expectation value of its angular momentum. For symmetry reasons, the angular momentum of the relative motion between projectile electron and target atom can only be transferred perpendicular to the collision plane. Thus, if the target atoms have no initial orientation, the final angular momentum of the atom will be perpendicular to the scattering plane. The

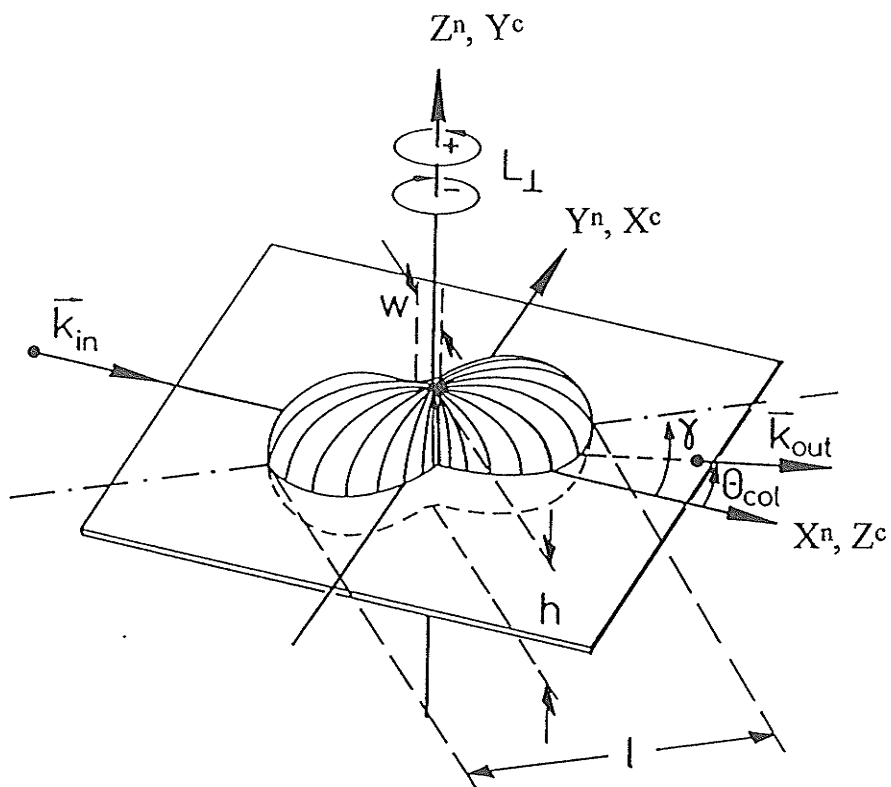


Figure 2.6. A 3-D side view of the angular part of an excited charge cloud in a p-state atom. The atom is characterized by the relative length ( $l$ ), width ( $w$ ) and height ( $h$ ), by its alignment angle  $\gamma$  and by its inherent angular momentum ( $L_{\perp}$ ). The collisional coordinate frames are illustrated. ( $x^a, y^a, z^a$ ) indicates the atomic frame, ( $x^n, y^n, z^n$ ) the natural frame, and ( $x^c, y^c, z^c$ ) the collision frame. Adopted from (Andersen 1988).

EICP are the parameters used to describe this detailed information about the excited atoms. These parameters are related to both diagonal and off-diagonal elements  $f(M')f^*(M)$  of the scattering density matrix.

The EICP have been defined in two coordinate frames as shown in Figure 2.6.

1) The Collision Frame (labeled in "c"). Its  $z^c$  axis is parallel to the incoming electron momentum vector  $k_{in}$ , its  $x^c$  axis is defined such that  $k_{out}$  points into the first or the second quadrant of the  $(x^c, y^c)$  plane. It is conventionally used in theoretical scattering calculations.

2) The Natural Frame (labeled in "n"). Its  $z^n$  axis is perpendicular to the scattering plane and along with the direction of positive angular momentum transfer. Its  $x^n$  axis is parallel to the incoming electron momentum vector  $k_{in}$ . Because of its connection with the symmetry of the problem, the quantities defined in this frame have explicit physical meanings and therefore it is the favored coordinate frame for experimental work.

We will concentrate on the EICP defined by Andersen et al (Andersen1988) in the natural frame. In the following, we will introduce the definition of EICP and their relations to scattering amplitudes for the electron impact excitation of P level in two-electron atoms.

1) The electron impact excitation of P state with conservation of atomic reflection symmetry

The most widely studied case in the field of electron-atom collision studies is the electron impact excitation of light atoms from singlet S state to singlet P state. For light atoms, the LS-coupling scheme can be assumed and

the influence of the spin-orbit interaction during the collision is neglected ( Percival Seaton hypothesis). Thus, the spin of the system is conserved and its orientation in space remains fixed. Since the total spin and the atomic electron orbital momentum are uncoupled, the excitation process is thus fully coherent and the excited state may be described by a linear superposition of magnetic substates of the P state

$$|{}^1P_1\rangle = f_{+1}^n|+1\rangle + f_0^n|0\rangle + f_{-1}^n|-1\rangle \quad 2.19$$

where the superscript  $n$  indicates the natural frame in which the quantization axis  $z^n$  is perpendicular to the scattering plane and  $f_M^n$  refers to the normalized scattering amplitude for the collisional excitation to  $M$  substate. We assume these amplitudes to be normalized to unity

$$|f_{+1}^n|^2 + |f_0^n|^2 + |f_{-1}^n|^2 = 1 \quad 2.20$$

and they are related to the standard scattering amplitudes  $f(M)$  by

$$f_M = \frac{f(M)}{\sigma^{1/2}} \quad 2.21$$

where  $\sigma$  refers to the differential cross section.

Furthermore, since the total spin is conserved, the reflection symmetry of the atomic wave function with respect to the scattering plane is conserved during the collision. Since the initial isotropic  ${}^1S_0$  state has positive reflection symmetry, all excited magnetic substates of  ${}^1P_1$  must also have positive

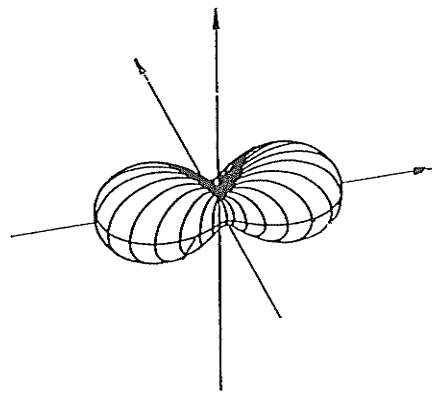
reflection symmetry. This implies that the excitation of  $|0\rangle$  is not allowed because of its negative symmetry. State 2.19 can be written as

$$|{}^1P_1\rangle = f_{+1}''|+1\rangle + f_{-1}''|-1\rangle \quad 2.22$$

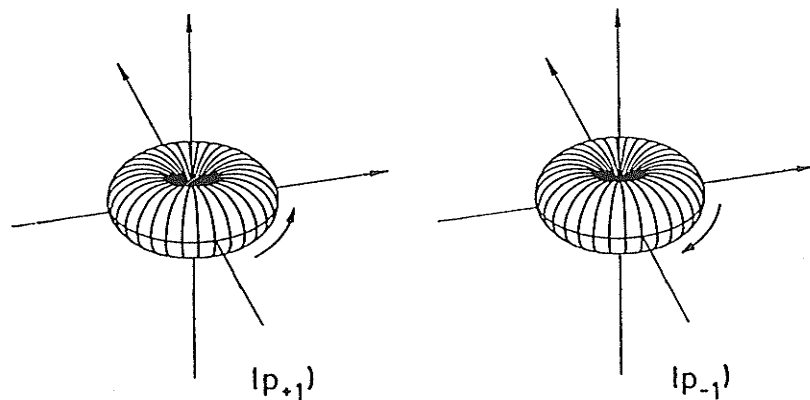
The angular part of the charge cloud density of this excited state is schematically illustrated on Fig.2.7a. In this case, the charge cloud density is composed of  $|+1\rangle$  with angular momentum +1 (we use atomic units, i.e.,  $\hbar = 1$ ) and  $|-1\rangle$  with angular momentum -1 perpendicular to the scattering plane (see Fig.2.7b). The scattering amplitudes  $f_{+1}''$  and  $f_{-1}''$  govern the alignment and orientation of the charge cloud. If  $f_{+1}'' > f_{-1}''$ , then the +1 component is dominant and the excited state has angular momentum expectation value  $1 > \langle L_z \rangle > 0$ . If  $f_{-1}'' > f_{+1}''$ , then the -1 component is dominant and  $-1 < \langle L_z \rangle < 0$ . It is worth pointing out that since  $f_0'' = 0$ , the relative height of the charge cloud is zero.

We now define the parameter of transferred angular momentum  $L_{\perp}$  in natural coordinate frame. Here  $\perp$  indicates that the angular momentum is transferred perpendicular to the scattering plane.  $L_{\perp}$  is defined as the expectation value of the angular momentum perpendicular to the scattering plane transferred to the atom during the collision. We can express  $L_{\perp}$  in terms of scattering amplitudes  $f_M''$

$$\begin{aligned} L_{\perp} &= \langle L_z \rangle \\ &= |f_{+1}''|^2 - |f_{-1}''|^2 = 2|f_{+1}''|^2 - 1 \end{aligned} \quad 2.23$$



(a)



(b)

Figure 2.7. The formation of an excited P-state (a) by superposing a  $|+\rangle$  state with angular momentum  $+1$  and a  $|-\rangle$  state with angular momentum  $-1$  (b). The shape and alignment of the angular part of the charge cloud density depend on the scattering amplitudes  $f_{+1}$  and  $f_{-1}$ .

The parameter of charge cloud anisotropy or charge cloud linear polarization  $P_l$  represents the degree of linear polarization of the excited atomic charge cloud and is given by

$$P_l = \frac{|\psi|_{\max}^2 - |\psi|_{\min}^2}{|\psi|_{\max}^2 + |\psi|_{\min}^2} \quad 2.24$$

$$= 2|f_1^n||f_{-1}^n|$$

where  $\psi$  refers to the wave function of the atom  $\langle x | P_l \rangle$ , with  $|P_l\rangle$  given by Eqn.2.22. It can be also expressed in terms of the relative length and width of the charge cloud density specified on Fig. 2.6

$$P_l = l - w \quad \text{with} \quad l + w = 1 \quad 2.25$$

or

$$l = \frac{1}{2}(1 + P_l) \quad \text{and} \quad w = \frac{1}{2}(1 - P_l) \quad 2.25'$$

The charge cloud alignment angle is the angle between the incident electron vector  $k_{in}$  and the maximum of the charge cloud density distribution (see Fig. 2.6).  $\gamma$  is linearly related to the phase difference between the amplitudes  $f_{+1}^n$  and  $f_{-1}^n$  in the natural frame.

$$\gamma = -\frac{1}{2} \arg(f_1^n f_{-1}^{n*}) \quad 2.26$$

It can be proven that  $P_l$  and  $L_l$  are related by

$$P_l^2 + L_l^2 = 1 \quad 2.27$$

Here we have defined the degree of polarization  $P^+$ . If  $P^+ = 1$ , the collisional excitation is said to be fully coherent and spin dependence in the collision is negligible. So  $P_l$  and  $\gamma$ , or  $L_\perp$  and  $\gamma$  along with the differential cross section  $\sigma$  can be used to completely describe the electron impact excitation from  $^1S_0$  to  $^1P_1$ , which only requires three independent density matrix elements.

If these coherence parameters and differential cross section are known, the complete information about the excitation can be obtained. The density matrix 2.12 can be expressed in terms of these parameters

$$\rho(^1P_1) = \frac{\sigma}{2} \begin{pmatrix} 1 + L_\perp & 0 & -P_l \exp(2i\gamma) \\ 0 & 0 & 0 \\ -P_l \exp(-2i\gamma) & 0 & 1 - L_\perp \end{pmatrix} \quad 2.28$$

where the natural coordinate frame has been used.

In practice, we can employ two sets of laser direction and polarization geometry  $(\theta_\lambda, \phi_\lambda, pol)$  in the superelastic scattering experiment to measure  $P_l$ ,  $\gamma$ , and  $L_\perp$ . The absolute value of scattering amplitudes can be determined from an additional measurement of the differential cross section  $\sigma$ .

2) The electron impact excitation of P state without conservation of atomic reflection symmetry

In general, the assumption of positive reflection symmetry for the wave function of the excited state with respect to the scattering plane can not be maintained during the collision. It may happen in electron impact excitation of a heavy atom that spin-orbit effects are so strong that they flip

the orientation of the total spin, thereby allowing population of the substate with negative reflection symmetry. Furthermore, since LS-coupling does not necessarily hold for the heavy atoms, the total angular momentum of the excited state  $J$  will be used to describe the excited state. We here study transitions from an isotropic  $^1S_0$  ground state to  $J = 1$  excited states that can be considered as a linear combination of  $^1P_1$  and  $^3P_1$  states ( so-called "intermediate" coupling scheme). Now the excitation from initial state  $^1S_0$  to magnetic substate  $|0\rangle$  in the natural frame ( $J = 1, M_J = 0$ ) is allowed.

In the natural frame  $M_J = \pm 1$  magnetic substates have positive reflection symmetry and are thus excited in transitions with conservation of total spin.  $f_{M_J}^n$  ( $M_J = \pm 1$ ) represents the scattering amplitude of the excitation without flip of the total spin and  $\langle f_{M_J}^n f_{M_J}^{n*} \rangle$  is the corresponding density matrix element where the bracket indicates the average over initial and sum over final spins since the spin of the projectile electron is unobserved. We can still define coherence parameters  $P_i^+$ ,  $\gamma$ , and  $L_1^+$  in the similar way as what we did from Eqn. 2.23 through Eqn. 2.26 to describe the electron collisional excitation to states with positive reflection symmetry. But we add a superscript "+" to refer to the positive reflection symmetry. We should also note that these parameters are used to describe the excitation to a  $|JM_J\rangle$  state.

The  $M_J = 0$  magnetic substate has negative reflection symmetry and is excited in transitions without conservation of the total spin.  $f_0^n$  represents the scattering amplitude of the excitation with flip of the total spin and  $\langle f_0^n f_0^{n*} \rangle$  is the corresponding density matrix element. We now define a new parameter

$$\rho_{00} = 2|f_0^n|^2 \quad 2.29$$

$\rho_{00}$  is called the height parameter and gives the relative probability for spin flip perpendicular to the scattering plane. Coherence parameters  $P_l^+$ ,  $\gamma$ , and  $L_{\perp}^+$  form the positive reflection symmetric part of the density matrix, while  $\rho_{00}$  forms the negative reflection symmetric part. The density matrix in the natural frame takes the following form

$$\rho(J=1) = \frac{\sigma}{2}(1 - \rho_{00}) \begin{pmatrix} 1 + L_{\perp}^+ & 0 & -P_l^+ \exp(2i\gamma) \\ 0 & 0 & 0 \\ -P_l^+ \exp(-2i\gamma) & 0 & 1 - L_{\perp}^+ \end{pmatrix} + \sigma \rho_{00} \begin{pmatrix} 0 & 0 & 0 \\ 0 & 1 & 0 \\ 0 & 0 & 0 \end{pmatrix} \quad 2.30$$

Eqn.2.30 shows the decomposition of the density matrix into two parts. The first part has positive reflection symmetry with respect to the scattering plane and gives information about the scattering under conservation of the total spin. The second part has negative reflection symmetry and represents the scattering associated with spin-flip. The degree of polarization is less than or equal to 1

$$P^+ = \sqrt{(P_l^+)^2 + (L_{\perp}^+)^2} \leq 1 \quad 2.31$$

This implies that  $P_l^+$  and  $L_{\perp}^+$  are independent parameters. For the electron impact excitation of atoms with spin-orbit interaction, four independent electron impact coherence parameters and the differential cross section are needed to fully describe the excitation process. They are  $P_l^+$ ,  $L_{\perp}^+$ ,

$\gamma$ ,  $\rho_{00}$  and  $\sigma$ . Among them, the height parameter  $\rho_{00}$  is associated with spin-orbit interaction. The physical picture of  $\rho_{00}$  is shown in Fig. 2.6 where  $\rho_{00}$  represents the relative height of the charge cloud density  $h$ . The relative length, width and height of the charge cloud are related to EICP by

$$\begin{aligned} l &= (1 - \rho_{00})^{\frac{1}{2}}(1 + P_l^+) \\ w &= (1 - \rho_{00})^{\frac{1}{2}}(1 - P_l^+) \\ h &= \rho_{00} \end{aligned} \quad 2.32$$

with

$$l + w + h = 1$$

In a real superelastic measurement, four sets of laser direction and polarization geometry have to be used to determine  $P_l^+$ ,  $L_{\perp}^+$ ,  $\gamma$  and  $\rho_{00}$  parameters that, along with the differential cross section  $\sigma$ , completely characterize the excitation process in case that spin-orbit interaction is not negligible.

An alternative set of electron impact coherence parameters was introduced by Blum et al. (Blum1980) and da Paixao et al. (da Paixao1980) in the collision coordinate frame. In the case of collisional excitations to P state with spin conservation, three independent parameters  $\sigma$ ,  $\lambda$  and  $\chi$  are required to describe this transition. Among them,  $\sigma$  is the differential cross section of the excitation to  $L = 1$  state and can be considered as the sum of differential cross sections for all magnetic sublevels in the collision frame  $\sigma = \sigma_0^c + 2\sigma_1^c$ .  $\lambda$  and  $\chi$  are defined as

$$\lambda = \frac{|f_0^c|^2}{|f_0^c|^2 + 2|f_1^c|^2} \quad 2.33$$

and

$$\chi = \arg\left(\frac{f_1^c}{f_0^c}\right) \quad 2.34$$

$\lambda$  is the projection of the charge cloud angular distribution onto the  $z^c$  axis and  $\chi$  represents the phase difference between scattering amplitudes  $f_1^c$  and  $f_0^c$ .

Sometimes it is more convenient to use Stokes parameters of the time-correlated photon to describe a P-state inelastic collisional excitation (Born1970). In a coincidence experiment, Stokes parameters are defined in terms of electron-photon coincidence intensities

$$P_1 = \frac{I(0^\circ) - I(90^\circ)}{I(0^\circ) + I(90^\circ)} = -2\text{Re}(f_1^n f_{-1}^{n*}) \quad 2.35$$

and

$$P_2 = \frac{I(45^\circ) - I(135^\circ)}{I(45^\circ) + I(135^\circ)} = 2\text{Im}(f_1^n f_{-1}^{n*}) \quad 2.36$$

where  $I(\psi)$  is the electron-photon coincidence intensity and  $\psi$  the polarization angle of linear polarized light with respect to the forward scattering direction, and

$$P_3 = \frac{I(\text{RHC}) - I(\text{LHC})}{I(\text{RHC}) + I(\text{LHC})} = |f_{-1}^n|^2 - |f_1^n|^2 \quad 2.37$$

where RHC and LHC refer to right-handed and left-handed circularly polarized light, respectively. The relationships between  $\{P_1, L_\perp, \gamma\}$  and the  $\{P_1, P_2, P_3\}$  in the fully coherent case are given by

$$P_1 + iP_2 = P_1 \exp(2i\gamma) \quad 2.38$$

and

$$P_3 = -L_\perp \quad 2.39$$

while the connections between  $\{\lambda, \chi\}$  and  $\{P_1, P_2, P_3\}$  are

$$P_1 = 2\lambda - 1 \quad 2.40$$

$$P_2 = -2\sqrt{\lambda(1-\lambda)} \cos \chi \quad 2.41$$

and

$$P_3 = 2\sqrt{\lambda(1-\lambda)} \sin \chi \quad 2.42$$

If the spin-orbit interaction is not negligible during the excitation, the fourth Stokes parameter  $P_4$  must be introduced to fully describe the collision process (Andersen1979).  $P_4$  refers to the measurement of time-correlated photon in the scattering plane and is related to the height parameter  $\rho_{00}$  (Andersen1988).

## 2.7 Theoretical Prediction of EICP by First Born Approximation

A projectile electron interacts with the target potential and is scattered at different polar angles as shown in Fig. 2.8. In the presence of a central potential, the scattered electron flux is axially symmetric along the incident beam direction and is independent of angle  $\phi$ . Since the incident electrons are monoenergetic and travel in  $z$  direction with wave vector  $k_0$ , the incident beam can be represented by a plane wave

$$F_0 \sim e^{ik_0 z} \quad 2.43$$

and the outgoing wave function for elastic and inelastic scattering takes the asymptotic form when  $r \rightarrow \infty$

$$F_0 \sim e^{ik_0 z} + f_0(\theta) \frac{e^{ik_0 r}}{r} \quad (\text{elastic scattering}) \quad 2.44$$

and

$$F_n \sim f_n(\theta) \frac{e^{ik_n r}}{r} \quad (\text{inelastic scattering}) \quad 2.45$$

We can then expand the wave function in terms of the complete set of eigenfunctions of the unperturbed atom  $u_n(r_{a1} \cdots r_{aN})$  and projectile electron wave function  $F_n(r_b)$

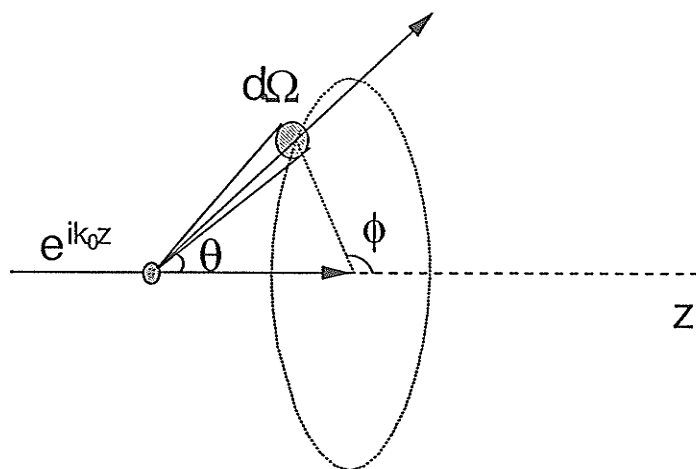


Figure 2.8. A diagram showing the electron scattering procedure. The plane wave  $\exp(ik_0z)$  represents the incident electron wavefunction.  $(\theta, \phi)$  is the polar angles. The scattered electron flux has axial symmetry about the z-axis.

$$\Psi(r_b, r_a) = \left( \sum_n + \int \right) u_n(r_{a1} \cdots r_{aN}) F_n(r_b) = S u_n(r_{a1} \cdots r_{aN}) F_n(r_b) \quad 2.46$$

where  $r_{ai}$  and  $r_b$  are the  $i$ th atomic electron coordinates and the beam electron coordinates,  $N$  is the number of atomic electrons, and the functions  $u_n(r_a)$  satisfy the Schrodinger equation for electrons in an unperturbed atomic potential. The perturbation potential resulting from the electron beam scattering from the atomic target can be given by  $\Delta V$  which contains the projectile electron potential energy term and the projectile electron-atom electron interaction term. By bringing Eqn. 2.46 into Schrodinger equation, we obtain

$$\left( \nabla_{r_b}^2 + \kappa_n^2 - \frac{2m_e}{\hbar^2} V_{nm} \right) F_n(r_b) = \frac{2m_e}{\hbar^2} S' V_{nm} F_m(r_b) \quad 2.47$$

where the prime indicates that the term  $m = n$  is to be omitted in the summation,  $\kappa_n$  is the wave number, and  $V_{nm}$  is defined as the matrix element

$$V_{nm} = \int u_n^*(r_{a1} \cdots r_{aN}) \Delta V u_m(r_{a1} \cdots r_{aN}) dr_{a1} \cdots dr_{aN} \quad 2.48$$

We have now an infinite set of coupled differential equations to solve in order to obtain the asymptotic form of the wave functions  $F_n(r_b)$ . Clearly, approximate methods must be used. The approximations consist of selecting only the most important matrix elements and putting all the others equal to zero.

The following basic assumptions are made for the first Born approximation (FBA) that was first introduced by Born in 1926 (Born1926):

1) The incident wave is undistorted by the interaction, so that we may represent the beam electron by an undistorted plane wave moving along the direction of incident electron  $n_0$ .

$$F_0(r_b) = \exp(i\kappa_0 n_0 \cdot r_b) \quad 2.49$$

2) Excitation to any final state  $n$  comes as the result of direct transition from the initial state, and intermediate states play no significant role, i.e. there is no coupling with intermediate states and  $V_{mn} = 0$  for  $m \neq 0$ , where  $m$  designates the initial state.

3) The potential energy of interaction between the scattered electron that produced the excitation and the atom in its initial state is small, so that distortion of the scattered wave can be neglected and thus  $V_{m0} = 0$

Under these assumptions, the set of Eqns 2.47 reduces to a single equation for excitation to state  $n$

$$(\nabla_b^2 + \kappa_n^2)F_n(r_b) = \frac{2m_e}{\hbar^2} V_{0n} \exp(i\kappa_0 n_0 \cdot r_b) \quad 2.50$$

with the boundary conditions

$$\begin{aligned} F_n(r_b) &\sim \frac{1}{r_b} f_n(\vartheta) \exp(i\kappa_n n_n \cdot r_b) \\ F_n(0) &= 0 \end{aligned} \quad 2.51$$

Under FBA, the incident and scattered particles are treated as plane waves  $e^{i\kappa_i r}$  and  $e^{i\kappa_f r}$  that remain undistorted by the interaction. Only forward transitions between the initial and final states  $i$  and  $f$  are considered,

and electron exchange and spin effects are not taken into account. A single equation provides the solution to the scattering problem and no coupled equations are involved. The FBA is valid for high-velocity impacts or small scattering angles that correspond to the small momentum transfer or the large impact parameter (long range scattering force).

Since both incident and scattered waves are considered as plane waves with linear momentum  $\kappa_i$  and  $\kappa_f$ , the amount of linear momentum transferred from projectile electron to target atom is  $\Delta\kappa = \kappa_f - \kappa_i$ . Thus the charge cloud of the excited atom has axial symmetry along  $\Delta\kappa$  in FBA. Since we start with singlet S state, the excited state is a pure p-orbital in the direction of  $\Delta\kappa$  with zero angular momentum transferred.

$$L_{\perp}^{(FBA)} = 0 \quad 2.52a$$

$$P_l^{(FBA)} = 1 \quad 2.52b$$

The alignment angle can be easily obtained from the vector geometry in Fig 2.9

$$\gamma^{(FBA)} = \tan^{-1}\left(\frac{\sin\theta_{col}}{\cos\theta_{col} - x}\right) \quad 2.52c$$

where  $x = [E_0 / (E_0 - \Delta E)]^{1/2}$  with  $E_0$  and  $\Delta E$  denoting impact energy and energy loss.

The experimental results show that at low impact energy and large scattering angles, FBA fails completely.  $\gamma$  does not follow FBA prediction,  $L_{\perp}$  may no longer be zero and  $P_l$  may be less than unity. At around the

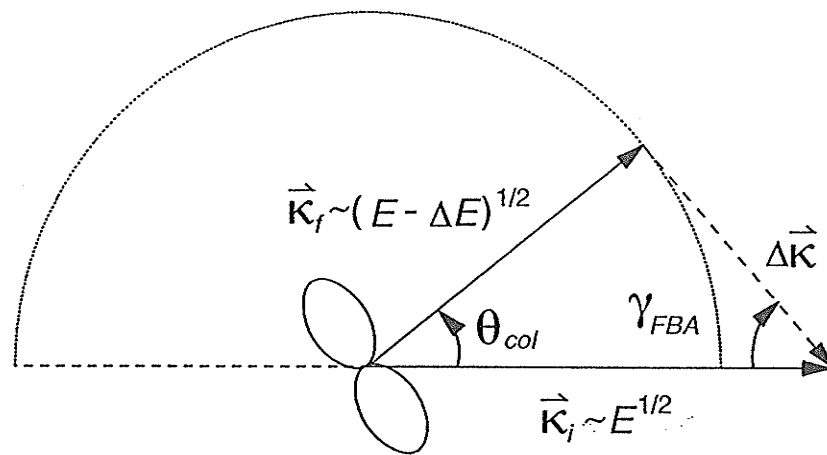


Figure 2. 9. A diagram for evaluating the alignment angle  $\gamma$  in the first Born approximation, in which the charge cloud of the excited state is purely linearly polarized ( $P_l = 1$  and  $L_l = 0$ ).

minimum of  $\gamma$  predicted by FBA,  $\gamma$  often has a drastic change and rotates even further, while  $L_{\perp}$  rises to its maximum and  $P_l$  drops down to its minimum. All these indicate that at low impact energy and large scattering angle which is associated with the deep penetration of scattered electron into target atom, the angular momentum transfer from projectile to target takes place and the excited target atom is actually not a pure p-orbital. The charge cloud does not align along the direction of linear momentum transfer.

The overall observed behavior of  $L_{\perp}$  in helium, the simplest two-electron atom, is summarized as following: The  $\theta_{col}$  can be divided into two regions; one region at small angles for which  $L_{\perp} > 0$  and another at large angles where  $L_{\perp} < 0$ . In between there is an angle for which  $L_{\perp} = 0$ . For symmetry reasons,  $L_{\perp} = 0$  at  $\theta_{col} = 0^{\circ}$  and  $180^{\circ}$ . This discussion can provide us with a qualitative picture of the variation of  $L_{\perp}$  against scattering angle and allows us to make some rough prediction on the behavior of coherence parameters  $L_{\perp}$ ,  $P_l$  and  $\gamma$ .

Any theoretical effort beyond FBA involves serious computations because one has to deal with the infinite set of coupled differential equations (Eqn.2.50). As the impact energy decreases, improved approximations can be made by considering more terms on the right side of Eqn. 2.50. The Distorted Wave Approximation (DWA) ignores transitions through intermediate states as does the FBA but takes account of the distortion of the incident and scattered waves by the static field of the target. By introducing a distortion potential, the distorted incident and scattered electron waves can be calculated (instead of plane waves). These wave functions are then used to carry out the first-order perturbation. A variety of distorted wave calculations have been developed to predict electron-atom scattering. A comprehensive discussion about DWA is given by Itikawa

(1986). At low incident electron energies, the close coupling calculation (CC) can give excellent results. In the CC approximation, the expansion (Eqn. 2.46) is truncated and a relatively small number of closely coupled terms are retained. Only a number of closely coupled equations have to be solved. This approximation can give accurate results at low electron energies if all of the target states lying close to the initial and final states in energy are included. The basic theoretical principle of CC can be found in Henry (1988). In the case of heavy atoms, spin-orbit interaction becomes important and relativistic effects should be taken into account. The relativistic distorted wave calculations (RDW) have been performed by including the relativistic correction terms (Zuo1991). The Dirac equation is solved in the presence of a distorted potential and the atomic and the projectile electrons are treated fully relativistically. All these theories can, to different extent, successfully predict the non zero transferred angular momentum ( $L_{\perp} \neq 0$ ), the less than 1 charge cloud anisotropy ( $P_l \leq 1$ ), and the sudden change in alignment angle ( $\gamma$ ) for targets from He to heavy atoms. However, as we will see in later chapters, these first-order perturbation theories do show considerable disagreement with experiments in predicting DCS and EICP at low impact energies and at large scattering angles.

## CHAPTER 3

### APPARATUS

#### 3.1 Introduction

In this Chapter, the description of the entire experimental apparatus for our electron scattering experiments will be given. For convenience of discussion, the apparatus is divided into six functional sub-systems and each of them is discussed in detail in different sections. Only a general description of the apparatus is included in this chapter. Parts of the apparatus may be modified for each particular experiment and details will be given in the following chapters. This chapter is organized as follows: 1) General description of the apparatus, 2) Vacuum system, 3) Laser and optical system, 4) Data collection system, 5) Electron spectrometer, 6) Electronics, 7) Metal vapor sources. The first section shows the overall system design and the functions of the apparatus. In section 2, the descriptions of vacuum chamber, vacuum pumps and gas handling system are given. The optical system including argon laser, ring dye laser and other optical components is described in section 3. In section 4, the channeltron multiplier, the electronics for data collection, computer controlled multi-channel scaler and the related software development are discussed. In section 5, the detailed design theory, construction and performance of electron guns and analyzer are given. The

electronics for the electron spectrometer is described in section 6. In the last section, the design and performance of metal vapor ovens is shown.

### **3.2 General Description of the Apparatus**

A schematic diagram of the entire apparatus is shown in Figure 3.1. At the heart of the apparatus (see Figure 3.2), incident electron and polarized laser beams interact with a metal vapor beam produced by an oven. The scattered electrons are detected by an electron energy analyzer. A channeltron multiplier is attached to the end of exit lens of the energy monochromator to detect electrons. The electron beam and detector view cone define the scattering plane and interaction center. Laser beam and target beam must be aligned at the interaction center. The electron beam is produced by a tungsten filament and is accelerated and focused in an electron gun. The linearly polarized laser beam comes from a ring dye laser pumped by an argon ion laser and passes a retardation plate that can be used to control the electric field vector of the light at the interaction region. Either electron gun or detector can be mounted on a stainless steel rotatable table coupled with a gear wheel that is attached on a feedthrough shaft and accessible from outside the vacuum chamber. A Faraday cup and a gas nozzle are also constructed and aligned at the interaction center. The Faraday cup is used for electron gun tuning and current calibration. The gas nozzle is installed to introduce helium or nitrogen for preliminary gun tuning and impact energy calibration.

The electron gun, detector, metal vapor source, rotatable table, Faraday cup and gas nozzle are housed in a stainless steel chamber. Several viewports are used to pass laser beam in different directions. The possible laser incident directions can be  $90^\circ$ ,  $45^\circ$  or  $0^\circ$  (in plane) with respect to the

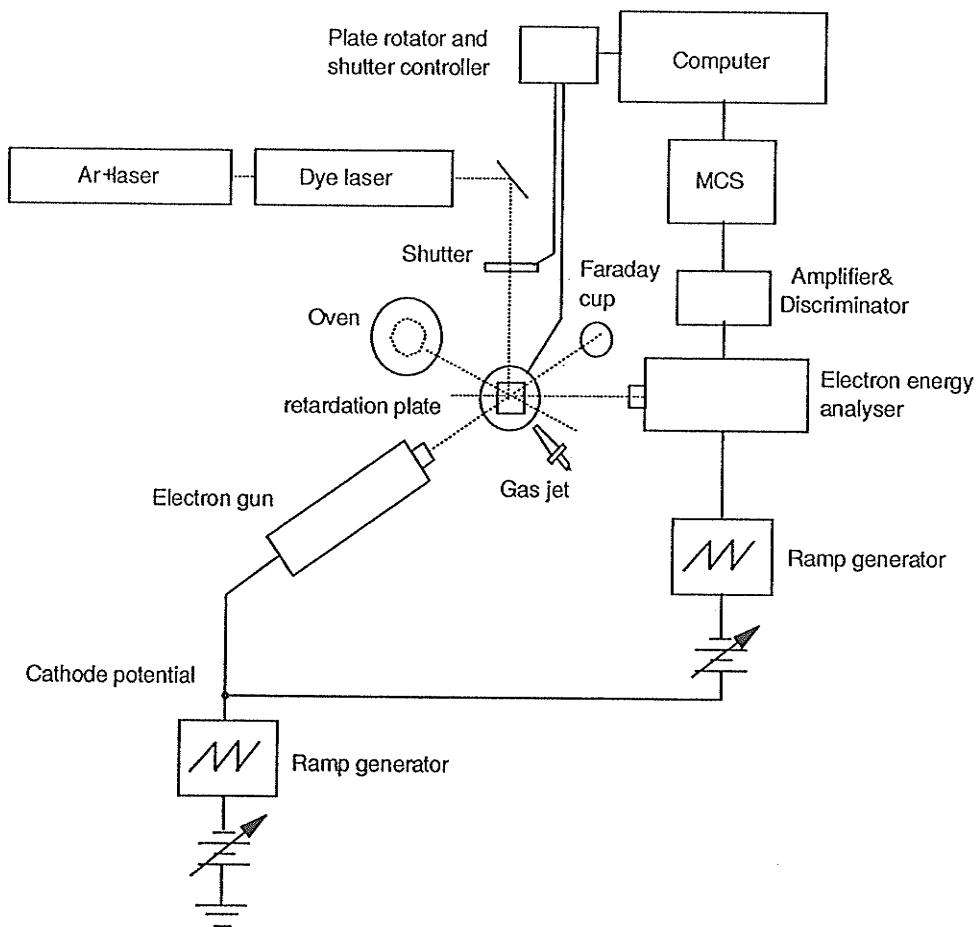


Figure 3.1. Schematic diagram of the apparatus for electron superrelastic-elastic scattering experiment.

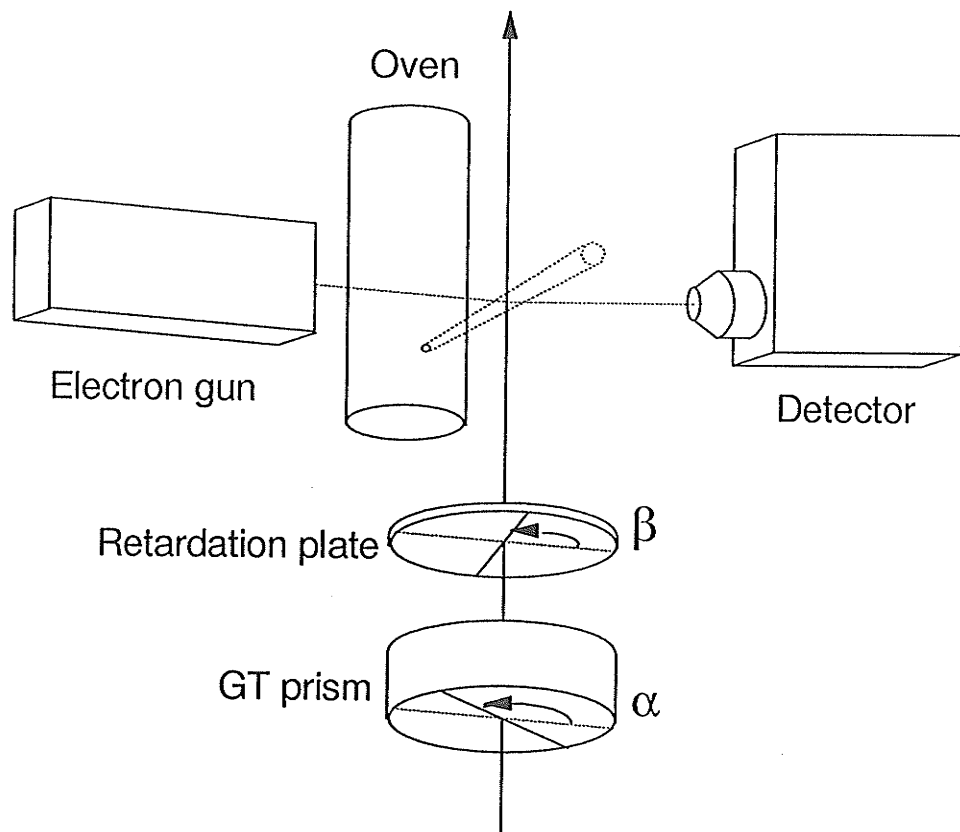


Figure 3.2. Schematic diagram of the interaction region.  $\alpha$  and  $\beta$  represent the angular displacements of GT prism transmission axis and of retardation plate fast axis, respectively, with respect to the forward-scattering angle.

scattering plane. All electrical wires are introduced into the vacuum chamber through several feedthroughs. The chamber is evacuated by an oil diffusion pump and a mechanical forepump.

Cancellation of the earth's magnetic field is accomplished with a  $\mu$ -metal can (nickel-iron alloy with high permeability). Residual magnetic fields at the interaction region are uniform and less than 25mG in all directions after degaussing has been done by flowing a high AC current through the  $\mu$ -metal can. With such a residual magnetic field we estimated that an electron beam at typical 10eV kinetic energy travels in a radius of curvature of 4.25m. This is equivalent to a  $2^\circ$  deflection of the electron beam within 30cm travel distance. In order to reduce the residual magnetic field, everything inside magnetic shield is made of magnetic free materials. Efforts were made to minimize the length of electrical wires carrying high current to reduce the induced magnetic field.

The scattering angle reading is made by connecting the shaft coupled to the rotatable table with a potentiometer outside the vacuum chamber, which can convert rotation angle of the rotatable table into resistance. A circuit was designed to measure the voltage drop across the potentiometer. The calibration between angle and voltage drop gives 0.0033V/degree conversion ratio. One half degree angular resolution for angle reading can be easily achieved.

The apparatus is designed to have the flexibility to rotate either gun or detector with the other one fixed on an aluminum platform in various possible locations. The metal vapor source is also hung on the platform in different positions depending on the geometry for each experiment. The Faraday cup can be mounted on either rotatable table or platform. Several optical

alignment procedures were developed to align the gun, detector and laser beam at the scattering center.

The vacuum chamber, baseplate and oil diffusion pump sit on an aluminum baseplate while most of the electronics are arranged on an electronic rack. Both units are very well grounded. All exposed surfaces surrounding the interaction region including the metal cases of gun and detector, oven shield, Faraday cup shield and gas nozzle are also carefully grounded to ensure zero electrical potential at interaction region.

### **3.3 Vacuum System**

A stainless steel bell jar of 27in in height and 36in in diameter is used as the vacuum chamber. A dovetail groove on the jar's base flange holds an O-ring to make the vacuum seal with a stainless steel baseplate. Viewports and feedthroughs are sealed with copper gaskets. An electropneumatically operated gate valve connects the chamber with a Varian VHS-6 oil diffusion pump that is roughed by a Varian SD-700 mechanical forepump. The diffusion pump has pumping speed of 2400 l/s for air and the ultimate vacuum of  $5 \times 10^{-9}$  torr. The forepump has pumping speed of 765 l/m and ultimate vacuum of  $10^{-4}$  torr. The background chamber pressure is measured with a Varian 843 ionization gauge controller and a 571 Bayard-Alpert ionization gauge tube. Foreline pressure can be read from a Varian 0531 thermocouple gauge tube. The best vacuum obtained in this chamber is  $1 \times 10^{-7}$  torr. A protection unit is employed to monitor chamber vacuum, foreline vacuum and diffusion pump body temperature. Whenever pump, electrical power or cooling water failures, or leaks take place in the vacuum system, the protection unit can close the gate valve and turn off the diffusion pump.

A MD6MU leak valve is used for the gas leak-in system. The leak valve is continuously controllable from  $10^{-5}$  to  $10^{-10}$  mbar l/s and the fully closed leak rate is below  $10^{-11}$  mbar l/s. The leak-in system can be rough-pumped separately by a mechanical pump. One terminal of the leak-in system is connected with the gas bottle, another terminal is led into the vacuum chamber. The gas is brought into the scattering region by a piece of stainless steel pipe and delivered to the scattering center through a molybdenum gas nozzle. In order to reduce the effect of mechanical pump oil diffusing back into the diffusion pump, a Nupro ss-4BMG valve is used to bleed air into foreline to keep foreline pressure at about 200 mtorr.

### **3.4 Laser and Optical System**

A Coherent Innova 90 argon ion laser is utilized to pump a Coherent CR-699 ring dye laser. A general discussion about ion lasers and dye lasers can be found in (Yariv1976) and (Hecht1992). The argon ion laser can produce reliable laser beam of high power in cw operation on a multitude of lines across the visible and in the near ultraviolet and infrared (Bridges1964). The principal excitation mechanism in noble gas ion laser is electron impact in high current dc discharges. Atoms are ionized in one collision, and subsequent excitation to a highly excited state occurs via subsequent collisions. The ions then relax, cascading to lower states with many possible relaxation routes and give out fluorescence. Inside the laser, an optical resonator is mounted on Super Invar rods to achieve the highest angular and length stability and the best rigidity. The typical linewidth is 4GHz that is the sum of inhomogeneous Doppler broadening, Zeeman splitting and homogeneous broadening due to the transition's natural lifetimes. Table 3.1

contains most of the transition line frequencies and output power for Innova 90.

All these take place in a plasma tube that must be able to withstand current density of  $700 \text{ A/cm}^2$  for arc discharge. A water supply system has been constructed to supply cooling water with constant pressure to the laser to dissipate heat. Two output power regulation modes are provided by the ion laser: light regulation control and current regulation control. The ion laser can give out constant maximum output power of 6watts. Other specifications of the ion laser are listed in Table 3.2.

The Coherent CR-699 ring dye laser can provide a single frequency, tunable, stabilized traveling light wave and is capable of locked scan operation across a 30GHz range. It eliminates power output limitations inherent in standing wave designs and can produce single frequency output levels as high as ten times those achievable by means of standing waves (Hecht1992).

In a standing wave dye laser, the nodes of the standing wave lie spaced across the dye jet. As the dye jet is illuminated by a high power pumping beam, each node becomes a region of unsaturated gain. These "spatial hole burning" modes have to be suppressed by increasing the finesse of intracavity etalons. This increases insertion loss and reduces conversion efficiency. For the ring laser, a traveling wave is formed in the cavity and the gain at the dye jet is uniform. The problem with standing wave operation does not exist in the ring laser. Therefore it can deliver more output power.

Unidirectional, traveling wave operation is achieved by means of an optical diode. The single frequency operation is obtained through the use of three optical elements: a three-plate birefringent filter, a thin etalon and a piezoelectric driven thick etalon. The birefringent filter can reduce the laser

Table 3.1. The transition line frequencies of Coherent Innova Ar Ion Laser.

Output Power Specification	
Wavelength (nm)	Output Power for Each Mode
514.5	2400
501.7	480
496.5	720
488.0	1800
476.5	720
472.7	240
465.8	180
457.9	420

Table 3.2. Specifications of Coherent Innovar 90 Ar Ion Laser.

Output Polarization	100:1 electric vector vertical
Beam Diameter	1.5mm at 1/e <sup>2</sup> points
Beam Divergence	0.5 mrad at 1/e <sup>2</sup> points
Long Term Power	
Stability	Current Regulation ±3%
	Light Regulation ±0.5%
Output Power	
Multiline (514.5-457.9nm)	6000mW

linewidth to about 2GHz. The thin etalon has a free spectral range of 200GHz, which is sufficient to enforce single longitudinal mode operation. The use of the thick etalon permits the longitudinal mode to be scanned. Overall effective linewidth resulting from all three elements is approximately 20MHz. A structure diagram of the dye laser is shown in Figure 3.3, and some most important features are listed in Table 3.3.

When the laser works in the locked mode, the oscillating mode is servo-locked to a stable reference point for the active stabilization. The error signal generated in a reference cavity is amplified and used to adjust the dye laser cavity length by driving a piezoelectric mounted folding mirror and a scanning Brewster plate to achieve frequency stabilization. The frequency scanning in the locked mode is accomplished by changing the reference frequency. The closed-loop stabilization causes the laser to track exactly, maintaining the narrow linewidth. Scans of up to 30 GHz can be made in the locked mode.

Our desired wave length of pumping light is around 553-555nm. The suitable dye for this wave length is Rhodamine 110 that has the efficiency peaked at 550nm. With Rhodamine 110 dye and in the best operation condition, the laser can yield output power of 1280mW in broadband operation and 850mW in single frequency operation using 6.0W pumping power from an argon ion laser. The output laser beam is linearly polarized in vertical direction.

Figure 3.4 presents an overall view of the optical system. An optical bench is constructed under the vacuum chamber. Two high reflectance mirrors are used to direct the laser beam into the interaction region. One mirror folds the laser beam toward the vacuum chamber. Another one sits on a mirror holder, which can translate and rotate the mirror so that the mirror

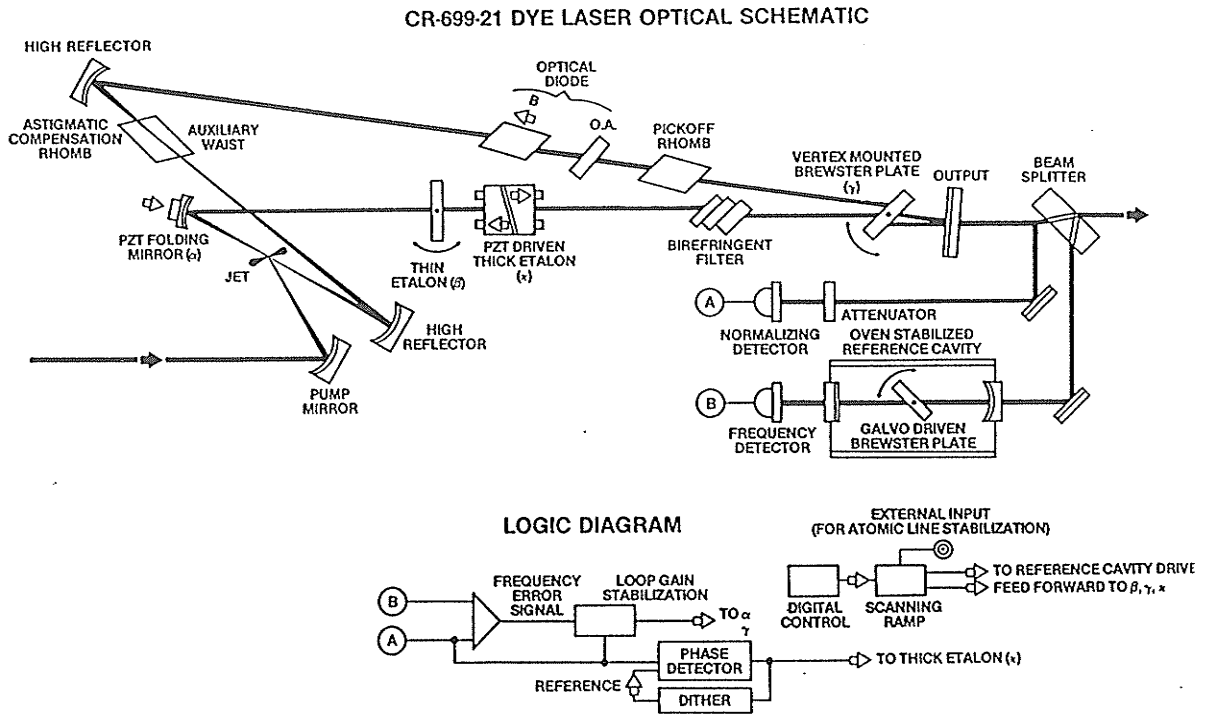


Figure 3.3. A structure diagram for a Coherent CR-699 ring dye laser. The light wave paths inside the laser are also indicated. Adopted from *Coherence Laser User's Manual*.

Table 3.3. Specifications of Coherent CR-699 Ring Dye Laser.

---

Output Power	800mW single frequency for 6Watts 514.5nm TEM <sub>00</sub> input at the peak of the dye tuning curve (~580nm).
Mode	TEM <sub>00</sub>
Beam Diameter	0.75mm
Beam Divergence	1.6mrad
Jitter (Effective Linewidth)	< 1MHz RMS at 10 KHz bandwidth
Frequency Drift	< 100 MHz/hour
Power Stability	5%/day

---

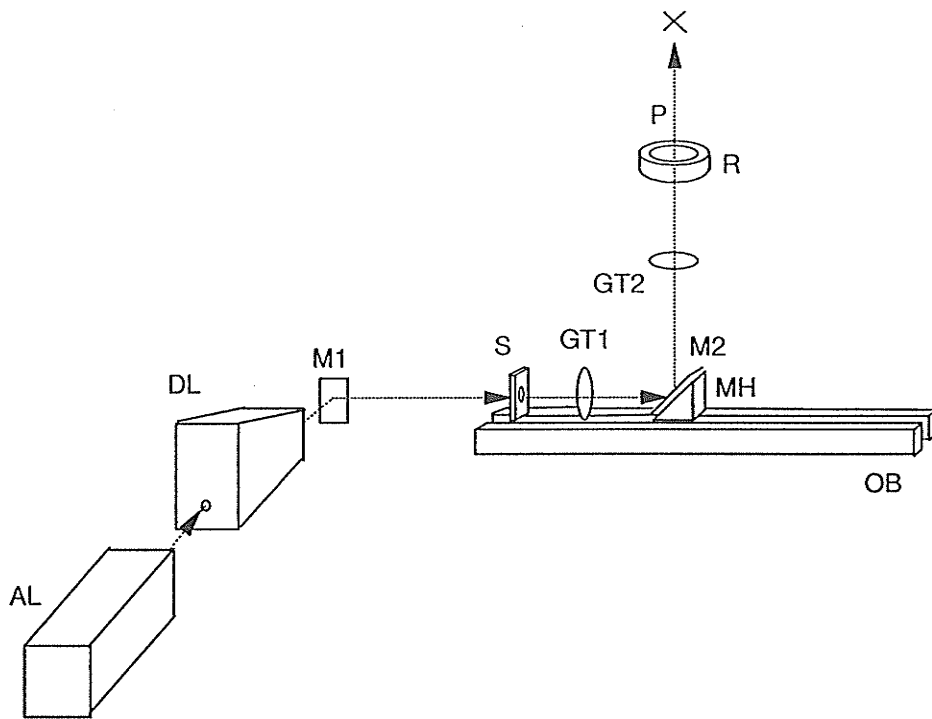
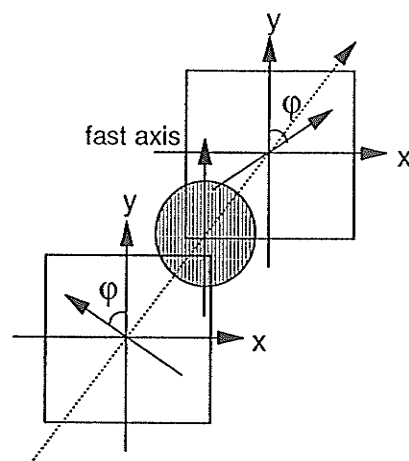
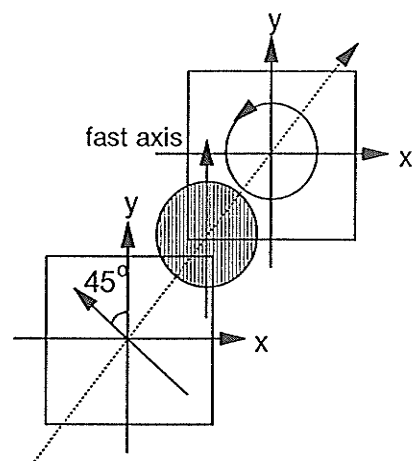


Figure 3.4a. A view of the overall laser optical system. The optical components are labeled as follows: Ar ion laser (AL), dye laser (DL), reflection mirrors (M1, M2), beam shutter (S), 3-D rotatable mirror holder (MH), Glan-Taylor prisms (GT1, GT2), optical bench (OB), retardation plate (P) and plate rotator (R).



Polarization optics of a half-wave retardation plate



Polarization optics of a quarter-wave retardation plate

Figure 3.4b. The polarization optics of retardation plates. A half-wave plate can rotate a linearly polarized light field vector by twice the angle between the light polarization direction and the fast axis of the plate. A quarter-wave plate can convert linearly polarized light at  $45^\circ$  angle with respect to the fast axis of the plate into circularly polarized light.

has enough freedom to bring a light beam shining on the mirror in any direction into the interaction center. A Glan-Taylor prism is employed as a linear polarizer to ensure that pure linearly polarized laser light strikes the retardation plate.

Before the laser beam enters the chamber, we manipulate the polarization state of the light. This can be accomplished by use of retardation plates. A retardation plate is made of optically anisotropic crystalline solid and the different indices of refraction between o-ray ( $n_o$ ) and e-ray ( $n_e$ ) within the solid can introduce a phase difference

$$\delta = \frac{2\pi}{\lambda}(n_o - n_e)d \quad 3.1$$

For  $\lambda/2$  retardation plate (half-wave plate), the phase difference between o-ray and e-ray is  $\pi$  and the electric field vector direction of the incident linearly polarized beam is rotated by twice the angle between linearly polarized direction of light and the fast axis of the plate. For  $\lambda/4$  plate (quarter-wave plate), the phase difference between o-ray and e-ray is  $\pi/2$  and a linear polarized light beam is converted into a circular polarized light beam. Commercial retardation plates are available.

In some cases, we used a half-wave plate to continuously rotate the optical electric field vector of the linearly polarized beam. A rotator assembly was constructed. The retardation plate was mounted on a holder that was attached to a hollow tube. The tube was coupled with a continuous synchronous motor through a pair of gears. A single arm was screwed on the rotator holder to chop a light beam emitted from a photoswitch to generate a pulse signal. The pulse signal was then sent to multichannel scaler to

synchronize retardation plate rotation with spectrum scan. Figure 3.5 shows the structure of the rotator. Details of the related electronic circuit can be found in Appendix 1 (i).

For other experiments, circularly polarized laser light was needed. We used a quarter-wave plate to convert the linearly polarized light into left-handed and right-handed circular light beams alternately. Figure 3.6 schematically describes the structure of rotator and the driving circuit. The diagram of pulse switching circuit is given in Appendix 1 (ii). The retardation plate was mounted on a plate holder and was attached to a hollow tube. A four arm chopper wheel chopped a light beam emitted from a photoswitch to generate controlling pulses. A stepper motor was driven by a pulse generator. Before the pulse series arrives at the stepper motor, it passes through a pulse switching circuit that is controlled by the ramp start pulse from I/O and the pulse generated from the photoswitch. The former one turns on the pulse series and starts the stepper motor. The later one turns the pulse series off and stops the motor. The circuit then waits for the next start pulse from MCS to switch on the motor and so on. Since the arms are separated by  $45^\circ$ , after calibrating the angle between the fast axis of  $\lambda/4$  plate and the incident beam polarization direction, the plate can generate a series of laser light polarization states in the order of right-handed circularly (RHC), linearly, left-handed circularly (LHC) and linearly polarization corresponding to the four arm positions. For the convenience of calibration, the plate holder and the four arm wheel can be rotated separately so that the fast axis angle calibration can be carried out while maintaining the arm wheel at start position.

Sometimes we also used the same arrangement to generate a group of linearly polarized light beams oscillating at  $0^\circ$ ,  $45^\circ$ ,  $90^\circ$  and  $135^\circ$  with respect

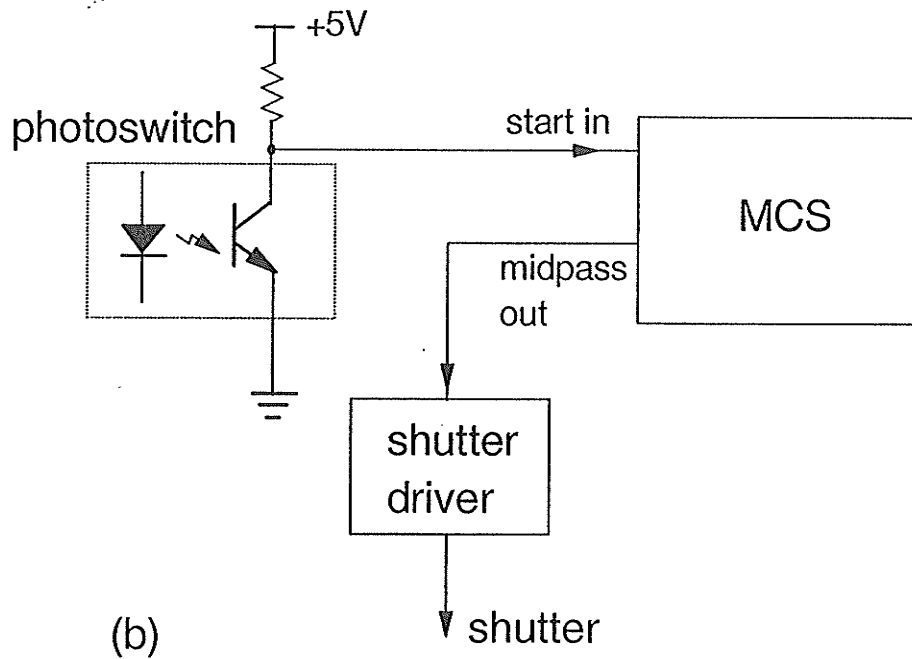
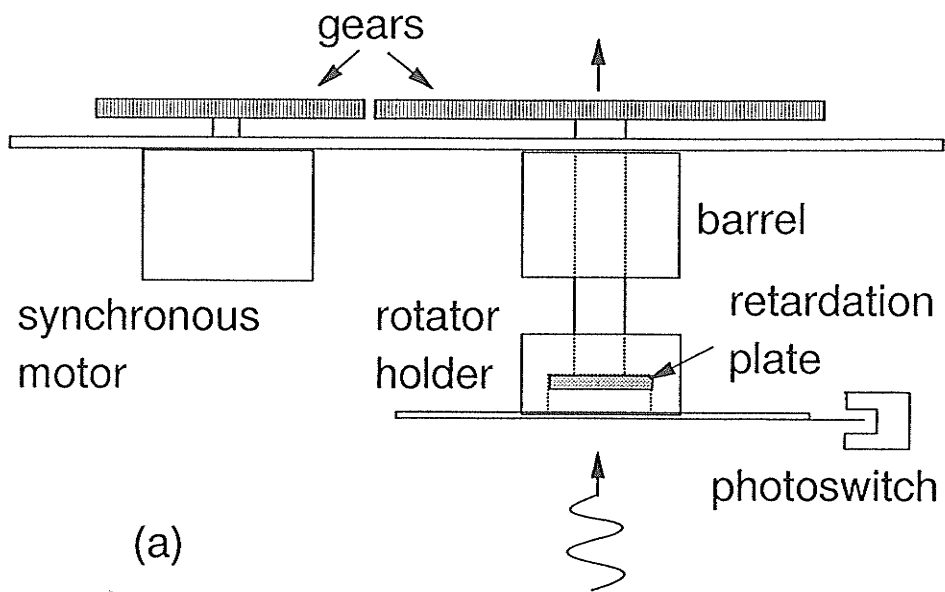
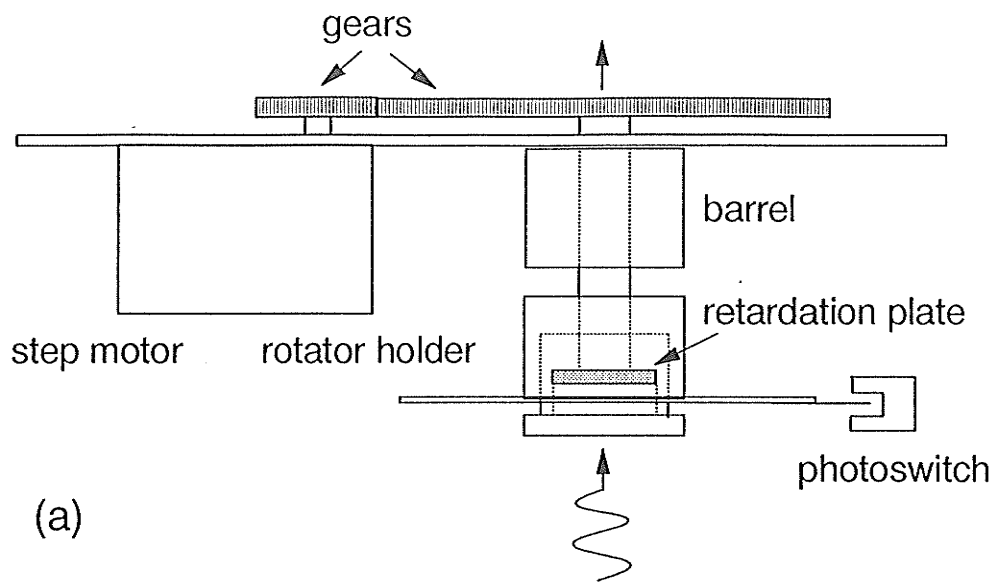
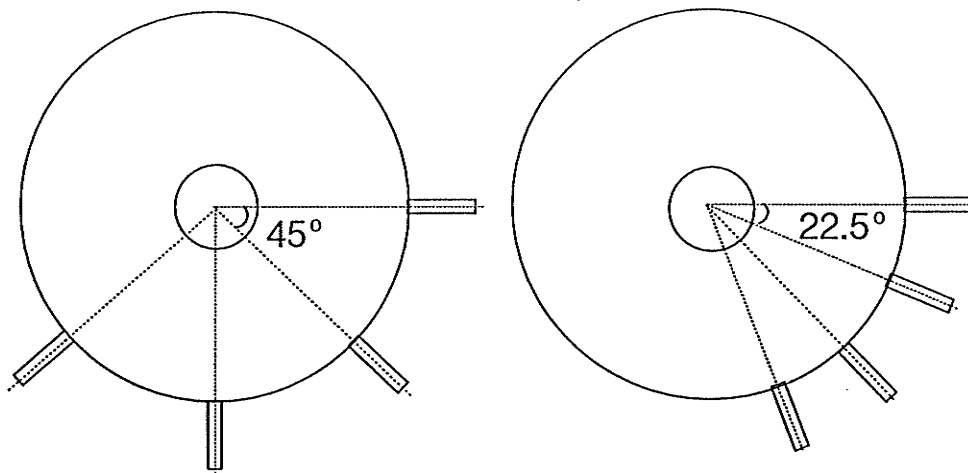


Figure 3.5. (a) Structure of the continuous retardation plate rotator. (b) The related electronic circuit. A synchronizing pulse signal can be generated and sent to MCS.



(a)

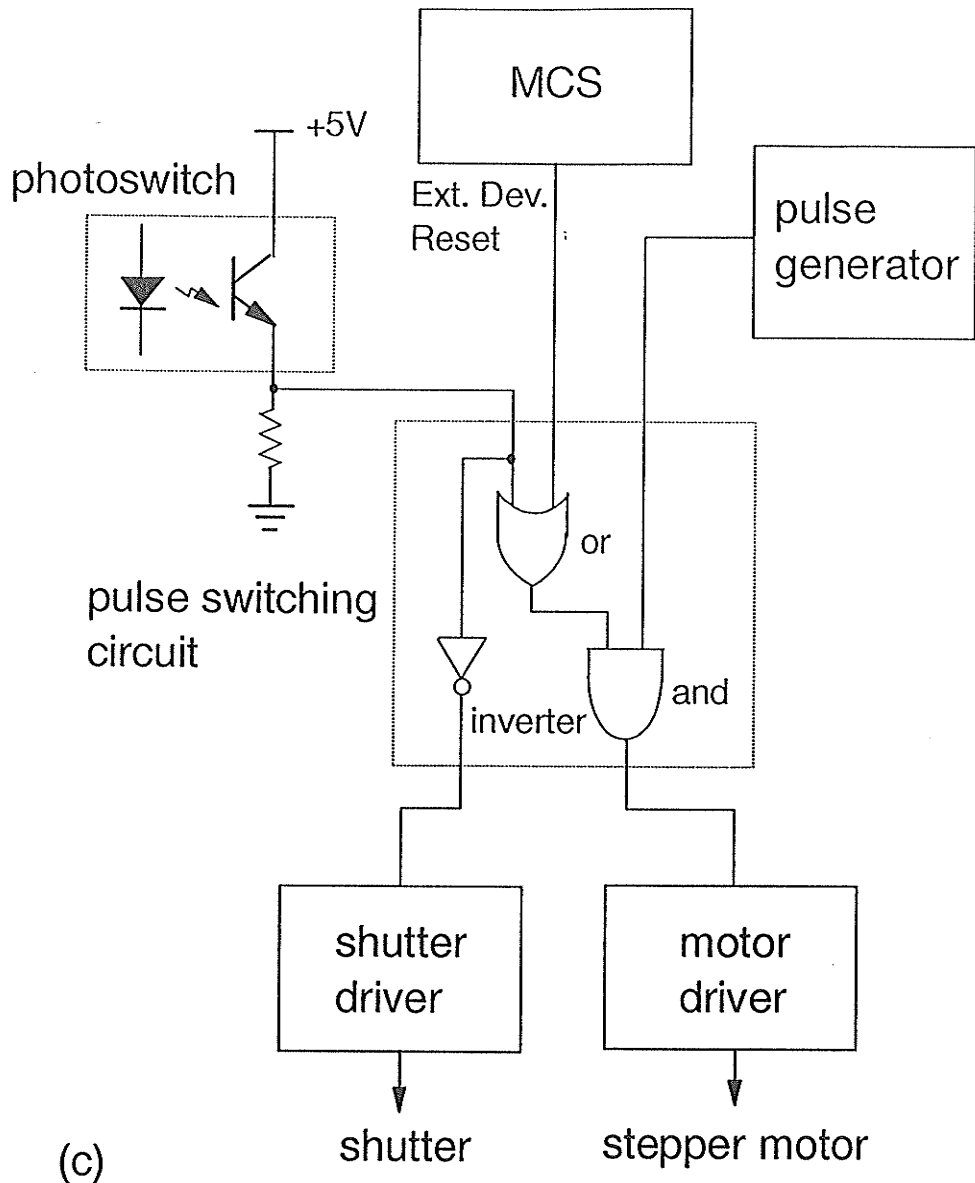


the chopper wheel  
for half-wave plate

the chopper wheel  
for quarter-wave plate

(b)

Figure 3.6. (a) Structure of the stepwise retardation plate rotator. (b) A view of chopper wheels which are used to stop retardation plates at certain angles. (c) The electronics controlling the retardation plate rotation. The origin of the "Ext. Dev. Reset" signal can be found in Figure 3.8. This signal activates the stepper motor to rotate the chopper wheel to the next position. The shutter is closed during the rotation.



(c)

to the forward scattering angle. The arms on the four arm chopper wheel were then separated by  $22.5^\circ$ .

A laser beam chopper is used for the laser-off spectrum accumulation. A piezoelectric crystal drives a metal shutter to close or open an aperture. The driving circuit of the piezoelectric crystal is basically a voltage doubler circuit and can supply 300V. The circuit can be controlled by the output voltage level either from MCS or retardation plate rotator. In this way we can synchronize the laser beam chopper with the MCS spectrum scan.

Several alignment gauges and procedures were developed for the laser light beam alignment. For each experimental arrangement gauges are needed to align the laser beam at the interaction center. Then an indicator on the ceiling and an aperture on the platform are set up to define the aligned light beam. Finer alignment of the laser beam can be done by adjusting the folding mirror while monitoring the superelastic signal.

### **3.5 Data Collection System**

The heart of the data collection system is an EG&G ORTEC multichannel scaler (MCS). The MCS is made up of a card that is plugged into an IBM PC computer and MCS emulation software that runs under DOS operation system. The MCS card is capable of storing data to its memory in as short as  $2\mu\text{s}$ . It can provide internal dwell time clock ranging from  $2\mu\text{s}$  to 30min. The histogrammed data, referred to as a spectrum in our case, can be up to 4096 channels in length with a minimum length of 4 channels. A dual-port memory interface on MCS gives the computer direct access to the data memory. Timing diagrams for internal and external start modes are given in Figure 3.7a, b with a pass of 4 channels. In the MCS, the source of the time

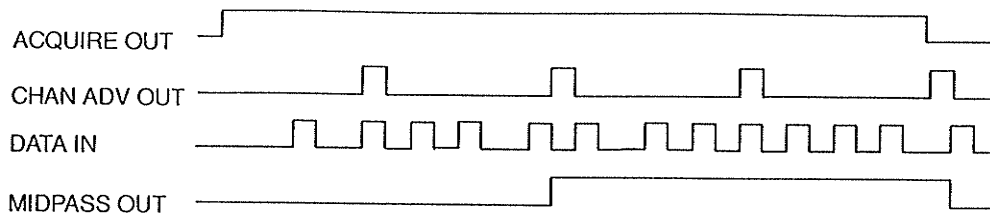


Figure 3.7a. Timing diagram, internal start and clock

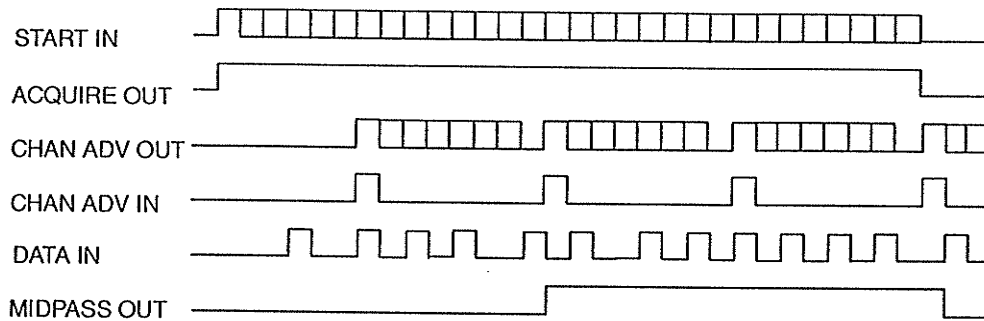


Figure 3.7b. Timing diagram, external start and clock.

- The Acquire output (ACQUIRE OUT) signal is used to signal when a pass is active.
- The Channel Advance Output (CHAN ADV OUT) signals a channel advance.
- The Midpass Output (MIDPASS OUT) signals the middle of a sweep.
- The Start Input (START IN) signals the MCS card to start a sweep.
- The Channel Advance Input (CHAN ADV IN) causes the MCS unit to advance to the next channel.
- The Data Input (DATA IN) is the input for the signal to be counted

base can be specified. If the internal time base is selected, the Dwell Time Clock located on the MCS card is used as the time base to cause the channel advance. If the external time base is selected, a rising edge on the CHN ADV IN input is used to cause the channel advance. It can also select the start of pass trigger. If an internal start of pass trigger is selected, the next pass is started as soon as processing has completed on the current pass. If external start of pass trigger is specified, the next pass is started when a rising edge occurs on the START IN input. ACQUIRE OUT, ACQUIRE IN and MIDPASS OUT can also be used to communicate with outside. The MCS emulator can run a series of commands that can control data collection and data storage and execute other DOS programs. Therefore, users are allowed to run their own programs under MCS Utilities Menu. A full description of the MCS system is given in the MCS Operator's Manual.

A PCL-720 digital I/O counter card is utilized as digital input and output register. It provides 32 digital input and 32 output channels and a programmable interval timer. The programmable timer includes 3 independent 16-bit counters, each with a count rate of up to 2.6MHz, and the control byte for programming. A detail description can be found in User's Manual.

An EG&G ORTEC MCS card, software and a PCL/720 digital I/O counter card are installed in an IBM PC 286 computer. A BNC panel is constructed in rear of the computer to extend wires from MCS and I/O cards for external connection. A wiring map is given in Figure 3.8 (a).

The timer output from pin 4 and 10 of Connector 5 in I/O card is sent into the computer through I/O input to serve as a time base for user's programs (see Figure 3.8 (b) and (c)). When the stepper motor is used to rotate the retardation plate, the external start of pass trigger pulse for MCS generated by user's program comes from an I/O output labeled START OUT

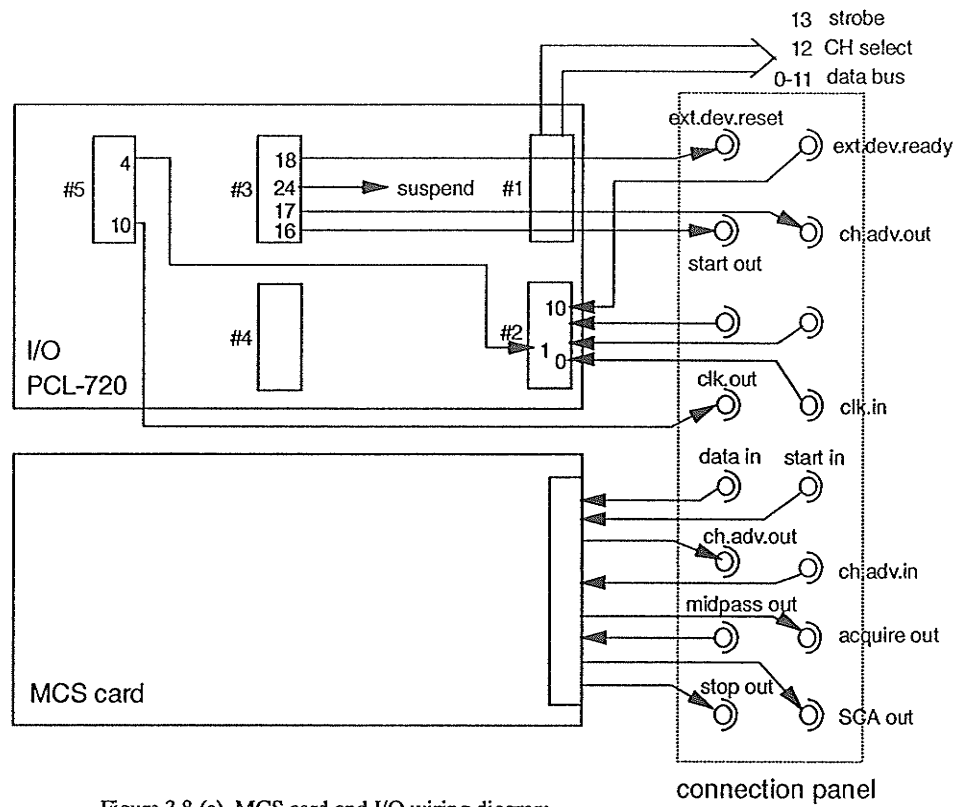
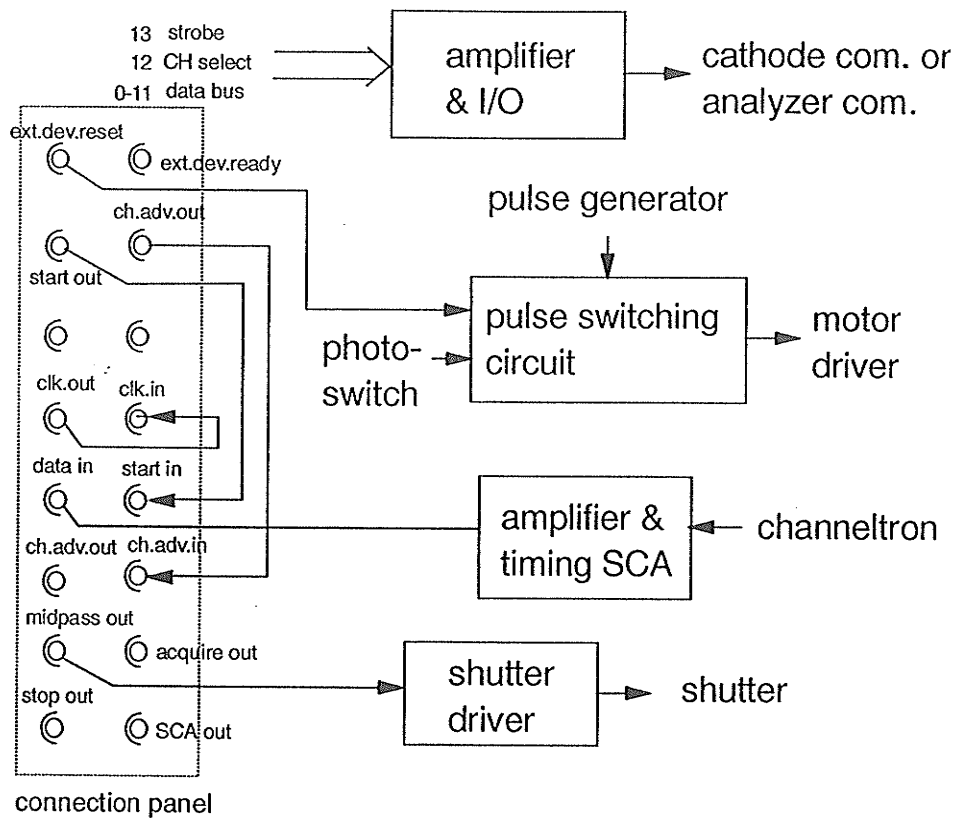
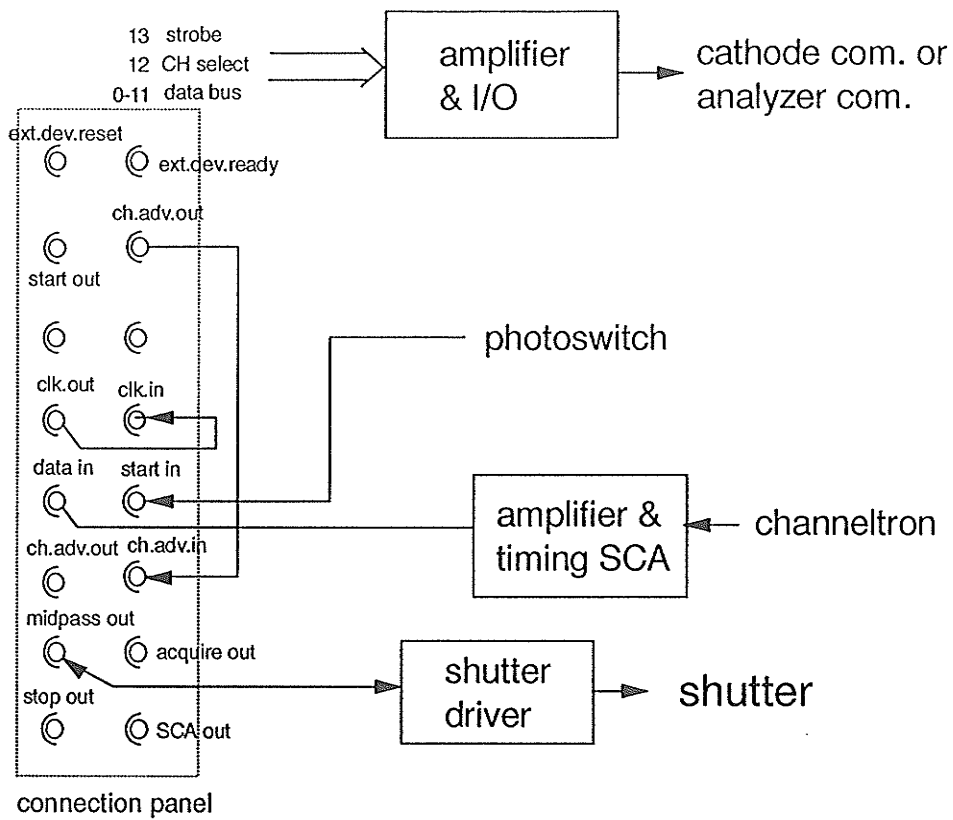


Figure 3.8 (a). MCS card and I/O wiring diagram



connection map for the step rotation mode

Figure 3.8 (b). The wiring diagram among MCS, I/O and external devices



connection map for the continuous rotation mode

Figure 3.8 (c). The wiring diagram among MCS, I/O and external devices

that is connected with MCS START IN. Another I/O output provides MCS with the channel advance pulse through CH ADV IN. External Device Reset pulse signal is used to trigger the stepper motor rotator when one ramp is completed. In case that the continuous rotator is used, the pulse generated in the photoswitch on the rotator circuit is sent into MCS through START IN to start a pass. MID PASS pulse signal can be used to operate the laser beam chopper. The channel selection signal, strobe and data bus produced by user's program are output to a programmable D/A.

A Galileo 4039 channeltron is mounted at the end of electron energy analyzer for electron detection. The energy selected electrons impinge on the channeltron cone surface and secondary electrons are generated. The secondary electrons then are accelerated by high voltage and bombard the surface to produce more electrons. The auxiliary circuit is shown in Figure 3.9. A high voltage power supply is used to provide the channeltron with 2000 - 3000V and the voltage is introduced into the vacuum chamber through a high voltage feedthrough. The negative pulse signal is amplified by an EG&G ORTEC 113 preamplifier. The signal is then further amplified by an EG&G ORTEC 572 amplifier and discriminated by an EG&G ORTEC timing SCA, on which the lower and higher levels of the acceptance window can be set. A EG&G ORTEC 441 ratemeter is used to monitor the count rate of the pulse signal. Finally the signal comes into MCS card through DATA IN terminal. The file saving programs have been written to save the collected spectra on the floppy disks.

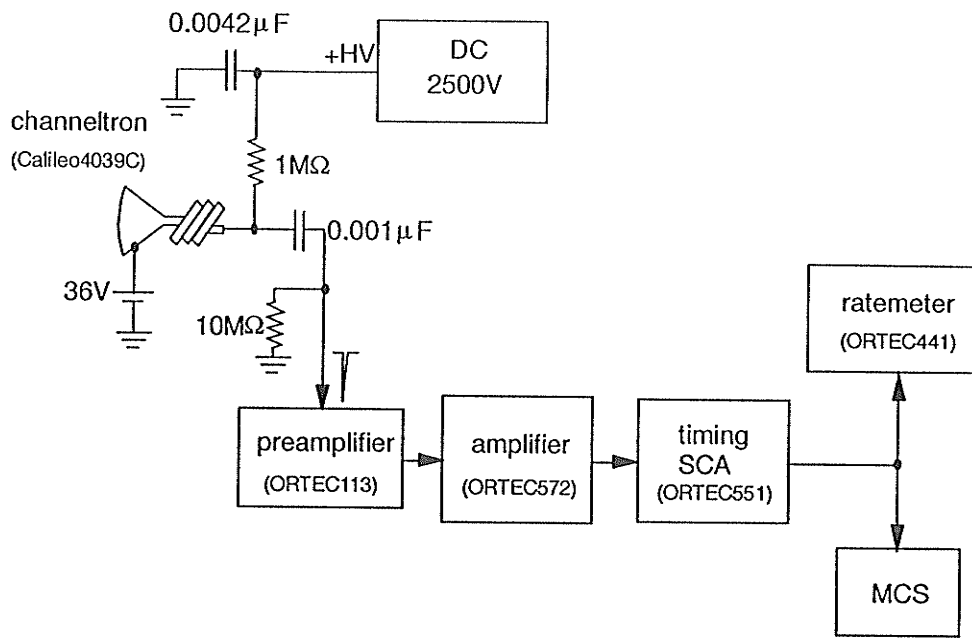


Figure 3.9. Schematic diagram for the data collection system and the channeltron auxiliary circuit.

### 3.6 Electron Spectrometer

The electron spectrometer consists of an electron gun, electron energy analyzer, Faraday cup and related power supplies. We currently have two electron gun assemblies. One is a high electron current density gun that was designed and constructed by Jet Propulsion Laboratory (Chutjian1979). Another one is a high energy resolution gun that is designed in this lab and machined by the work shop of Department of Physics, University of Manitoba. The analyzer is also loaned by JPL. A detailed discussion about the design and performance of these electron optics will be given in next section.

Figure 3.10 shows a schematic diagram of the electron spectrometer system. Electrons injected from the filament are accelerated and focused inside the electron gun. The potential difference between the interaction region (surrounded with ground potential) and the filament tip bias defines the final kinetic energy of the electrons ( i.e. impact energy ) at the interaction center. A negative bias, namely cathode common, on the filament is provided by a DC power supply in series with a ramp generator that can linearly change the impact energy against MCS channel number.

After an electron collides with target atom, it can be scattered into three possible channels: elastic, inelastic or superelastic channel, and carries certain residual kinetic energy. The residual energy refers to the remnant kinetic energy of electrons after the collision and can be defined as

$$\textit{impact energy} = \textit{energy loss} + \textit{residual energy}$$

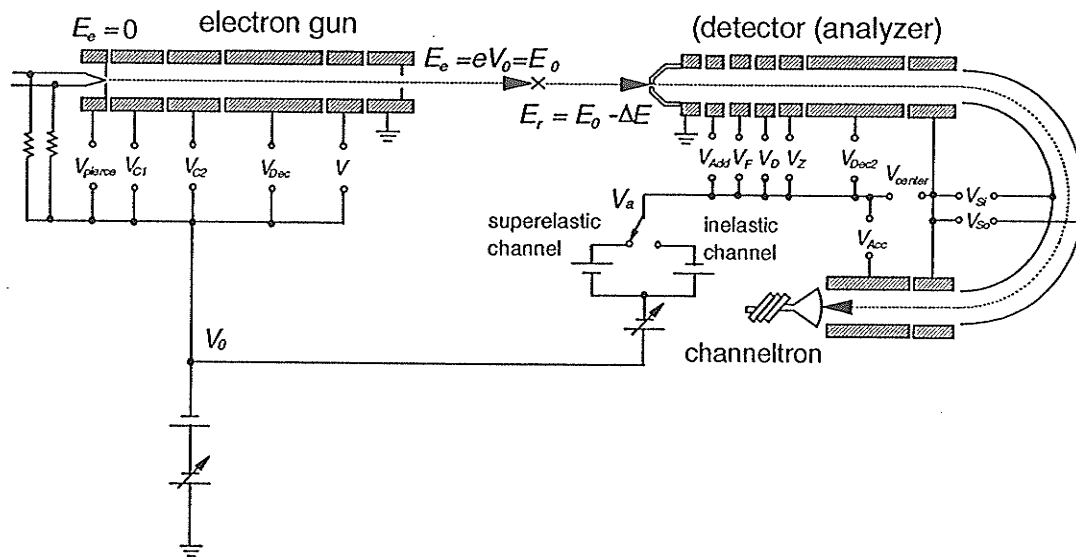


Figure 3.10. Schematic diagram of electron scattering spectrometer.  $V_0$  represents the cathode common potential,  $V_a$  the analyzer common potential,  $E_e$  the incident electron kinetic energy,  $E_0$  the impact energy,  $E_r$  the residual energy of scattered electron, and  $\Delta E$  the electron kinetic energy loss. The lens potentials are also indicated.

The detection of the scattering signal magnitude at certain energy loss (or gain) enables us to investigate the electron collisional excitation between the corresponding atomic energy levels. The electron analyzer functions as an energy monochromator to admit electrons with certain kinetic energy. The common potential of the analyzer is provided by the same type of DC power supply and the ramp generator as those used for cathode common, but the ramp generator now scans the energy loss. When analyzer common changes resulting from the energy loss scan, the energy transmission window sweeps throughout the desired range of residual energy to admit the electrons with certain kinetic energy, and an energy loss (or gain) spectrum can be obtained. A typical energy loss spectrum is shown in Figure 3.11 that contains the electron scattering signal in all three scattering channels. Since the analyzer common potential is referenced to the cathode potential, zero analyzer common bias corresponds to the location of elastic peak on energy loss spectrum and the superelastic peak locates at the symmetric location of the inelastic peak for the same transition with respect to the elastic peak. A switch is installed to change the polarity of the DC power supply for the analyzer common. This allows us to scan the analyzer common potential on both inelastic and superelastic channels.

The ramp wave function is generated in a RAMP program and sent out of computer through the I/O port. A Kepco SN 500-122 Digital Programmer is employed to convert the digital data from I/O port into analog signal and provide the electron spectrometer with variable voltage supply to scan energy loss or impact energy. This instrument can provide voltage range of 0 -  $\pm 10V$  and maximum output current of  $\pm 2mA$  with linearity error of  $\pm 1/2$  LSB. The bus line can carry 12 bit binary that allows a voltage resolution of

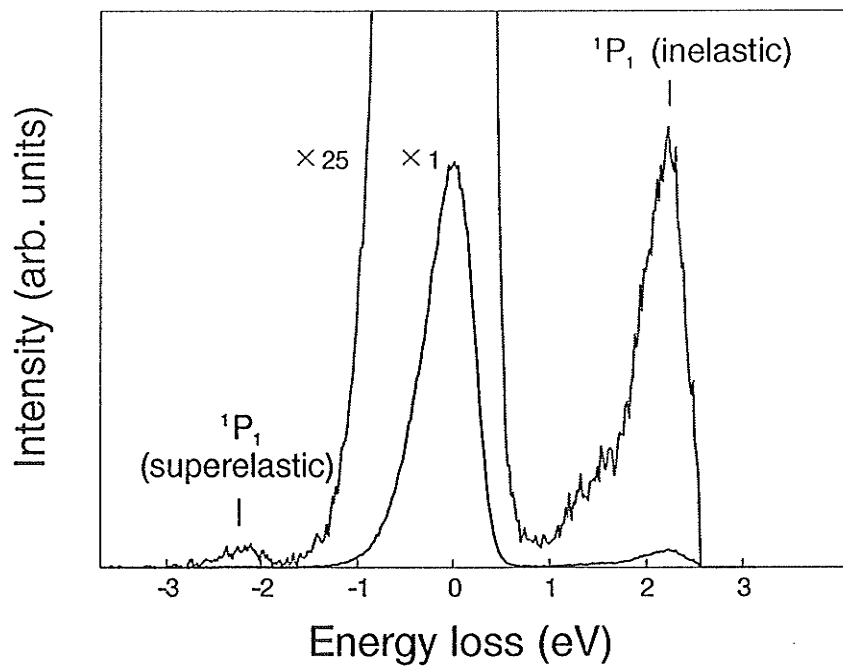


Figure 3.11. A typical energy loss spectrum of laser excited  $^{138}\text{Ba}$  that contains  $^1P_1$  features in both inelastic and superelastic channels. Both the original (X1) and magnified (X25) versions of the spectrum are shown.

1 part in 1000. It provides users with two separate channels to program independently.

The voltage output of each channel from the digital programmer is amplified by a Kepco NTC 200 programming interface. It can supply 0 - 200V and 0- 10mA output with slewing rate of 1V/ $\mu$ sec. The 8 hour drift is less than 20 $\mu$ V and 5nA. Ripple and noise is 0.05% or 50mV, whichever is greater. The output voltage is varied by changing the external voltage control resistor. A resistance switch board was constructed for the control resistor variation.

The DC bias on each channel is generated by a Kepco HB 4A regulated DC supply. Continuously variable DC output ranges from 0 to 325V in five overlapping incremental ranges with the voltage resolution of 0.02% of maximum voltage. The ripple is less than 0.001V rms, maximum and temperature coefficient less than 0.01% per °C. Output voltage varies less than 0.01% or 2mV, whichever is greater over a period of 3 hours after warm-up.

RAMP programs, consisting of RSET.BAS and RMAIN.BAS, were developed in Quick BASIC and compiled into executable files under DOS. Command programs were also written to run RAMP programs in MCS emulator. A set of ramp parameters can be setup and saved in a temporary file in RSET, including number of passes, dwell time, ramp length, ramp height, number of ramps, jump channel and jump height. It also enables us to select either impact energy or energy loss channel to run the ramps.

The main function of RMAIN is to: 1) generate the ramps with the parameters given by RSET, 2) send the digital data of the wave form to I/O and a strobe pulse to inform the digital programmer to collect digital data from I/O, 3) set the rate and modes for clocks on the I/O card and place

channel advance pulses on I/O output, 4) place start trigger pulse on I/O output when one pass is completed and send out external device reset pulse to I/O output when a ramp is over, 5) return the data accumulated in each channel of MCS memory to computer and display the spectrum on screen, 6) offer operation functions of Fast Scan, Suspend, Stop at End and Single Pass Scan, 7) lock the voltage scan anywhere on the ramp and consequently output a certain voltage level associated with a selected channel on the spectrum. RAMP program can generate ramps with the ramp height varied between 0 and 10V. The program can generate a number of ramps in one pass and produce a voltage jump at the indicated channel on one ramp. The pass length can be chosen between 4 and 4096 channels. The ramp lock function provides us with the convenience to lock energy loss or impact energy at any feature on the spectrum. The resolution of the spectrum is determined by the actual ramp height (not include jump) to the pass length ratio. The original programs for data acquisition are attached in Appendix 3.

### **3.7 Electron Optics**

#### **3.7.1 General Principle**

Theoretical aspects of electron optical designs are extensively covered in the literature (Dahl1973, Grivet1965 and Moore1983). Only an outline of the design consideration will be presented here. The properties of charged-particle beams are analogous in many respects to those of photon beams and the laws of geometrical optics can be applied to electron optics. The electrostatic lenses produce equipotential surfaces with shapes similar to those of light wave fronts in optical lenses. A charged particle passing across

these surfaces is accelerated or decelerated, and its path will be curved so as to produce a focusing effect.

Similar to light optics, in electron optics, a luminous object is usually defined by an aperture, called a window, which is uniformly illuminated from behind by a stream of charged particles (see Figure 3.12). The angular spread of particles emanating from the window is limited by a second aperture called a pupil which determines the half angle  $\theta$  of rays from each point on an object defined by a window. Consider the optical system illustrated in Figure 3.13, in which an object defined by a window at  $z_1$  is imaged at  $z_2$ . The rays emanating from a point  $(x_1, z_1)$  at the edge of the object are limited by a pupil to fall within a cone defined by a half angle  $\theta_1$ , which is called the pencil angle. The angle of incidence  $\alpha_1$  of the central ray from  $(x_1, z_1)$  on the plane of the pupil is referred to as the beam angle. The rays emanating from each point on the image appear to be limited by an aperture (image pupil) that corresponds to the object pupil. An image-pencil angle  $\theta_2$  and beam angle  $\alpha_2$  from a point  $(x_2, z_2)$  at the edge of the image are defined with respect to this image pupil. It should be noticed that window and pupil can also locate on image side. In this case, the images of them on object side play the role of window and pupil.

Since the charged particle's path is curved continuously across the electrostatic lens, electron optical lenses are thick lenses. The focal points of a thick lens are located by focal lengths,  $f_1$  and  $f_2$ , measured from principal planes  $H_1$  and  $H_2$ . The locations of the focal points with respect to the central plane are given by  $F_1$  and  $F_2$ , and hence the distances from the central plane to the principal planes are  $F_1 - f_1$  and  $F_2 - f_2$ . The object and image distances with respect to the principal planes are  $p$  and  $q$ , and with respect to the

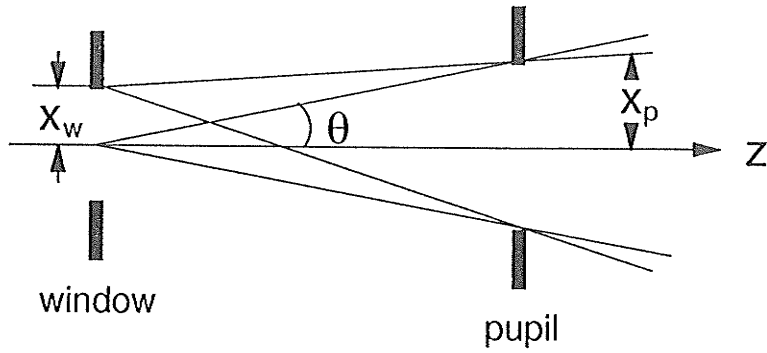


Figure 3.12. A pupil determining the half angle  $\theta$  of rays from each point on an object defined by a window.  $x_w$  is the window radius and  $x_p$  the pupil radius.

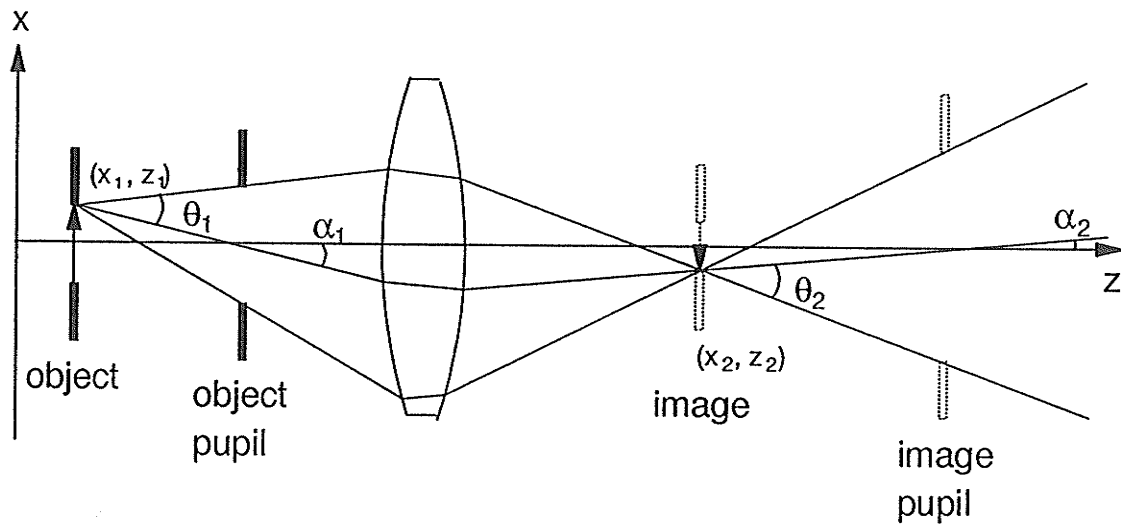


Figure 3.13. Relation of object pencil angle  $\theta_1$  and beam angle  $\alpha_1$  to image pencil angle  $\theta_2$  and beam angle  $\alpha_2$ .  $(x_1, z_1)$  and  $(x_2, z_2)$  are the coordinates of points at the edge of the object and at the edge of the image respectively.

central plane are  $P$  and  $Q$ , respectively. The linear and angular magnifications are given by

$$M = \frac{x_2}{x_1} = \frac{f_2 - q}{f_2} = \frac{f_1}{f_1 - p} \quad 3.1$$

$$m = \frac{\theta_1}{\theta_2} = \frac{f_1 - p}{f_2} = \frac{f_1}{f_2 - q} \quad 3.2$$

The most widely used lenses for focusing the low energy charged particles are cylindrical and aperture lenses with rotational symmetry about the central axis. Double cylinder, triple cylinder, two and three aperture lens geometries are commonly used in electron optical design. The numerical data about the focal properties of various types of lens geometries are given in the book *Electrostatic Lenses* by Harting and Read (Harting 1976). These data are determined from numerical solutions of the equation of motion of an electron in a lens field and have inaccuracies of the order of 1%.

The energy distribution of electrons emitted from a thermionic cathode is given by the Boltzmann equation

$$I(E) = I_0 \frac{2}{\pi^{1/2}} \frac{E^{1/2}}{(kT)^{3/2}} \exp\left(-\frac{E}{kT}\right) \quad 3.3$$

where  $E$  is the kinetic energy of electrons and  $T$  is the cathode temperature. The full width at half-maximum,  $\Delta E_{1/2}$  is  $1.79kT$ . The maximum current that can be drawn from a cathode of area  $A$  and work function  $\phi_w$  is given by the Richardson equation

$$I \approx 120T^2 A \exp\left(-\frac{\phi_w}{kT}\right) \quad 3.4$$

At a normal cathode operation temperature of 3000°K,  $\Delta E_{1/2} \approx 0.5\text{eV}$ . It is possible to improve the resolution by lowering the cathode temperature  $T$  as indicated in Eqn. 3.3. But the emission current drops quite rapidly and the lower limit for suitable currents is approximately 1000°K, which implies  $\Delta E_{1/2} \approx 0.15\text{eV}$ . Consequently, to achieve high resolution, some kind of electron energy monochromator is required for both electron gun and detector.

The 180° spherical (hemispherical) sector is often utilized, which employs an inverse-square-law field created by placing a potential across a pair of concentric spherical electrodes. The electrical potentials on inner and outer spheres for transmission of a particle of energy  $E=qV$  are given by

$$V_{outer} \approx V\left(2\frac{R_0}{R_2} - 1\right) \quad 3.5$$

and

$$V_{inner} \approx V\left(2\frac{R_0}{R_1} - 1\right) \quad 3.6$$

The definitions of  $R_0$ ,  $R_1$  and  $R_2$  are given in Figure 3.14. The energy resolution is (Trajmar1968)

$$\frac{\Delta E}{E} = \frac{\omega}{2R_0} + \frac{(\Delta\alpha)^2}{2} \quad 3.7$$

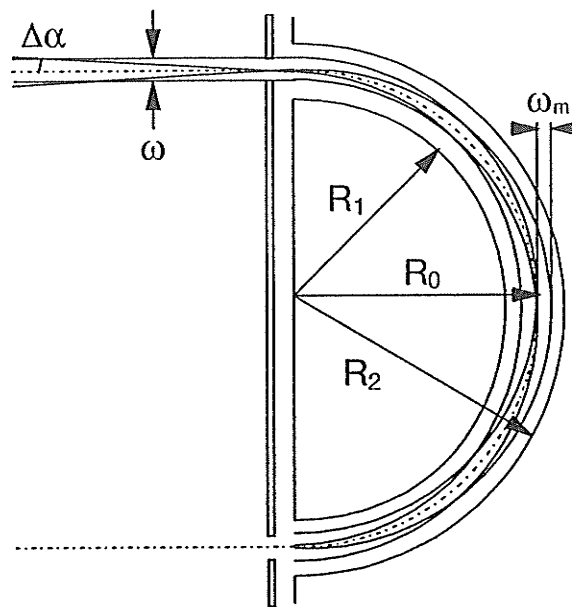


Figure 3.14. The hemispherical analyzer:  $R_1$  is the radius of the inner hemisphere,  $R_2$  the radius of the outer hemisphere,  $R_0$  the radius of the central path,  $\omega$  the diameter of the entrance and exit apertures,  $\omega_m$  the maximum angular deviation of an incident trajectory with respect to the central path, and  $\Delta\alpha$  the maximum deviation of a trajectory from the central path within the analyzer.

where  $\Delta\alpha$  is the angular deviation of the beam and  $\omega$  is the diameter of the entrance and exit slits. The maximum deviation of a trajectory from the central path within the analyzer is

$$\frac{\omega_m}{R_0} = \frac{\Delta E}{E} + \Delta\alpha + \frac{1}{2\Delta\alpha} \left( \frac{\omega}{2R_0} + \frac{\Delta E}{E} \right)^2 \quad 3.8$$

### 3.7.2 High Resolution Electron Gun Design

This gun is designed to resolve the electron transition features of heavy metal atoms. The typical energy spacing between these transition features can be as small as 100meV, so the overall energy resolution of the spectrometer should be in the same order. For current electron spectrometer arrangement and target density, the electron beam current has to be on the order of hundreds nA for us to obtain an acceptable signal to noise ratio. The electron beam should be parallel, with the beam diameter not much larger than that of the target beam (0.35cm in this case).

The structure of the high resolution gun is presented schematically in Figure 3.15. It consists of a hairpin filament, an electron extraction diode, an entrance lens stack, a spherical energy analyzer and an exit lens stack. The detailed theoretical description about the design of the electron extraction diode is given by Bernius et al.(Bernius1988). Electrons start in a Pierce-Wehnelt extraction diode using a hairpin as the cathode. An ensemble of trajectories is launched from the cathode, accelerated by the potential on the anode (see Figure 3.16). Those rays transmitted through the Wehnelt aperture

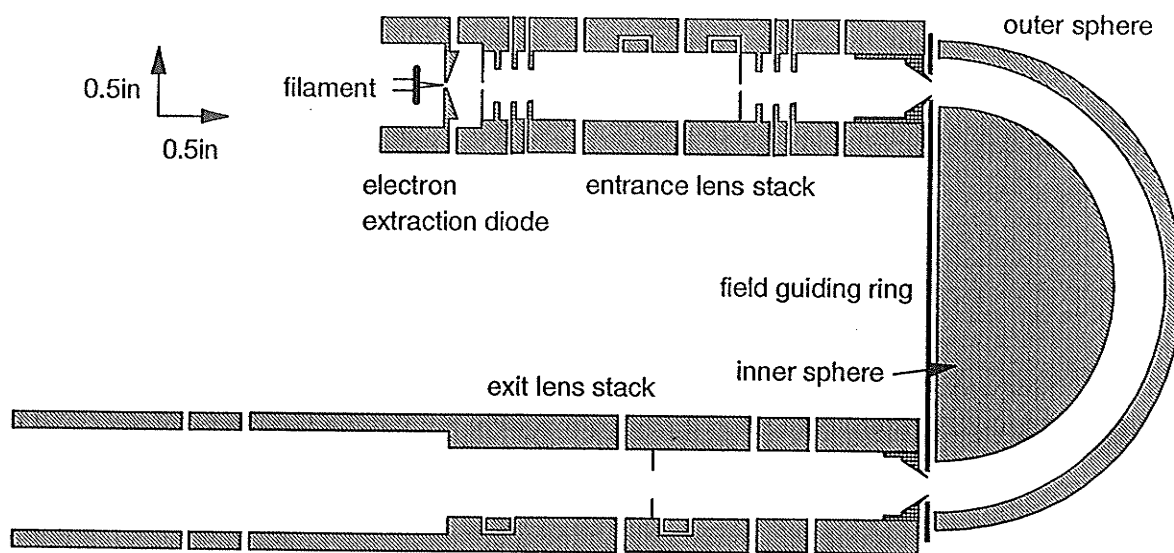


Figure 3.15. The structure of the high energy resolution gun. The detailed descriptions about extraction diode, entrance lens, hemispherical energy monochromator and exit lens are given in the text.

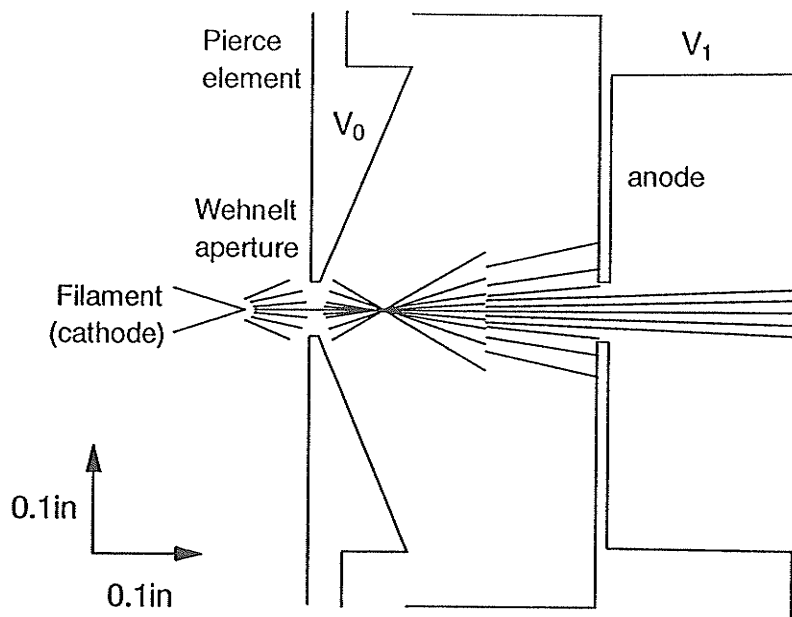


Figure 3.16. Asymptotic rays of electron beam in the electron extraction region.  $V_0$  denotes the applied voltage on Pierce element and  $V_1$  the voltage on the anode. The cross-over between Wehnelt cup and anode serves as the object of the gun electron optics. The location of the cross-over depends on the filament position, spacing between Pierce element and anode,  $V_0$  and  $V_1$ .

and initially directed radially outward at the cathode are folded over the first caustic located between the Wehnelt cup and the anode, which then acts as the electron source for the optical system of the lens. Computer modelling of the designed diode has been carried out with the Simion PC/PS2 ion trajectory simulation package (EG&G) and the detailed results for various Pierce-Wehnelt spacing distances and Pierce voltage bias  $V_0$  are given in Appendix 2.

The function of the entrance lens stack can be analogous to a microscope. The electron source is located in front of the first focal plane of the first triple aperture lens and focused on the first focal plane of the second triple aperture lens. Therefore, the outgoing beams from the second triple lens are parallel as illustrated in Figure 3.17. The first aperture ( $w_1$ ) plays the role of a window and defines the luminous area of the electron source. The image of the second aperture formed by the first triple lens ( $P_1$ ) functions as a pupil and determines the pencil angle. Meanwhile the second aperture also serve as a pupil for the second triple lens ( $P_2$ ) and the image of  $P_1$  is on the  $F_{B2}$  plane of the second triple lens. Using Eqn. 3.1 and 3.2, we can obtain the linear magnification  $M = -4$  and angular magnification  $m = 4$  for the whole system. The cross-over on  $F_{B2}$  plane is the image of the electron source area limited in size by  $P_1$  and acts as the object for the spherical monochromator with well-defined size and deviation angle. In our design, the first aperture is chosen to be 0.030in in diameter and the second aperture is 0.120in in diameter. This results in a cross-over of 0.120in in diameter on  $F_{B2}$  plane and a luminous area of 0.030in in diameter on  $F_{A1}$  plane. The angular deviation of the outgoing rays  $\alpha_2$  is about 12 degrees. The results of computer simulation of the entrance lens stack design carried out using Simion are shown in Appendix 2 for various voltage configurations.

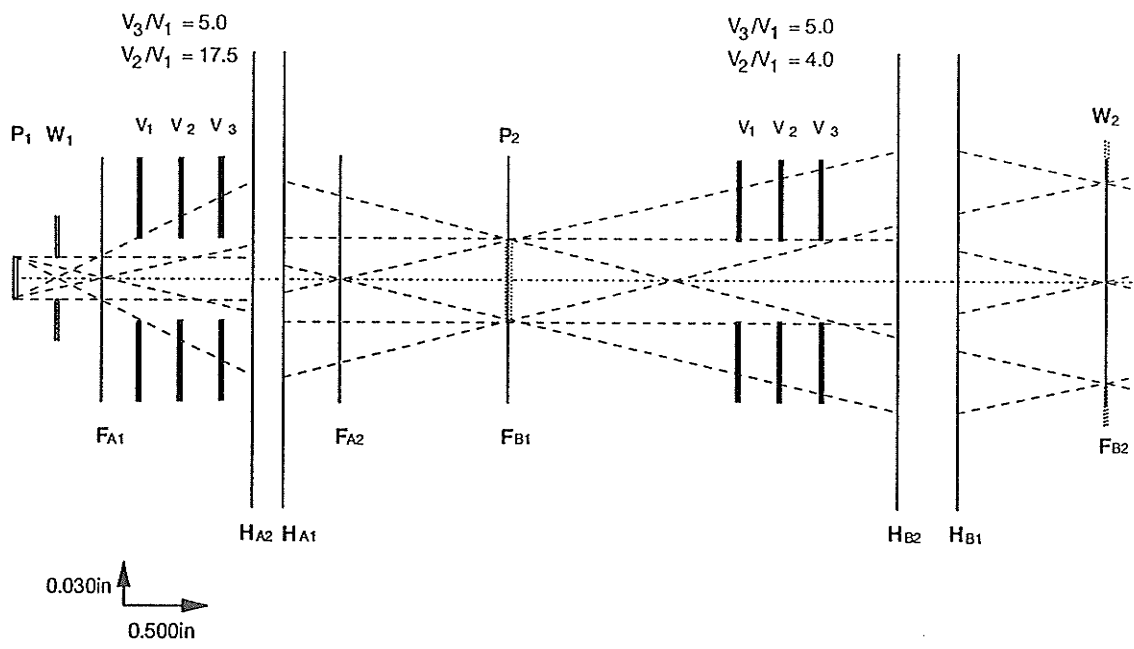


Figure 3.17. The schematic of two triple-aperture lens assemblies (A and B) constituting the entrance lens stack and the configuration of applied voltages. The diagram also shows the electron optics and the ray diagram of electron beam under the given voltage configuration. H and F represent the principal plane and focal plane of each triple aperture lens.

The  $180^\circ$  spherical monochromator is placed next to the final entrance lens so that the image of the electron source produced by the entrance lenses is located at the entrance slit of the hemispherical sectors. The kinetic energy of transmitting electrons is determined by the potential difference between the cathode and the final lens on entrance side. Apertures of 0.1in in diameter are used at entrance and exit slits of the monochromator to strip off electrons that are emitted too far away from beam axis or have too high a transverse momentum. With these parameters, we can predict from Eqn. 3.7 that the energy resolution of the monochromator alone is about 110meV with  $R_0 = 1.0\text{in}$  and  $E = 2\text{V}$ . The maximum deviation of the electron trajectory from the central path is  $0.22R_0$  as calculated from Eqn. 3.8. A pair of hemispherical sectors with  $R_1 = 1.31\text{in}$  and  $R_2 = 1.68\text{in}$  are employed in current design.

The exit lens stack consists of two triple cylinder lenses and the second focal plane of the first triple lens ( $F_{2A}$ ) is coincident with the first focal plane of the second triple lens ( $F_{1B}$ ). With this arrangement, the parallel outgoing electron beam from the exit slit of the monochromator is focused at infinity by the exit lens stack. In other words, the image of the electron source at the exit slit has a crossover at the second focal plane of the second triple lens, that is, 1.5in away from the final lens element in our design (see Figure 3.18). An aperture of 0.125in in diameter is placed at the position of beam waist where  $F_{2A}$  and  $F_{1B}$  fall at the same plane. Since the linear magnification of the exit triple lenses is  $M = 1$ , the final size of the electron beam waist at interaction center is about 0.12in in diameter.

The lenses of the gun and hemispherical sectors are constructed from copper and apertures are made of molybdenum. All apertures and hemispherical sector surfaces are sooted to maintain stable surface potentials

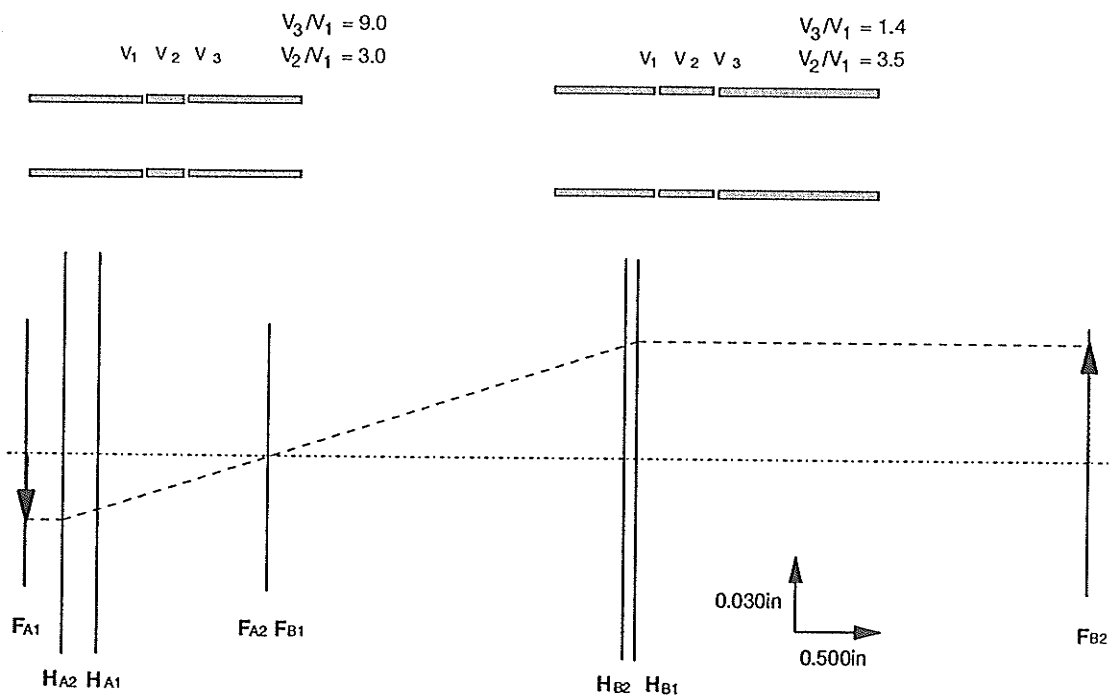


Figure 3.18. (a) The schematic of two cylindrical lenses ( indicated as A and B) which constitute the exit lens stack and the configuration of applied voltages. (b) The electron optics and the ray diagram of electron beam under the given voltage configuration. An object at the first focal plane of lens A is focused at the second focal plane of lens B. H and F represent the principal plane and focal plane of each triple cylindrical lens.

during operation. The tungsten filament is mounted on an adjustable ceramic pole holder that is slide fit into a stainless steel housing. All lens elements of entrance and exit stacks are coaxially mounted on two pairs of ceramic rods, and are attached on entrance and exit sides of the monochromator. A pair of holes are drilled on the outer hemispherical sector for optical alignment of the two lens stacks. Two pairs of deflectors are installed in each of the lens stacks to steer the electron beam in 2-D space.

The performance test of the high resolution gun gave satisfactory results. The overall energy resolution of the spectrometer system can reach 70meV with the high resolution gun, compared with 0.5eV using a high intensity gun. The typical emission current is 300nA measured with a Faraday cup. The electron beam profile is demonstrated in Figure 3.19 with angular resolution of  $2^\circ$  full width at half height. A series of test spectra are shown in Fig. 3.20. The energy resolution of 70meV can be achieved with this gun design. The voltages applied on lens elements are not the same as predicted values. This is probably because the actual electron object source is at the electron cloud formed in front of the filament hairpin instead of filament itself and the location of the electron cloud is unpredictable. Another possible factor is the electron repulsion force that could be strong enough to change the course of electron trajectories at the beam cross over region where the electron density is quite high. The gun retuning for different impact energies can be made by adjusting the potentials of only two lens elements (L4A and L4B), which allow us to change the impact energy easily. The gun can operate reasonably well at impact energy as low as 5eV.

The power supply of the gun consists of a number of voltage regulator cards to provide an adjustable regulated potential to each individual lens. The voltage regulator is designed to generate a regulated current of 1mA that

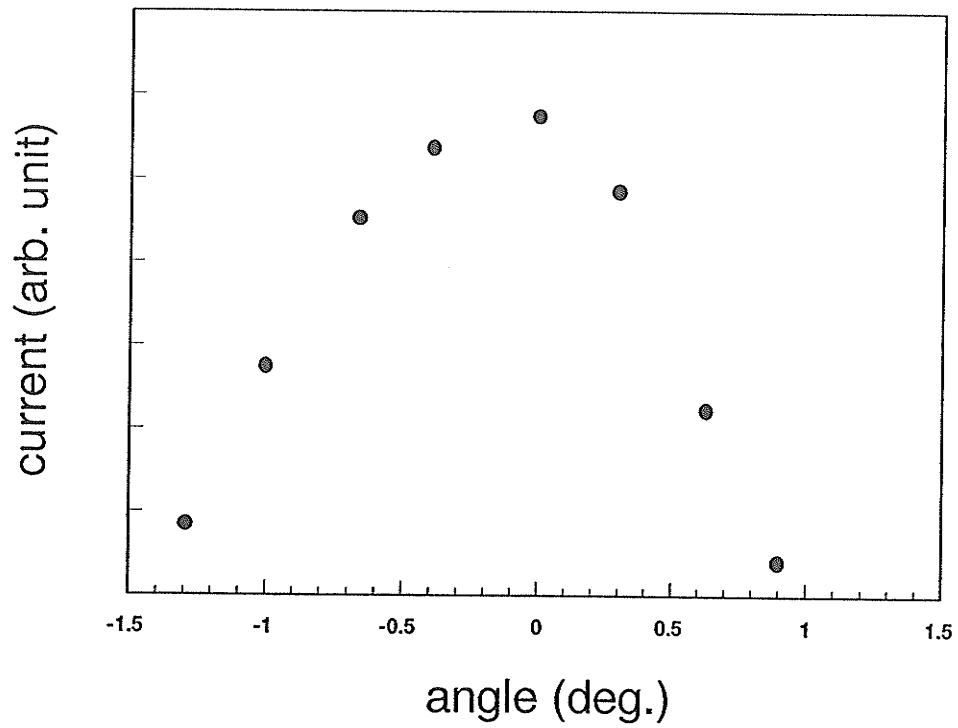


Figure 3.19. The angular distribution of electron beam emitted from the high energy resolution gun. The relative current density is measured on outer hemisphere of the electron detector. X axis represents the angular deviation from forward-scattering direction.

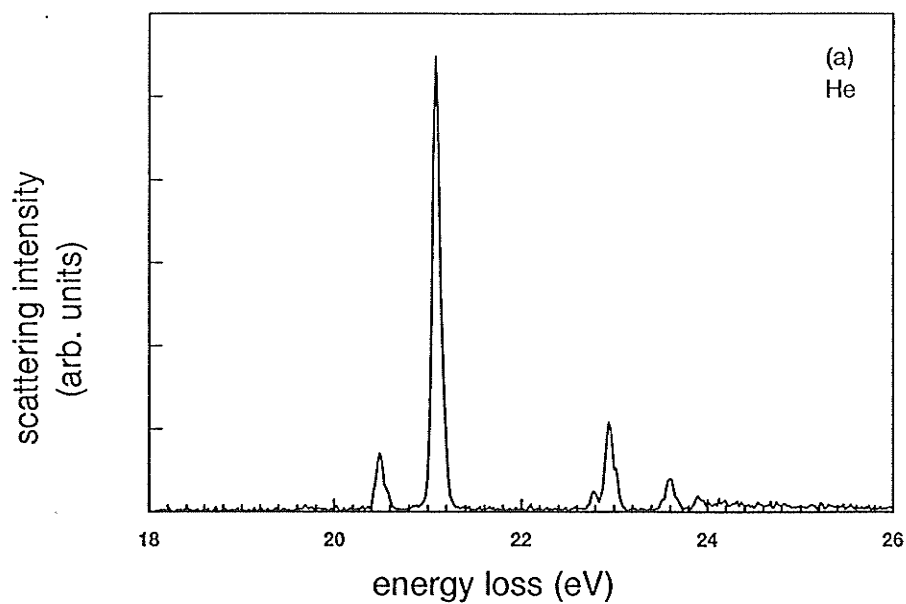
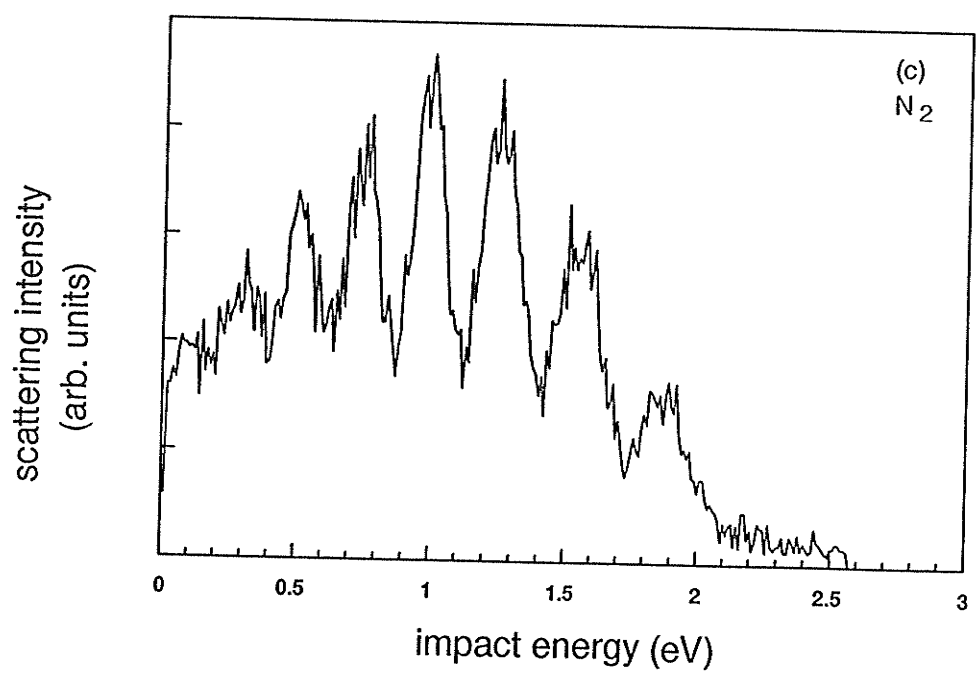
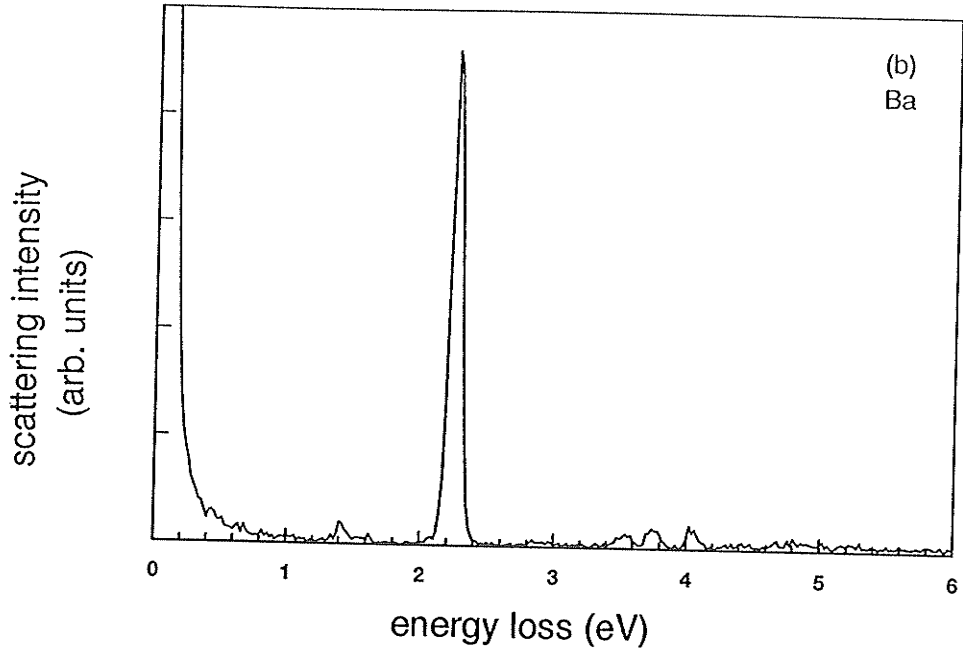


Figure 3.20. Electron impact spectra for the high resolution electron gun test, (a) An energy loss spectrum of helium taken at scattering angle of 13 degrees and with impact energy of 30 eV. (b) An energy loss spectrum of barium taken at scattering angle of 10 degrees and with impact energy of 20 eV. (c) Molecular nitrogen  $v = 0$  to  $v = 1$  inelastic scattering resonance features at scattering angle of 30 degrees. The observed structure corresponds to the excitation of vibrational levels of the  $N_2^-$  negative ion resonance.



flows through a potentiometer across the current output and the reference point. In this way, the desired voltage can be produced, depending on the value of the resistance of the potentiometer. A circuit diagram is given in Appendix 1 (iii). Appendix 1 (iv) shows the diagram of the gun power supply. A 318V DC power is supplied by a Lambda 28M regulated power supply to the regulator cards and the voltage output from the regulator can be varied with respect to the cathode potential. The negative bias of -24V is provided by a Calex dual power supply, which allows the output voltage to cross zero. Because the transmission of electrons is critically sensitive to the potentials on the hemispheres, more stable and accurate potentials are required for the hemispheres in the detector. Two Lambda LSC-A-02 regulated power supplies are utilized here to provide the potentials with regulation stability of 0.01%, ripple and noise of 250microvolts rms. External resistors are used to control the output voltages. The ratio of the potentials between inner and outer hemispheres can be preset by a ten-turn potentiometer. According to Eqn. 3.5 and 3.6, the potentiometer must be adjusted so that

$$\frac{V_{inner} - V_0}{V_{outer} - V_0} = -\frac{R_2}{R_1} \quad 3.9$$

holds for hemisphere radii  $R_1$  and  $R_2$ . The output voltages for each lens and the electron emission currents on each aperture can be measured by a Keithley 175 autoranging multimeter and a Keithley 485 autoranging picoammeter, respectively. A pair of high precision resistors (0.1% accuracy) are used to ensure that the potential on the filament tip is exactly the same as the cathode potential. The filament current is provided by a Lambda LA-200 current regulated power supply.

### 3.7.3 High Intensity Gun

This gun was designed and constructed in JPL and the detailed principle of design has been discussed by Chutjian (Chutjian1979). The basic consideration of the gun design is that the gun can yield an intense current over a wide energy range (1-100eV). A schematic diagram of the gun and the shape of asymptotic rays is shown in Figure 3.21a and Figure 3.21b, respectively. The start of the design consists of a Pierce extraction diode in which electrons are drawn from a filament hairpin by a potential  $V_2 = 80V$ . A real entrance window is denoted as  $w_1$ , and virtual entrance pupil as  $p_1$ . The function of lenses 2 and 3 is to form an intermediate image of  $w_1$  and  $p_1$ , denoted as  $w_2$  and  $p_2$ , respectively. The window  $w_1$  was placed near the first focal point of lens 2 so that the intermediate beam angle in element  $V_3$  is small (0.01rad). Element  $V_3$  is thus a suitable location of a spatter aperture ( $s_1$ ). Lenses 4 and 5 form a three element variable focus lens whose purpose is to focus  $w_2$  at  $w_3$  (located at the scattering center) over a wide range of final electron energies. The intermediate pupil  $p_2$  is focused at  $p_3$ . A second spatter aperture  $s_2$  was placed at the end of element  $V_6$ .

Stainless steel is used for the gun lens elements while the apertures are made of molybdenum. We have simulated the electron trajectories of this gun design with Simion. Good agreement is obtained between the voltage configuration given by Chutjian and the one predicted by Simion. The real test of the gun also indicated that the gun works well with the voltage configuration given by Chutjian. When a tungsten hairpin filament is used, the gun can deliver, typically, a 1-2  $\mu A$  electron current with an energy resolution of approximately 0.5eV FWHM. The divergence angle is measured to be  $6^\circ$ .

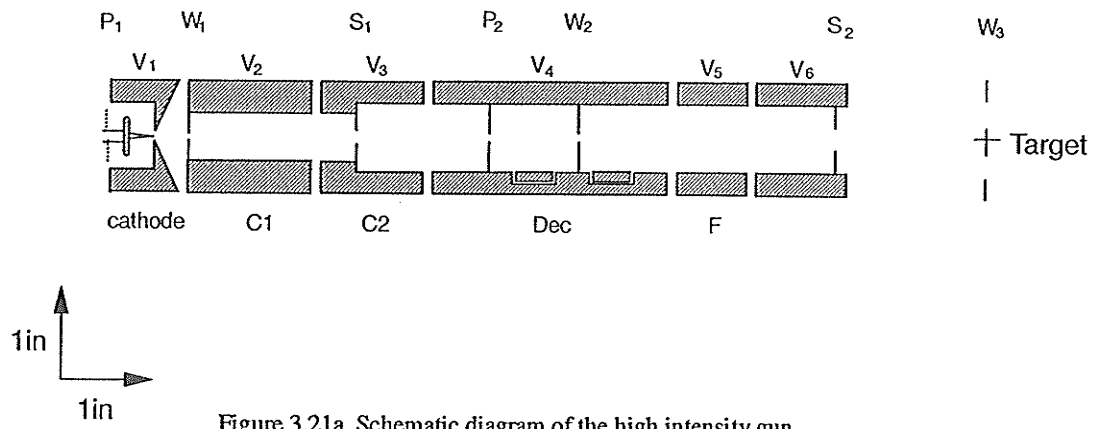


Figure 3.21a. Schematic diagram of the high intensity gun.

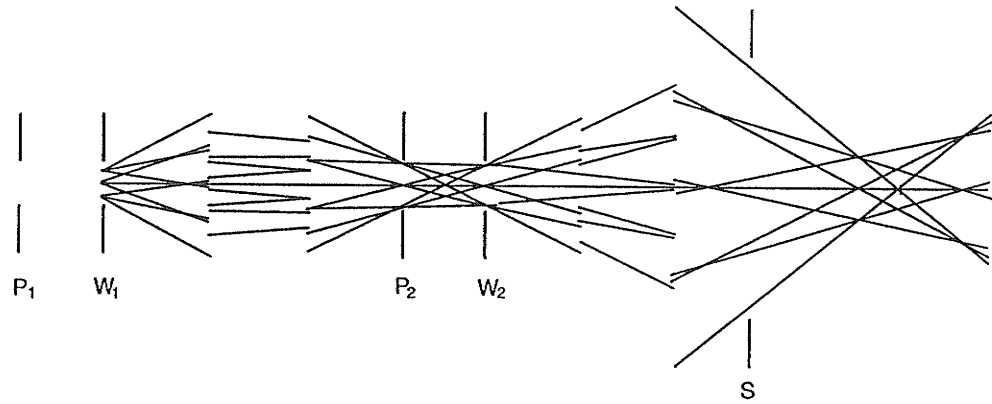


Figure 3.21b. Asymtotic rays for operation of the gun at impact energy of 20eV ( in the high mode).  
Adopted from Ref.(Chutjian1979).

The circuit diagram of the power supply is given in Appendix 1 (v). The same current regulator cards as mentioned in Part A) are installed in this power supply.

### 3.7.4 Detector

The geometrical arrangement of the electron detector is shown in Figure 3.22. This system consists of an entrance lens stack, a hemispherical monochromator, an exit lens, channeltron house and channeltron multiplier. The system was designed and constructed in JPL. The detailed design procedure can be found in Chutjian's work (Chutjian1979). As mentioned in Part B, the two main design criteria were to provide at the exit plane ( $w_3$ ) a real image of a fixed final energy, whose location is independent of scattered electron energy, and to place the final exit pupil at infinity. A collimated beam at the output of the entrance lens stack is provided, which can prevent loss of electrons within the monochromator. The fixed energy of electron at  $w_3$  is taken to be 2eV. In order to improve the energy resolution of the analyzer, the electrons must be decelerated prior to their entering the monochromator. This can be accomplished by using a decelerating lens. An energy analyzer can be used to scan over the energy loss range of interest by varying the analyzer common potential  $V_a$  (see Figure 3.10). A satisfactory method for the scanning is to fix the monochromator potential at that voltage that allows transmission of electrons of the certain kinetic energy and to scan the analyzer common to pass electrons with various residual energies. The transmission intensity of electrons versus analyzer potential is then a measure of electron impact excitation of the atomic target.

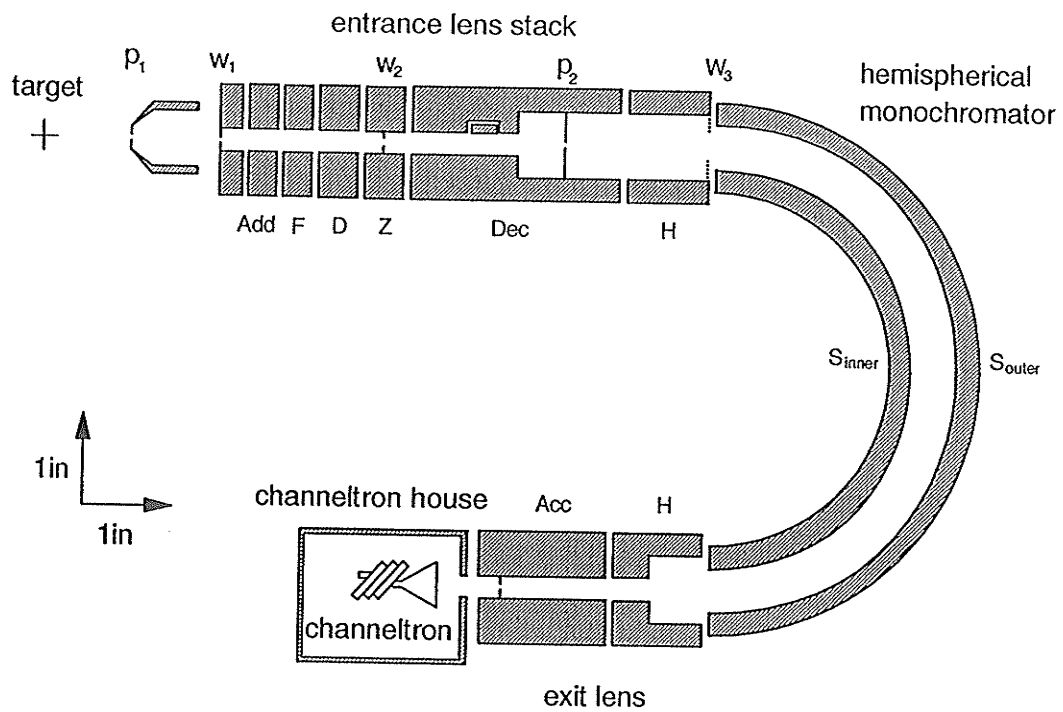


Figure 3.22. Schematic of the electron detector (analyzer). The location of windows and pupils are indicated in the diagram.

A pair of hemispheres with inner diameter of 4.50in and outer diameter of 5.50in are utilized in the energy analyzer. The function of the exit lens is to focus the image at monochromator exit slit to channeltron acceptance cone. A channeltron housing was designed to prevent strong electrical field from the high potential on channeltron from leaking out. The surfaces of lenses and hemispheres are coated with gold and sputtered. The upper limit of the energy resolution is 70mV, estimated from the overall resolution of the spectrometer system. The detection viewcone is determined by the aperture on the nozzle and the aperture on the energy-add lens and is estimated to be approximately 6.3°.

The power supply for the detector is similar to the ones for guns as shown in Appendix 1 (vi).

### **3.8 Metal Vapor Source**

High temperature is needed to produce the atomic beam target for the electron collision experiment. The minimum operating temperature for a metal source to deliver enough target density is 500°C for ytterbium and 700°C for barium. The present metal vapor beam source consists of a tubular stainless steel crucible, a resistive, coaxial heating wire, a thermocouple, a stainless steel thermal shield and a current regulated power supply.

The crucible is wrapped with the heating wire that has close thermal contact with the crucible body. A tunnel of 0.040in in diameter is drilled to release the metal vapor from a chamber that contains the metal sample. A nickel coated stainless steel plug is pressed against a knife edge to seal the crucible. The high temperature evaporates the metal sample and the metal vapor pressure builds up inside the crucible chamber. A beam of metal vapor

pours out from the chamber into the vacuum. Care has been taken in the design to reduce the thermal conduction from the crucible into the surrounding objects by using high temperature ceramic rods to support the crucible.

Atoms leave the source by effusion if the source pressure and the tunnel diameter are chosen such that the atoms pass through the tunnel without collisions. The effusion of atom beam has been discussed in the works by Ramsey (Ramsey1958) and Valyi (Valyi1977). In the case of thin apertures, when the tunnel length  $l \sim 0$ , the condition under which effusion can take place can be expressed as

$$d \ll \lambda_A \quad 3.10$$

where  $d$  is the diameter of the aperture and  $\lambda_A$  is the collision mean free path of atoms in the source which, in terms of gas kinetic theory, is given by the formula

$$\lambda_A = \frac{1}{\sqrt{2}\sigma_k n} \quad 3.11$$

where  $n$  is the number of atoms per unit volume,  $\sigma_k$  is the collision cross section of atoms defined as  $\sigma_k = \pi\delta^2 / 4$ , and  $\delta$  is the atomic diameter.

If the beam of atoms is emitted by effusion across a aperture of width  $d$  and length  $l \sim 0$ , then the number of atoms in the solid angle  $d\omega$  effusing in the direction of angle  $\Theta$  is given by the expression

$$dN = \frac{d\omega}{4\pi} n\bar{v}A_s \cos\Theta \quad 3.12$$

where  $A_s$  is the area of the cross section of the aperture. The angular distribution of the beam density is of cosine type. Taking the particle mass to be  $m$  and assuming Maxwellian particle velocity distribution in the source, the mean particle velocity  $\bar{v}$  can be expressed as

$$\bar{v} = \sqrt{\frac{8kT}{\pi m}} \quad 3.13$$

The number of particles effusing from the source in all directions during unit time is obtained by integrating Eqn. 3.12 over the solid angle  $2\pi$

$$N = \frac{1}{4} n \bar{v} A_s \quad 3.14$$

If a thin tunnel is used for the exit, a beam with good collimation can be produced and the angular distribution of the atoms flying out from the source changes according to the ratio  $l/d$  as is apparent from Figure 3.23. The change in the angular distribution can be explained by the fact that the atoms flying into the tunnel at a large angle collide with the tunnel wall and have less chance of flying out from the source. To prevent the collisions between atoms and the wall in a tunnel, the pressure has to be chosen such that

$$l \leq \lambda_A \quad 3.15$$

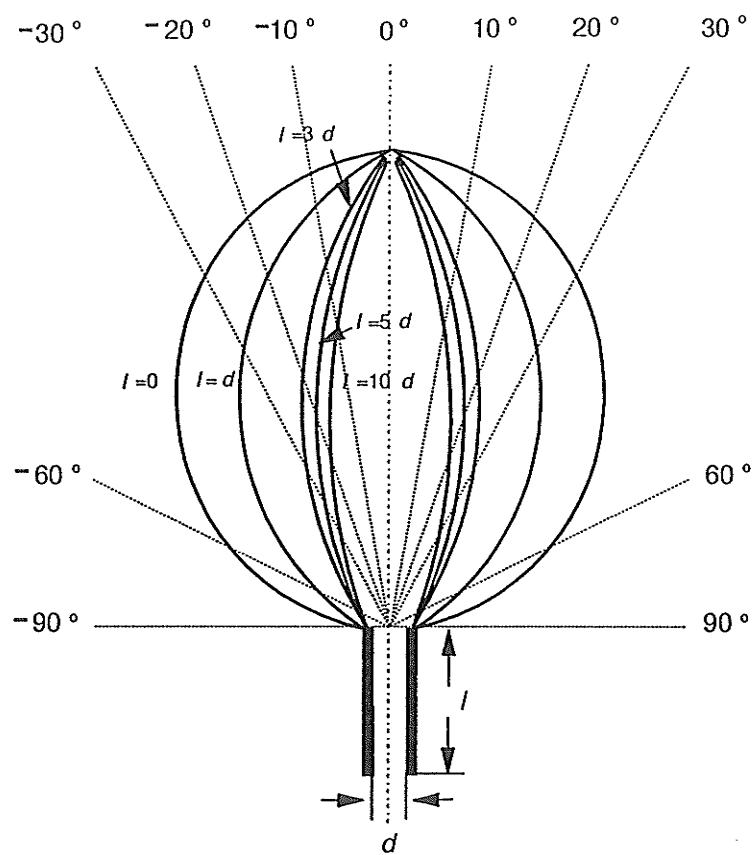


Figure 3.23. Relative angular distributions of atom beams emitted from atom source through a tube of diameter  $d$  and of different lengths  $l$ . Adopted from (Valyi 1977)

The number of atoms effusing out of the tunnel during unit time can be expressed only by introducing a reduction coefficient symbolized by  $\xi$

$$N = \frac{1}{4} \xi n \bar{v} A_s \quad 3.16$$

The reduction coefficient  $\xi$  has been already evaluated for the tunnels of different shapes. If  $d$  stands for the diameter of circular tunnel and  $l$  for the length of the tunnel, the reduction coefficient is given for  $d \ll l$  by

$$\xi = \frac{4d}{3l} \quad 3.17$$

The density of the atom beam at the exit of the tunnel can be derived from Eqn. 3.16

$$n_{exit} = \frac{1}{4} \xi n \quad 3.18$$

The value of the half angle of the atom beam, associated with the half beam intensity has been calculated

$$\theta_{\frac{1}{2}} = \frac{0.84d}{l} \quad 3.19$$

The ratio  $l/d$  can be chosen such that it corresponds to the  $\theta_{1/2}$  in the given geometry of the apparatus. This increases the useful fraction of the emitted beam and also the utilization efficiency of the material. In practice, the vapor pressure may be so high that Eqn. 3.15 can not hold. Under this

circumstance, the above procedure can only give us a qualitative estimation in the beam shape.

The real procedure for the beam shape determination can be started from the determination of the metal vapor pressure in the chamber. The vapor pressures of ytterbium and barium atoms at various temperatures are given in Table 3.4. The metal vapor density can thus be calculated using the ideal gas law. The atom beam density at the exit of the tunnel and the half angle of the beam  $\theta_{1/2}$  can be obtained from Eqn. 3.18 and Eqn. 3.19, respectively, while  $\xi$  is given by Eqn. 3.17. The atom beam spreads when it flies towards the interaction region and the beam density at the interaction region is then determined by the half angle  $\theta_{1/2}$ , the flight distance of atoms before they reach the interaction center, and the diameter of the tunnel.

Since radiation plays the major role in the dissipation of heat under the vacuum, a thermal shield is necessary to reduce the thermal radiation and maintain a high temperature in the metal source. Thermal shield can also concentrate the stray metal vapor on its inner surface to reduce the chamber contamination. A thin aperture of 0.060in in diameter on the thermal shield defines the atom beam direction and leads to the collimation of the beam. The collimation angle depends on the size of the aperture on the crucible and the one on the shield. In our current design the beam is collimated within 12° full angle, which leads to a beam size of 0.10in in diameter at the interaction center of 0.5in away from the thermal shield. A ARI aerOrod coaxial heater is used as heat source for the crucible. A constant DC current of typically, 1.5 to 2.0A flows through the heater to deliver up to 160Watts power, which is enough to heat up the metal source to the operating temperatures.

A chromel-alumel thermo couple is attached to the crucible to measure the temperature of the metal source in respect to the room

Table 3.4. The barium and ytterbium vapor pressure vs. temperature.

Pressure (atm.)	Temperature (°C)
Barium	
10 <sup>-10</sup>	360
10 <sup>-9</sup>	409
10 <sup>-8</sup>	466
10 <sup>-7</sup>	533
10 <sup>-6</sup>	614
10 <sup>-5</sup>	712
10 <sup>-4</sup>	843
10 <sup>-3</sup>	1015
10 <sup>-2</sup>	1250
10 <sup>-1</sup>	1590
1	2125
Ytterbium	
10 <sup>-10</sup>	228
10 <sup>-9</sup>	262
10 <sup>-8</sup>	301
10 <sup>-7</sup>	346
10 <sup>-6</sup>	400
10 <sup>-5</sup>	463
10 <sup>-4</sup>	541
10 <sup>-3</sup>	638
10 <sup>-2</sup>	775
10 <sup>-1</sup>	943
1	1194

temperature. The error limit of standard chromel-alumel thermocouple is about  $\pm 2^{\circ}\text{C}$  below  $280^{\circ}\text{C}$  and  $\pm 0.75\%$  above  $280^{\circ}\text{C}$ . The voltage output vs temperature curve of chromel-alumel thermo couple is approximately linear and the voltage output at the typical operation temperature is on the order of  $20\text{mV}$ , which can be easily measured with ordinary voltmeter.

## CHAPTER 4

# MEASUREMENTS OF ELECTRON IMPACT COHERENCE PARAMETERS FOR ELECTRON-IMPACT EXCITATION OF $^{138}\text{Ba}(\dots 6s6p \ ^1P_1)$

### 4.1 Introduction

A comprehensive review of electron impact coherence parameter measurements and theory has been introduced in Chapter 2. A set of physically appealing EICP ( namely  $P_l^+$ ,  $\gamma$ ,  $L_\perp$  and  $\rho_{00}$  ) have been defined by Andersen et al (Andersen1988), which describe the shape and dynamics of an excited charge cloud. For the most widely studied cases in the EICP investigation, efforts have been applied to the study of s to p excitation with the aim toward measuring the relative phases and magnitudes of scattering amplitudes that describe the excitation.

Experimental determination of EICP's for alkaline-earth metal targets has been accomplished using both electron-photon coincidence and superelastic techniques. The coincidence method has been employed by Brunger et al. (Brunger1989), Zohny et al. (Zohny1990), and Hamdy et al. (Hamdy1991) to measure EICP's for the Mg  $3^1P_1$ , Ca  $4^1P_1$ , and Sr  $5^1P_1$

excitations, respectively. Further measurements on Ca and Sr were reported by Hamdy et al. (Hamdy1993) and Beyer et al (Beyer). Superelastic scattering experiments have been used to measure EICP's for the Ca  $4^1P_1$  excitation by Law and Teubner (Law1993).

Electron-photon coincidence measurement applied to metallic elements such as alkalis and alkaline earth are somewhat difficult, because of the requirement for long measurement time in this type of experiment. On the other hand, superelastic scattering experiments using laser-excited atoms are more efficient. Orders of magnitude reduction in the data collection time proves to be essential for the experiments in the case of metal atom studies. The duration of an experiment is constrained by the vaporization rate of the finite metal sample and is usually on the order of 30 hours. Because of the high monochromaticity of the dye laser, we can isolate the specific hyperfine levels belonging to a certain isotope. This therefore allows us to eliminate the effect of hyperfine depolarization and offers us isotope selectivity.

The superelastic scattering technique has been applied to the study of barium by Register et al (Register1983) in an attempt to measure EICP for excitation of the  $^{138}\text{Ba}(\dots 6s6p \ ^1P_1)$  level. The notation of Moore (Moore1958) is used to designate this energy level under the assumption that it is predominantly an LS coupled  $^1P_1$  state but contains a substantial contribution from the  $(\dots 5d6p)$  configuration (Clark1989). Barium provides an attractive atomic target for the experimentalist since it is relatively straightforward to produce barium vapor beams and the excitation of the  $^1P_1$  level with 553.5nm radiation is easily accomplished using a Rhodamine 110 dye laser. The  $^{138}\text{Ba}$  energy level structure is uncomplicated by hyperfine structure and the laser pumping process is therefore simple to describe.

Barium offers considerable scientific interest as a target for electron-scattering studies. Like the other alkaline-earth elements, it consists essentially of a simple system of two valence electrons bound to a relatively inert core and offers a natural extension to studies carried out on the helium atom that is, by far, the most extensively investigated collision target. With an atomic number of  $Z=56$ , we can consider barium to be a "heavy atom" in which spin-dependent forces may play a role during the electron collision. The  $J=0$  to  $J=1$  transition in this atom can be compared with an analogous transition in the heavy rare gases, which have been the focus of study by several groups carrying out electron-photon coincidence experiments (Corr1990)(Murray1990)(Martus1991).

Determination of EICP for the excitation of  $^{138}\text{Ba}(\dots 6s6p \ ^1P_1)$  is also of considerable theoretical interest. The present investigation of barium is motivated, in part, by ongoing theoretical effort to calculate these EICP. In particular, results employing first-order perturbative theories have been reasonably successful in predicting EICP for the excitation of rare gas targets (Bartschat1987, da Paixao1984 and Zuo1992). Such approaches have been recently applied to the calculation of EICP for the barium ( $6s^2 \ ^1S_0$ ) to ( $6s6p \ ^1P_1$ ) excitation (Clark1989 and Srivastava1992). The unitarized distorted-wave approximation (UDWA) has been utilized by Clark et al (Clark1989). This approach employs a description of the atomic structure that is relativistic to the extent that the mass correction and Darwin terms are included in the calculation of radial wave functions. The continuum electron is treated nonrelativistically. The importance of spin nonconservation in the collision through exchange excitation can, therefore, be predicted with this theory, while the amplitude for direct spin flip of the projectile electron is not calculable. The atomic-structure calculations show that the barium  $^1P_1$  state is

predominantly LS coupled and, as a consequence, UDWA theory predicts spin to be conserved during the collisional interaction and gives  $\rho_{00} = 0$ . Calculations of barium EICP with a fully relativistic distorted-wave (RDW) theory have recently been reported (Srivastava1992). This theory utilizes Dirac-Fork target states and solutions to the Dirac equation in the presence of a distortion potential. Although the atomic-structure calculations used in this theory also give a purely LS-coupled  $^1P_1$  state, some relativistic effects (spin-dependent) properties of the scattering were predicted, namely a nonzero spin-polarization function  $S_p$ . The manifestation of relativistic effects through the EICP was again predicted to be negligible (i.e.  $\rho_{00} \leq 10^{-4}$ ). Both theories, therefore, suggest an analogy between the barium  $^1S_0$  to  $^1P_1$  excitation and the helium  $1^1S_0$  to  $2^1P_1$  excitation. Two-state close-coupling calculations were carried out by Fabrikant to predict DCS (Fabrikant1980) and EICP (Fabrikant1985) at 20eV impact energy. These calculations involved a nonrelativistic approach in which semiempirical atomic wave functions were employed and exchange between the incident electron and core target electrons was ignored.

In general, the charge cloud may have mixed reflection symmetry due to the presence of spin-dependent terms in the interaction Hamiltonian. Our initial rationale behind the study of barium EICP was to investigate the influence of spin-dependent forces acting during the collision. When  $\rho_{00} = 0$  the scattering can be described purely in terms of LS coupling. In this case the two coherence parameters  $P_l^+$  and  $L_l^+$  are related by  $(P_l^+)^2 + (L_l^+)^2 = 1$  and only two independent parameters are needed to describe the scattering process.

In the first reported study of superelastic scattering from laser-excited barium, Register et al (Register1983) arranged their experimental geometry so

that optical excitation of the (...  $6s6p\ ^1P_1$ ) level was accomplished by a laser beam located in the scattering plane ( an "in-plane" experiment). These investigators were unable to extract EICP because they found that, at small scattering angles, the superelastic scattering signal was asymmetric to reflection of the polarization vector with respect to the scattering plane and this is in contradiction with theoretical predictions. Further investigation by Zetner et al (Zetner1989) pinpointed the cause of this asymmetry and revealed that "in-plane" superelastic scattering experiments are strongly influenced by the small but finite spatial extent of the scattering volume even at scattering angles far from zero. This influence manifests itself in the above mentioned asymmetry as well as in a severe reduction in the sensitivity of the superelastic scattering signal to the polarization direction of the linearly polarized laser beam — an effect we will refer to as "depolarization" of the scattering signal. Further modelling calculations showed that superelastic experiments employing a laser beam perpendicular to the scattering plane ( $\pi/2$  out-of-plane) are insensitive to the finite volume effect at medium and large scattering angles.

The electron impact coherence parameters, in combination with differential cross section (DCS), can yield magnetic sublevel partial differential cross section (PDCS). Magnetic sublevel PDCS generated by the appropriate combinations of EICP and DCS have been presented by Csanak et al. (Csanak1992 and Csanak1993) in a comparison of experiment and theory for electron impact excitation of the  $n^1P_1$  of helium.

Magnetic sublevel PDCS differ from conventionally measured DCS in that the latter quantity involves an average over initial magnetic sublevels and sum over final magnetic sublevels of the squared moduli of the scattering amplitudes. Hummer and Burns (Hummer1986) have measured magnetic

sublevel PDCS for excitation of the He( $3^1P$ ) level using electron-photon coincidence techniques.

In this chapter, the EICP  $P_l^+$ ,  $\gamma$  and  $L_{\perp}^+$  for electron collision excitation of  $^{138}\text{Ba}(\dots 6s6p\ 6^1P_1)$  are measured using the superelastic scattering method. The present experiment was configured to allow the laser beam to strike the atomic target at  $90^\circ$  to the scattering plane. The coherence parameters  $P_l^+$  and  $\gamma$  are measured using linearly polarized laser light while  $L_{\perp}^+$  is obtained by use of circularly polarized light. We have extended our  $L_{\perp}^+$  measurements to large scattering angles at various impact energies and demonstrated pronounced structure in its angular dependence. The direct comparison between experiment and existing theories is most meaningful when scattering-angle coverage is complete enough to display the phenomena predicted by theoretical calculations. Detailed comparison will be made with the UDWA calculations of Clark et al. (Clark1989), the RDW calculations of Srivastava et al. (Srivastava1992), and the close-coupling theory of Fabrikant (Fabrikant1985). We then derived  $\chi$  parameter devised by Blum et al. (Blum1980) and da Paixao et al (da Paixao1980) using our results of measured EICP. Furthermore we extracted magnetic sublevel partial differential cross sections for electron collision excitation of ( $\dots 6s6p\ 6^1P_1$ ) level based on the sublevel-averaged DCS measurements of Jensen et al (Jensen1978) and Wang et al (Wang1994) in combination with our measured EICP results.

## 4.2 Measurement Theory

The theory of electron scattering by laser-excited atoms developed by Macek and Hertel (Macek1974) has been introduced in Chapter 2. The superelastic

scattering intensity  $I^s$  for an experiment can be given by Eqn.2.7 with all the notations defined. This general expression can be arranged, for deexcitation of a  $J = 1$  to  $J = 0$  state, to give the explicit dependence of  $I^s$  on the EICP  $\{\lambda, \tilde{\chi}, \Delta, \epsilon\}$  and the polarization state of the laser light at the scattering target. For a purely linear-polarized laser beam passing through a retardation plate (which introduces a phase retardation of  $\delta$ ), the polarization state at the target is generally elliptical, and we can write

$$I^s = \frac{\bar{C}}{3} \{A + B' [\cos(2\alpha - 2\beta) \cos 2\beta - \sin(2\alpha - 2\beta) + B'' [\cos(2\alpha - 2\beta) \sin 2\beta + \sin(2\alpha - 2\beta) \cos 2\beta \cos \delta + C \sin(2\alpha - 2\beta) \sin \delta], \quad 4.1$$

where

$$\begin{aligned} \bar{C} &= \frac{C_i}{2} \sum_{m_s, m_{s_2}} |f(nJM_J k_2 m_{s_2}, n_0 0 0 k_1 m_{s_1})|^2 \\ A &= 1 + \frac{1}{4}(1 - 3\lambda)(3 \cos^2 \theta_{\bar{n}} - 1) + \frac{3}{2} \sqrt{\lambda(\lambda - 1)} \cos \tilde{\chi} \cos \Delta \sin 2\theta_{\bar{n}} \cos \phi_{\bar{n}} \\ &\quad + \frac{3}{4}(\lambda - 1) \cos \epsilon \sin^2 \theta_{\bar{n}} \cos 2\phi_{\bar{n}} \\ B' &= -\frac{3}{4} \sin^2 \theta_{\bar{n}} (1 - 3\lambda) + 3 \cos \theta_{\bar{n}} \sin \theta_{\bar{n}} \cos \phi_{\bar{n}} \sqrt{\lambda(1 - \lambda)} \cos \tilde{\chi} \cos \Delta \\ &\quad - \frac{3}{2} (1 - \frac{1}{2} \sin^2 \theta_{\bar{n}}) \cos 2\phi_{\bar{n}} (\lambda - 1) \cos \epsilon \\ B'' &= -3 \sin \phi_{\bar{n}} \sin \theta_{\bar{n}} \sqrt{\lambda(1 - \lambda)} \cos \tilde{\chi} \cos \Delta + \frac{3}{2} \sin 2\phi_{\bar{n}} \cos \theta_{\bar{n}} (\lambda - 1) \cos \epsilon \\ C &= -3 \sqrt{\lambda(1 - \lambda)} \sin \tilde{\chi} \cos \Delta \sin \theta_{\bar{n}} \sin \phi_{\bar{n}} \end{aligned}$$

The details about the coordinate system and the definition of angles  $\theta_{\bar{n}}, \phi_{\bar{n}}, \alpha$  and  $\beta$  are shown in Figure 4.1 (also referred to Ref. (Zetner1990)). A brief discussion of the relevant coordinate system is given in the following. In the superelastic-scattering experiment, the electrons are characterized by the momentum of the incident electron ( $k_i$ ) and scattered electron ( $k_p$ ) for the superelastic-scattering process. For the inverse inelastic process, we use the notation  $k_{in}$  and  $k_{out}$  for the momentum of the incident and scattered electrons,

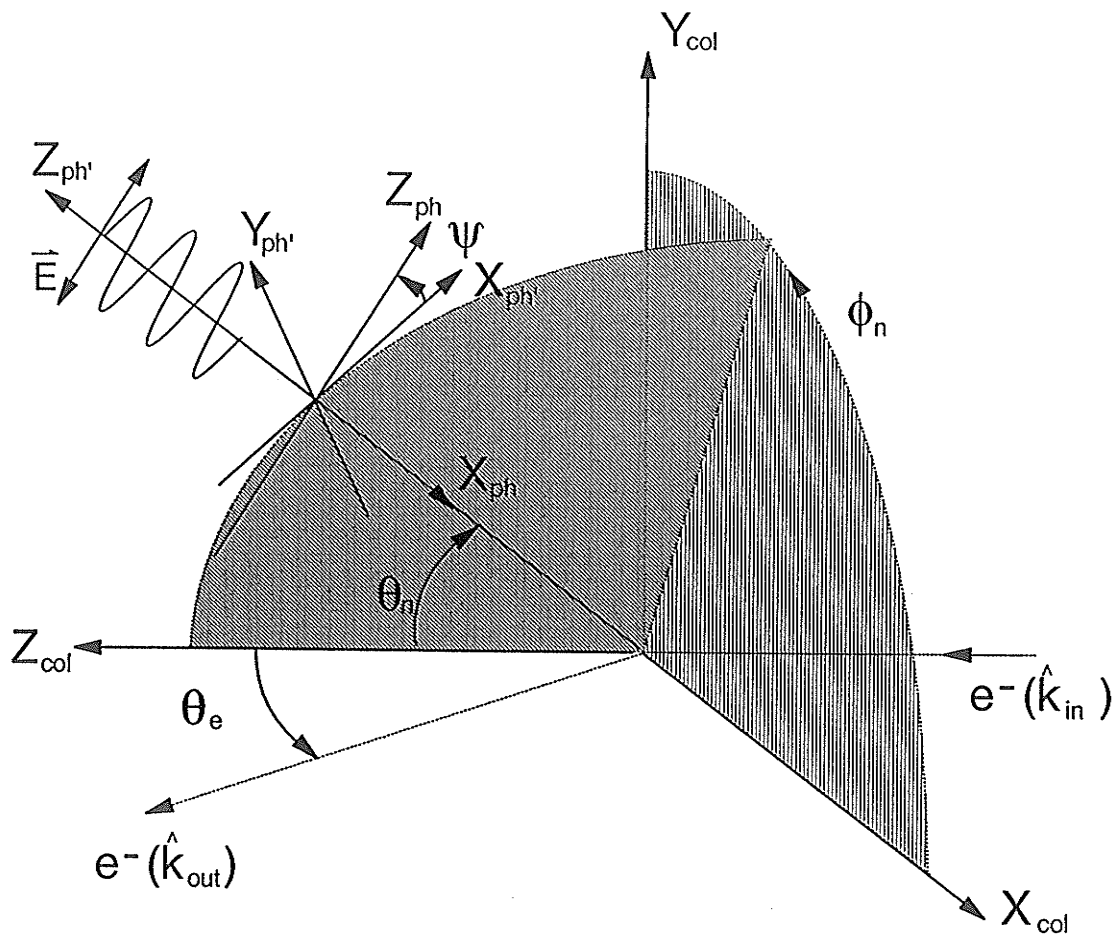


Figure 4. 1. The details about the coordinate systems and the definition of angles involved.  $(X_{col}, Y_{col}, Z_{col})$  denotes the collision frame,  $(X_{ph}, Y_{ph}, Z_{ph})$  the photon frame, and  $(X_{ph'}, Y_{ph'}, Z_{ph'})$  the laser frame. The diagram also gives the laser light propagation and linear polarization directions, and the incoming and scattered electron directions for the inelastic-scattering process. In the case of elliptically polarized light, the polarization light state will be the superposition of two polarization light states polarized in orthogonal directions and with phase shift  $\delta$ .

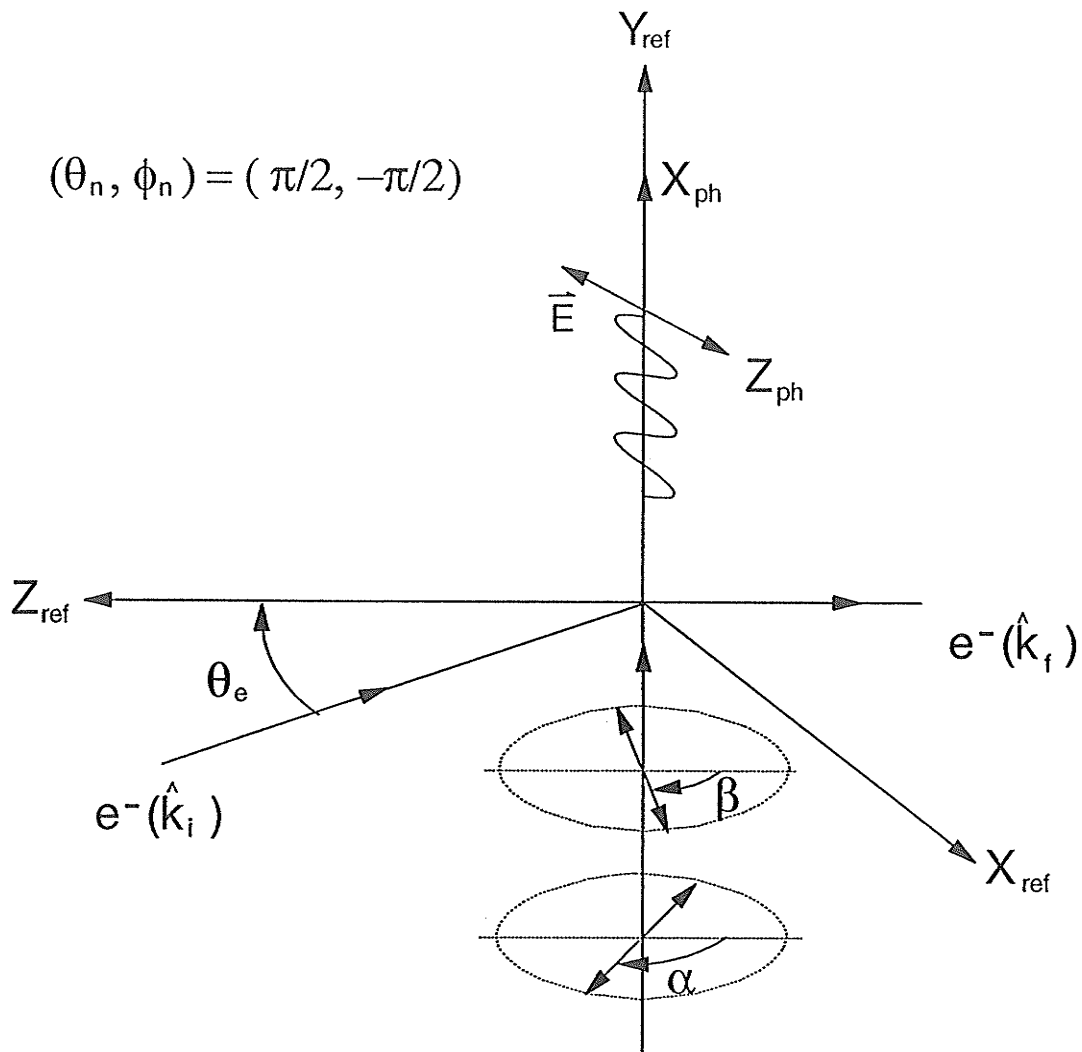


Figure 4.2. The specific geometry employed in our superelastic-scattering experiment when a half-wave retardation plate is used. In this case, the spherical polar angle  $(\theta_n, \phi_n)$  are set to be  $(\pi/2, -\pi/2)$ .

respectively. The correspondence of these two processes has been illustrated in Chapter 2 (see Figure 2.1 and Figure 2.3). The collision frame is also defined in Figure 2.6 and is denoted as  $(X_{col}, Y_{col}, Z_{col})$  in our coordinate system. A "laser frame"  $(X_{ph'}, Y_{ph'}, Z_{ph'})$  is defined such that  $Z_{ph'}$  is selected along the laser line of incidence but against the direction of incidence. The polar angles of the positive  $Z_{ph'}$  axis in the collision frame are denoted by  $\theta_{\vec{n}}$  and  $\phi_{\vec{n}}$ . The positive  $X_{ph'}$  axis is chosen to lie in the  $[Z_{ph'}, Z_{col}]$  plane in such a way that the laser frame  $[X_{ph'}, Y_{ph'}, Z_{ph'}]$  is obtained from the collision frame  $[X_{col}, Y_{col}, Z_{col}]$  through rotations by Euler angles  $(\theta_{\vec{n}}, \phi_{\vec{n}}, 0)$ . Then  $\alpha$  denotes the angle between the laser beam electric-field vector and the positive  $X_{ph'}$  axis (before the beam traverses the retardation plate), while  $\beta$  gives the angle between the fast axis of the retardation plate and the positive  $X_{ph'}$  axis. Rotation of a right-handed screw in the direction of increasing  $\alpha$ ,  $\beta$  defines the  $Z_{ph'}$  axis.

The experimental arrangement adopted in the present investigation fixes the electron detector and allows the electron-beam source to rotate. In our arrangement, the laser incidence direction is in the positive  $Y_{col}$  direction. Hence, for a scattering event occurring at the origin of the reference frame, the spherical polar angles  $(\theta_{\vec{n}}, \phi_{\vec{n}})$  are given by  $(\pi/2, -\pi/2)$ . The laser beam incidence and polarization geometry for our experimental arrangement is shown in Figure 4.2. Also notice that we use  $k_i$  and  $k_f$  here to characterize the electrons in the superelastic-scattering process. With this set of polar angles, the superelastic-scattering intensity formula Eqn. 4.1 can be simply expressed in terms of natural-frame EICP,

$$I^s(\beta - \alpha) = \frac{A\bar{C}}{3} \left\{ 1 + \frac{P_l^+}{2} (1 + \cos \delta) \cos(2\alpha - 2\gamma) \right\}$$

$$\begin{aligned}
& + \frac{P_l^+}{2}(1 - \cos\delta)\cos(4\beta - 2\gamma - 2\alpha) \\
& + L_{\perp} \sin\delta\sin(2\beta - 2\alpha)
\end{aligned}
\tag{4.2}$$

For a fixed  $\alpha$ , the measured dependence of  $I^s$  on  $\beta$  can thus be used to readily extract the coherence parameters.

### 4.3 Experimental Details of $P_l^+$ , $\gamma$ and $L_{\perp}^+$ Measurement

The general description of the experimental apparatus has been given in Chapter 3. The high intensity electron gun is rotatable with respect to a fixed, hemispherical electron detector. Typical beam current at the interaction region is about 200nA with energy resolution of 0.5eV and with about  $\pm 2^\circ$  beam divergence. The linearly polarized laser light from the ring dye laser pumped by the argon ion laser is incident upon the target Ba vapor beam from below the scattering plane and strikes the scattering plane perpendicularly. The metal-vapor source is heated to a typical operating temperature of about 760°C and produces a beam collimation of 10:1 with typical number density of the order of  $7 \times 10^{10} \text{cm}^{-3}$  at the interaction region. A Glan-Taylor prism was employed in the present work to ensure linear polarization of the incident laser light. Typical laser powers of 100mW in single mode were used.

Before entering the vacuum chamber viewport, the beam traverses a retardation plate ( $\lambda/2$  or  $\lambda/4$  at 555nm). By continuously rotating a  $\lambda/2$  plate with constant angular speed, we can generate a light beam with rotating linear polarized electric field vector at the collision center. By using a  $\lambda/4$  plate, we can convert linearly polarized laser light into circularly polarized light at the

collision center if the fast axis of the plate is properly aligned with respect to the GT prism transmission axis.

The polarization state of the laser light at the interaction region is determined by the true value of the phase retardation introduced by the retardation plate (possibly not exactly  $\delta = \pi$  for  $\lambda/2$  plate and  $\delta = \pi/2$  for  $\lambda/4$  plate), as well as the possible presence of stress-induced birefringence in the bottom viewport. In the present experiments we employed multiple-order quartz retardation plates that were specified as  $\lambda/2$  or  $\lambda/4$  at  $\lambda = 555\text{nm}$ . Diagnostic measurements as described by Wedding, Mikosza, and Williams (Wedding1991) were carried out to determine  $\cos\delta$ . Figure 4.3 is a schematic of a polarizer-analyzer combination used to determine the retardation of a plate that was initially designed to characterize the polarization of light. The polarization analyzer is composed of a polarizer (Pol#1) and a retarder. An additional linear polarizer (Pol#2) with its transmission axis defining the reference axis  $x$  was included before the polarization analyzer. The additional polarizer transmits linearly polarized light to be incident upon the analyzer. The transmitted intensity of the polarizer-analyzer system is (Wedding1991)

$$I(\alpha, \beta, \delta) = I_0 \{1 + P_1 [\cos 2(\alpha - \beta) \cos 2\beta - \sin 2(\alpha - \beta) \sin 2\beta \cos \delta]\}$$

4.3

where  $\alpha$  is the angular displacement of transmission axis of Pol#2 with respect to  $x$ -axis ( i.e. the direction of the transmission axis of Pol#1),  $\beta$  the angular displacement of fast axis of the retarder with respect to  $x$ -axis, and  $P_1$  the Stokes parameter of the incident light.

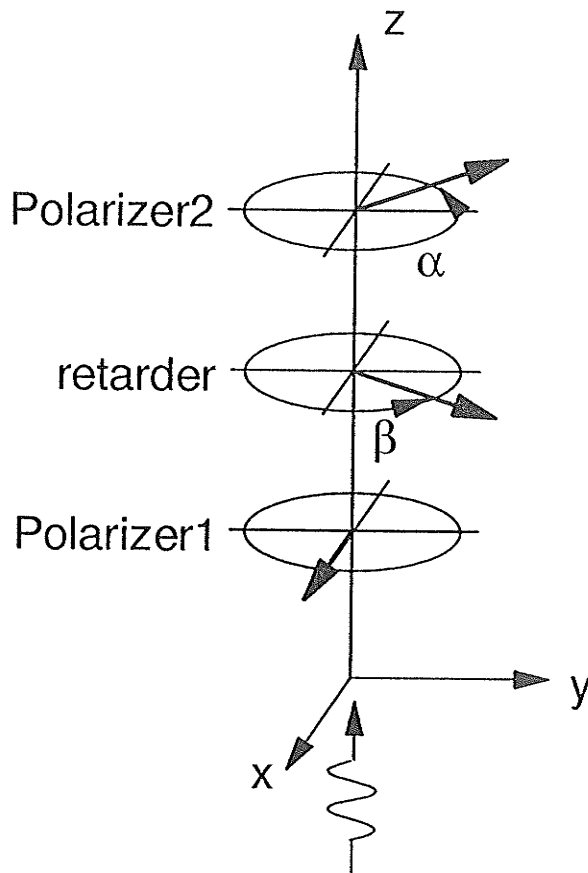


Figure4.3. Schematic of a polarizer-analyzer combination. The arrows on polarizers indicate the direction of transmission axes and the arrow on retarder is in the direction of fast axis. The first polarizer is used to define linearly polarized light characterized by  $P_1$ . The transmission axis of the second polarizer is set to be at angle  $\alpha$  with respect to the one of Polarizer1.  $\beta$  is the angle of the fast axis of retarder with respect to the transmission axis of Polarizer1.

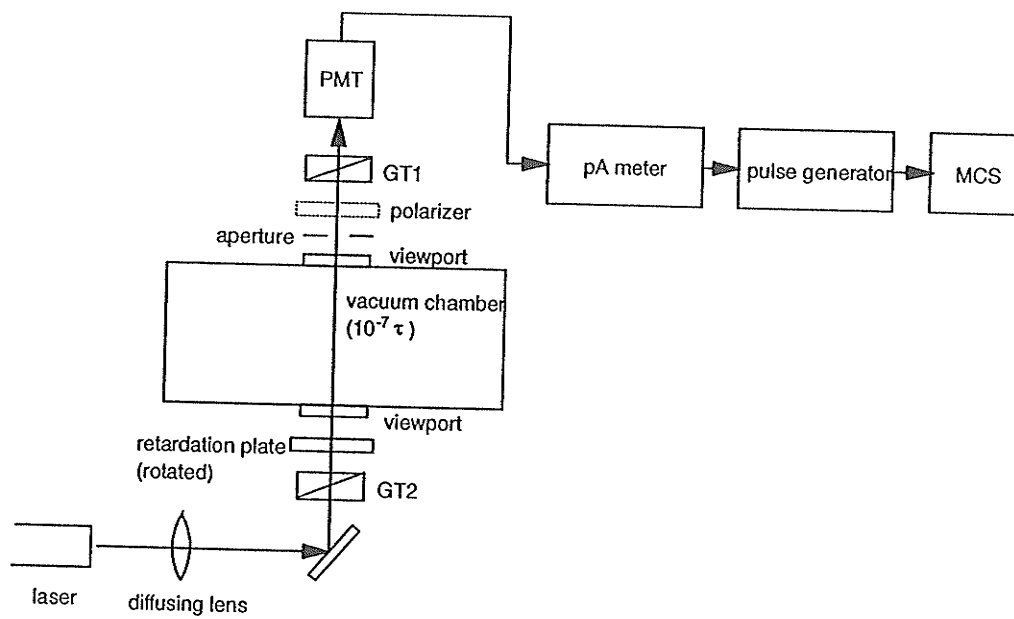


Figure 4.4. The setup for measurement of phase retardation introduced by retardation plate and by viewport. For the viewport measurement, retardation plate is taken away and GT1 is rotated.

If the incident laser light is linearly polarized (i.e.,  $P_1 = 1$ ) and  $\alpha$  is set to be  $45^\circ$  with respect to the transmission axis of Pol#1, Eqn 4.3 can be rewritten as

$$I(45^\circ, \beta, \delta) \propto 1 + \frac{(1 - \cos\delta)}{2} \sin 4\beta \quad 4.4$$

The retardation  $\delta$  can be thus extracted from the modulation depth of  $\sin 4\beta$  oscillation. The experimental setup is shown in Figure 4.4. The laser was tuned at Ba resonance wavelength  $\lambda = 553.5\text{nm}$ . A series of measurements were carried out to test the polarization of Glan-Taylor prism polarizer, the effect of the reflection mirror on polarized light and the birefringent effect of the viewport under the stress. We found that the GT prism can produce perfect linearly polarized light (100% polarization), the effect of the mirror on polarized light and the birefringent effect of the viewport are negligible. By setting the angle between transmission axes of GT#1 and GT#2 ( $\alpha$ ) equal to  $45^\circ$ , we performed the measurement by continuously rotating the retardation plate. The transmitted light was then registered by a photomultiplier, converted into frequency signal and collected by MCS. By fitting the modulation spectrum on Eqn. 4.4, we determined that  $\cos\delta = -0.970(\pm 0.02)$  for the  $\lambda/2$  plate and  $\cos\delta = -0.374(\pm 0.02)$  for the  $\lambda/4$  plate.

For  $P_1^+$  and  $\gamma$  measurements, a  $\lambda/2$  retardation plate was mounted on a rotator driven by a synchronous motor and was continuously rotated to produce a rotating linearly polarized laser light in the interaction region. A synchronization pulse generated by the plate rotator triggers the start of data acquisition by the MCS (as described in Section 3.4). In this way, a

"polarization modulation spectrum" of the superelastic-scattering signal versus retarder rotation angle  $\beta$  can be accumulated. The use of an electrically controlled shutter triggered by the midpass signal from MCS allows the accumulation of background signal in the second half of each polarization modulation spectrum.

In the case of  $L_{\perp}^{+}$  measurements, a quarter-wave retardation plate ( $\delta = \pi/2$ ) converts linearly polarized incident light from Glan-Taylor prism into left-handed, right-handed circularly or linearly polarized light. We set the RAMP program to collect a spectrum of superelastic-scattering signal corresponding to laser excitation by LHC, RHC, linear polarized light beams and background in a single pass (four-quarter spectrum). The collection of each quarter of the spectrum by MCS is triggered by the synchronizing pulse from the rotator. After the data collection for one laser polarization is finished, the rotator changes the orientation of the  $\lambda/4$  plate to produce another laser polarization state.

For the purpose of  $L_{\perp}^{+}$  measurements, we mounted the quarter-wave retardation plate on the stepper motor driven rotator and installed a four arm chopper wheel on which arms are separated by  $45^{\circ}$ . In order to generate "perfect" circularly polarized light at the collision center for  $L_{\perp}$  measurement, the fast axis of quarter-wave retardation plate must be aligned at  $45^{\circ}$  with respect to the transmission axis of Glan-Taylor prism. We completed the alignment by following this procedure: The laser was tuned on barium  $^1P_1$  transition frequency. A linear polarizer was mounted on the top viewport as a polarization analyzer. In absence of the  $\lambda/4$  plate, the polarizer was set to cross the linearly polarized laser beam from the Glan-Taylor prism and minimum transmitted light was observed. The retardation plate rotator was preset at its supposed position to produce linearly polarized light. We then

mounted the  $\lambda/4$  plate in the plate holder and rotated the plate holder until a minimum transmitted light was obtained. In this position, the fast axis of the  $\lambda/4$  plate is either parallel or perpendicular to the transmission axis of the Glan-Taylor prism and the light transmitted from the  $\lambda/4$  plate is linearly polarized. This indicates that the  $\lambda/4$  plate rotated  $45^\circ$  forward and backward can generate circularly polarized light beams of opposite handedness at the collision region. The accuracy of this alignment was estimated to be  $\pm 1^\circ$ , which is basically determined by the  $1^\circ$  angular increment of the step motor.

The energy levels of barium atom below 3eV are given in Table 4.1 (Moore1958). In naturally occurring barium, the isotopes with atomic mass units 138, 137, 136, 135, 134, 132, and 130 are present in 71.66%, 11.32%, 7.81%, 6.59%, 2.42%, 0.10%, and 0.10% abundance, respectively. The nuclear spin for the even isotopes is zero and for the odd isotopes is  $3/2$ . So there is no hyperfine structure in the 138 isotope (with  $I = 0$ ). The 138 isotope is dominant in abundance and the energy gaps between 138 and other isotopes for ( $\dots 6s6p \ ^1P_1$ ) transition are larger than 70MHz, which enables us to tune the dye laser on the 138 isotope. An additional check on the laser tuning can be made by use of a polarizer to monitor the fluorescence. If laser is tuned on the odd isotope, the fluorescence light is not completely linearly polarized (even though the excitation light is fully linearly polarized) because of the depolarization caused by hyperfine structure. On the contrary, because of the absence of hyperfine effect, the fluorescence emitted from even isotope (like  $^{138}\text{Ba}$ ) is purely linearly polarized.

The schematic diagram of laser pumping process in Ba is shown in Figure 4.5. Laser light tuned at  $^1S_0$  to  $^1P_1$  transition excites atom to  $^1P_1$  level. Consequently, three electron-collision deexcitation processes (superelastic

Table 4.1. list of energy levels of barium below 3eV.

Ground state ( $1s^2 2s^2 2p^6 3s^2 3p^6 3d^{10} 4s^2 4p^6 4d^{10} 5s^2 5p^6$ )  $6s^2 \ ^1S_0$   
 Ionization energy 5.212eV

Designation	J	Level (eV)
$6s^2 \ ^1S$	0	0.00
$6s5d \ ^3D$	1	1.120
$6s5d \ ^3D$	2	1.143
$6s5d \ ^3D$	3	1.190
$6s5d \ ^1D$	2	1.413
$6s6p \ ^3P$	0	1.521
$6s6p \ ^3P$	1	1.567
$6s6p \ ^3P$	2	1.676
$6s6p \ ^1P$	1	2.240
$5d6p \ ^3F$	2	2.736
$5d6p \ ^3F$	3	2.845
$5d6p \ ^3F$	4	2.946
$5d^2 \ ^1D$	2	2.860
$5d6p \ ^1D$	2	2.861
$5d^2 \ ^3P$	0	2.878
$5d^2 \ ^3P$	1	2.911
$5d^2 \ ^3P$	2	2.966

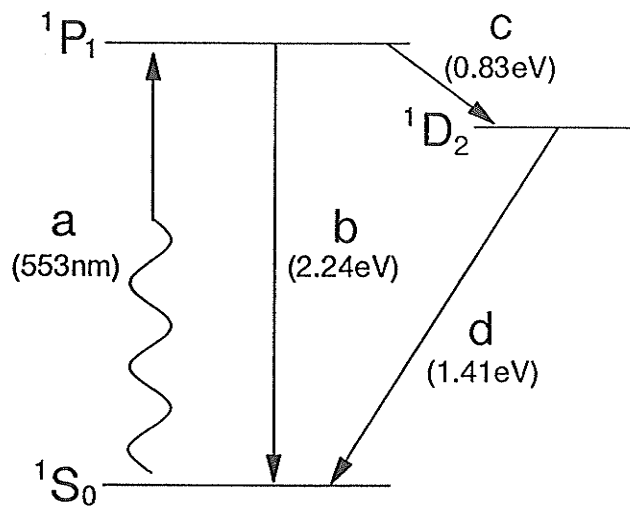


Figure 4.5. Laser pumping excitation of  $^{138}\text{Ba}$  (...6s6p) and the electron collisional deexcitation transitions following the excitation. Process (a) represents laser pumping excitation of  $^1P_1$  at 553nm, (b) electron collisional deexcitation from  $^1P_1$  to  $^1S_0$ , (c) deexcitation from  $^1P_1$  to  $^1D_2$ , and (d) deexcitation from  $^1D_2$  to  $^1S_0$ .

scattering) take place:  $^1P_1$  to  $^1S_0$  at 2.24eV,  $^1P_1$  to  $^1D_2$  at 0.83eV and  $^1D_2$  to  $^1S_0$  at 1.41eV.

The optical pumping of the Ba (...6s6p  $^1P_1$ ) level at 553.5nm is somewhat complicated by the presence of a non-negligible branching ratio to the lower lying  $^1D$  metastable level. A systematic investigation of the effect of  $^1D$  level on the pumping process has been carried out by Register et al (Register1983). By assuming a branching ratio of 1:700 to the  $^1D$  level, they calculated the population distribution among  $^1S$ ,  $^1P$  and  $^1D$  levels and estimated that under their experimental condition, the populations on  $^1P$  and  $^1S$  are dominant. We have performed a similar investigation for our experimental condition by solving three-level rate equations and the similar results were achieved. Therefore, we conclude that under current laser power and pumping time, most population still remains within pumping cycle and does not end up at  $^1D$  level.

The superelastic-scattering experiment began with accumulation of an energy loss spectrum at an impact energy  $E_0^S = E_0 - \Delta E$  until the superelastic-scattering feature in  $^1P_1 - ^1S_0$  deexcitation transition is strong enough to be located (see Fig. 3.11). The typical energy resolution of 0.5eV was obtained. The superelastic-scattering intensity to inelastic-scattering intensity ratio for this transition was approximately 1:50. We then locked the electron spectrometer at energy loss of -2.24eV — the  $^1P_1$  to  $^1S_0$  superelastic-scattering feature. The typical count rate at  $10^\circ$  scattering angle was about 100Hz. The apparatus was ready to take a polarization modulation spectrum.

Several calibrations were applied to the data. Impact energy was calibrated against the known position of the He  $2^2S$  Feshbach resonance at 19.37eV. To do so, we locked the energy loss at the peak of elastic-scattering

signal and scanned the impact energy to accumulate a scattering intensity vs impact energy spectrum. The impact energy was then calibrated with respect to the resonance feature. The typical voltage discrepancy is less than 50mV and is caused by contact potentials in the electron spectrometer and residual electrical and magnetic fields at the interaction region.

Zero scattering angle was determined by monitoring superelastic scattering to the left and right. For  $P_l^+$  and  $\gamma$  measurement we made use of the symmetries  $P_l^+(\theta) = P_l^+(-\theta)$ ,  $\gamma(\theta) = -\gamma(-\theta)$  and  $\bar{I}^s(\theta) = \bar{I}^s(-\theta)$  to calibrate zero scattering angle, where  $\bar{I}^s$  refers to an average of  $I^s$  over retarder rotation angle  $\beta$ . For  $L_\perp^+$  measurement, since there is no sharp angular variation on  $L_\perp^+$  curve, we calibrated the scattering angle by calculating  $(1 - L_\perp^2)^{1/2}$  and aligned the observed minimum with the corresponding minimum previously measured in  $P_l^+$ . In our current experiment, we are not able to distinguish between RHC polarized light from LHC polarized light and thus to determine the sign of  $L_\perp$  experimentally. We normalized the sign of  $L_\perp^+$  to theory at one small scattering angle. The validity of this normalization relies on the theoretically predicted behavior of  $L_\perp^+$  for electron impact excitation of 1P state. A comprehensive discussion about  $L_\perp^+$  behavior will be given in later section. This calibration was estimated to be accurate to within  $\pm 1^\circ$ . This calibration technique differs slightly from the traditional  $\theta = 0$  calibration which uses the symmetry  $\text{DCS}(\theta) = \text{DCS}(-\theta)$ , where DCS is the differential cross section for excitation of a forward-peaked inelastic feature. We chose this method because, in the case of superelastic scattering, the background count rate is very low even at very small scattering angles and it is much simpler to account for the background contribution to a superelastic-scattering spectrum. The zero degree scattering angle

determined in this way differed by  $2^\circ$  from its value determined by optical alignment of gun and detector.

For the purpose of measuring  $\gamma$ , it was also necessary to determine the position in a polarization modulation spectrum where the major axis of the polarization ellipse (representing the elliptical polarization state of the laser light at target) aligns with the forward-scattering direction. This calibration involved the use of a photomultiplier tube to monitor laser-induced fluorescence modulation (see Figure 4.6). A well-defined fluorescence observation direction was set by removing the electron gun cathode and rotating the gun into a known position between the interaction region and the photomultiplier viewport. The fluorescence detection view cone was therefore determined by collimating apertures in the electron gun (giving a detection solid angle of  $0.001\text{sr}$ ). Minima in the fluorescence polarization modulation spectra occur when the major axis of the laser beam polarization ellipse is aligned with the fluorescence observation direction. By analyzing the modulation spectrum, we can determine the laser polarization direction with respect to the observation direction. Since the angle displacement between the forward-scattering direction and the observation direction is known, we can then determine the angle of laser polarization elliptical axis with respect to the forward-scattering direction.

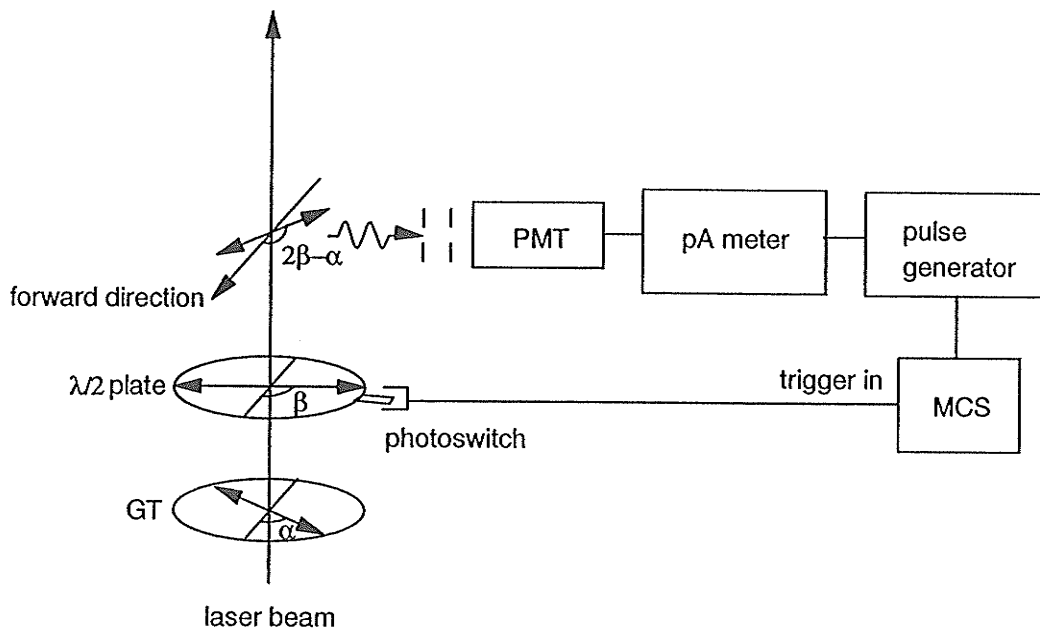


Figure 4.6. The setup for the alignment angle ( $\gamma$ ) calibration.  $\alpha$ ,  $\beta$  are defined in the text.

## 4.4. Data Analysis

### 4.4.1 For $P_l^+$ and $\gamma$ Measurement

Examination of Eqn.4.2 reveals that a perfect half-wave retardation plate ( $\delta = \pi$ ) will allow the straight-forward extraction of  $P_l^+$  and  $\gamma$  through a measurement of the depth of modulation and phase of  $I^s$  as a function of  $\beta$ . In this case the laser light is linearly polarized at the target. We can reduce Eqn. 4.2 to a more explicit expression by setting  $\delta = \pi$

$$I^s(\beta - \alpha) = \frac{A\bar{C}}{3} \{1 + P_l^+ \cos(4\beta - 2\gamma - 2\alpha)\} \quad 4.5$$

In analyzing the background-corrected spectra, we observed a small "slow" modulation of the intensity resulting from the term in Eqn. 4.2 that involves  $L_{\perp}$ . This term arises since our retardation plate is characterized by a phase retardation that differs from  $\pi$  at Ba resonance frequency 553.5nm and, hence,  $\sin\delta$  is not equal to zero. By examining Eqn. 4.2, we found that two cycles of the signal intensity oscillation involving  $P_l^+$  cover one cycle of the slow modulation caused by  $L_{\perp}$ . In order to eliminate the slow-modulation component from a spectrum, we added a "shift" version of the spectrum to the original spectrum and formed the sum

$$I^s(\beta - \alpha) + I^s(\beta - \alpha + \frac{\pi}{2}) = I_0^s \{1 + \eta \cos(4\beta - 2\gamma - 2\alpha)\} \quad 4.4$$

where  $I^s(\beta - \alpha)$  is expressed in Eqn. 4.2 and  $\eta$  can be expressed as

$$\eta = \frac{P_l^+(1 - \cos\delta)}{2 + P_l^+(1 + \cos\delta)\cos(2\alpha - 2\gamma)} \quad 4.5$$

In this way, the slow modulation associated with  $L_{\perp}$  is eliminated.

Extraction of  $P_l^+$  and  $\gamma$  parameters was carried out by fitting the superelastic-scattering polarization modulation spectra to Eqn. 4.4. in the following way. A background subtraction was first carried out by integrating the background spectrum over all MCS channels in the spectrum, dividing the integrated counts by the number of channels, and subtracting this result from each channel in the signal plus background spectrum. The spectrum was then fit by a two-parameter ( $\eta$ ,  $\gamma$ ) nonlinear least-squares method which approximates the  $\chi^2$  hypersurface near its minimum as parabolic. The error in a fitting parameter is approximately given by the change in this parameter that causes  $\chi^2$  to increase by one from its minimum value. Details are discussed by Bevington (Bevington1969). For the best fitting result, sometimes integration of the signal spectrum is necessary ( usually by integrating over two or four neighboring channels) to improve the statistics of the spectrum. A series of signal spectra taken at different scattering angles ( after the subtraction of background ) along with the best fitting curves are presented in Figure 4.7. The parameter  $P_l^+$  was extracted from the fitting parameters through the relation

$$P_l^+ = \frac{2\eta}{1 - \cos\delta - \eta(1 + \cos\delta)\cos(2\alpha - 2\gamma)} \quad 4.6$$

with our measured value of  $\cos\delta = -0.970$  and a value of  $\alpha$  determined to be  $0^\circ (\pm 5^\circ)$ . For a "true"  $\lambda/2$  plate (i.e.,  $\delta = \pi$ ),  $P_l^+$  is equal to  $\eta$ . Summing the

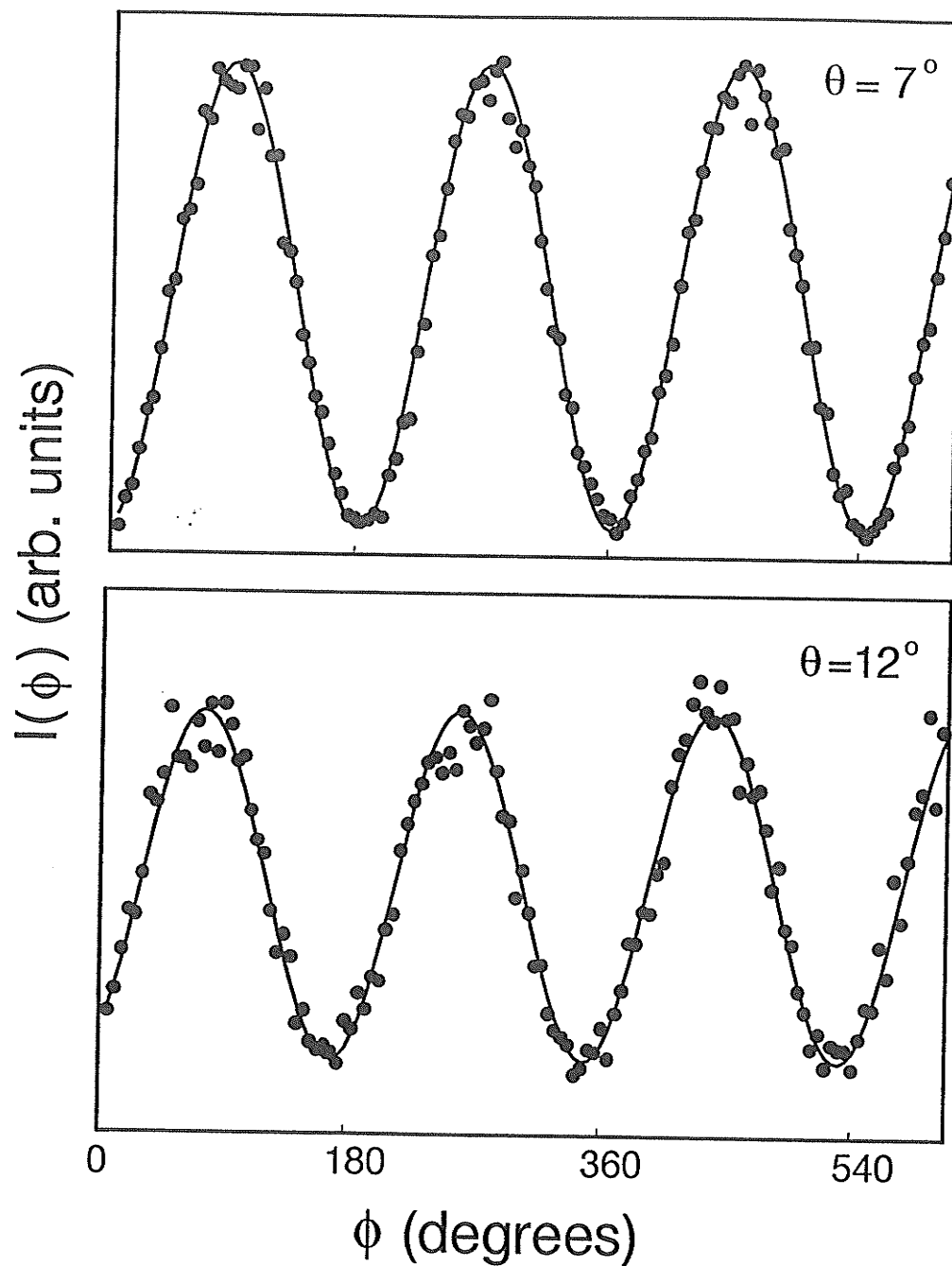
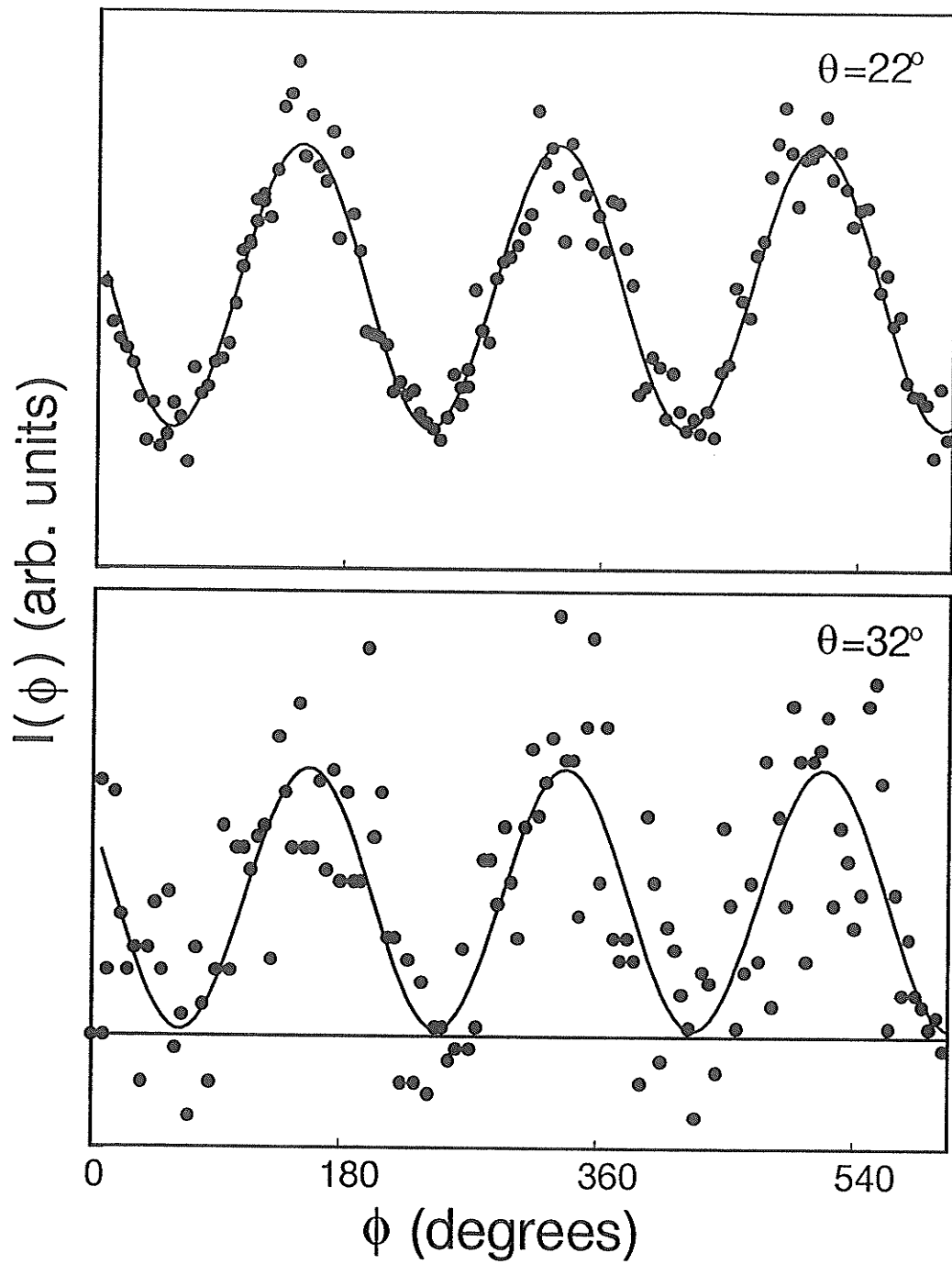


Figure 4.7. A series of polarization modulation spectra of superelastic signal intensity at different scattering angles.  $\phi$  represents the calibrated angle between laser field vector direction and the forward scattering direction.



continuation of Figure 4.7

spectrum in this way has the added benefit of eliminating slow modulation of the superelastic-scattering signal, which may arise through a slight deviation of the incident laser beam by the rotating retardation plate. We note, however, that such beam steering was not visibly discernible.

#### 4.4.2. For $L_{\perp}$ Measurement

By bringing  $\beta - \alpha = 0, \pi/2, -\pi/4$  and  $+\pi/4$  ( $\beta - \alpha$  is the angle between the retardation plate fast axis and the laser polarization vector direction) into Eqn. 4.2, we get the expression representing the superelastic-scattering signal intensity at each laser polarization state

$$\begin{aligned}
 I^S(0) &\propto 1 + P_l^+ \cos(2\alpha - 2\gamma) \\
 I^S(\frac{\pi}{2}) &\propto 1 + P_l^+ \cos(2\alpha - 2\gamma) \\
 I^S(+\frac{\pi}{4}) &\propto 1 + P_l^+ \cos\delta \cos(2\alpha - 2\gamma) + L_{\perp} \sin\delta \\
 I^S(-\frac{\pi}{4}) &\propto 1 + P_l^+ \cos\delta \cos(2\alpha - 2\gamma) - L_{\perp} \sin\delta
 \end{aligned}
 \tag{4.7}$$

For a 'perfect'  $\lambda/4$  retardation plate ( $\delta = \pi/2$ ), it can be easily shown that  $L_{\perp}$  can be extracted from Eqn.4.2 or Eqn. 4.7 and expressed in terms of superelastic-scattering signal intensity  $I^S(\beta)$  with  $\beta = \pm\pi/4$

$$L_{\perp} = \frac{I^S(+\frac{\pi}{4}) - I^S(-\frac{\pi}{4})}{I^S(+\frac{\pi}{4}) + I^S(-\frac{\pi}{4})}
 \tag{4.8}$$

Deviation from the 'perfect' phase retardation (namely,  $\cos\delta = 0$  for  $\lambda/4$  plate) forced us to use a more complicated scheme to extract  $L_{\perp}$  from Eqn. 4.2. We define the ratio

$$R = \frac{I^S(\frac{\pi}{4}) - I^S(0)\cos\delta}{I^S(-\frac{\pi}{4}) + I^S(0)\cos\delta} \quad 4.9$$

from which we get  $L_{\perp}$  by the relation

$$L_{\perp} = \frac{R-1}{R+1} \left( \frac{1-\cos\delta}{1+\cos\delta} \right)^{1/2} \quad 4.10$$

The measurement of  $I^S(\pi/2)$  is redundant with the  $I^S(0)$  measurement (i.e.,  $I^S(0)$  should be equal to  $I^S(\pi/2)$ ) but allows us to determine whether rotation of the  $\lambda/4$  plate introduces any steering of the laser beam away from the target region. A series of signal spectra taken at different scattering angles (before the subtraction of background) are presented in Figure 4.8.

The first step of  $L_{\perp}$  extraction was to integrate the counts of superelastic-scattering signal over each quarter of the spectrum and divide the integrated counts by the number of channels. The results of integration represent the averaged signal plus background intensities corresponding to laser excitation by RHC, LHC and linear polarized light (namely,  $\beta = \pm\pi/4$  and 0), and the averaged background intensity. A background subtraction was performed by dividing the integrated counts of background quarter by the number of channels, and subtracting this result from the averaged signal plus background count of each quarter. We then used these results (background-corrected  $I^S(\pm\frac{\pi}{4}), I^S(0)$  or  $I^S(\frac{\pi}{2})$ ) along with our measurement of  $\cos\delta$  into Eqn. 4.9 and 4.10 to get  $L_{\perp}$ . The error bars represent statistical uncertainty of the integration. By comparing the  $L_{\perp}$  results before and after the phase retardation correction, we found that there is a significant influence of phase deviation from  $\pi/2$  on  $L_{\perp}$  measurement results at the region of large

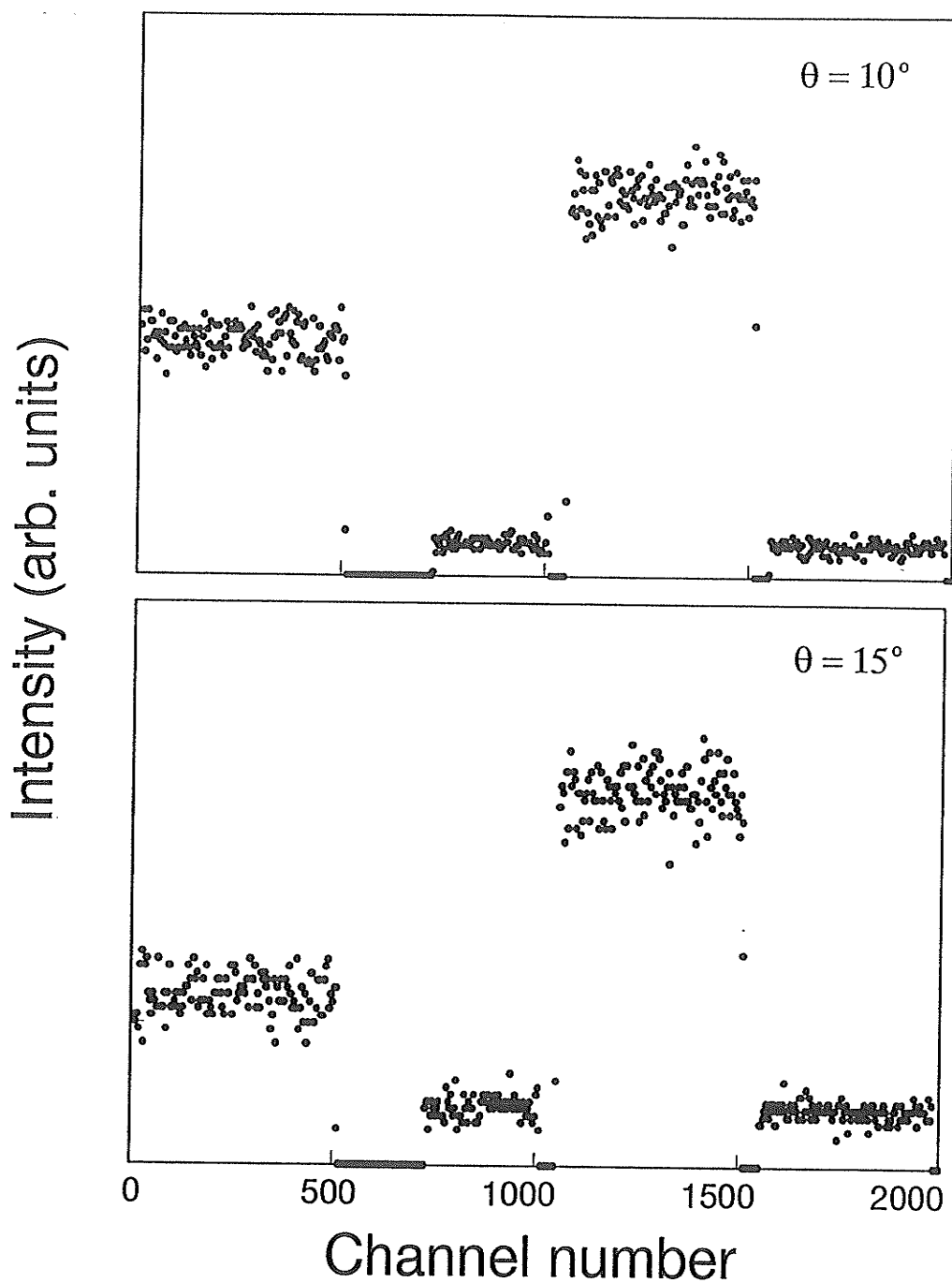
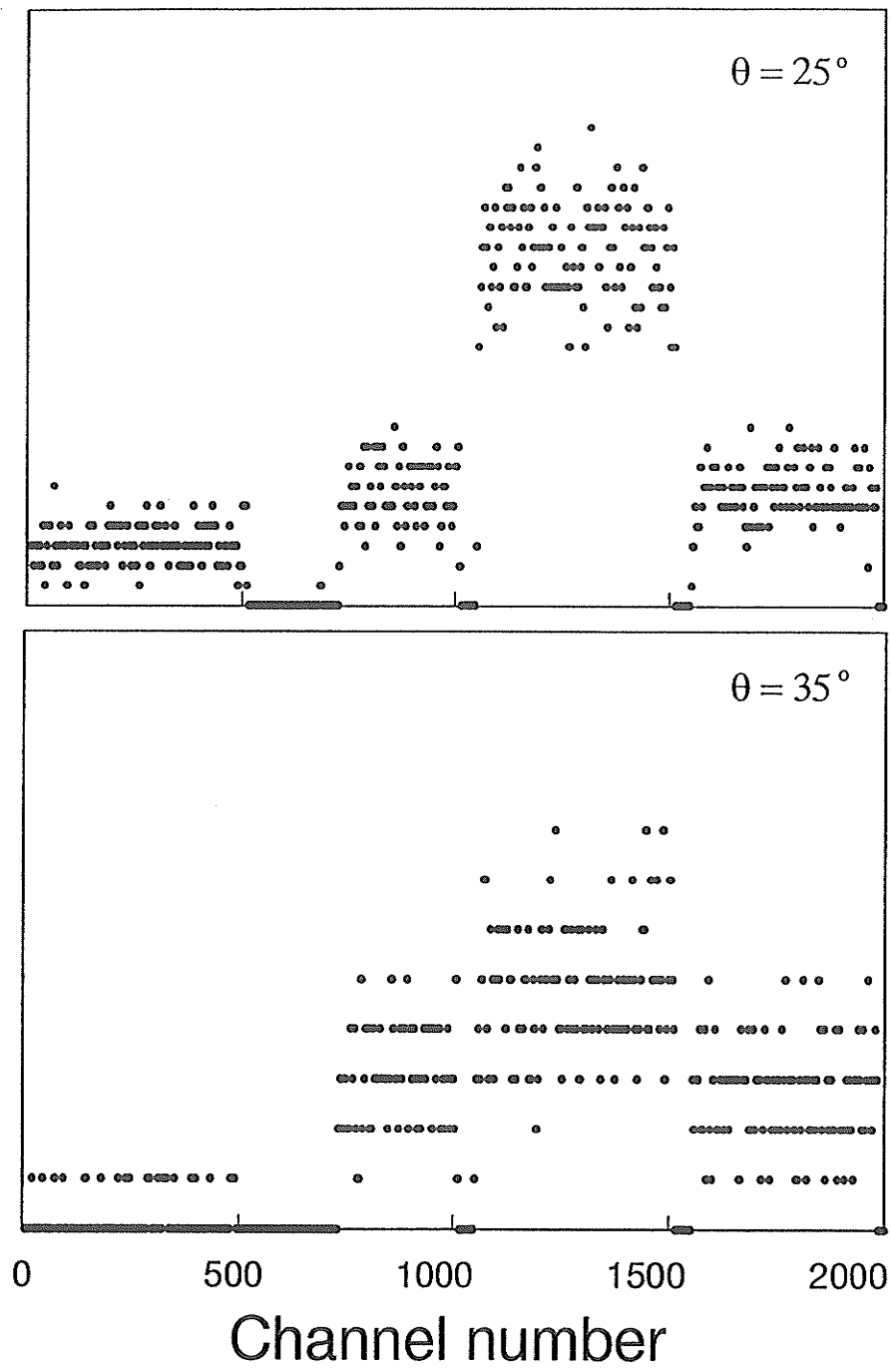


Figure 4.8. A group of spectra of superelastic-scattering signal taken at different scattering angles when a quarter-wave plate is rotated. The first and third quarter of spectra correspond to circularly polarized light while the second and fourth quarter of spectra to linearly polarized light. The first part of the second quarter is the accumulation of background (laser-off).

Intensity (arb. units)



Continuation of Figure 4.8.

$L_{\perp}$  values. The phase deviation can reduce measurement results by up to 20% at some scattering angles.

#### 4.5. Results and Discussion

The experimental results are tabulated in Table 4.2 and presented graphically in Figure 4.9 through 4.13. In part (a) and (b) of Figure 4.9 and 4.13, (b) and (c) of Figure 4.10 - 4.12, charge-cloud alignment parameters ( $P_l^+$  and  $\gamma$ ) measured by means of superelastic scattering at impact energies  $E_0^S = 7.76\text{eV}$ ,  $17.76\text{eV}$ ,  $34.5\text{eV}$ ,  $47.76\text{eV}$  and  $77.76\text{eV}$  are compared with calculations carried out for impact energies  $E_0 = 10\text{eV}$ ,  $20\text{eV}$ ,  $36.7\text{eV}$ ,  $50\text{eV}$  and  $80\text{eV}$ . The transferred orbital angular momentum ( $L_{\perp}$ ) measurement results are graphically shown in part (a) of Figure 4.10 to 4.12 at impact energies  $E_0^S = 17.76\text{eV}$ ,  $34.5\text{eV}$  and  $47.76\text{eV}$  and compared with calculations carried out for impact energies  $E_0 = 20\text{eV}$ ,  $36.7\text{eV}$  and  $50\text{eV}$ . It is appropriate to compare EICP's extracted from superelastic-scattering experiments with incident electron energy  $E_0^S$  to theoretical parameters calculated for the time-inverse inelastic collision involving incident electrons with energy  $E_0 = E_0^S + \Delta E$ , where  $\Delta E = 2.24\text{eV}$  is the excitation energy of the Ba(...6s6p  $6^1P_1$ ) state. As we have discussed in Chapter 2, superelastic and inelastic collisions are related by time-reversal symmetry of the scattering amplitudes. EICP's extracted from a superelastic-scattering measurement are the same as EICP's extracted from an electron-photon coincidence experiment involving the time-inverse inelastic collision for Ba ( $^1P_1$  to  $^1S_0$ ) excitation.

In order to discuss the relation between our observations and the theoretical results, we have carried out modeling calculations that average the theory over an interaction volume of finite spatial extent. This type of

Table 4.2. Summary of measured EICP values obtained by superelastic-scattering of electrons with incident kinetic energy  $E_0^S$  ( $E_0 = 2.24\text{eV}$ ) and the derived degree of coherence  $P^+$ . The uncertainty in the last digits are given in parentheses.

$$E_0^S = 7.76\text{eV} \quad (E_0 = 10.0\text{eV})$$

$\theta$ (deg)	$P_t^+$	$\gamma$
4	0.82(3)	-83(4)
6.5	0.87(3)	-44(4)
9	0.87(3)	-50(4)
11.5	0.88(3)	-57(4)
14	0.87(3)	-63(4)
19	0.84(3)	-71(4)
24	0.81(5)	-78(5)
34	0.82(5)	65(5)
44	0.70(5)	25(5)
54	0.56(6)	-9(5)

$$E_0^S = 17.76\text{eV} \quad (E_0 = 20.0\text{eV})$$

$\theta$ (deg)	$P_t^+$	$\gamma$	$L_{\perp}$	$P^+$
1	0.65(3)	-25(4)		
3	0.81(3)	-46(4)		
5			0.25(7)	
6	0.85(3)	-58(4)		0.92(6)
8	0.87(3)	-69(4)	0.42(7)	0.97(6)
10	0.83(3)	-73(4)	0.52(7)	0.98(6)
12			0.59(7)	
13	0.75(3)	-85(4)		0.96(6)
15			0.63(7)	
17			0.80(7)	
18	0.55(3)	85(5)		0.99(8)

20			0.88(7)	
23	0.28(5)	70(5)		0.98(8)
25	0.18(3)	61(5)	0.97(7)	0.94(8)
28	0.19(3)	30(5)	1.02(10)	1.04(9)
30	0.31(5)	23(7)	0.90(7)	1.00(8)
33	0.57(5)	17(4)		0.97(9)
35			0.67(7)	
38	0.86(5)	13(4)		0.99(8)
40			0.34(7)	
43	0.99(6)	5(4)		1.00(7)
44			0.02(7)	
48	0.93(8)	-7(4)		0.93(9)
50			-0.13(7)	
55			-0.13(9)	
60			0.01(9)	
65			0.30(16)	
70			0.51(36)	
76			0.68(14)	
81			-0.21(12)	
86			-0.79(26)	

---


$$E_0^S = 34.50\text{eV} \quad (E_0 = 36.67\text{eV})$$


---

$\theta$ (deg)	$P_t^+$	$\gamma$	$L_{\perp}$	$P^+$
3	0.66(3)	-53(4)		0.67(4)
4			0.18(7)	
5	0.87(3)	-72(4)		0.90(5)
7			0.34(7)	
8	0.88(3)	-82(4)		0.96(6)
10			0.42(7)	
11	0.75(3)	-84(4)		0.91(7)
12			0.58(7)	
14	0.62(5)	-93(4)		0.98(9)
15			0.81(7)	
16	0.36(5)	-99(4)		0.96(8)
17			0.92(7)	
19	0.14(3)	-19(7)	0.96(7)	0.97(8)

21	0.40(8)	-20(4)		1.00(10)
22			0.88(7)	
24	0.52(8)	-24(4)		0.94(10)
25			0.77(7)	
27	0.65(8)	-28(4)	0.68(7)	0.96(11)
30			0.64(7)	
32	0.67(8)	-25(4)		0.91(11)
35			0.60(8)	
37	0.70(8)	-16(5)		
40			0.38(7)	
45			0.22(10)	
50			0.06(10)	
54			0.00(10)	
60			0.07(10)	
65			0.39(10)	
70			0.37(27)	
73			0.18(18)	
78			-0.78(24)	
84			-0.91(27)	
89			-0.90(26)	
94			-0.64(19)	

---


$$E_0^S = 47.76\text{eV} \quad (E_0 = 40.0\text{eV})$$


---

$\theta$ (deg)	$P_t^+$	$\gamma$	$L_{\perp}$	$P^+$
4			0.20(7)	
5	0.91(3)	-76(4)		0.94(5)
7	0.85(3)	-83(4)	0.29(7)	0.90(5)
9	0.77(3)	-90(4)	0.48(7)	0.90(6)
11	0.61(3)	-90(4)		0.89(7)
12			0.71(7)	
13	0.38(3)	-105(4)		0.94(8)
14			0.92(8)	
15	0.05(3)	-84(10)		0.93(7)
16			0.88(7)	
17	0.41(3)	-24(4)		0.93(8)
19	0.60(5)	-29(3)	0.66(7)	0.89(9)

21	0.67(5)	-30(4)		0.86(8)
22			0.52(7)	
23	0.73(5)	-34(3)		0.86(8)
24			0.43(7)	
25	0.81(5)	-32(3)		0.91(8)
26			0.44(7)	
27	0.81(5)	-35(4)		0.93(8)
28			0.48(7)	
29	0.82(5)	-34(4)		0.95(8)
31			0.47(7)	
33	0.76(8)	-35(4)		0.91(11)
34			0.50(7)	
37			0.53(9)	
42			0.54(12)	
47			0.29(14)	
52			0.02(16)	
57			-0.15(23)	

---

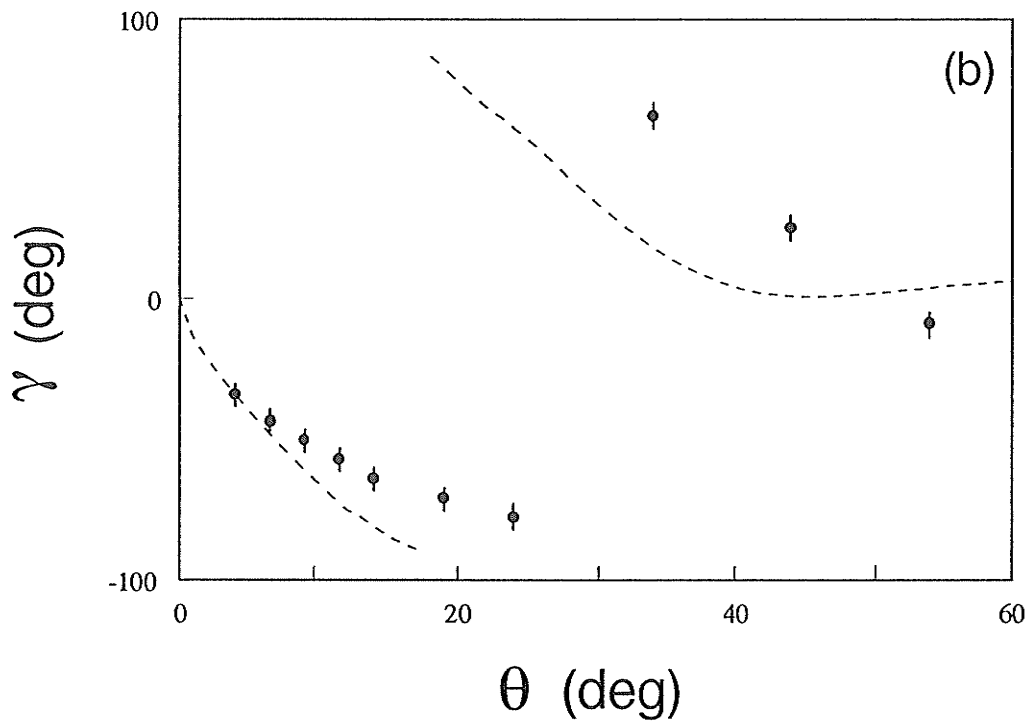
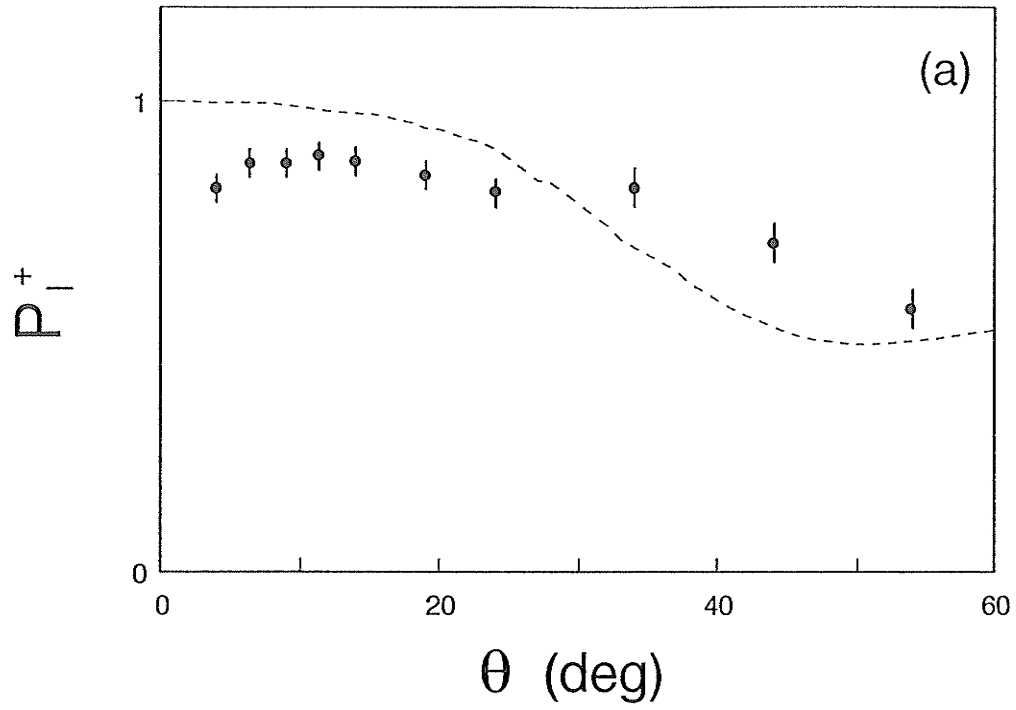

$$E_0^S = 77.76\text{eV} \quad (E_0 = 80.0\text{eV})$$


---

$\theta$ (deg)	$P_l^+$	$\gamma$
5	0.89(3)	-83(4)
7	0.82(3)	-86(4)
9	0.76(3)	-92(4)
11	0.66(3)	-88(4)
13	0.22(3)	-82(4)
15	0.47(3)	-26(3)
17	0.68(6)	-31(3)
19	0.70(6)	-36(4)

---

Figure 4.9. (a) Comparison of the  $P_l^+$  parameter (circles with error bars) with UDWA calculation of Clark et al. (Clark1989) (dashed curve). The measurements were obtained in superelastic-scattering experiments involving incident electrons with kinetic energy  $E_0^S = 7.76$  eV, while the calculation describe an inelastic collision involving incident electrons with kinetic energy  $E_0 = 10.0$  eV (b) Same as (a) except for the alignment parameter  $\gamma$ .



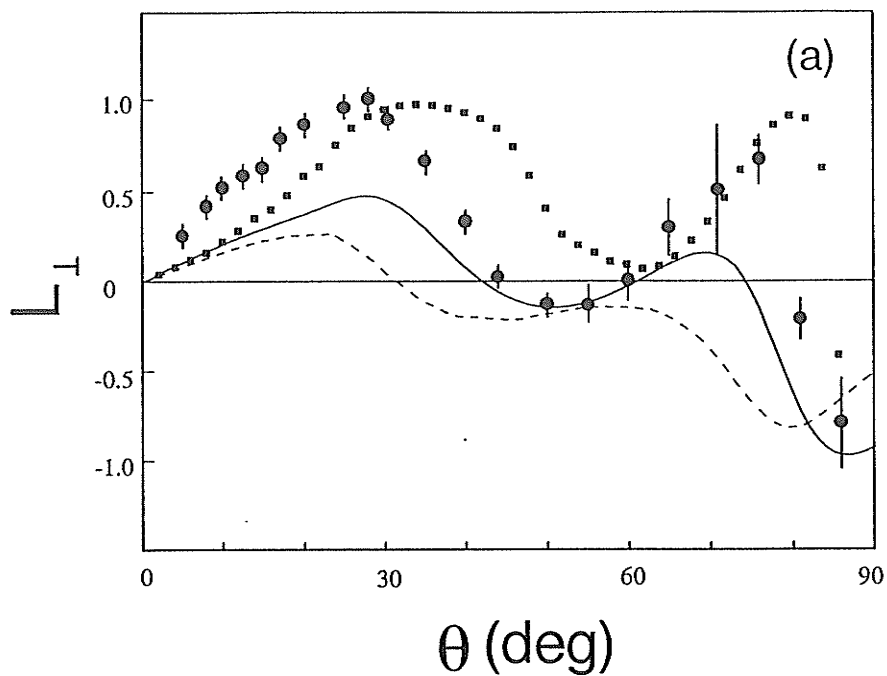
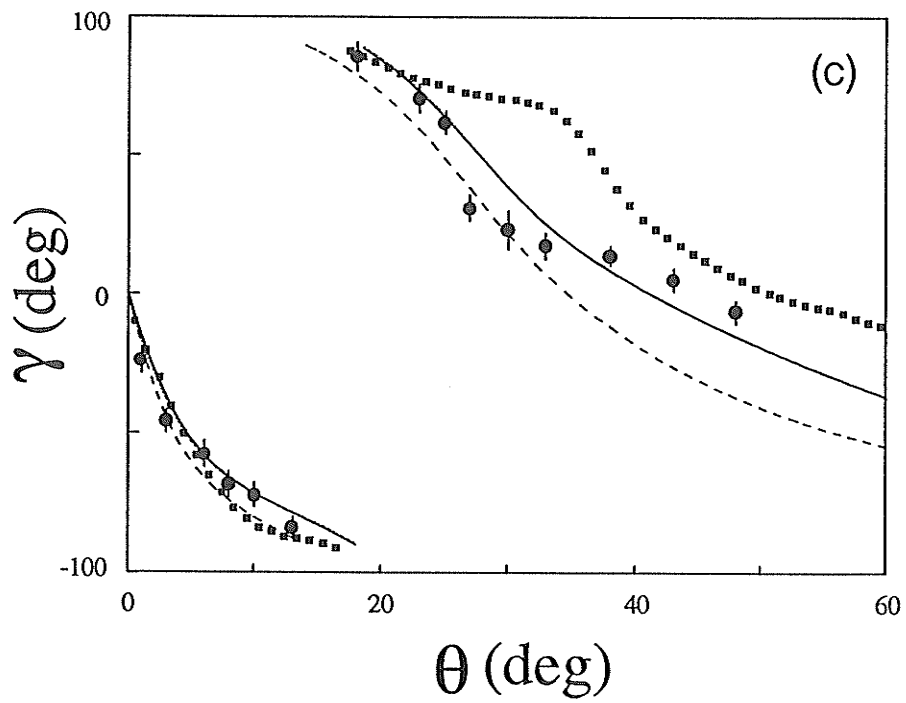
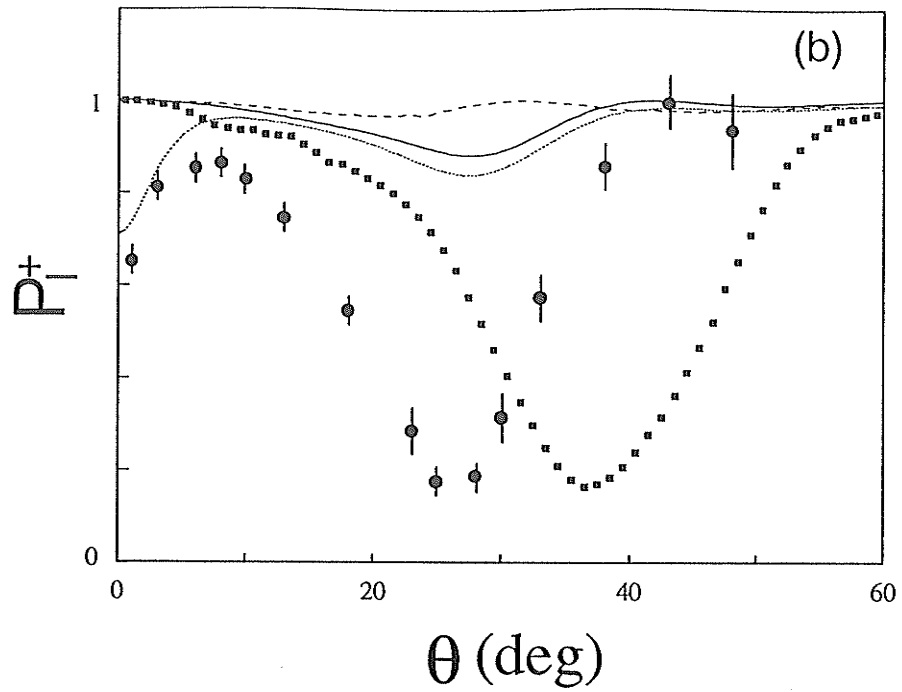


Figure 4.10. (a) Comparison of the  $L_{\perp}$  parameter (circles with error bars) with UDWA calculations of Clark et al. (Clark1989) (dashed curve), RDW calculations of Srivastava et al. (Srivastava1992) (solid curve), and the close-coupling calculations of Fabrikant (Fabrikant1985) (squares). The measurements were obtained in superelastic-scattering experiments involving incident electrons with kinetic energy  $E_0 = 17.76$  eV, while the calculations describe an inelastic collision involving incident electrons with kinetic energy  $E_0^S = 20.0$  eV. The dotted curve represents the results of a modeling calculation (which employs the RDW EICP) carried out to show the effect of an interaction volume that subtends an angle of 4 degrees at the detector (b) Same as (a) except for the alignment parameter  $P_l^+$ . (c) Same as (a) except for the  $\gamma$  parameter.



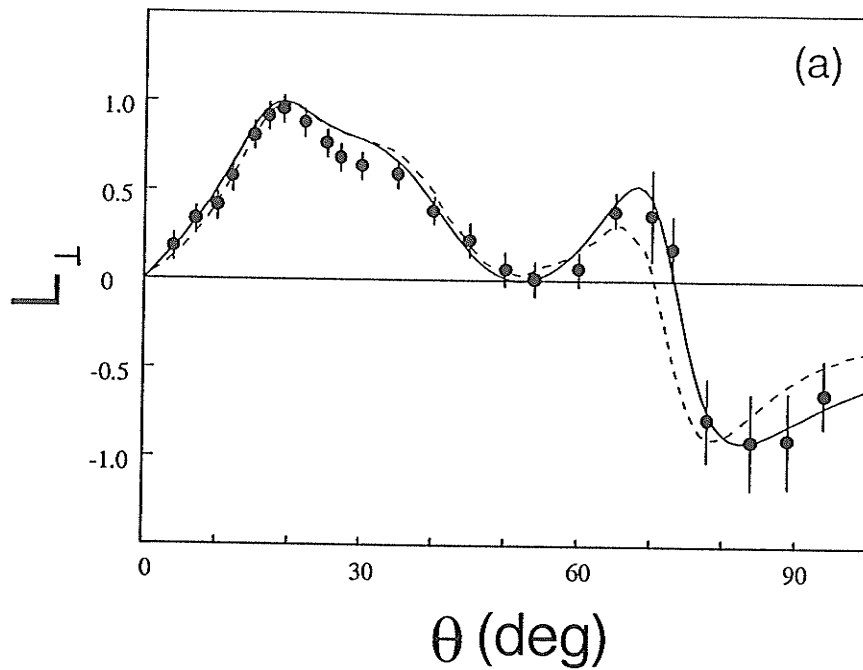
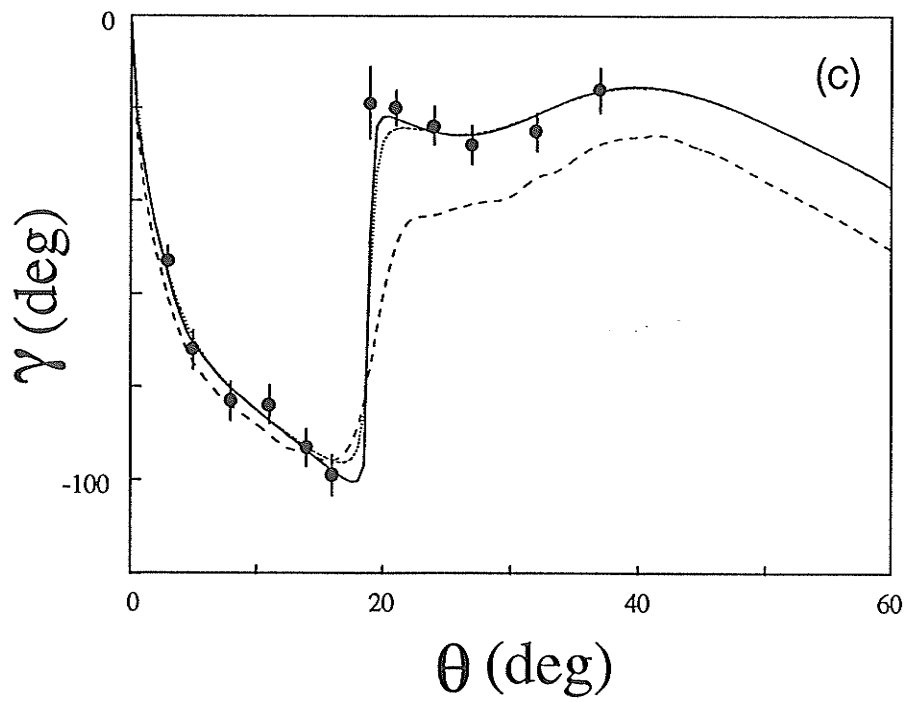
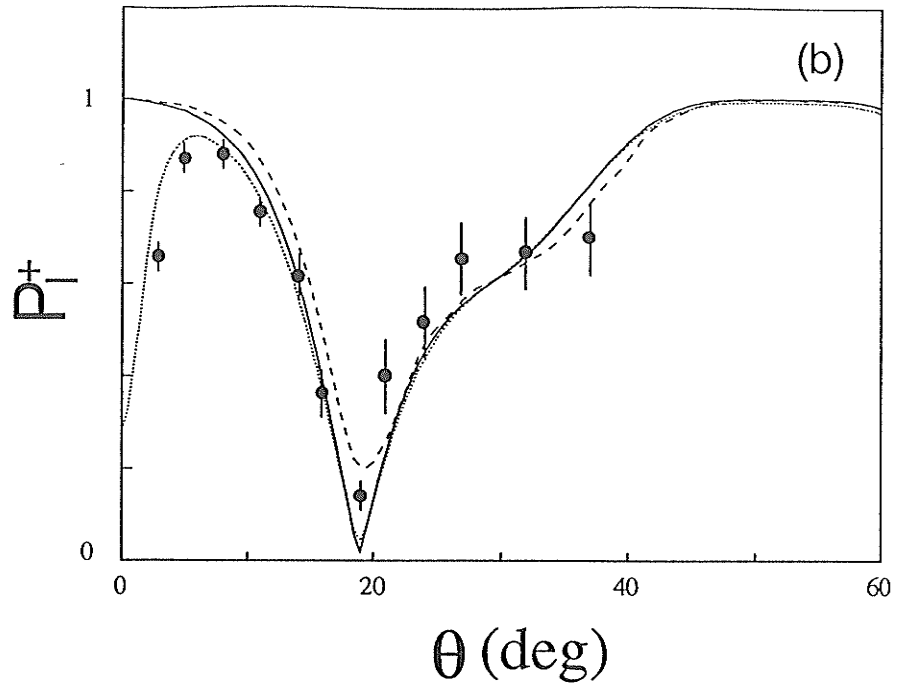


Figure 4.11. (a) Comparison of the  $L_{\perp}$  parameter (circles with error bars) with UDWA calculations of Clark et al. (Clark1989) (dashed curve), RDW calculations of Srivastava et al. (Srivastava1992) (solid curve). The measurements were obtained in superelastic-scattering experiments involving incident electrons with kinetic energy  $E_0^S = 34.5$  eV, while the calculations describe an inelastic collision involving incident electrons with kinetic energy  $E_0 = 36.67$  eV. The dotted curve represents the results of a modeling calculation (which employs the RDW EICP) carried out to show the effect of an interaction volume that subtends an angle of 4 degrees at the detector (b) Same as (a) except for the  $P_I^+$  parameter. (c) Same as (a) except for the  $\gamma$  parameter.



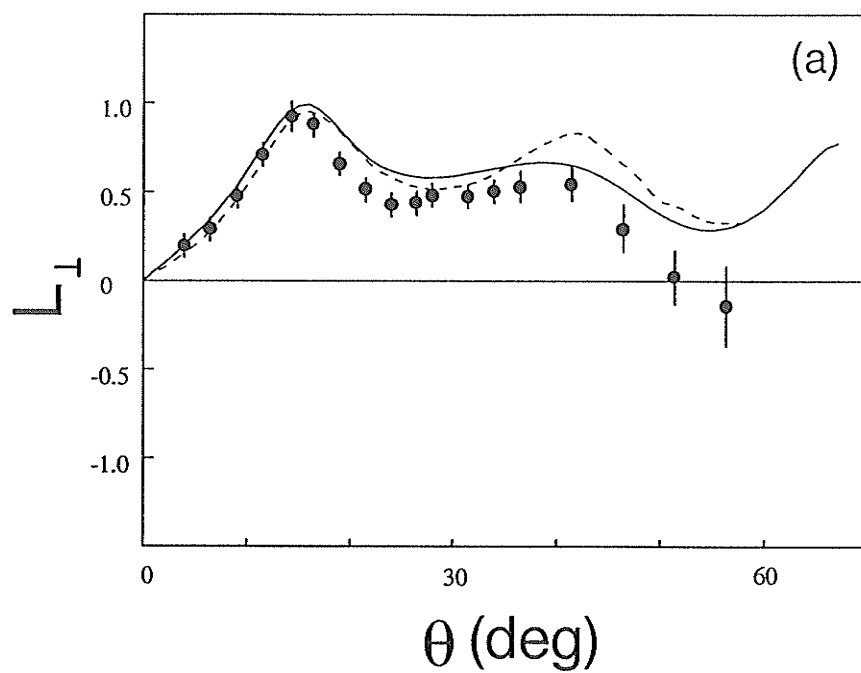
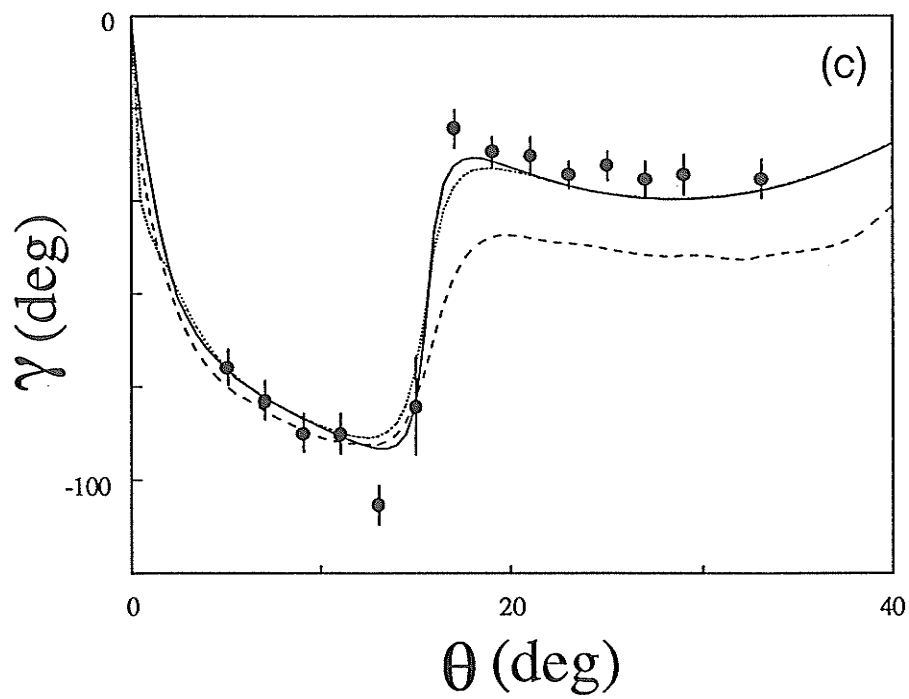
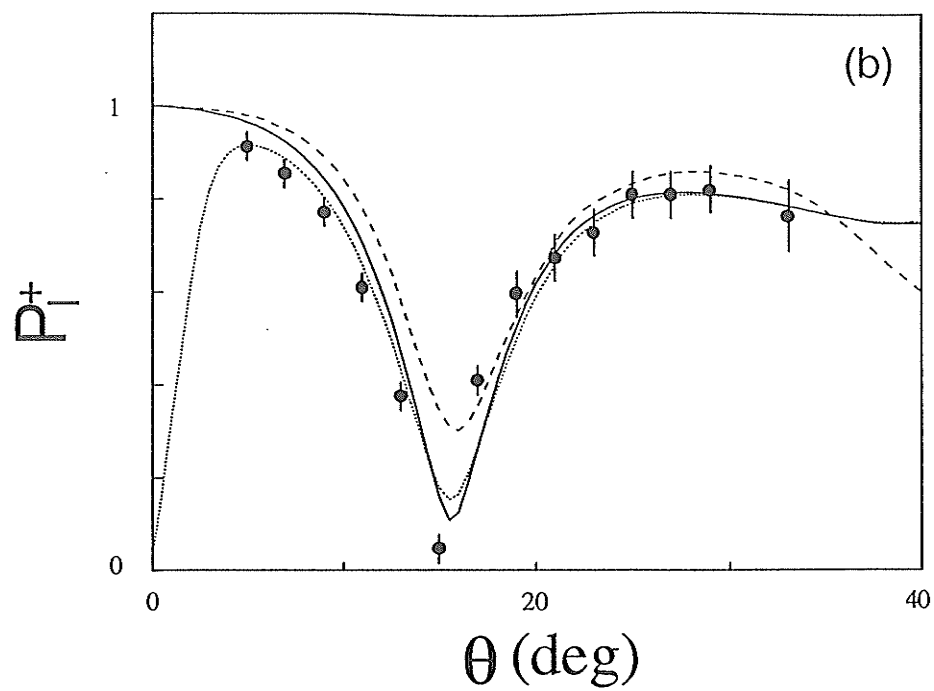


Figure 4.12. Same as Figure 4.11 (a), (b) and (c) except for  $E_0^S = 47.76$  eV and  $E_0 = 50.0$  eV.



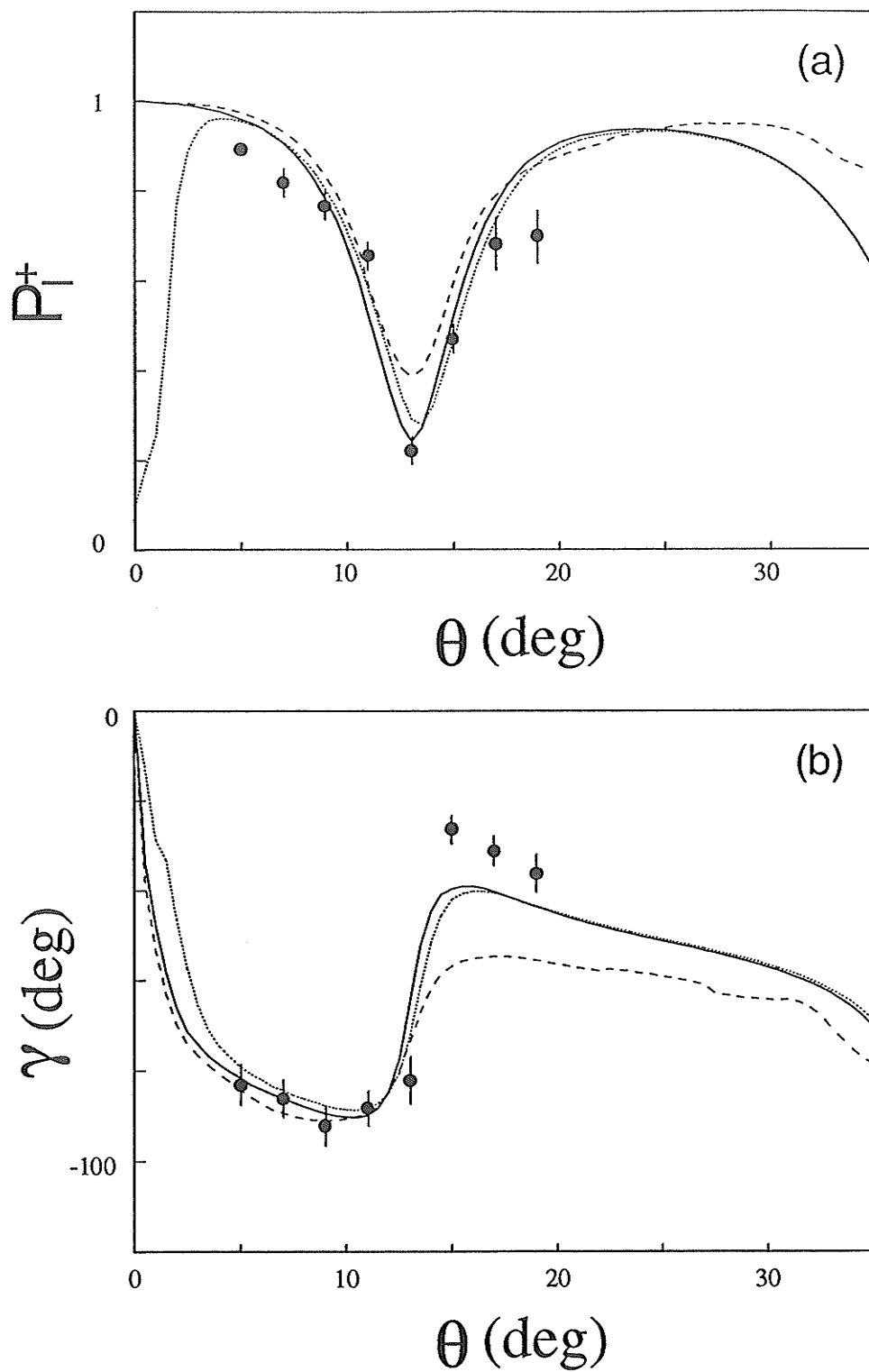


Figure 4.13. Same as Figure 4.11 (a) and (b) except for  $E_0^S = 77.76$  eV and  $E_0 = 80.0$  eV.

modelling calculation is identical to that described by Zetner et al (Zetner1990) except that it is applied to the '90° out-of-plane' geometry of the present experiment rather than the 'in-plane' geometry discussed in that work. A BASIC program developed by Zetner was used for the modelling calculation. Our model calculates scattering signal arising from an extended scattering volume represented by an ensemble of collision events, each of which defines a 'true' scattering plane and scattering angle. The apparatus itself defines a scattering angle ( the angular separation between electron gun and detector axes). The spatial distribution of the extended scattering volume is physically defined by the overlap of the electron beam, atomic beam, laser beam and electron detection viewcone. For the modelling calculations we simulated the effect of a finite interaction volume, at a given nominal scattering angle, by averaging the signal associated with electrons superelastically scattered into 25 discrete directions within the acceptance viewcone of the detector. The contribution to the overall scattering signal from any one of these 25 scattering events was weighted by the value of the differential cross section at the true scattering angle defined by the incident and scattered electron directions associated with that particular event.

We have carried out modelling calculations for  $P_l^+$ ,  $\gamma$  and  $L_{\perp}$ , and found that the finite interaction volume has an apparent influence on  $P_l^+$  and  $\gamma$  but is very insignificant for  $L_{\perp}$ . Modelling calculations presented in Figure 4.14 shows the effect of detector viewcones on  $P_l^+$  and  $\gamma$  which subtend angles of 2°, 4° and 6° at the interaction region. Deviation from the full curve (DWA calculation with no account of finite interaction volume effects) increases with increasing angular size of the viewcone. The 6° viewcone corresponds to an upper limit set by collimation apertures at the detector front end. The effect of such an extended interaction volume on the measurement

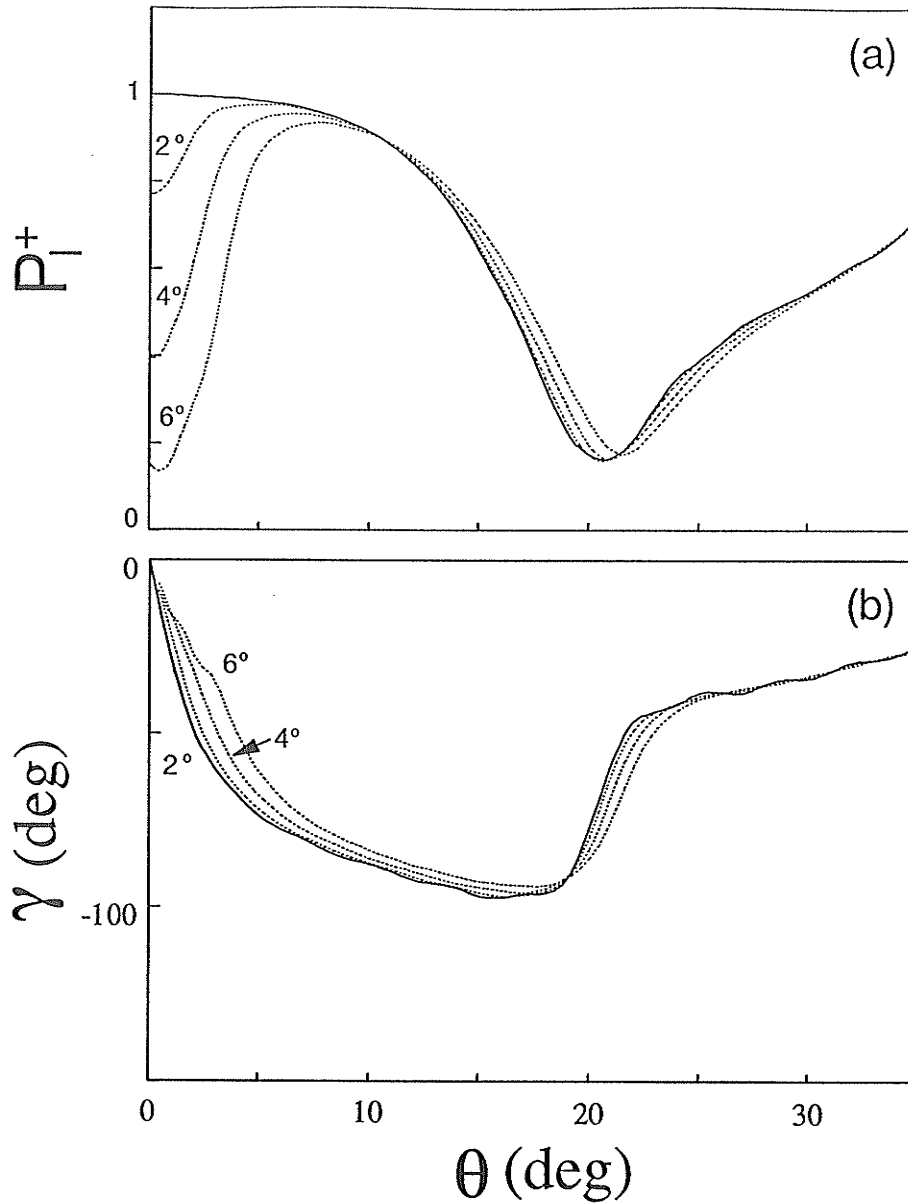


Figure 4.14 The results of modeling calculations to show the effect of finite interaction volumes on  $P_l^+$  parameter (a) and  $\gamma$  parameter (b). The solid curve represents DWA calculation results of Clark et al. (Clark1989) for  $E_0 = 20\text{eV}$ . The dotted curves are the modelling calculation results which subtend angles of 2, 4 and 6 degrees.

of  $P_l^+$  and  $\gamma$  EICP is not surprising. Near zero degrees scattering angle, different collision events contributing to the measured signal can define true scattering planes and true scattering angles that differ radically from their nominal counterparts. This can be illustrated by considering a collision event that scatters an electron out of the nominal scattering plane (but into the detector viewcone). Near zero degrees nominal scattering angle such an event can define a true scattering plane that is nearly perpendicular to the nominal scattering plane. Hence, for this particular collision event, an in-plane experimental geometry is defined rather than the nominal  $90^\circ$  out-of-plane geometry. Likewise, the true scattering angle, corresponding to a detected collision event, can lie anywhere within a range determined by the angular size of the detector viewcone. For a collision event that scatters an electron out of the nominal scattering plane, the difference between the true and nominal scattering angle is largest near zero degrees nominal scattering angle (refer to Fig. 3(a) of (Zetner1990)). The influence of a finite interaction volume on the measurement beyond  $5^\circ$  scattering angle is minimal for a detector viewcone of  $4^\circ$ . Now we can explain why the interaction volume of finite extent does not have significant influence on  $L_\perp$ . The magnitude of  $L_\perp$  is very low at small scattering angles. Therefore we expect a small "depolarization" of  $L_\perp$  resulting from averaging of scattering events over a spatial extent. In Figure 4.9 - 4.13, modelling calculations (employing the RDW theory) are represented by dotted lines. We simulated the effect of a finite interaction volume by taking the detector acceptance view cone to be  $4^\circ$ . As seen from the figures (especially Fig. 4.14), this influence can strongly affect the measured values of  $P_l^+$  at small scattering angle but is negligible except for near-zero scattering angles. We can therefore safely compare experiment and theory outside of this region. Since the modelling calculation

indicated that the measurement of  $L_{\perp}$  was negligibly affected by the interaction volume size even at near-forward-scattering angles. It is therefore legitimate to directly compare experimental and theoretical results for  $L_{\perp}$  over the whole range of scattering angles studied.

Radiation trapping arises from the reabsorption of radiation emitted spontaneously by the laser-excited atoms in the interaction region. The spontaneous emission is not polarized and can contribute an isotropic component to the superelastic signal. When the atom number density is high enough, depolarization effect can result in reduction of the magnitude of EICP.

Hertel and Stoll (Hertel1977) have discussed the conditions under which radiation trapping can be disregarded in collision experiments with laser-excited atoms. The estimation of the maximum atom number density tolerable has been presented as follows: In the center of the excitation region, the spectral spontaneous radiation density is

$$u_{\nu} \leq \frac{n_e}{n_0} n_0 \frac{hD/2}{\tau \Delta v_{1/2}} \quad 4.11$$

where  $\Delta v_{1/2}$  is the FWHM of the atom beam velocity distribution,  $n_0$  is the total number density of atoms,  $n_e$  the number density of excited atoms, and  $\tau$  the spontaneous lifetime.  $D$  represents the beam diameter.

For barium  $6^1P_1$  excitation where  $n_e/n_0 \approx 0.5$ , we may neglect the trapped radiation when, say, the spontaneous radiation density in the center of the beam  $u_{\nu} \approx 5 \times 10^{-14}$  erg sec/cm<sup>3</sup>. (This number was given by Hertel and Stoll for sodium. Because of the similarity between barium and sodium in aspects of lifetime and radiation frequency of their P state, we assume that

barium has the similar  $u_v$ ). For a typical beam  $D \approx 2\text{mm}$   $\tau = 10^{-8}$  sec and  $\Delta v_{1/2} \approx 3 \times 10^4$  cm/sec, the atom number density must be below  $5 \times 10^{11}$  atoms/cm<sup>3</sup>. Thus in our experimental conditions, the atom number density (about  $7 \times 10^{10}$ /cm<sup>3</sup>) falls within this regime where depolarization by radiation trapping should be small. Further corroboration is provided by the presence of measured  $P_l^+$  values that fall close to unity. Since all of our measurements were taken under the same experimental conditions, we assume that radiation trapping plays an unimportant role in all the measurements.

We have chosen error bars to represent statistical uncertainty of the data as well as any systematic uncertainty (small, but unknown, contribution from radiation trapping, small deviation of the laser incidence direction from the normal direction to the nominal scattering plane). We have found that the error bar can be substantially reduced by taking signal and background spectra in the same pass.

The experimental results exhibit behavior similar to that which has been observed in electron-photon coincidence studies of  $1^1S_0$  to  $2^1P$  excitation in helium (Andersen 1988). Pronounced minima in the charge-cloud linear-polarization parameter  $P_l^+$  are evident at all impact energies studied. At impact energies of  $E_0 = 36.7\text{eV}$ ,  $50\text{eV}$  and  $80\text{eV}$ , the minimum in  $P_l^+$  is accompanied by a rapid change in alignment angle  $\gamma$ , which is the expected behavior for the excitation of a near-circular atomic state. At  $E_0 = 20\text{eV}$ , however, the alignment angle undergoes a comparatively smooth decrease with increasing scattering angle, suggestive of He  $1^1S_0$  to  $2^1P$  observations closer to the excitation threshold.

It is seen from the experimental data that the first order Born approximation fails completely at large scattering angles. The prediction of FBA is that  $P_l^+ \equiv 1$ ,  $L_{\perp} \equiv 0$  and  $\gamma$  follows the smooth function of Eqn. 2.52c.

But the experiment data exhibit pronounced minima in  $P_l^+$  parameter and rapid change in  $\gamma$  simultaneously. At the same angle when  $P_l^+$  goes to minima,  $L_{\perp}$  reaches about 1. As we pointed out in Chapter 2, the discrepancy between FBA and the measurement results at large scattering angle and low impact energy is associated with the deep penetration of scattered electron into target atom.

In general, with the exception of low impact energies ( $E_0 = 10$  and  $20\text{eV}$ ), the agreement between experiment and distorted-wave theories for  $P_l^+$  and  $\gamma$  is excellent (see Figure 4.11 through 4.13). The RDW theory is somewhat more successful both in reproducing the locations and depths of minimum in  $P_l^+$  and in accurately predicting the behavior of  $\gamma$ . It is probably not the fully relativistic nature of this calculation that is responsible for its superiority over the UDWA results. Over the range of scattering angles where agreement between experiment and theory is good, it is expected that relativistic (i.e., spin-dependent) effects contribute negligibly to the  $^1S_0$  to  $^1P_1$  excitation in barium. This has been borne out (theoretically) by both UDWA and RDW calculations. It is likely that observed differences between two theoretical results arise from differences in the details of the calculations, particularly the use of different distortion potentials.

At the impact energy  $E_0 = 10\text{eV}$ , the measured  $P_l^+$  exhibits structureless angular behavior and is affected by the finite interaction volume at scattering angles up to 10 degrees (as shown in Figure 4.9). The UDWA theory also predicts a relatively flat behavior of  $P_l^+$  but shows a shallow minima at about  $50^\circ$ . The agreement between experiment and theory is qualitative for  $P_l^+$  but is reasonably good for  $\gamma$ . UDWA theory seems to predict a faster variation on angular behavior of both  $P_l^+$  and  $\gamma$ . The structureless nature of  $P_l^+$  for low impact energy results from the fact that

electrons with low kinetic energy can not penetrate deeply into the target (especially for those scattered to small angles) and consequently it can not transfer much angular momentum to the target. This gives rise to a constant large value in  $P_l^+$  associated with a small value in the transferred angular momentum  $L_\perp$ .

At the impact energy  $E_0 = 20\text{eV}$ , both distorted-wave theories fail completely to reproduce the observed deep minimum in  $P_l^+$ , although a very shallow minimum in the observed location is indicated by RDW calculations (Figure 4.10). Both theories, however, are very successful in predicting the observed alignment-angle behavior. This can be viewed in slightly different terms. If we assume that relativistic effects play no role in the barium s to p excitation at this impact energy and over this range of scattering angles (as theory suggests), then the excited-state charge cloud can be considered to possess pure positive-reflection symmetry, the '+' superscript on  $P_l^+$  becomes superfluous, and we can write (Andersen1988)

$$\frac{\langle f_1^n f_{-1}^{n*} \rangle}{\text{Tr}[\rho]} = -\frac{1}{2} P_l \exp(-2i\gamma) \quad 4.12$$

where  $\langle f_1^n f_{-1}^{n*} \rangle$  is the off-diagonal element of the density matrix  $\rho$ , expressed in the natural coordinate frame. Since predicted and observed behavior of  $\gamma$  can be in excellent agreement while severe discrepancies in  $P_l^+$  can exist, it is apparent through Eqn. 4.12 that calculation of the phase difference between scattering amplitudes is less sensitive to scattering-theory approximations than the calculation of their magnitudes. In fact,  $P_l^+$  is determined by the magnitude of a ratio of bilinear combinations of scattering amplitudes. Small errors in the calculation of these amplitudes, which represent the primary

quantities obtained from theory, can be amplified in such a ratio. We point out, however, that both distorted-wave theories are reasonably successful in predicting the observed DCS (given by  $\text{Tr}[\rho]$ ) at 20eV impact energy and scattering angle less than  $30^\circ$  (Srivastava1992) (with the UDWA calculation fitting the available experimental data more closely). We also point out that this disparity in predictive power for  $\gamma$  behavior and  $P_l^+$  behavior has been observed by Martus, Zheng, and Becker (Martus1991) in the comparison of their heavy-noble-gas measurements to first-order perturbative theories.

It is well understood that distorted-wave theories should begin to fail at lower impact energies although, in the present case, it is somewhat surprising that 20 eV (approximately nine times the barium ( $6s6p\ ^1P$ ) excitation threshold) should be categorized as a low impact energy. More meaningful comparison of our  $E_0 = 20\text{eV}$  data might be made with close-coupling calculations (for example), which have been demonstrated to succeed at near-threshold impact energies. Figure 4.10(a), (b) and (c) include a comparison of present experimental results with the close-coupling calculations of Fabrikant (Fabrikant1985) at  $E_0 = 20\text{eV}$ . The deep minimum in  $P_l^+$  is clearly predicted by this theory; however, the location of this minimum is shifted in scattering angle with respect to the experimentally observed minimum. Agreement with the observed behavior of the alignment angle  $\gamma$  is excellent below about  $20^\circ$  scattering angle, but significant discrepancies exist outside of this region. It is interesting to note, however, that the close-coupling theory predicts a noticeable 'shoulder' in the  $\gamma$  versus  $\theta$  behavior when the calculated  $P_l^+$  goes through a minimum. In other words, near the minimum in  $P_l^+$ , the decrease in  $\gamma$  is more rapid than in regions of scattering angle on either side of the minimum. The same type of shoulder is discernible in the experimental  $\gamma$  values near the observed minimum in  $P_l^+$ . In this respect, a correspondence

can be made between the behavior of  $\gamma$  at  $E_0 = 20\text{eV}$  and the rapid variations in  $\gamma$  observed at higher impact energies near the associated minima in  $P_l^+$ . Unlike the distorted-wave theories, close-coupling calculations seem capable of qualitatively predicting this aspect of the behavior of  $\gamma$  at low impact energy. Andersen et al. have summarized available experimental and calculated results for excitation of the He  $2^1P_1$  state (Andersen1988). They pointed out that close coupling calculation, in comparison with other theories, can reproduce the experimental results with very good agreement at low energies up to  $30\text{eV}$  (threshold is  $21.2\text{eV}$ ). So it is not surprising that close coupling calculation works reasonably well for the barium at impact energy about 10 times of the threshold. Finally, we bring to the reader's attention a comparison, made by Clark *et al.* (Clark1989), of the close-coupling and UDWA predictions for the barium ( $6s6p\ ^1P$ ) DCS at  $20\text{ eV}$  impact energy. These two theories show very close agreement in the DCS below, approximately,  $70^\circ$  scattering angle in spite of the dramatic disagreement in  $P_l^+$  over this range of angles. This, again, highlights the sensitivity of ratios of bilinear combinations of scattering amplitudes to theoretical approximations and demonstrates the effectiveness of EICP measurements in providing a more rigorous test of these approximations.

The  $L_\perp$  coherence parameter is an interesting probe of the electron-atom collision dynamics. It gives the expectation value of the orbital angular momentum (measured in the perpendicular direction to the scattering plane) transferred by an inelastic collision. Typically, for such simple systems as hydrogen and helium,  $L_\perp$  will vary monotonically with scattering angle in such a way that it is positive at small angles and increases from zero (in the forward-scattering direction) to a maximum, then decreases to change sign and reach a minimum, returning to zero in the backward-scattering direction.

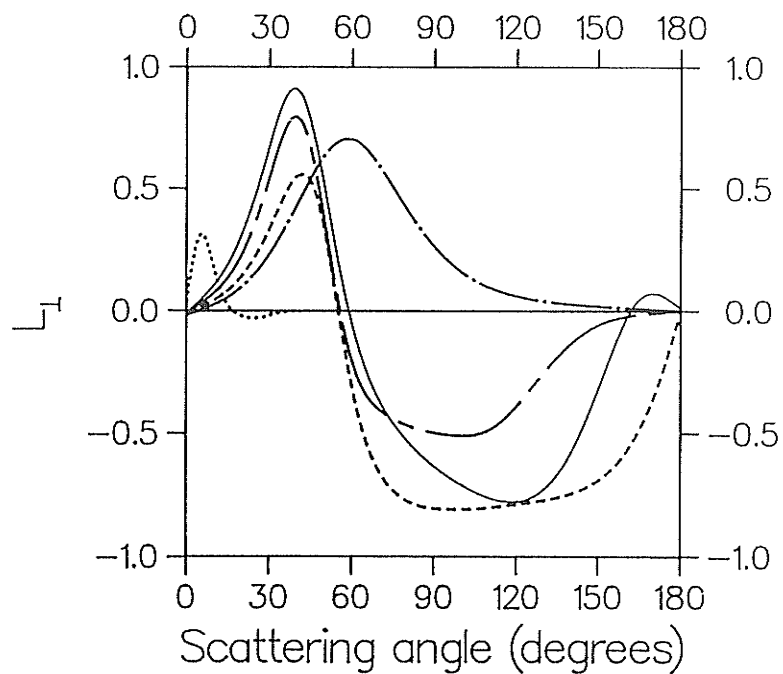
The forward-scattered electrons reach the target with a large scattering parameter and have a weak interaction with the target, while the backward-scattered electrons reach the target with a zero scattering parameter and head-on collisions take place for these electrons. Therefore, the vanishing of  $L_{\perp}$  in the forward- and backward-scattering directions can be understood classically by noting that the projectile electron exerts no torque on the target atom in these two situations.

Several 'universal' features of the behavior of  $L_{\perp}$  parameter have been observed for electron-impact excitation of simple systems such as hydrogen and helium. These are discussed by Lin et al. (Lin1989). These authors have investigated the orientation parameter  $\langle L_y \rangle$  (in collision frame) and alignment parameter  $\gamma$  of atomic excited states of hydrogen and helium atoms formed in collision with electrons (and with other particles as well). They searched for general trends and similarities in the calculated  $\langle L_y \rangle$  in order to assess the possibility of simple models for interpreting the variation of the sign in  $\langle L_y \rangle$ . They found that for electron impact, except for electron scattering at large angles, the sign of  $\langle L_y \rangle$  (i.e.  $L_{\perp}$  in nature frame) is positive, consistent with the classical model with an attractive force. The angles where  $\langle L_y \rangle$  has maximum, minimum and zero values become smaller at increasing impact energies. A simple semiempirical scaling of  $\langle L_y \rangle$  for electron-impact excitations to 2p states was found and the general behavior of  $\langle L_y \rangle$  and  $\gamma$  was analyzed for different impact energies.

The relatively simple behavior of  $L_{\perp}$  prompted the development of a semiclassical model (Steph1980) which linked the sign of this parameter to the attractive (+sign) or repulsive (-sign) nature of the collisional interaction. According to this model, electrons suffering glancing collisions experience a net attractive force while backward-scattering electrons penetrate deep into

the atomic electron charge cloud and experience a repulsion. The attractive interactions were attributed to the polarization potentials for glancing collisions (small scattering angle) and the repulsive interactions were attributed to the Coulomb repulsion between the incident electron and the target electrons for close collision ( large scattering angle). Madison, Csanak, and Cartwright subsequently demonstrated the inadequacies of this model by reproducing the observed  $L_{\perp}$  behavior using the distorted-wave Born approximation and a purely attractive interaction potential (Madison1986). The importance of this work was twofold. It showed that the introduction of distortion into the entrance and exit scattering channels in a first-order theory was sufficient to yield reasonably quantitative agreement with observation of  $L_{\perp}$ . In the absence of such distortion one obtains the first Born approximation that fails completely by giving  $L_{\perp} = 0$  for all scattering angle. Second, by performing a partial-wave expansion of the entrance and exit scattering channels and introducing distortion selectively into the various partial waves, these authors concluded that the angular behavior of  $L_{\perp}$  arises from quantum mechanical interference among the distorted partial waves and does not lend itself to a simple semiclassical interpretation.

In an interesting quantum mechanical study by Madison et al (Madison1986), the partial wave dependence of  $L_{\perp}$  was systematically calculated in the FOMB theory. They found that the distortion of the  $l = 0, 1, 2$  incident partial waves plays a significant role for obtaining the characteristic shape of  $L_{\perp}(\theta_{col})$ . The  $l = 0$  and  $1$  distortion explains the forward positive sign, while the d-wave is predominantly responsible for the sign reversal of  $L_{\perp}$  at larger scattering angles. This is illustrated in Figure 4.15. One major point discussed by Madison et al is the importance of the nuclear attraction as the dominant force, determining the sign of the orientation for small scattering



- .....  $l_p = 0$
- · - · -  $l_p = 0, 1$
- - -  $l_p = 0, 1, 2$
- - - -  $l_p = 0, 1, 2, 3$
- $l_p = 0 - 7$

Figure 4.15. Transferred angular momentum for electron impact excitation of He  $2^1P$  at 81.6 eV in FOMB approximation.  $l_p = 0, 1, \dots$  refers to the incident electron partial waves. Adopted from (Andersen1988).

angles. The pure static potential is always attractive as soon as the electron penetrates the atom. The electron repulsion and the long range polarization potential are found not to be crucial for the shape of  $L_{\perp}(\theta_{col})$ . It is thus clear that the negative sign of  $L_{\perp}$  at large  $\theta_{col}$  cannot be attributed to a repulsive interaction but rather to the deep penetration of the scattered particle into the potential and the resulting phase shifts and interference effects. Recognizing this fact we note that there is no simple classical interpretation for the negative  $L_{\perp}$  for electron-impact excitations. A quantum mechanical interpretation has to be used to explain this phenomenon.

In the excitation of He  $2^1P$  by 80eV electrons, distorted partial waves up to  $l = 2$  were shown to make the dominant contribution. For the Ba  $6^1P_1$  excitation measured in the present work, we would expect significant contributions from higher-order partial waves with the resultant quantum-mechanical interference giving rise to a more highly structured angular behavior of  $L_{\perp}$ . Figure 4.10(a), 4.11(a) and 4.12(a), in which we compare our present measurements with available theory, illustrate that this is indeed the case. The angular variation of  $L_{\perp}$  exhibits pronounced structure and is substantially different from that occurring in H and He excitation. We do, however, note a resemblance to  $L_{\perp}$  behavior predicted and observed in Ca (Zohny1990, Hamdy1993 and Srivastava1992), Sr (Hamdy1991, Hamdy1993, Beyer and Srivastava1992), and, in some cases, the heavier rare gases (Andersen1988, Corr1990 and Machado1991).

At impact energy  $E_0=20\text{eV}$  quantitative agreement between experiment and theory is poor, although all three theories reproduce, to some extent, qualitative aspects of the angular behavior of  $L_{\perp}$ . The failure of the first-order perturbative theories (UDWA and RDW) is not surprising at this low impact energy. The CC approach should be more successful in this regime but the

two-state, nonexchange, nonrelativistic treatment adopted by Fabrikant (Fabrikant1985) can only predict the height and width of the maxima in  $L_{\perp}$ , but fails to reproduce the angular behavior of  $L_{\perp}$  adequately.

Comparison of the first-order perturbative theories with experiment at  $E_0 = 36.7\text{eV}$  reveals excellent quantitative agreement out to  $92^\circ$  scattering angles. An interesting situation occurs, however, at  $E_0 = 50\text{eV}$  in which a discrepancy between theory and experiment develops beyond the first maximum in  $L_{\perp}$  and worsens with increasing scattering angle to the point where both UDWA and RDW theories fail to predict an apparent sign change in  $L_{\perp}$  near  $60^\circ$  scattering angle.

In Figure 4.16 the present  $L_{\perp}$  measurements are combined with our earlier  $P_l^+$  measurements to give  $P^+$ , the degree of polarization that is defined in Chapter 2, using  $P^+ = [(P_l^+)^2 + (L_{\perp})^2]^{1/2}$ . If  $P^+ = 1$ , the excitation is considered to be fully coherent and spin dependence in the collision is negligible. Over the range of impact energies and scattering angles presented in the figures, it is clear that  $P^+ = 1$  to within experimental error limits. We note that large error bars in the case of  $E_0 = 50\text{eV}$  arise partly due to calibration uncertainty in the scattering angle. At this impact energy both  $P_l^+$  and  $L_{\perp}$  vary rapidly with angle and small uncertainties can give large variations in  $P^+$ . The fully coherent nature of the Ba  $6^1P_1$  excitation is predicted by both UDWA and RDW theories. We point out, however, that the RDW theory does give a nonzero spin-polarization function but the manifestation of spin effects in the EICP's is predicted to be small. The solid lines in Figure 4.16 results from a calculation which models the effect of the finite interaction volume on  $P^+$  using RDW EICP's.

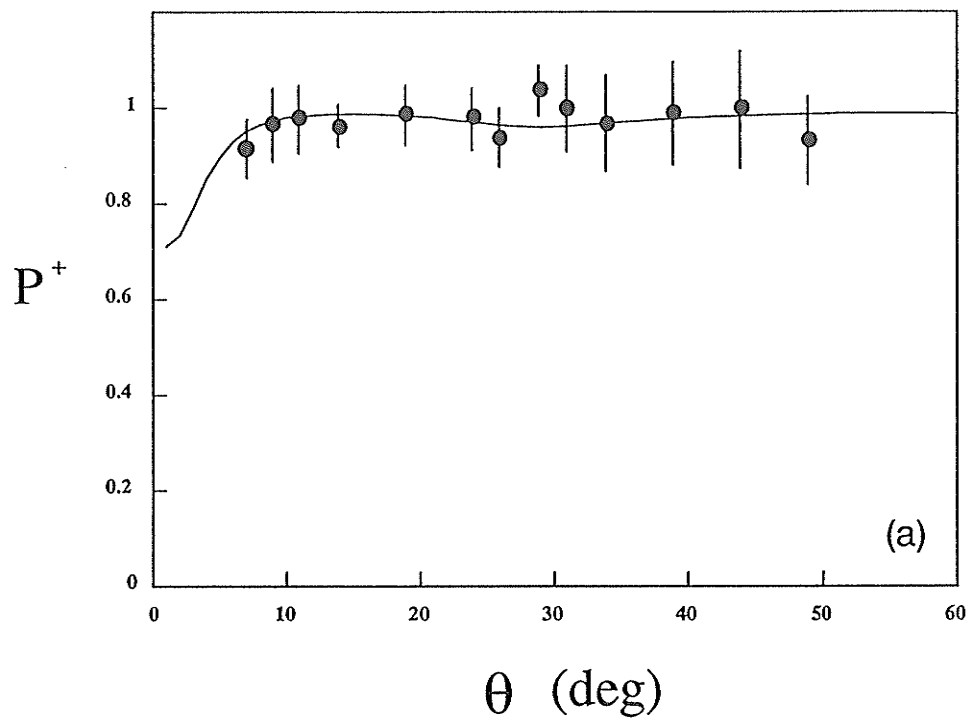
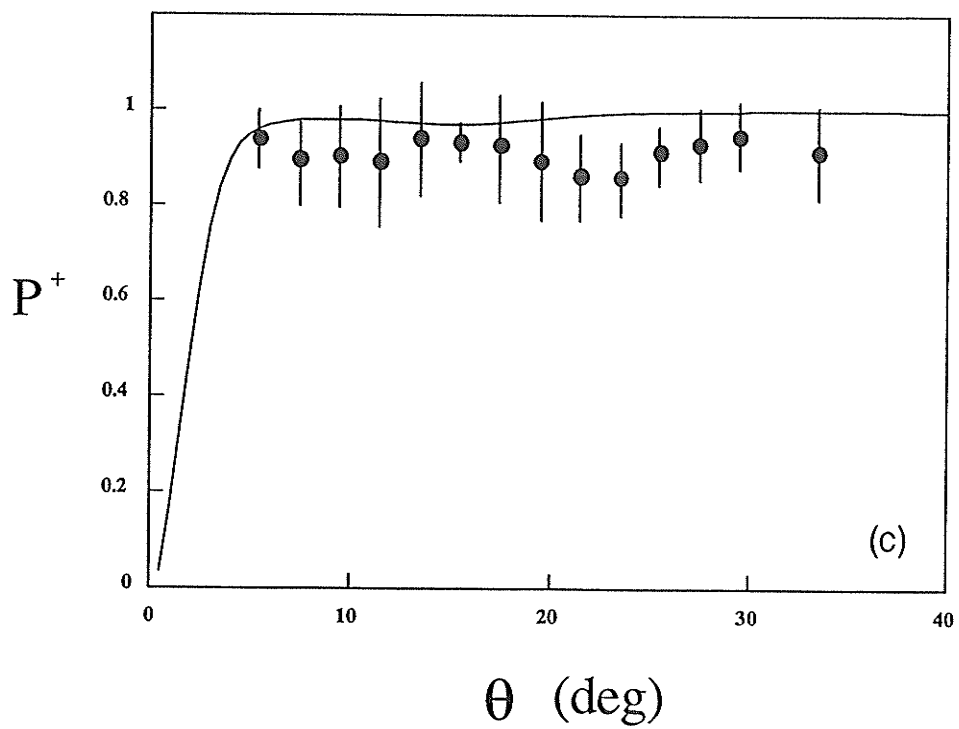
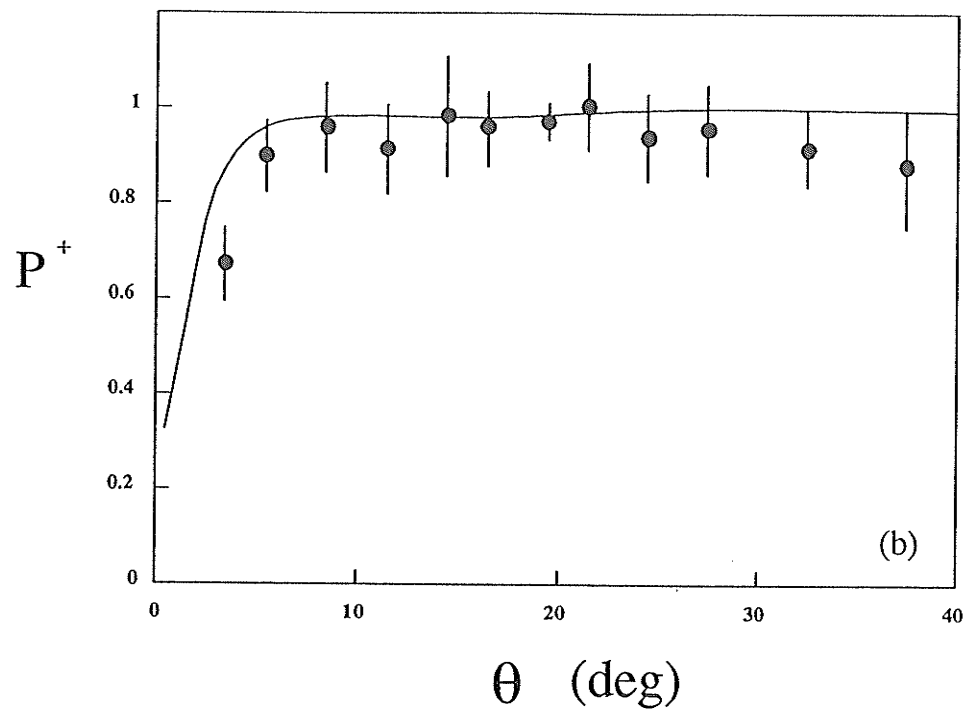


Figure 4.16. (a) The degree of polarization  $P^+$  for  $E_0 = 20\text{eV}$ . Measured values (circles with error bars) were obtained by combining the measured  $P_l^+$  and  $L_{\perp}$  results. The solid line represents a calculation which models the effect of a finite interaction volume using the RDW EICP of srivastava (Srivastava1992). (b) Same as (a) except  $E_0 = 36.7\text{eV}$ . (c) Same as (a) except  $E_0 = 50\text{eV}$ .



Another set of EICP's ( $\lambda, \tilde{\chi}, \epsilon, \Delta$ ) defined in collision frame by Blum, da Paixao, and Csanak (Blum1980 and da Paixao1980) is also used to describe the electron-impact excitation processes. Among these parameters,  $\lambda$  is the most physically meaningful parameter and represents the ratio of partial differential cross section (PDCS) for  $M^c = 0$  ( magnetic sublevel in collision frame) to differential cross section (see Eqn. 2.33). Therefore, if  $\lambda$  is known, we can derive PDCS from existing DCS. Based on the relationships between these two sets of parameters, we have derived  $\lambda$  parameters using our experimental EICP results and then obtained PDCS (see Section 4.6).

The first step of present work is to use rearranged Eqn. 2.38 and 2.40 to calculate  $\lambda$  parameter from available results of previously measured  $P^+, \gamma$ ,  $L_{\perp}$  and  $P_l$  Stokes parameters

$$\lambda = \frac{P_l + 1}{2} \quad 4.13$$

and

$$P_l = P_l^+ \cos 2\gamma \quad 4.14$$

$P^+$  and  $\gamma$  values are either measured directly in superelastic-scattering experiments or derived from measured  $L_{\perp}$  values. Some of the  $P_l$  parameter was measured incidentally with  $L_{\perp}$  measurement.

All  $\lambda$  values derived from different measured EICP's for impact energies  $E_0 = 10, 20, 36.7, 50$  and  $80\text{eV}$  are tabulated in Table 4.3. Error limits on the derived  $\lambda$  values reflect both statistical and systematic uncertainty in the primary measurements. The  $\lambda$  versus scattering angle behavior is also graphically plotted in Figure 4.17. The  $\lambda$  values and error bars on the graph were determined by best fitting the raw data of  $\lambda$  and their

Table 4.3. Summary of experimentally derived values of the  $\lambda$  parameter. Numbers in parentheses indicate the uncertainty in the last digits.

$\theta$ (deg)	$E_0$ (eV)				
	10	20	36.7	50	80
4	0.68(6)		0.19(6)	0.13(6)	
5		0.32(6)			0.08(2)
6	0.55(6)				
7			0.05(2)	0.04(2)	0.08(2)
8		0.18(4)			
9	0.38(7)			0.06(3)	0.12(2)
10		0.14(3)	0.06(2)		
11	0.31(7)				0.18(3)
12		0.12(2)	0.11(2)	0.19(4)	
13					0.39(2)
14	0.20(6)			0.33(6)	
15		0.15(2)	0.23(2)		0.65(3)
16				0.51(9)	
17		0.20(2)	0.38(3)		0.66(5)
19	0.11(5)		0.58(6)	0.67(7)	0.61(5)
20		0.29(3)			
21					
22			0.67(5)	0.72(9)	
23					0.55(5)
24	0.08(5)			0.73(10)	
25		0.45(3)	0.70(6)		
26				0.71(9)	
27			0.71(6)		
28		0.56(4)			
30		0.64(6)	0.74(6)		
31				0.66(8)	
34	0.24(6)			0.68(8)	
35		0.83(5)	0.80(11)		
37				0.73(10)	
40		0.96(2)	0.91(8)		

42				0.81(11)
44	0.72(5)	1.00(1)		
45			0.96(6)	
47				0.89(11)
50		0.97(4)	0.94(8)	
52				0.93(14)
54	0.77(4)		0.91(14)	
55		0.90(8)		
60		0.82(14)	0.81(16)	
65		0.71(19)	0.72(22)	
70		0.59(20)	0.54(31)	

---

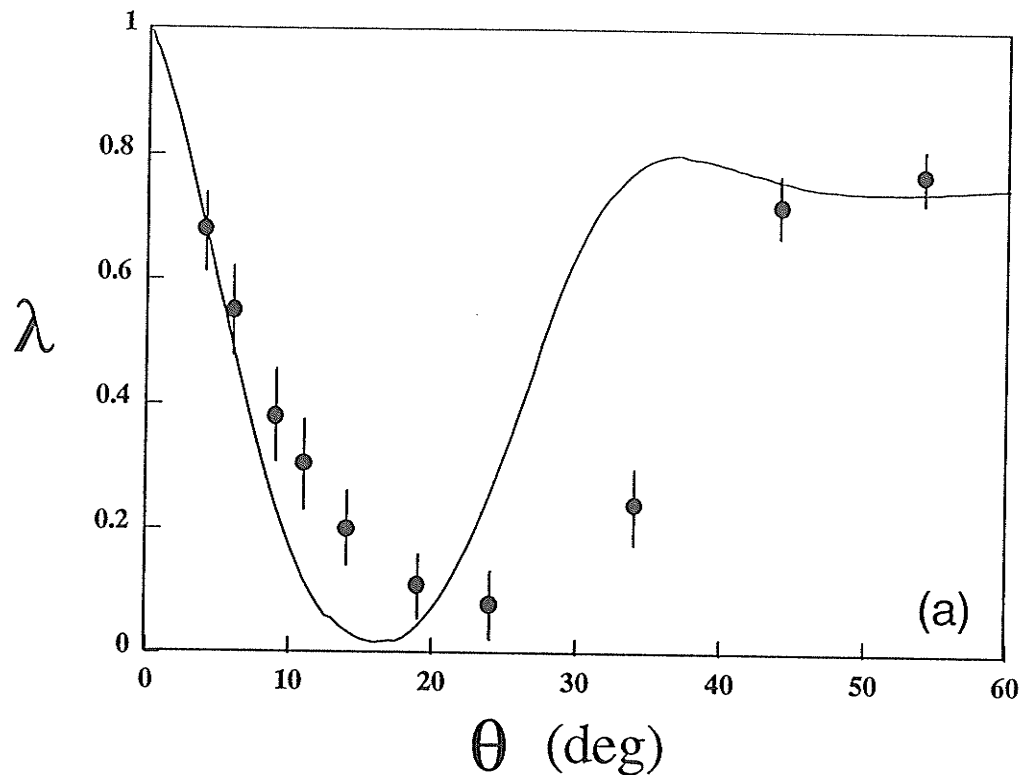
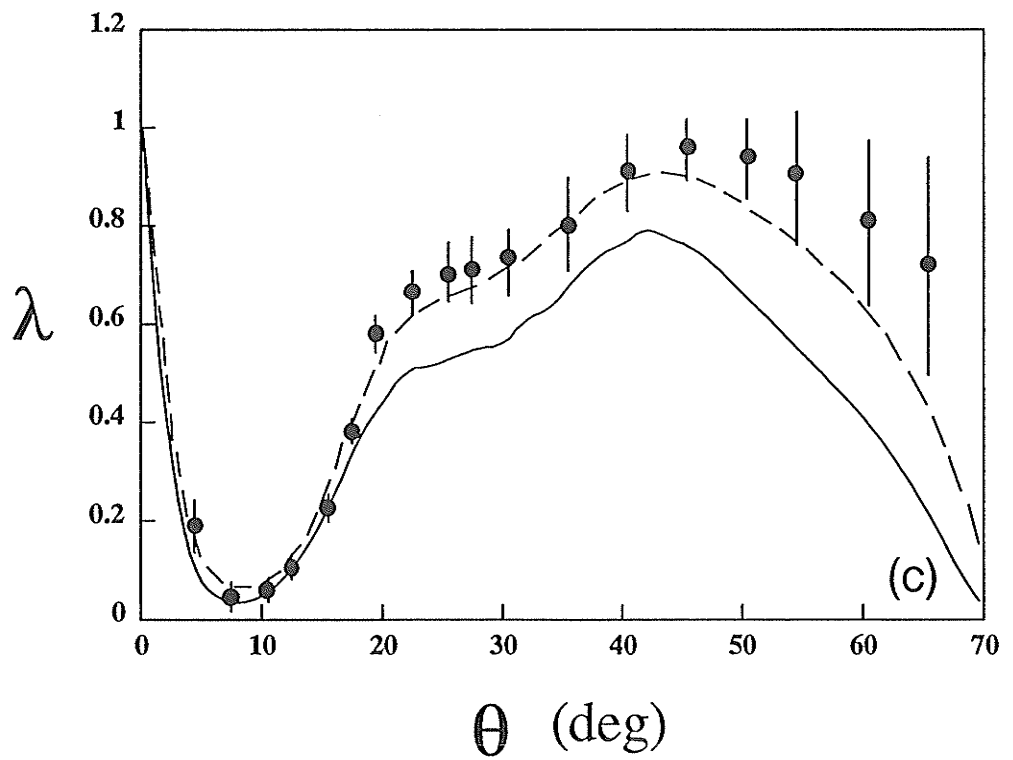
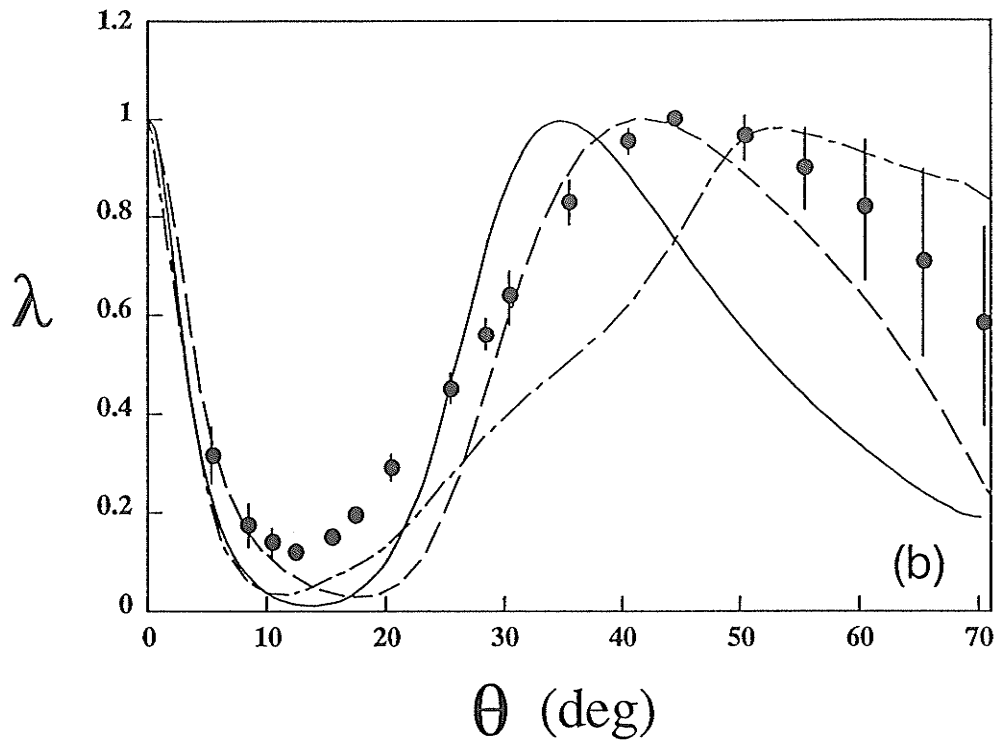
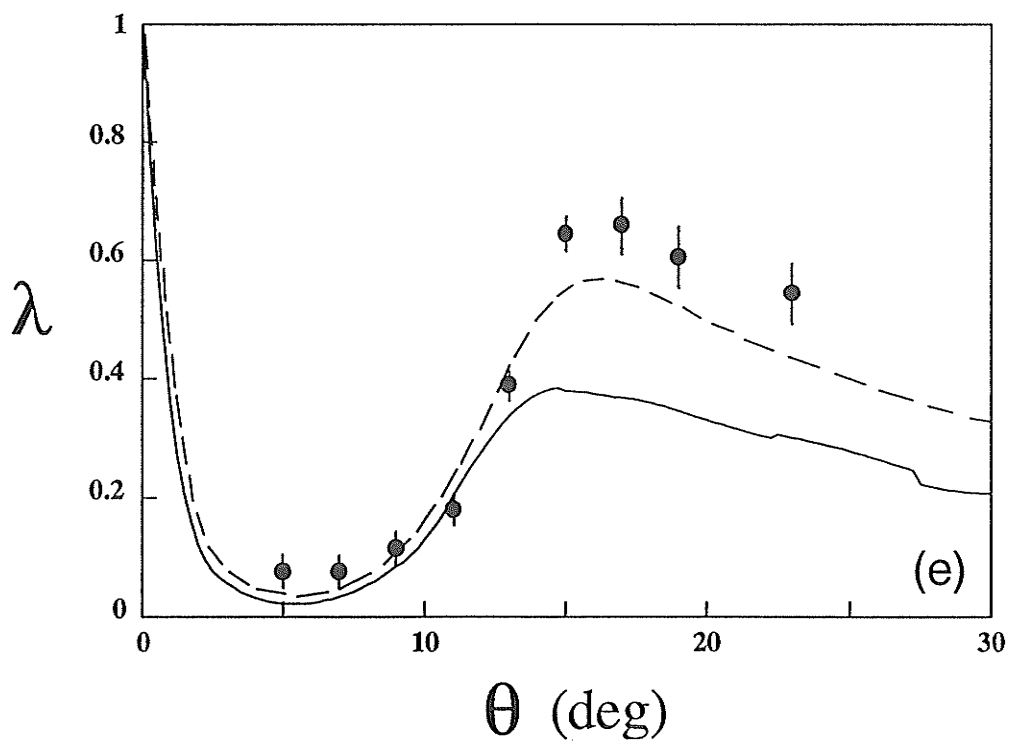
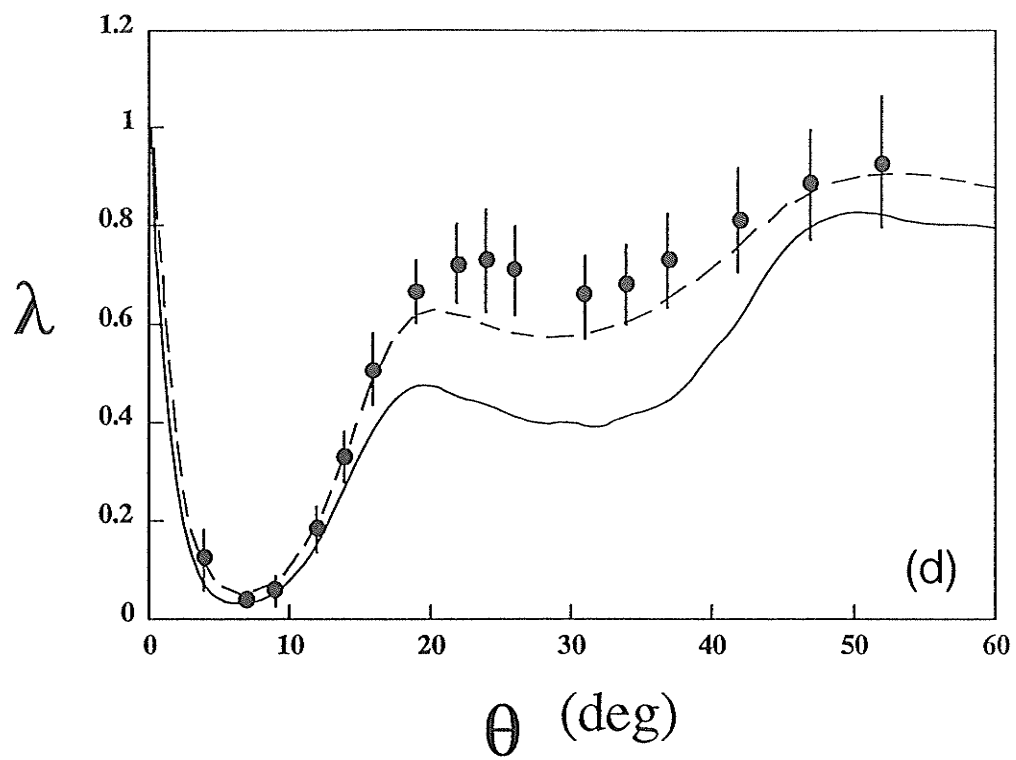


Fig 4.17. (a) Experimentally derived values of the  $\lambda$  parameter (circles with error bars) at an impact energy of  $E_0 = 10\text{eV}$ . The full curve represents the UDWA calculation of Clark et al (Clark1989). (b) Experimental derived values of the  $\lambda$  parameter at an impact energy at  $E_0 = 20\text{eV}$ . The full curve represents the UDWA calculation of Clark et al (Clark1989). The broken curve represents the RDW theory of Srivastava et al (Srivastava1992). The chain curve represents the close-coupling calculation of Fabrikant (Fabrikant1985). (c) Experimental derived values of the parameter at an impact energy at  $E_0 = 36.7\text{eV}$ . The full curve represents the UDWA calculation of Clark et al. The broken curve represents the RDW theory of Srivastava et al. (d) Same as (c) except  $E_0 = 50\text{eV}$ . (e) Same as (c) except  $E_0 = 80\text{eV}$ .





upper and lower error limits, respectively. In this way we obtained the  $\lambda$  values and corresponding error bars by taking weighted average over data points possibly at the same angle. The  $P_l^+$  measurements suffer from a severe systematic error at small scattering angles caused by the influence of a scattering volume of finite extent. We have used deconvolution method to 'unfold' this effect from  $P_l^+$  measurements at lower impact energy in order to give undistorted values of  $\lambda$ . This was done by making a smooth extrapolation from the known value of  $P_l^+ = 1$  at zero degree scattering angle to the first data point unaffected by the volume effect.

Figure 4.17 also compares derived  $\lambda$  values with available theory. Calculations based on UDWA of Clark et al (Clark1989) are shown for all impact energies. The RDW theory of Srivastava et al (Srivastava1992) is presented for impact energies  $E_0 = 20, 37.5, 50$  and  $80\text{eV}$ . A close-coupling calculation carried out by Fabrikant (Fabrikant1985) at  $E_0 = 20\text{eV}$  is also given. Excellent quantitative agreement is apparent in the case of the RDW calculations for  $E_0 = 36.7, 50$  and  $80\text{eV}$ . Quantitative agreement is exhibited by UDWA results at these impact energies at the smaller scattering angles. This theory tends to underestimate the value of  $\lambda$  at larger scattering angles but gives good qualitative agreement with the angular behavior of this parameter. At  $E_0 = 20\text{eV}$ , the first-order perturbative theories (RDW and UDWA) show only qualitative agreement with observations since they are approaching the low impact energy limit of their range of applicability. The close coupling calculation also shows qualitative aspects of the behavior of  $\lambda$  at  $E_0 = 20\text{eV}$  but is unable to give good quantitative agreement. Surprisingly, the qualitative behavior of the  $E_0 = 10\text{eV}$  data is reasonably represented by the UDWA calculation.

#### 4.6 Determination of PDCS for (...6s6p 6<sup>1</sup>P<sub>1</sub>) Excitation

The general expression of the differential cross section for a particular scattering process has been given in Chapter 2. If the excited state contains some sublevels, we can define a partial differential cross section (PDCS) in the similar way. But the numerator now represents the flux of scattered particles that excite target atoms to each particular substate. The DCS of this particular state equals the summation of PDCS over all of its substates. In the case of <sup>1</sup>S<sub>0</sub> to <sup>1</sup>P<sub>1</sub> transition, there are three magnetic substates existing ( $M_J = -1, 0, 1$ ). PDCS( $M = -1$ ), PDCS( $M = 0$ ) and PDCS( $M = 1$ ) constitute the differential cross sections (DCS) for <sup>1</sup>P<sub>1</sub> excitation

$$\text{DCS}(^1P_1) = \text{PDCS}(M = -1) + \text{PDCS}(M = 0) + \text{PDCS}(M = 1) \quad 4.15$$

The magnetic sublevel PDCS will be presented in two alternative forms, namely, 'collision frame' and 'natural frame'. Two of the EICP, namely  $L_{\perp}$  and  $\lambda$ , have special significance for the present work in that they can be expressed directly in terms of the magnetic sublevel PDCS. If we adopt the notation PDCS ( $M^n$ ) to refer to the partial differential cross section for excitation of the  $M$ th magnetic sublevel in the natural frame and PDCS ( $M^c$ ) to refer to the partial differential cross section of the  $M$ th magnetic sublevel in the collision frame then

$$\lambda = \frac{\text{PDCS}(M^c = 0)}{\text{DCS}} \quad 4.16$$

and

$$L_{\perp} = \frac{\text{PDCS}(M^n = +1) - \text{PDCS}(M^n = -1)}{\text{PDCS}(M^n = +1) + \text{PDCS}(M^n = -1)} \quad 4.17$$

Partial differential cross sections can be extracted from Eqn. 4.16 and 4.17 with the help of the further relations

$$\text{DCS} = \text{PDCS}(M^c = 0) + 2\text{PDCS}(M^c = 1) \quad 4.18$$

and

$$\text{DCS} = \text{PDCS}(M^n = +1) + \text{PDCS}(M^n = -1) \quad 4.19$$

Eqn. 4.18 makes use of the relation  $\text{PDCS}(M^c = +1) = \text{PDCS}(M^c = -1)$  that follows from the symmetry properties of the scattering amplitudes under reflection in the scattering plane. Eqn. 4.19 holds when excitation of a pure singlet P state takes place in the absence of spin-orbit coupling acting on the continuum electron. Under these conditions, the collisionally excited charge cloud must possess positive reflective reflection symmetry with respect to the scattering plane, in which case  $\text{PDCS}(M^n = 0) = 0$  and  $(P_{\parallel}^+)^2 + (L_{\perp})^2 = 1$ . This characterizes a completely coherent collision process. We have verified this directly by demonstrating that  $(P_{\parallel}^+)^2 + (L_{\perp})^2 = 1$  for impact energies  $E_0 = 20\text{eV}$ ,  $37\text{eV}$  and  $50\text{eV}$  up to the scattering angles  $\theta = 48^\circ$ ,  $37^\circ$  and  $33^\circ$  respectively. In the present work we assume that coherent excitation of the Ba  $6^1\text{P}$  level takes place outside of the kinematic range for which direct experimental evidence exists and extract magnetic sublevel partial differential cross sections based on this assumption using the following formulae:

$$\begin{aligned}
\text{PDCS}(M^c = 0) &= \lambda \text{DCS} \\
\text{PDCS}(M^c = 1) &= \frac{1}{2}(1 - \lambda) \text{DCS} \\
\text{PDCS}(M^n = +1) &= \frac{1}{2}(1 + L_{\perp}) \text{DCS} \\
\text{PDCS}(M^n = -1) &= \frac{1}{2}(1 - L_{\perp}) \text{DCS}
\end{aligned}
\tag{4.20}$$

These equations are developed by using Eqn 4.16 through 4.19. Eqn. 4.20 were then used to convert available theoretical results for the EICP and DCS into partial differential cross section.

The experimentally derived  $\lambda$  values and the  $L_{\perp}$  measurements of our previous superelastic-scattering experiment were used in combination with the absolute DCS measurements of Wang et al (Wang1994) (for  $E_0 = 10, 20\text{eV}$ ) and Jensen et al (Jensen1978) ( for  $E_0 = 36.7, 50$  and  $80\text{eV}$ ) to give partial differential cross sections by Eqn. 4.20.  $L_{\perp}$  values used for PDCS calculation were averaged by best fitting the data points resulting from both  $L_{\perp}$  and  $P_l^+$  measurements . In order to obtain the absolute DCS values at  $E_0 = 36.7\text{eV}$  and  $50\text{eV}$ , we plotted the excitation function curve ( DCS versus  $E_0$ ) for the Jensen et al data and interpolated DCS at these impact energies from the curve. Partial differential cross sections were calculated at those scattering angles for which absolute DCS measurements were available. Interpolation in scattering angle was therefore required to give the appropriate  $\lambda$  and  $L_{\perp}$  values at these scattering angles. The collision frame partial differential cross section ( PDCS( $M^c=0$ ) and PDCS( $M^c=1$ )) and the natural frame partial differential cross sections (PDCS( $M^n=+1$ ) and PDCS( $M^n=-1$ )) for  $E_0 = 20\text{eV}$  and  $36.7\text{eV}$  are plotted in Figure 4.18 and 4.19. Readers can refer to (Li1994) for diagrams for other impact energies (  $10\text{eV}$ ,  $50\text{eV}$  and  $80\text{eV}$ ). The summary of PDCS results for all energies is given in Table 4.4.

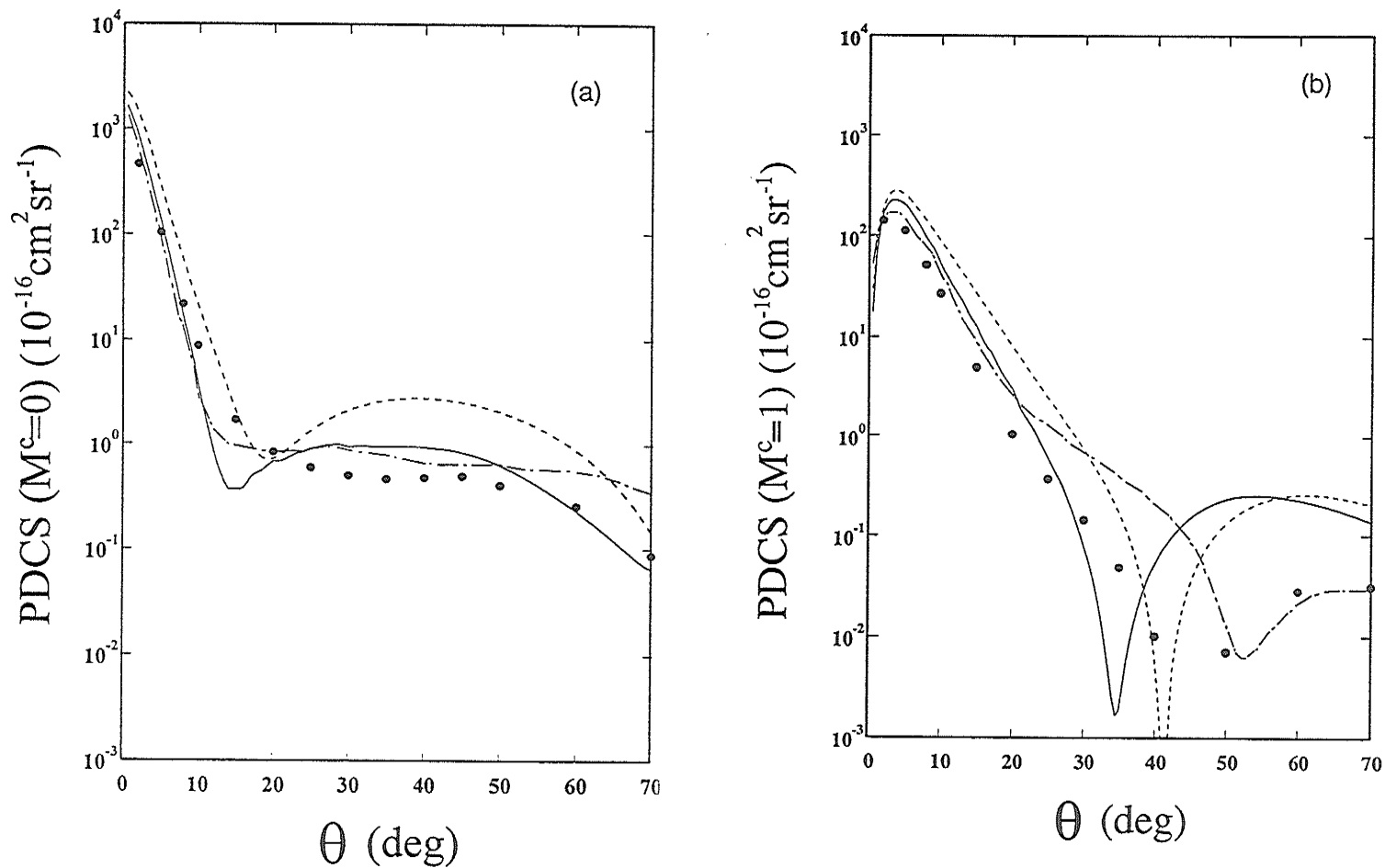


Figure 4.18(a) and (b). Collision frame partial differential cross sections PDCS ( $M^c=0$ ) and PDCS ( $M^c=1$ ) for impact energy  $E_0 = 20\text{eV}$ . Full circles represent experimentally derived values. The full curve represents the PDCS derived from the UDWA calculation of Clark et al (Clark1989). The broken curve represents the PDCS derived from the RDW calculation of Srivastava et al (Srivastava1992). The chain curve represents the PDCS derived from the close-coupling calculation of Fabrikant (Fabrikant1980)(Fabrikant 1985).

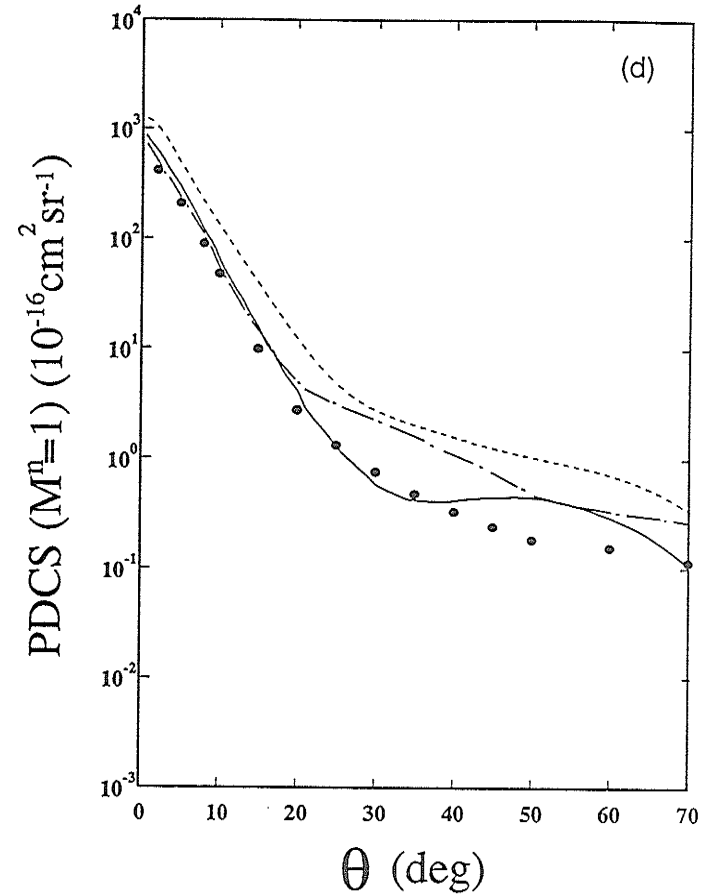
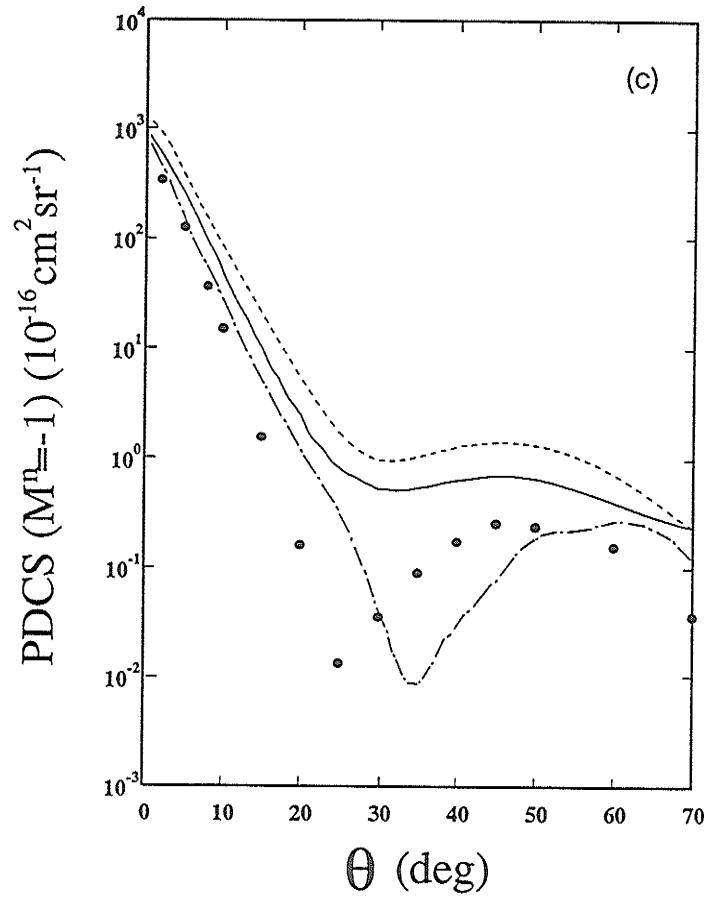


Figure 4.18(c) and (d). Natural frame partial differential cross sections PDCS ( $M^n = +1$ ) and PDCS ( $M^n = -1$ ) for impact energy  $E_0 = 20$  eV. Full circles represent experimentally derived values. The full curve represents the PDCS derived from the UDWA calculation of Clark et al (Clark 1989). The broken curve represents the PDCS derived from the RDW calculation of Srivastava et al (Srivastava 1992). The chain curve represents the PDCS derived from the close-coupling calculation of Fabrikant (Fabrikant 1980)(Fabrikant 1985).

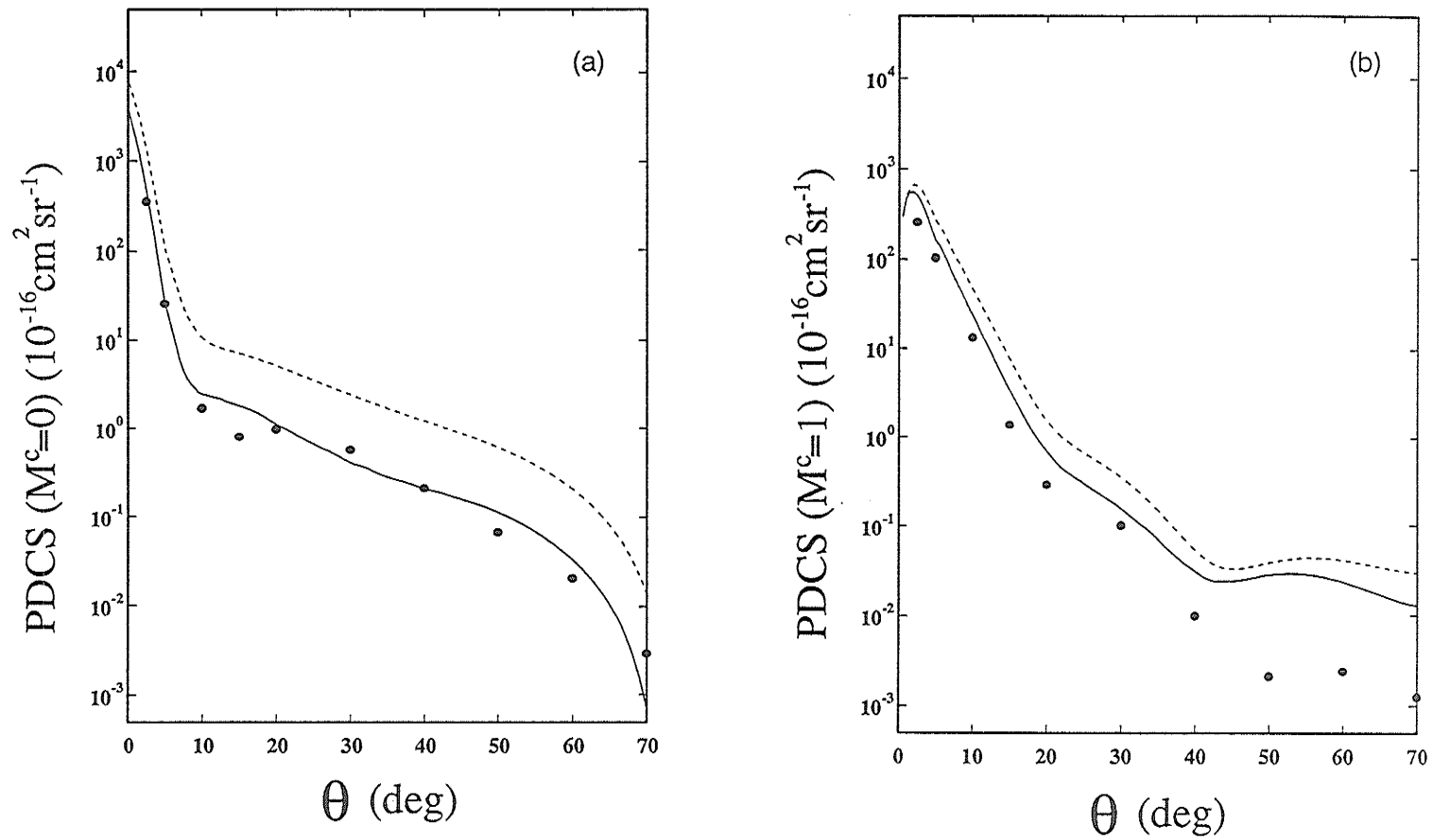


Figure 4.19(a) and (b). Collision frame partial differential cross sections PDCS ( $M^c=0$ ) and PDCS ( $M^c=1$ ) for impact energy  $E_0 = 36.7\text{eV}$ . Full circles represent experimentally derived values. The full curve represents the PDCS derived from the UDWA calculation of Clark et al (Clark1989). The broken curve represents the PDCS derived from the RDW calculation of Srivastava et al (Srivastava1992).

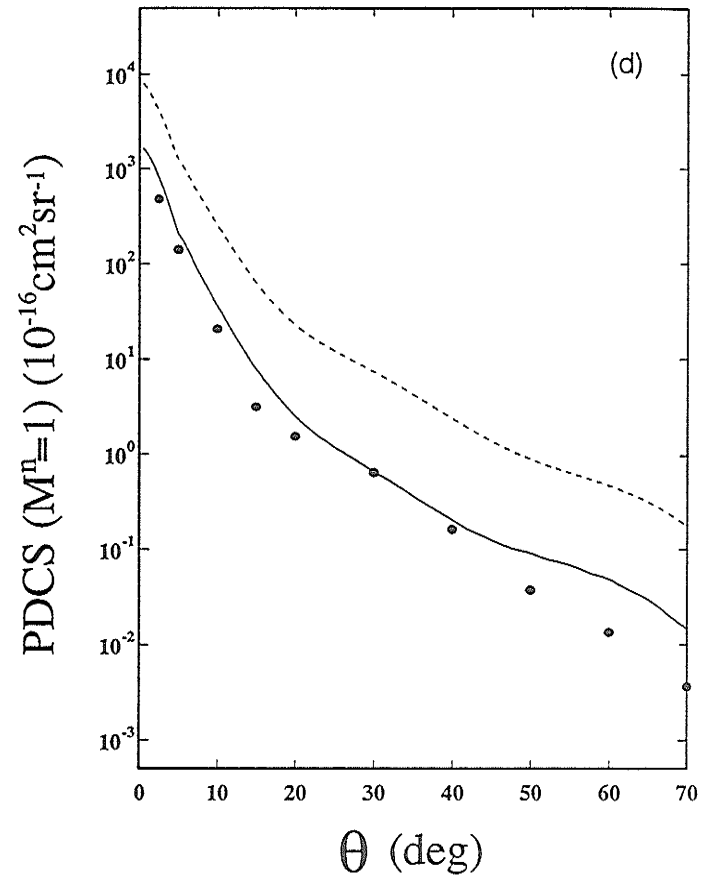
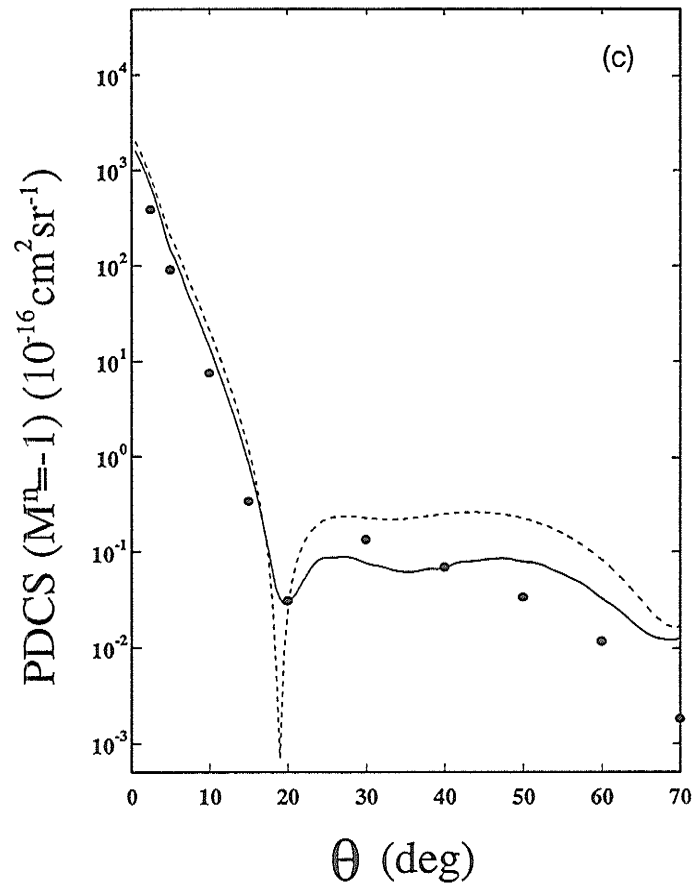


Figure 4.19(c) and (d). Natural frame partial differential cross sections PDCS ( $M^l=0$ ) and PDCS ( $M^l=1$ ) for impact energy  $E_0 = 36.7 \text{ eV}$ . Full circles represent experimentally derived values. The full curve represents the PDCS derived from the UDWA calculation of Clark et al (Clark 1989). The broken curve represents the PDCS derived from the RDW calculation of Srivastava et al (Srivastava 1992).

Table 4.4. Summary of PDCS values extracted from measured DCS and measured EICP. Numbers in parentheses indicate the uncertainty in the last digits.

$\theta$ (deg)	PDCS			
	$M^c=0$	$M^c=1$	$M^n=+1$	$M^n=-1$
$E_0 = 10.0\text{eV}$				
2	236	25.0		
5	124	38.0		
8	58.1	38.5		
10	38.8	37.6		
15	8.73	20.6		
20	1.69	7.61		
25	0.490	2.63		
30	0.360	1.07		
35	0.320	0.400		
40	0.361	0.130		
45	0.375	0.660		
50	0.354	0.500		
$E_0 = 20.0\text{eV}$				
2	464	142	412	337
5	104	113	207	124
8	21.7	51.2	88.0	36.0
10	8.71	26.7	47.3	14.9
15	1.71	4.85	9.86	1.54
20	0.840	1.03	2.75	0.160
25	0.599	0.366	1.32	0.0133
30	0.504	0.142	0.752	0.0354
35	0.464	0.048	0.470	0.0894
40	0.478	0.010	0.326	0.172
45	0.494	0.008	0.240	0.254
50	0.405	0.007	0.183	0.237
60	0.256	0.028	0.156	0.156
70	0.088	0.031	0.114	0.0360

$\theta$ (deg)	PDCS			
	$M^c=0$	$M^c=1$	$M^n=+1$	$M^n=-1$
$E_0 = 36.7\text{eV}$				
2.5	353	254	477	383
5	25.3	102	140	90.3
10	1.68	13.2	20.5	7.49
15	0.799	1.38	3.21	0.337
20	0.969	0.291	1.52	0.0310
30	0.566	0.102	0.635	0.135
40	0.209	0.100	0.161	0.0690
50	0.0667	0.00210	0.0373	0.0337
60	0.0203	0.00240	0.0134	0.0116
70	0.00292	0.00124	0.00360	0.00180
$E_0 = 50.0\text{eV}$				
2.5	281	229	411	329
5	13.3	88.4	117	73.2
10	1.49	8.01	13.7	3.85
15	1.27	0.915	3.07	0.0310
20	1.02	0.229	1.17	0.306
30	0.502	0.129	0.562	0.198
40	0.111	0.0156	0.110	0.0323
50	0.0317	0.00138	0.0193	0.0152
$E_0 = 80.0\text{eV}$				
3	97.3	201		
5	12.2	74.9		
10	1.04	3.06		
15	2.25	0.606		
20	1.28	0.452		

Error limits for the derived PDCS are not shown in the figures but are taken to be the square root of the sum of the squares of errors contributed by the EICP and absolute DCS measurements. For the most part, the overall error is dominated by uncertainty in the absolute DCS. The resulting uncertainty in the absolute DCS measured by Wang et al is quoted to be  $\pm 25\%$  while the uncertainty in the absolute DCS of Jensen et al is quoted as  $\pm 50\%$ . Associating a nominal uncertainty of  $\pm 10\%$  with the coherence parameters  $\lambda$  and  $L_{\perp}$ , we estimate that the error in the relative PDCS is  $\pm 11\%$  for  $E_0 = 10\text{eV}$  and  $E_0 = 20\text{eV}$ , and  $\pm 18\%$  for  $E_0 = 37\text{eV}$ ,  $50\text{eV}$  and  $80\text{eV}$ . Using error propagation, we calculate that the absolute PDCS is uncertain by  $\pm 27\%$  for  $E_0 = 10\text{eV}$  and  $20\text{eV}$  and uncertain by  $\pm 51\%$  for  $E_0 = 37\text{eV}$ ,  $50\text{eV}$  and  $80\text{eV}$ .

Comparison of the derived, experimental,  $\text{PDCS}(M^c)$  with theory reveals excellent agreement with the UDWA approach of Clark et al (Clark1989) except at the lower impact energies ( $E_0 = 10\text{eV}$  and  $E_0 = 20\text{eV}$ ). The RDW theory of Srivastava et al (Srivastava1992), however, seems to overestimate these PDCS at most impact energies although qualitative agreement with the angular behavior is found. Similar conclusions can be drawn in the comparison of theory with derived  $\text{PDCS}(M^n)$  behavior. The UDWA calculations agree remarkably well with experimental  $\text{PDCS}(M^n = +1)$  at all impact energies studied while RDW calculations again overestimate this cross section. The  $\text{PDCS}(M^n = -1)$  seems to provide a more critical test of theory than the  $\text{PDCS}(M^n = +1)$ . At  $E_0 = 20\text{eV}$ , the striking dip in  $\text{PDCS}(M^n = -1)$  is only minimally apparent in the calculations. While this lack of agreement is understandable at low impact energy, ( $E_0 = 20\text{eV}$ ), a similar, less severe, discrepancy is observable at  $E_0 = 50\text{eV}$ . We note that the

theoretical calculations presented in the figures were not convoluted with the finite angular resolution associated with measurements of the DCS and EICP.

Finally, we point out that comparison of the two first-order perturbative theories with experiment leads to an interesting observation. Earlier work on the EICP for Ba( $6^1P_1$ ) excitation and the present results for the  $\lambda$  parameter show that the RDW theory gives excellent agreement (at least at the higher impact energies) with the data, surpassing the predictive power of the UDWA theory. On the other hand, in many cases, the RDW partial differential cross sections systematically overestimate the measured PDCS, especially at larger scattering angles, while the UDWA results give good quantitative agreement with measurements. Apparently, the problem associated with RDW predictions of PDCS magnitudes disappears when appropriate ratios of the PDCS are taken to give the corresponding EICP. It seems, therefore, that successful theoretical predictions of the EICP do not necessarily guarantee successful theoretical predictions of cross sections. We conclude that experimental determinations of both EICP and absolute cross sections are required in order to adequately test any given theory.

#### 4.7 Conclusion

We have measured charge-cloud alignment parameters  $P_l^+$  and  $\gamma$  for the collisional excitation of  $^{138}\text{Ba}$  ( $6s6p\ ^1P_1$ ) state at electron-impact energies  $E_0 = 10\text{ eV}, 20\text{ eV}, 36.7\text{ eV}, 50\text{ eV}$  and  $80\text{ eV}$  and transferred angular momentum  $L_\perp$  at  $E_0 = 20\text{ eV}, 36.7\text{ eV}$  and  $50\text{ eV}$  using the superelastic-scattering technique. At each impact energy, the scattering-angle coverage has been sufficient to allow the observation of pronounced structure in the behavior of these parameters. At the higher impact energies studied (namely  $E_0 = 36.7\text{ eV}$ ,

50eV, and 80eV), minima in  $P_l^+$  are accompanied by rapid changes in the alignment angle. At lower impact energy studied ( $E_0 = 10\text{eV}$  and  $20\text{eV}$ ), the alignment-angle behavior is characterized by a generally smooth decrease with increasing scattering angle, although there is some evidence of weak structure corresponding to a somewhat more rapid variation over the narrow range of scattering angles in which  $P_l^+$  passes through a minimum. The first maximum in  $L_{\perp}$  occurs when  $P_l^+$  reaches its minimum. The angular behavior of these parameters shows pronounced structures which exhibit some similarities to predicted and observed behavior in the heavy rare gases such as the general trends observed in the  $1^1\text{S}$  to  $2^1\text{P}$  excitation in helium.

Comparison of our experimental results for the alignment-angle parameter  $\gamma$  with two different distorted-wave theories reveals generally very good agreement at all impact energies and scattering angles studied, especially in the case of the fully relativistic calculation. Agreement between experimental and theoretical results is also quite good for  $P_l^+$  at impact energies of  $E_0 = 36.7\text{eV}$ ,  $50\text{eV}$ , and  $80\text{eV}$ , and for  $L_{\perp}$  at  $E_0 = 36.7\text{eV}$ ,  $50\text{eV}$ .

Distorted wave theory (DWA) gives qualitative prediction in  $P_l^+$  at  $E_0 = 10\text{eV}$ . Both distorted-wave theories (DWA and RDW) fail completely to reproduce the observed behavior of  $P_l^+$  and  $L_{\perp}$  at  $E_0 = 20\text{eV}$ . The close-coupling calculation of Fabrikant reproduces, qualitatively, the observed  $P_l^+$  behavior in that a minimum of correct depth and width is predicted. The calculated minimum, however, is shifted to a larger scattering angle with respect to the observed minimum. Similarly it also reproduces the first maximum of correct height and width for  $L_{\perp}$  which is shifted to a larger scattering angle. This theory, unlike the distorted-wave theories, also indicates the presence of weak structure in the behavior of  $\gamma$  over the region

where  $P_l^+$  falls to a minimum, although comparison with experiment again reveals only qualitative agreement.

We have combined the present results with earlier measurements of  $P_l^+$  in order to calculate  $P^+$ , the degree of polarization. Observation that  $P^+ = 1$  over the range of impact energies and scattering angles studied indicates that the Ba  $6^1P_1$  excitation is fully coherent and the role of spin dependent forces is small in this regime. This is in agreement with the predictions of available first-order perturbative theories.

The measured EICP's have been used to derive  $\lambda$  parameter. Generally, the comparison between experimental results and RDW calculations shows an excellent agreement at  $E_0 = 36.7\text{eV}$ ,  $50\text{eV}$  and  $80\text{eV}$ . UDWA only exhibits good agreement at the smaller scattering angle at these energies. At lower impact energies, all theories (UDWA, RDW and CC) are only able to qualitatively reproduce the experimentally derived  $\lambda$ .

Finally, we have used our measured and experimentally derived EICP's in combination with the absolute DCS measurements of Wang et al and Jensen et al. to yield PDCS in collision frame and nature frame. Comparison was made between derived PDCS and theoretical calculations.

In the current measurement, we have employed two techniques, namely polarization modulation spectrum method ( for  $P_l^+$  and  $\gamma$  measurement) and four-quarter spectrum method ( for  $L_{\perp}$  measurement). The former method, except for the fluorescence polarization measurement, does not require any optical polarization alignment, while the latter one, in comparison with the former, results in smaller statistical error but involves a complicated polarization alignment procedure of the retardation plate. Therefore efforts have to be made in the optical alignment to reduce measurement error due to misalignment of the optics.

## CHAPTER 5

### THE STUDIES OF ELECTRON SCATTERING EXCITATION OF $^{174}\text{Yb}$

#### 5.1 Introduction

Recently, a number of studies, both theoretical and experimental, have appeared in which inelastic electron scattering from heavy, two-electron, close-shell atoms has been investigated. Such atoms belong to the "Group II" classification of elements comprising the alkaline-earth elements in addition to the transition metals Zn, Cd and Hg. The lanthanide element Yb and the actinide element No also exhibit the same type of electronic shell structure. Electron impact excitation of these atoms provides a physically interesting contrast to the case of helium, the simplest two-electron system. The  $1s^2$  to  $1s2p$  transition in helium has been well studied and invites comparison with corresponding excitations in heavy two-electron systems. Unlike helium, however, in which LS coupling holds well, many of the heavier two-electron systems are affected by the spin-orbit interaction. In the case of Hg and Yb, for example, with atomic numbers  $Z = 80$  and  $Z = 70$ , respectively, this gives rise to "intercombination" radiative transitions connecting the  $^3P_1$  excited state to the  $^1S_0$  ground state. The ( $J = 1$ ) P states in these atoms are well described

by a linear combination of LS coupled singlet and triplet states in the so-called "intermediate" coupling scheme.

Experimental techniques in electron scattering are presently capable of generating comprehensive sets of observables with which to test theory. In addition to the measurement of the differential cross sections (DCS), methods namely, electron-photon coincidence experiments and superelastic-scattering experiments, have been developed to investigate the "fine details" of the scattering process as characterized by the electron impact coherence parameters (EICP). Because of the spin-orbit interaction in these atoms, the collisional excitation may not preserve atomic reflection symmetry. Instead of two, as in the case of barium, we need four independent EICP to describe this excitation process, namely  $P_l^+$ ,  $\gamma$ ,  $L_\perp$  and  $\rho_{00}$  (height parameter).

In comparison with the extensive body of data becoming available for rare gases like helium, detailed characterization of inelastic electron scattering from Group II elements by DCS and EICP measurements is still rather limited in the intermediate impact energy regime of 20eV to 100eV. Sohn and Hanne (Sohn1992) described EICP measurements for the  $^1S_0$  to  $^3P_1$  excitation in Hg using the electron-photon coincidence technique with both unpolarized and polarized electrons at impact energies of 8eV and 15eV. In addition, EICP for Hg  $6^1P_1$  level at 50eV impact energy have been reported by Pascual et al (Pascual1993) while DCS measurements for impact energies in the range of 7eV to 25eV have been made by Danjo et al (Danjo1993).

So far, very little experimental work has been done on ytterbium. As a representative of the rare-earth group, ytterbium has an intense and simple energy-loss spectrum because it has a closed-shell, ground level configuration with two (6s) valence electrons. Many electron energy-loss spectral features are therefore relatively straightforward to identify. Ytterbium requires the

lowest heating temperature ( about 550°C) relative to other rare-earth elements to achieve a sufficient vapor pressure. The (...6s6p  $^3P_1$ ) level (at 555.6nm) can be prepared by dye laser and thus scattering experiments with laser-excited Yb atoms are feasible to. The relatively simple level structure of ytterbium allows us to resolve most of the electron collisional excitation features with our current electron spectrometer and isolate the transition we want to study. It is thus an ideal sample for cross-beam DCS measurement. Furthermore, ytterbium is a heavy atom ( $Z=70$ ) and can therefore provide a testing ground for the importance of relativistic effects ( i.e. spin-orbit coupling is nonnegligible). From a theoretical standpoint, this atom provides an interesting collision target since its shell structure has much in common with Group II atoms. Calculational approaches developed to treat electron scattering from closed shell atoms at intermediate impact energies, such as the first-order perturbative theories of Srivastava et al (Srivastava1992 and Srivastava1992b), Clark et al (Clark1989) and Bartschat and Madison (Bartschat1987) should be suitable. Structure calculations for the first excited P state of the Yb atom should not be prohibitively difficult since the single configuration (6s6p) approximation has been used with some success in calculating Yb-He and Yb-Ne interatomic potentials (Zagrebin1992). So far theoretical calculations of relativistic distorted wave approximation by Srivastava et al (Srivastava1995) and unitarized distorted wave approximation by Clark et al (Clark) are available for EICP and DCS at  $E_0 = 20\text{eV}$  and  $40\text{eV}$ . UDWA results from Clark were used for the purpose of normalization of our experimental DCS results. Shimon et al used electron-impact excitation method to measure the excitation functions of ytterbium atom and determine effective cross sections for most of the strong transitions. The intercombination line ( $6^1S_0 - 6^3P_1$ ) in ytterbium spectrum was detected.

The existence of such intense intercombination transitions clearly indicates the breakdown of LS-coupling in a ytterbium atom. Differential scattering has been studied by Kasakov and Khristoforov (Kasakov 1983) for near-threshold impact energies. The aim of this work was to investigate strong resonance features in the excitation function ( $\theta = 90^\circ$ ) for the elastic ( $\dots 6s6p \ ^1P_1$ ) and ( $\dots 6s6p \ ^3P_{0,1,2}$ ) scattering channels.

In this chapter we report the preliminary explorations into electron scattering from ytterbium atom. Coherence parameters  $P_1, P_2$  and  $L_\perp^+$  were measured by superelastic-scattering method and differential cross sections were measured by conventional cross-beam inelastic-scattering method. In Section 5.2, we will present the measurement results of coherence parameters  $P_1, P_2$  and  $L_\perp^+$  for the excitation of  $6^3P_1$  level using superelastic-scattering method. The DCS measurement results for the excitation of  $6^1P_1$  level are given in Section 5.3. In Section 5.4, some preliminary results of energy loss spectra of electron scattering from laser-excited Yb are shown.

## 5.2 Superelastic Electron Scattering from Laser-Excited $^{174}\text{Yb}(\dots 6s6p \ 6^3P_1)$

### 5.2.1 Experimental Details

For  $L_\perp^+$  measurement in the  $^{174}\text{Yb}(\dots 6s6p \ 6^3P_1)$  transition, the apparatus was identical to that described in our investigation of the  $L_\perp^+$  parameter for  $^1S_0$  to  $^1P_1$  excitation in  $^{138}\text{Ba}$  (see Section 4.3). The high-intensity electron gun was used here. The scattered electron detector was fixed in position while the electron gun was rotatable. The total energy resolution of the spectrometer

system is about 0.5eV. The operation temperature for the metal vapor beam oven is about 550°C for ytterbium.

The dye laser using Rhodamine 110 was tuned to the intercombination transition at  $\lambda = 555.6$  nm. There is no hyperfine effect for ytterbium isotope 174 ( $I = 0$ ). The isotope shifts of the intercombination line are 954.76MHz between isotope 174 and 176, and 1000.28MHz between isotope 172 and 174 (Clark1979). These isotope shifts can be easily resolved by the single mode bandwidth of our laser. The abundance for  $^{174}\text{Yb}$  is 31.81%, in comparison with 21.81% for  $^{172}\text{Yb}$  and 12.73% for  $^{176}\text{Yb}$ . Hence, we can tune our laser at isotope 174 without any contamination from other isotopes.

For  $L_{\perp}^{+}$  measurement, we still used the experimental scheme discussed in Section 4.3 to generate circularly-polarized laser light with a  $\lambda/4$  quartz retardation plate ( $\lambda/4$  at 555 nm). The same procedure as discussed in Section 4.3 was followed to align the starting direction of the fast axis of the  $\lambda/4$  to be  $45^{\circ}$  (or  $135^{\circ}$ ) with respect to the forward scattering direction so that the circularly polarized light can be obtained. The laser light struck the interaction region at an incidence direction normal to the scattering plane. The superelastic-scattering signal corresponding to laser excitation by RHC, LHC and linearly polarized laser light was detected by the channeltron and accumulated in MCS. Each spectrum contains the accumulated counts of superelastically scattered electrons corresponding to these polarization states as well as counts of background (namely, four-quarter spectrum).

We need to use Eqn. 4.2. to express  $P_1$  and  $P_2$  parameters in terms of superelastic scattering signal intensities. With  $\delta = \pi/2$ , the superelastic scattering signal intensities corresponding to  $\beta - \alpha = 0^{\circ}, 22.5^{\circ}, 45^{\circ}$  and  $67.5^{\circ}$  are

$$\begin{aligned}
I^S(0) &\propto 1 + P_l^+ \cos(2\alpha - 2\gamma) \\
I^S(\frac{\pi}{4}) &\propto 1 - P_l^+ \cos(2\alpha - 2\gamma) \\
I^S(\frac{\pi}{8}) &\propto 1 + P_l^+ \sin(2\alpha - 2\gamma) \\
I^S(\frac{3\pi}{8}) &\propto 1 - P_l^+ \sin(2\alpha - 2\gamma)
\end{aligned}
\tag{5.1}$$

where  $\alpha$  is defined as the laser polarization vector direction with respect to the forward scattering angle and  $\beta - \alpha$  is the angle between retardation plate fast axis and the laser linear polarization direction. By properly setting  $\alpha$  ( $\alpha = 90^\circ (\pm 5^\circ)$  in this case), we can use Eqn. 2.38 to express Stokes parameters in terms of superelastic-scattering signal intensities

$$P_1 = \frac{I^S(\frac{\pi}{4}) - I^S(0)}{I^S(\frac{\pi}{4}) + I^S(0)} \tag{5.2}$$

$$P_2 = \frac{I^S(\frac{3\pi}{8}) - I^S(\frac{\pi}{8})}{I^S(\frac{3\pi}{8}) + I^S(\frac{\pi}{8})} \tag{5.3}$$

In order to measure  $P_1$  and  $P_2$  parameters, we should obtain signal intensity of electrons superelastically scattered from atoms by setting the fast axis of a half-wave retardation plate to be  $\beta - \alpha = 0^\circ, 22.5^\circ, 45^\circ$  and  $67.5^\circ$ . Since the linearly polarized laser field vector rotates twice as fast as the retardation plate fast axis, the linearly polarized light with the field vectors oscillating at  $0^\circ, 45^\circ, 90^\circ$  and  $135^\circ$  with respect to the laser field vector direction is introduced at the scattering center. We mounted the half-wave retardation plate on the stepper motor driven rotator and installed a four arm chopper wheel on which arms are separated by  $22.5^\circ$  between each other.

After aligning the laser polarization direction with respect to the forward scattering direction, we can generate linearly polarized light oscillating at  $0^\circ$ ,  $45^\circ$ ,  $90^\circ$  and  $135^\circ$  (with respect to the zero scattering angle). In order to align the correct laser polarization direction, first of all, the gun was positioned at the forward-scattering direction to define the nominal zero angle. We then preset the rotator at the position which should give rise to linearly polarized light oscillating at the forward scattering direction, rotated the  $\lambda/2$  plate holder until the minimum laser-excited Yb fluorescence intensity was observed, and then locked the plate holder with the rotator. In this position, laser polarization direction at the collision center was aligned along the forward scattering direction. Now the four segments of the spectrum correspond to the signal intensity of electrons superelastically scattered from atoms excited by linearly polarized laser light with the polarization directions at  $0^\circ$ ,  $45^\circ$ ,  $90^\circ$  and  $135^\circ$  with respect to the forward-scattering direction.

The same procedure as mentioned in Chapter 4 was followed to calibrate impact energy and forward scattering angle. Impact energy was calibrated against He  $2^2S$  resonance and the zero scattering angle was determined by monitoring the symmetric superelastic signal to the left and the right. The superelastic-scattering experiment began with accumulation of an energy loss spectrum at an impact energy  $E_0^S = E_0 - \Delta E$  until the superelastic-scattering feature in  $^3P_1 - ^1S_0$  deexcitation transition was strong enough to be located. We then locked the electron spectrometer at energy loss of  $-2.23\text{eV}$  — the  $^3P_1 - ^1S_0$  superelastic-scattering feature and accumulated the scattering signal in different laser polarization directions. We found that the superelastic-scattering intensity for this transition is considerably lower than that of the  $^1P_1 - ^1S_0$  transition in barium. Thus a longer accumulation time was

needed to overcome poor signal to noise ratio. The typical count rate at  $10^\circ$  scattering angle was about 20Hz.

## 5.2.2 Results and Discussions

The designation of ytterbium configurations and their energy levels are given by (Martin1978) and Table 5.1 lists some of the features. The energy levels of  ${}^3P_{0,1,2}$  ( $4f^{14}(1S)6s6p$ ) are 2.14, 2.23 and 2.44eV, respectively.

Coherence parameters  $P_1$ ,  $P_2$  and  $L_1^+$  were extracted from available superelastic-scattering signal using Eqn. 5.1, 5.2 and 4.8, respectively. All measured coherence parameters are listed in Table 5.2. Figure 5.1(a) and 5.2 (a) show the angular behavior of  $P_3$  ( $P_3 = -L_1^+$ , see Eqn. 2.39) for incident electron energies of  $E_0^S = 17.77\text{eV}$  and  $37.77\text{eV}$ , respectively, measured in superelastic-scattering experiments. Part (b) and (c) of Figure 5.1 and 5.2 are results of  $P_1$  and  $P_2$  parameters for incident electron energies of  $E_0^S = 17.77\text{eV}$  and  $37.77\text{eV}$  respectively. From  $P_1$  and  $P_2$  parameters,  $P_1^+$  was obtained and plotted in Figure 5.3. The superelastic scattering is related, by time-reversal, to corresponding inelastic excitations occurring at impact energies  $E_0 = 20.0\text{eV}$  and  $40.0\text{eV}$  respectively.

The  ${}^3P_1$  transition in ytterbium at  $\lambda = 555.6\text{nm}$  is very close to the specified wavelength  $\lambda = 555\text{nm}$  for the  $\lambda/4$  retardation plate we used. So we can consider it as a "perfect" quarter-wave plate ( $\cos\delta = 0$ ) and ignore its deviation from  $\delta = \pi/2$  phase retardation.

This transition is spin-forbidden ( $\Delta S \neq 0$ ) which results from the spin-exchange interaction. When the projectile electron penetrates deep into the target atom during the collision, it may exchange spin with one of the target electron with opposite spin orientation. This can results in the spin flip of the

Table 5.1. List of ytterbium spectral features.

Ground state  $(1s^2 2s^2 2p^6 3s^2 3p^6 3d^{10} 4s^2 4p^6 4d^{10} 5s^2 5p^6) 4f^{14} 6s^2 \ ^1S_0$   
 Ionization energy  $6.25394 \pm 0.00003 \text{ eV}$

Configuration	Term	$J$	Level (eV)
$4f^{14}(^1S)6s6p$	$^3P$	0	2.14
$4f^{14}(^1S)6s6p$	$^3P$	1	2.23
$4f^{14}(^1S)6s6p$	$^3P$	2	2.44
$4f^{14}(^1S)6s6p$	$^1P$	1	3.11
$4f^{14}(^1S)5d6s$	$^1D$	2	3.42
$4f^{14}(^1S)6s7s$	$^1S$	0	4.26
$4f^{14}(^1S)6s7p$	$^3P$	1	4.73
$4f^{14}(^1S)6s7p$	$^1P$	1	5.03
$4f^{14}(^1S)6s7p$	$^3P$	1	5.41

Table 5.2. Summary of measured EICP obtained by superelastic-scattering of electrons and experimentally derived EICP at impact energy  $E_0^S$  ( $E_0 - 2.23\text{eV}$ ). The uncertainties in the last digits are given in parentheses.

$$E_0^S = 17.76\text{eV} \quad (E_0 = 20.0\text{eV})$$

$\theta$ (deg)	$P_1$	$P_2$	$P_3(-L_1^+)$	$P_l^+$	$\gamma$
5	-0.68(4)	-0.45(9)		0.81(8)	
10	-0.84(6)	-0.07(10)	-0.17(3)	0.85(7)	
15	-0.71(17)	-0.16(27)	-0.21(3)	0.73(23)	
20			-0.23(5)		
30			-0.33(7)		
40			-0.35(10)		
50			-0.50(33)		

$$E_0^S = 37.76\text{eV} \quad (E_0 = 40.0\text{eV})$$

$\theta$ (deg)	$P_1$	$P_2$	$P_3(-L_1^+)$	$P_l^+$	$\gamma$
5	-0.85(3)	-0.29(8)		0.90(5)	
6			-0.16(2)		
9			-0.19(3)		
10	-0.82(7)	0.16(12)		0.83(8)	
14			-0.33(4)		
15	-0.58(30)	0.54(37)		0.80(48)	
17.5	-0.27(16)	0.45(25)		0.52(29)	
19			-0.63(11)		
20	-0.12(29)	0.30(50)		0.33(58)	
24			-0.51(29)		
29			-0.45(22)		

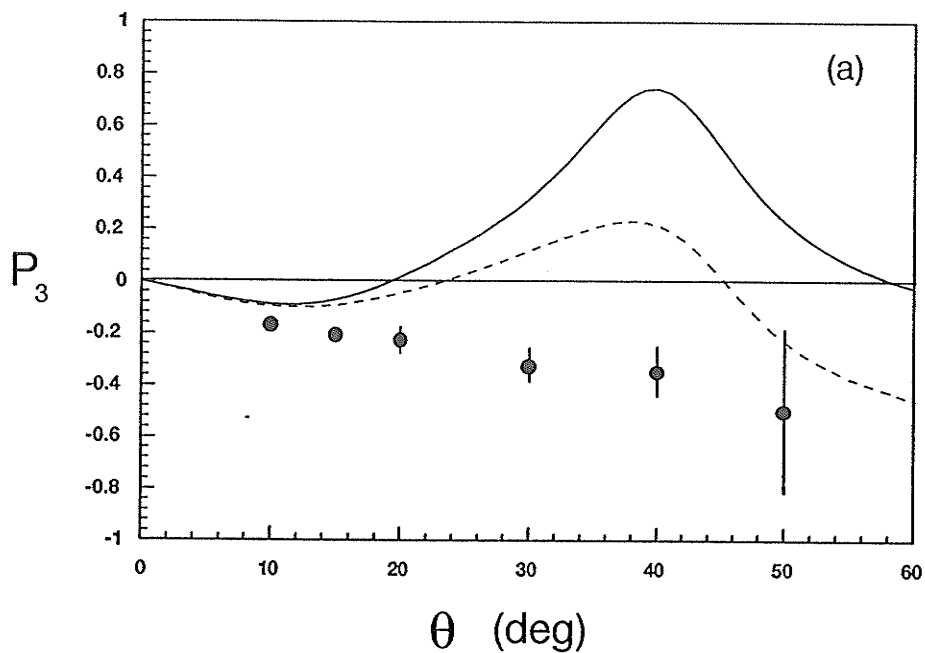
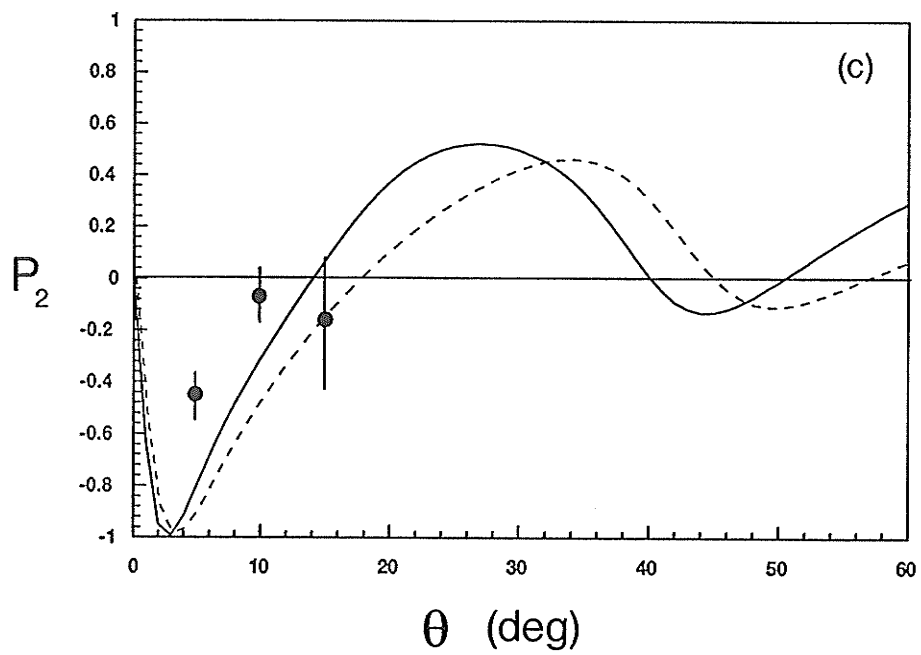
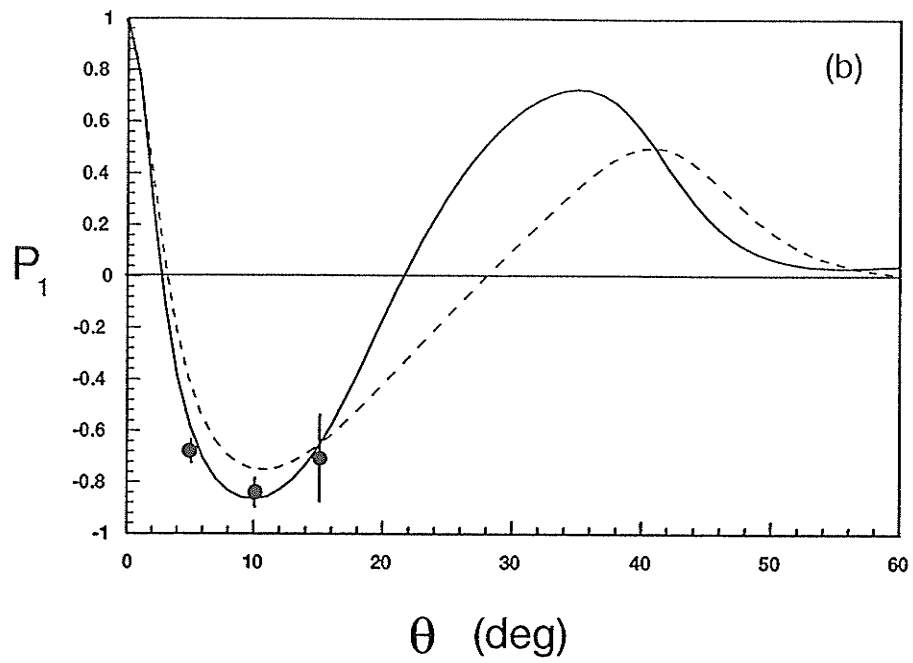


Figure 5.1. (a) Comparison of the measured  $P_3$  ( $-L\Delta$ ) parameter (circles with error bars) with UDWA calculations of Clark et al. (Clark) (solid curve), and RDW calculations of Srivastava et al. (Srivastava1995) (dashed curve). The measurements were obtained in superelastic-scattering experiments involving incident electrons with kinetic energy  $E\delta = 17.77\text{eV}$ , while the calculations describe an inelastic collision involving incident electrons with kinetic energy  $E_0 = 20\text{eV}$ . (b) Same as (a) except for  $P_1$  parameter. (c) Same as (a) except for  $P_2$  parameter.



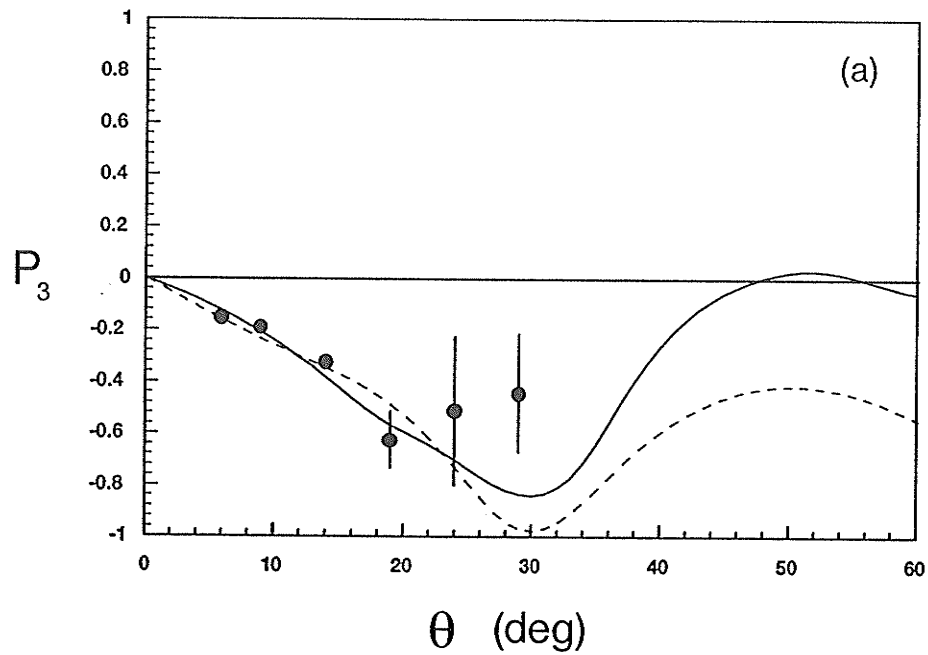
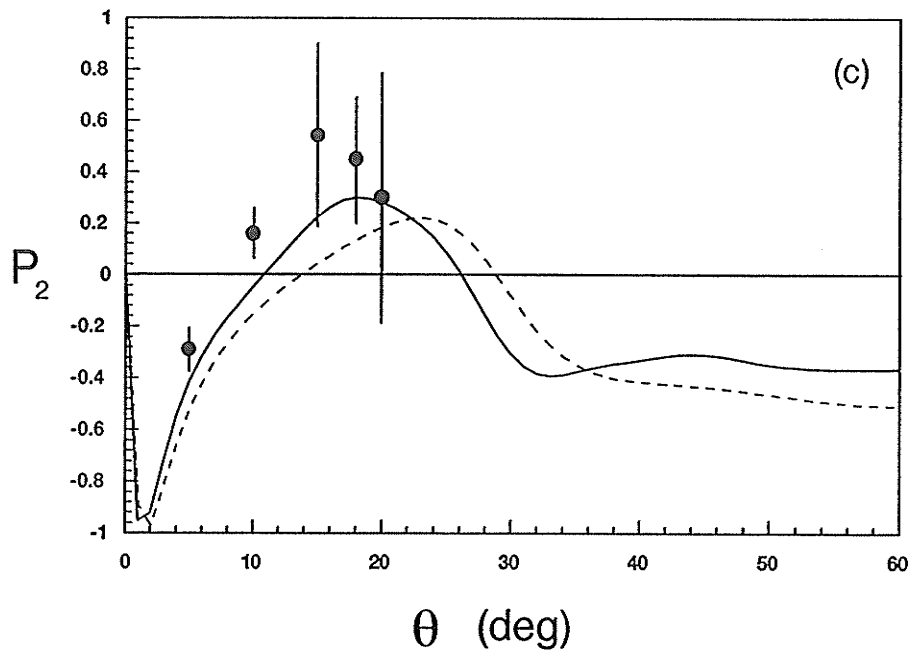
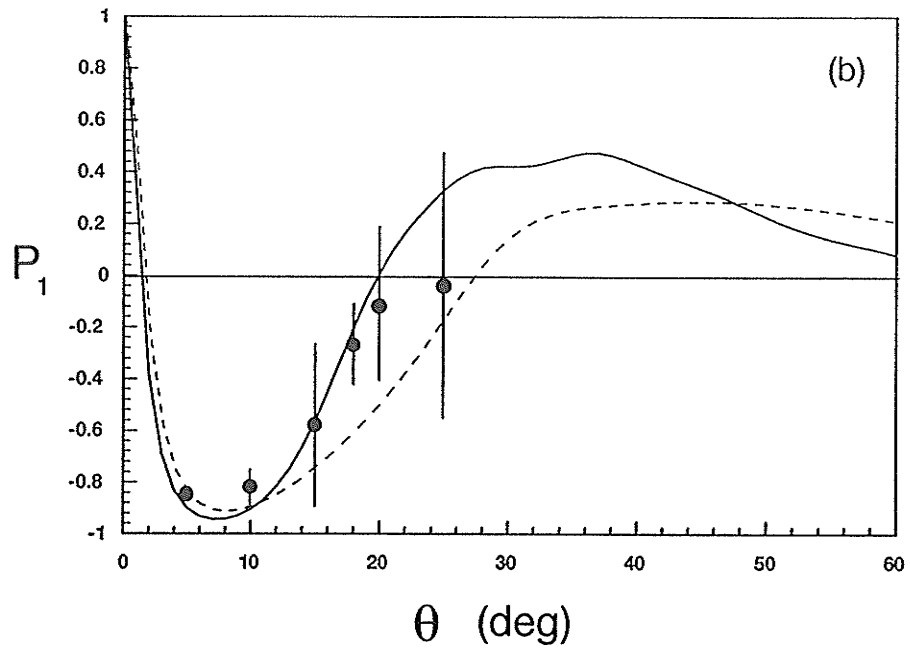


Figure 5.2. (a) Comparison of the measured  $P_3$  ( $-L1$ ) parameter (circles with error bars) with UDWA calculations of Clark et al. (Clark) (solid curve), and RDW calculations of Srivastava et al. (Srivastava1995) (dashed curve). The measurements were obtained in superelastic-scattering experiments involving incident electrons with kinetic energy  $E_0^s = 37.77\text{eV}$ , while the calculations describe an inelastic collision involving incident electrons with kinetic energy  $E_0 = 40\text{eV}$ . (b) Same as (a) except for  $P_1$  parameter. (c) Same as (a) except for  $P_2$  parameter.



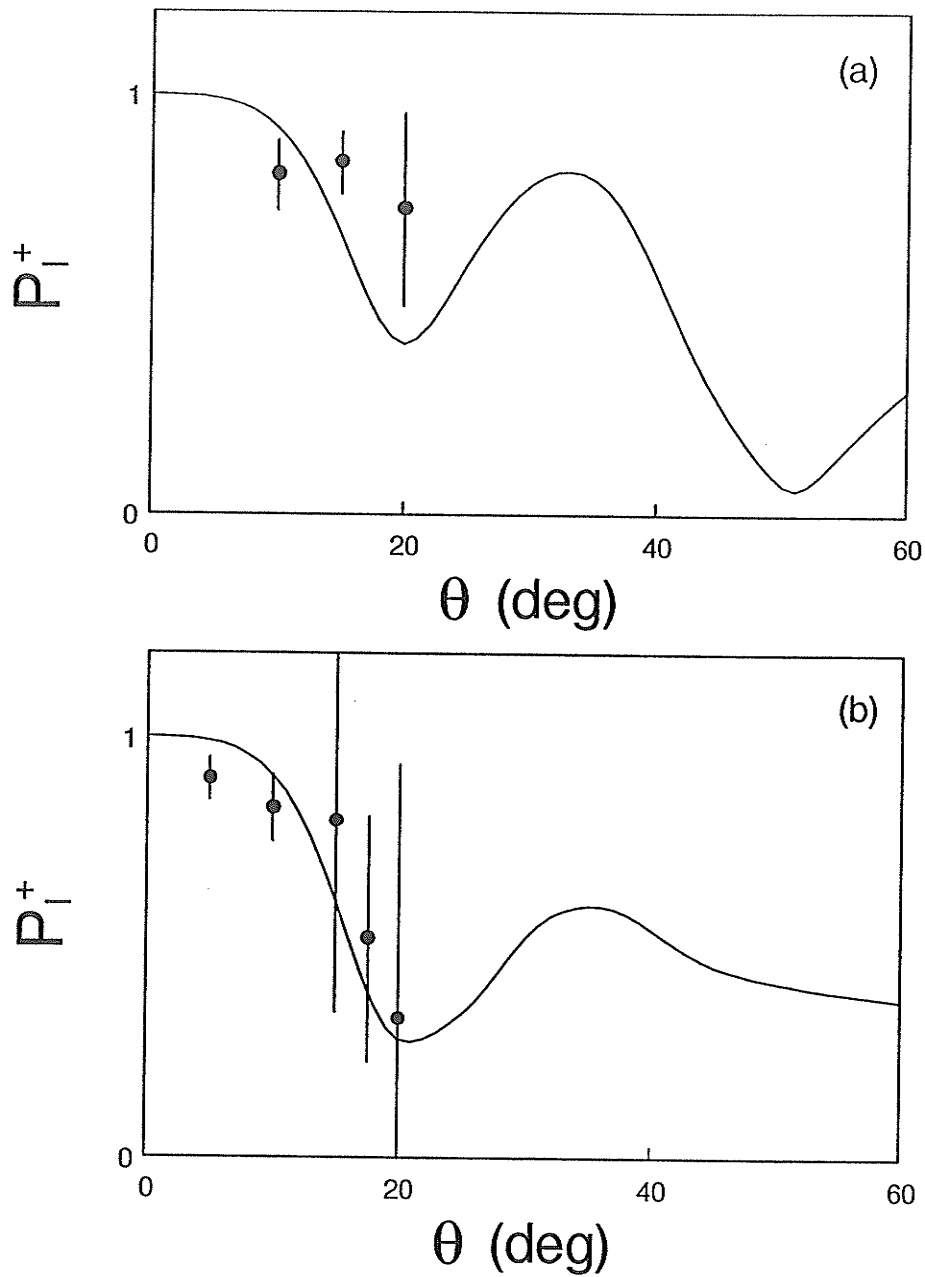


Figure 5.3. (a) Experimentally derived values of the  $P_l^+$  parameter (circles with error bars) at an impact energy of  $E_0 = 20$  eV. The full curve represents the UDWA calculation of Clark et al (Clark). (b) Same as (a) except  $E_0 = 40$  eV.

projectile electron. The exchange interaction is short range in nature because it is confined to a volume roughly the size of the charge-cloud probability density of the atom. Thus spin-exchange effects are significant for scattering at small impact parameters, i.e., scattering by larger angles. (Impact parameter is defined as the closest distance of approach of an electron to the target, if the particles would be incapable of interaction). At low electron impact energies ( within a few eV of threshold), spin-forbidden transitions actually dominate the energy loss spectra in most cases. However, the cross sections for optically allowed transitions increase at intermediate electron energies and peak at about 10 times the threshold energy and then decrease gradually.

Hall and Read (Hall1984) discussed collisions involving very small impact parameters, in which the projectile electron comes close enough to the target for electron exchange to become possible. This process can cause a singlet-triplet transition and is favored at low impact energy and large scattering angle that correspond to deep penetration of projectile electron and longer interaction time between target atom and electron. Suppose that a two-electron atom is initially in a singlet state ( $S = 0$ ), with its two valence electrons having spin opposed ( $m_1 = 1/2, m_2 = -1/2$ ). If the projectile electron has spin up ( $m_3 = 1/2$ ) and exchanges roles with  $m_2$ , the atom will be left in a triplet state ( $S = 1$ ) with ( $m_1 = 1/2, m_2 = 1/2$ ), while the scattered electron has spin down ( $m_3 = -1/2$ ). Therefore, spin-exchange effect results in spin-flip of the projectile electron and the change of multiplicity of the target atom.

At  $E_0 = 20\text{eV}$ , Both UDWA and RDW methods totally fail by predicting  $L_1^+$  to be negative sign at medium scattering angles between  $20^\circ$  and  $50^\circ$ . It is not surprising to see that theory does not work well at low impact energies. We note that, as in all cases of electron impact excited s to p

transitions reported so far, for any atom, the  $L_{\perp}^{+}$  parameter is positive at small scattering angles. In particular, this behavior has been observed in the analogous  $^1S_0$  to  $^3P_1$  excitation of Hg at low impact energy of 8eV (Sohn1992). Aspects of the "universal" behavior of  $L_{\perp}^{+}$  with scattering angle, for s to p excitations, have been discussed in Chapter 4 (also refer to Lin et al (Lin1989)). However, the theoretical calculations do reproduce  $P_3$  at  $E_0 = 40\text{eV}$  with reasonable agreement.

It is interesting to observe the difference between the angular behavior of  $L_{\perp}^{+}$  for the  $^1S_0$  to  $6^3P_1$  transition in Yb and the corresponding  $L_{\perp}^{+}$  behavior in the Ba  $^1S_0$  to  $6^1P_1$  excitation. They distinguish each other in that the former one is optically forbidden transition while the later one is optically allowed. Barium provides an interesting, comparative system since LS coupling gives a good description of the electron collision dynamics involved in excitation of the  $6^1P_1$  state, despite the rather large atomic number ( $Z = 56$ ) of this atom, and the excitation energy of the Ba  $6^1P_1$  state is very nearly equal to that of the Yb  $6^3P_1$  state. Comparison of our Yb results with previous Ba measurements of the  $6^1P_1$  excitation at  $E_0 = 20\text{eV}$  (see Chapter 3) reveals striking differences. The  $L_{\perp}^{+}$  parameter in Ba exhibits an angular behavior characterized by a rise through positive values to a maximum of  $L_{\perp}^{+} = 1$  near  $\theta = 27^{\circ}$  followed by a zero crossing near  $\theta = 42^{\circ}$  and a minimum of  $L_{\perp}^{+} = -0.2$  near  $\theta = 50^{\circ}$ . Over this same range of scattering angles,  $L_{\perp}^{+}$  for the  $^1S_0$  to  $^3P_1$  excitation in Yb exhibits a slow, structureless increase through positive values to an observed value of about 0.35 at  $\theta = 40^{\circ}$ . Error limits for the  $\theta = 50^{\circ}$  data point are large, but  $L_{\perp}^{+}$  clearly remains positive at this angle. The physical origin of this radical dissimilarity in  $L_{\perp}^{+}$  behavior for these two transitions may lie in the important role electron exchange processes play in the Yb  $6^3P_1$  excitation. Although intermediate coupling holds for the Yb  $6^3P_1$

state, the triplet component predominates, as evidenced by the 555.6nm line excitation function measurement of Shimon et al (Shimon1981) which is strongly peaked at threshold ( making allowances for cascade enhancement at large impact energies). On the other hand, excitation of the Ba  $6^1P_1$  LS coupled state at  $E_0 = 20\text{eV}$  is probably dominated by direct (non-exchange) scattering that would be dynamically favored at this impact energy ( about ten times the excitation threshold) and at small scattering angles. At  $E_0 = 40\text{eV}$ , the observed  $L_1^+$  angular behavior in Yb begins to resemble the Ba data (  $E_0 = 37\text{eV}$ ) somewhat insofar as a pronounced small-angle maximum is becoming apparent. This may indicate the increasing importance of the singlet admixture in the Yb  $6^3P_1$  state to electron scattering and the less important role electron exchange processes play at higher impact energies.

Our experimental results of  $P_1$  and  $P_2$  are also compared with theoretical calculations. UDWA by Clark and RDW by Srivastava are currently available for  $P_1$  and  $P_2$  parameters at impact energies of 20eV and 40eV. Although only qualitative agreement is achieved, both theories do reproduce  $P_1$  and  $P_2$  to some extent for these impact energies, particularly  $P_1$  parameter for which theories have excellent agreement with experimental results.  $P_1^+$  parameter can be obtained from  $P_1$  and  $P_2$  by expression  $P_1^+ = \sqrt{(P_1)^2 + (P_2)^2}$ . The similar comparison for  $P_1^+$  between Ba  $6^1P_1$  excitation and Yb  $6^3P_1$  excitation also reveals that the structure of  $P_1^+$  for Yb  $6^3P_1$  excitation is rather flatter than that for Ba. It is also apparent that at  $E_0 = 40\text{eV}$ ,  $P_1^+$  behavior shows more structure than that at  $E_0 = 20\text{eV}$  and begins to resemble  $P_1^+$  for Ba. All these observations enhance our previous conclusion made for  $L_1^+$  that electron exchange processes may play important roles in the Yb  $6^3P_1$  excitation at low impact energies and that the importance of direct (non-exchange) scattering increases at higher impact energies.

When spin-orbit interaction is not negligible, the degree of polarization  $P^+$  is less than 1. So  $P^+ \leq 1$  is an indication that spin flip may take place and the total spin of the system is no longer conserved. Unfortunately, in our case it is not meaningful to present  $P^+$  due to the poor statistics of our data. However, we noted that  $P^+ = \sqrt{P_1^2 + P_2^2 + P_3^2} < 1$  has been predicted by RDW calculation of Srivastava et al (Srivastava1995). A quantitative understanding about the effects of electron exchange and spin-orbit interaction in the collisional excitation of the Yb  $6^3P_1$  level requires investigation into other EICP, notably  $\rho_{00}$  defined by Andersen et al or the  $\cos\epsilon$  parameter defined by da Paixao et al (da Paixao1980). As discussed in chapter 2,  $\rho_{00}$  represents the scattering amplitude associated with spin-flip caused by electron spin exchange or spin-orbit interaction during the collision when LS coupling breaks down and spin-orbit interaction becomes non-negligible. These scattering processes give rise to a negative reflection symmetry component of the charge cloud with respect to the scattering plane and the  $M_j = 0$  magnetic substate can be excited.  $\rho_{00}$  is thus a height parameter which characterizes the charge cloud component oscillating outside the scattering plane ( as described in Figure 2.7 ). In order to obtain information about the spin-orbit interaction, experiments involving in-plane laser beam geometry have to be carried out.

### **5.3 DCS for Electron Impact Excitation of the (...6s6p $6^1P_1$ ) Level in Yb**

#### **5.3.1 Experimental Details**

The conventional cross-beam method was used for ytterbium differential cross section measurements. Figure 5.4 shows a schematic diagram of the experimental arrangement and beam geometry at the

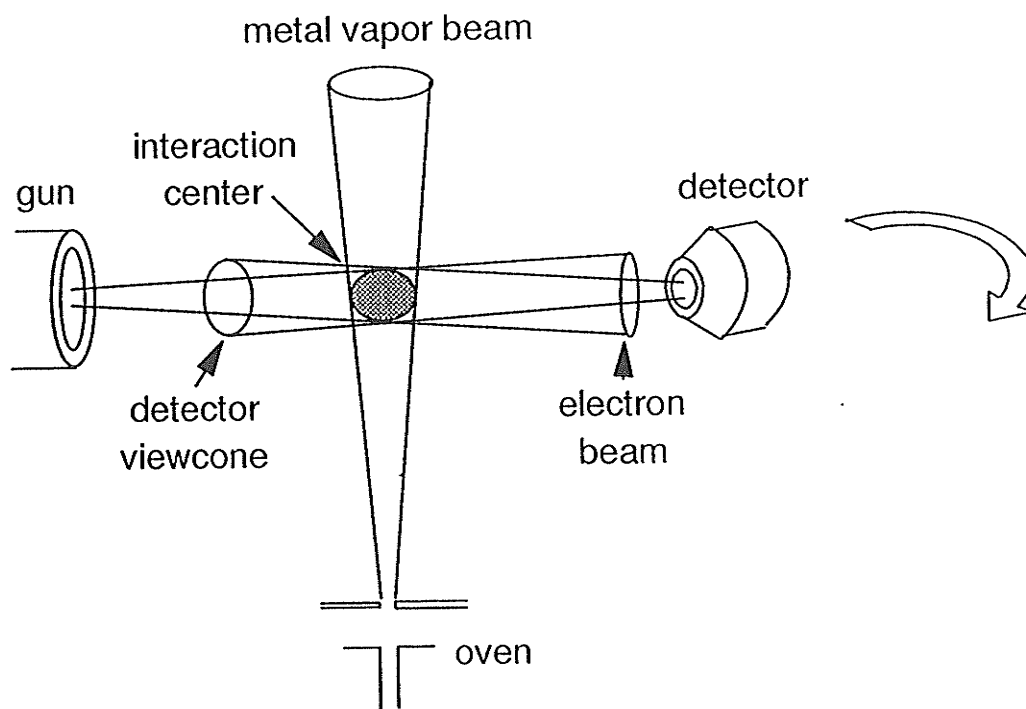


Figure 5.4. Beam geometry of a cross-beam setup for DCS measurements. The interaction region is determined by the overlap of the metal vapor beam, the electron beam and the detector viewcone. For the current experiment, The gun is fixed in position and detector is rotatable.

interaction center. An overall description of the apparatus has been given in Chapter 3. The high energy resolution gun consists of three entrance lenses, two exit lenses and a single hemispherical energy analyzer that delivers, typically, 200nA beam current with an overall energy resolution of less than 80mV (FWHM) and an angular resolution of  $2^\circ$  (FWHM).

The new design of the metal vapor beam source differs from the old design by using a tubular stainless steel crucible with an extra long orifice for beam collimation. The crucible resides in a stainless steel thermal shield with an extra small aperture to pass the metal vapor beam. Collimation of the beam is determined by the extra long orifice of 0.5in in length and 0.032in in diameter, and the 0.030in diameter aperture on the thermal shield that is located 0.5in away from the interaction region. The metal vapor beam width at the interaction region has been measured to be approximately 0.040in by means of intercepting the beam with a clean metal surface. At operating temperature, the typical target density is estimated to be  $2 \times 10^{13} \text{cm}^{-3}$ .

The definition of differential cross section has been given in Eqn. 2.17. The scattered electron intensity registered in the detector represents DCS at a certain scattering angle in some arbitrary scale which is determined by detection efficiency, the size of detector view cone, the size of interaction region, electron and target beam intensities, and so on. If we intend to measure the DCS, we must keep the denominator of Eqn. 2.17 unchanged when we change scattering angle. Therefore efforts have to be made to maintain a constant size of interaction volume, the shape of electron beam, electron beam and target beam intensities during the experiment. The establishment of a reference scattering intensity is an effective method to cancel most of these variations. In the optimized system operation condition, the electron scattering intensity at a reference angle can be used as a known

signal level for normalization. If any variation in the system operation condition occurs, the electron scattering intensity at the reference angle to the established signal level ratio is taken as the normalization factor to re-scale the scattering intensity. In this way, most of the signal intensity variation caused by system condition change can be eliminated.

In order to minimize the variation of interaction region volume during the experiment, the metal vapor beam is introduced perpendicularly to the scattering plane and the electron gun is fixed in position while the electron analyzer is attached to the rotatable table. The scattering apparatus is housed within a one layer  $\mu$ -metal magnetic shield. Residual magnetic fields at the interaction region are uniform and less than 25mG in all directions. We have estimated that the residual magnetic field can cause less than  $3^\circ$  deflection for 5eV electron beam in 30cm travel distance. This can be easily adjusted back by the deflectors in electron gun and analyzer. The deflection angle is approximately proportional to  $1/\sqrt{E_0}$  where  $E_0$  is the incident electron kinetic energy. The influence from residual field on incident electrons would be smaller for higher impact energies.

Before actual DCS measurements, the calibration of impact energy and the calibration of the zero scattering angle have to be made. The impact energy was calibrated against the known position of helium  $2^2S$  elastic scattering resonance (19.37eV) at scattering angle  $\theta = 90^\circ$ . The zero scattering angle was found by maximizing the inelastic scattering electron count rate of singlet P feature in ytterbium. The zero degree scattering angle determined in this way differed by three degrees from its value determined by optical alignment of gun and detector. Furthermore, the reference angle (at 10 degrees) was established for electron gun current normalization to minimize the influence of spectrometer operation drift during the measurement.

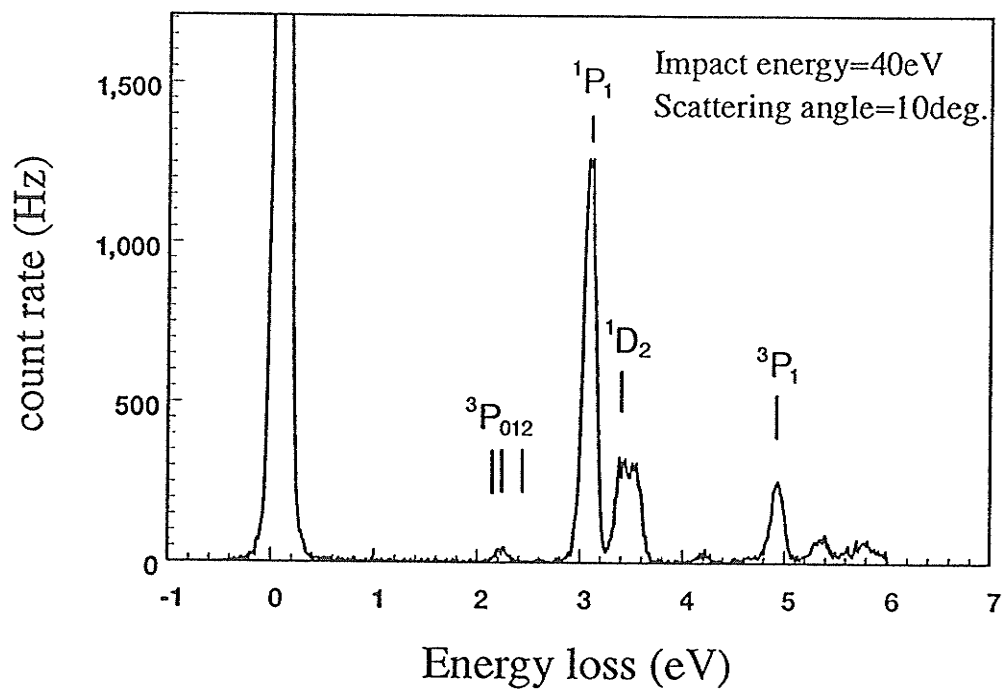


Figure 5.5. A typical energy loss spectrum of ytterbium. The spectrum was taken with impact energy of 40eV and at scattering angle of 10 degrees. The electron impact transition features were identified using Reference (Martin1978).

The incident electrons struck the ytterbium target in the direction perpendicular to the metal vapor beam and were detected at a certain scattering angle. The electron scattering intensity associated with the electron collisional excitation of  $6s6p\ ^1P_1$  level was measured as a function of the scattering angle at fixed impact energies. The measurements were performed at incident electron kinetic energies (impact energy)  $E_0 = 5\text{eV}, 10\text{eV}, 20\text{eV}, 40\text{eV}$  and  $80\text{eV}$  and at various scattering angles ranging from  $2^\circ$  to  $70^\circ$ . A typical energy loss spectrum is shown in Figure 5.5 with some features identified. Reference (Martin1978) was used for the designation of these spectral transition features. At each scattering angle and impact energy, an energy loss spectrum was accumulated. The energy loss then was locked at the peak of  $^1P_1$  feature and ratemeter reading of inelastic electron scattering signal at 10 degrees was taken as reference for normalization. The relative differential cross section was obtained by integrating  $^1P_1$  energy loss feature profile and normalizing the integration to the count rate (in frequency) of corresponding  $^1P_1$  feature at the reference angle.

### 5.3.2 Data analysis

Our measured data gives us the angular distribution of the relative differential cross section. There are several possibilities to normalize our measured relative differential cross sections into absolute scale.

In the present work, we normalized our measured relative differential cross section to the differential cross section obtained from UDWA calculation at small scattering angle. The arguments for the validity of this procedure are: 1) This calculation has worked very well to predict barium cross sections (Clark1989). 2) The angular distributions of differential cross

section for both experimental and calculational results have the similar shape. 3) Since UDWA is a Born type approximation, it should be able to reproduce experimental results at small scattering angles and at higher impact energies. These points support our conclusion that the UDWA result should be a good prediction on ytterbium DCS at higher impact energies and thus it is valid to use it to normalize our experimental results. We normalized our measured DCS at  $10^\circ$  to the UDWA calculation result at the same angle.

In crossed-beam scattering experiments the cross section is related to the measured scattered signal intensity by a complicated expression involving geometrical and instrumental functions. The cross section averaged over the instrumental angular resolution can be expressed as the product of the measured signal intensity and a proportionality function. Under real experimental conditions, we use extended scattering volumes and non-localized non-uniform target density and incident beam flux distributions. As a consequence, an angular dependence is introduced into the proportionality function. The effect of the change of scattering geometry with scattering angle is called "volume effect" and was fully investigated by Brinkmann and Trajmar (Brinkmann1981).

In present work, a modelling calculation program was developed by P. Johnson in this laboratory to calculate the correcting factor function for the volume effect in current experimental condition and instrumental geometry. An array of discrete points was setup to represent the collision centers in a finite volume. Each collision center defines a scattering angle differing from the nominal scattering angle. The effective DCS at this nominal angle will be the DCS averaged over all collision center at different true scattering angles. The averaging was weighted by the electron beam density profile, target

spatial distribution and the acceptance efficiency distribution of the detector viewcone.

The determination of the metal vapor beam size was performed by projecting the metal beam on a clean aluminum surface. The beam size was roughly determined by the distances of the interaction center and the aluminum surface from the metal source, and the diameter of the circular pattern of metal deposited on the surface. The electron beam profile was measured by reading out the beam current directly on the detector at zero scattering angle (as shown in Figure 3.19). The acceptance viewcone of the detector basically depends on the first two apertures and the spacing between them. By these procedures, the diameter of the metal vapor beam was determined to be about 0.1in (at the interaction center), the diameter of the electron beam to be 0.07in, and the acceptance angle of the detector to be  $4^\circ$ . We found that the correcting factor function for volume effect is sensitive to the size of atom beam and impact energy but is insensitive to the size of electron beam and acceptance angle. Figure 5.6 gives the angular behavior of the correcting factor for various experimental conditions.

Finally, the absolute DCS is obtained by multiplying the normalized experimental data with the corresponding correcting factor function for volume correction.

We have attempted to normalize the integral cross section of our measurement to the experimental result of effective integral cross section obtained by Shimon et al (Shimon1981). Their measurement was conducted using the method of intersecting atomic and electron beams and the photoelectric detection of the spectral line intensities. The excitation functions for spectral lines of the strongest transitions were given in their work. We discovered that their result of integral cross sections for (...6s6p

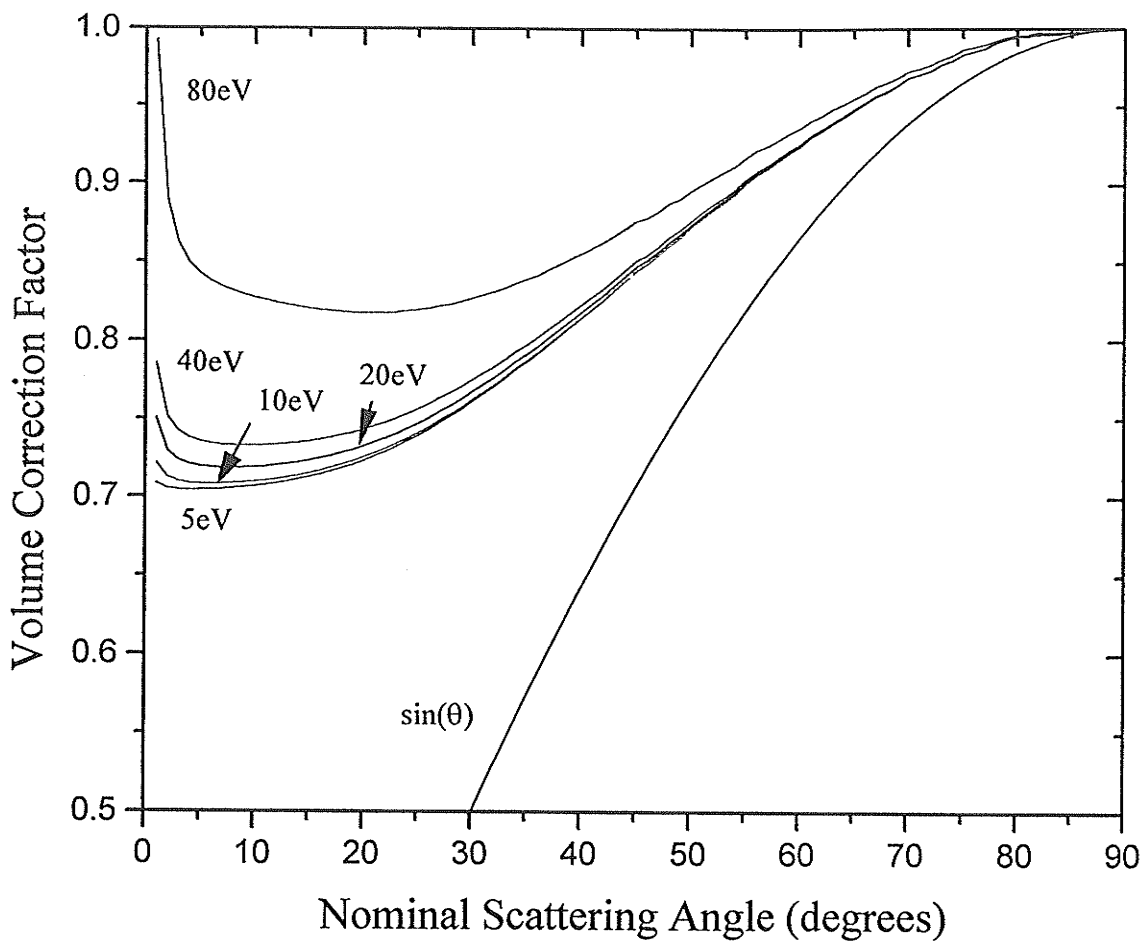


Figure. 5.6. The volume correction factor vs. electron scattering angles for impact energies 5, 10, 20, 40 and 80eV. The calculation was carried out under the condition that the diameter of the metal vapour beam = 0.1in, the diameter of the electron beam = 0.07in and the acceptance angle of the detector = 4°

$^1P_1$ ) transition at impact energies ranging from 5eV to 80eV is approximately one order of magnitude smaller than the theoretical calculational results of unitarized distorted wave approximation method (as shown on Table 5.3). A larger discrepancy is also found between their results and calculational result of relativistic distorted wave method by Srivastava et al (Srivastava and Srivastava1995). We expect that the discrepancies would be even larger if cascade contributions were taken into account in Shimon's work. We then decided not to use this normalization procedure.

### 5.3.3 Results and discussion

The normalized DCS measurement results for Yb (...6s6p $^1P_1$ ) excitation at 5, 10, 20, 40, 80eV impact energies are tabulated in Table 5.4 and graphically shown in Figure 5.7 through 5.11. The error bars only represent the statistical error from the relative DCS determination. Since measured DCS were normalized to theoretical calculations, we are unable to estimate the errors from our normalization procedure. The volume effect corrections have been applied on our experimental data. The present experimental results are compared with the unitarized distorted wave approximation of Clark et al (Clark) and the relativistic distorted wave (RDW) calculation of Srivastava et al (Srivastava).

At the low impact energy of 5eV, the angular behavior of the measured DCS only agrees with UDWA and RDW results qualitatively (Figure 5.7 ). It is not surprising to see that both first-order Born type approximations fail to predict the shape of DCS angular distribution at impact energy that is lower than Yb ionization threshold. In our previous results of electron impact coherence parameter measurement (see Chapter 4), we have demonstrated the

Table 5.3. Summary of integrated cross section obtained from UDWA calculation of Clark et al (Clark), RDW calculation of Srivastava et al (Srivastava) and measurement results of Shimon et al (Shimon1981) at different impact energies.

	integrated cross section ( $10^{-16}\text{cm}^2$ )				
	5eV	10eV	20eV	40eV	80eV
UDWA					
(Clark et al)	31.98	38.98	41.63	31.64	21.26
RDW					
(Srivastava et al)	88.07	62.51	58.53	39.96	
Experiment					
(Shimon et al)	0.663	4.333	4.612	3.252	2.070

Table 5.4. Summary of measured differential cross sections obtained by cross-beam method. Numbers in parentheses indicate the uncertainty in the last digits.

$\theta$ (deg)	$E_0$ (eV)		
	5.0	10.0	20.0
2	28.5(1.6)		754(27)
3		144(4)	
4			516(5)
5	27.6(2.2)	134(3)	409(13)
6			320(4)
7	26.3(2.7)	122(3)	
8			178(4)
9			
10	23.2(3.0)	94.6(3)	97.7(0.5)
12			
15	14.2(1.3)	38.1(1.3)	19.2(2)
20	8.68(0.82)	12.9(0.3)	5.23(0.28)
25	4.90(0.40)	4.87(0.13)	1.47(0.12)
29			

$\theta$ (deg)	$E_o$ (eV)		
	5.0	10.0	20.0
30	2.64(0.12)	2.02(0.02)	0.583(0.086)
35		0.931(0.073)	0.353(0.053)
40	1.11(0.05)	0.583(0.702)	0.245(0.035)
45			0.180(0.036)
50	0.785(0.034)	0.338(0.054)	0.133(0.046)
52			
55			0.0996(0.055)
60	0.823(0.034)		0.00820(0.00634)
65	0.733(0.083)	0.240(0.050)	0.00724(0.00659)

$\theta$ (deg)	$E_o$ (eV)	
	40.0	80.0
2	1031(87)	1.477(70)
3	785(44)	773(36)
4	547(17)	409(16)
5	347(37)	240(24)
6	234(22)	125(15)
7	156(7)	71(7)
8	101(1)	40(5)
9	66.1(1.1)	
10	42.7(1.9)	12.1(2.4)
12		4.15(0.75)
15	5.85(0.39)	1.90(0.24)
20	1.30(0.22)	0.930(0.127)
25	0.731(0.023)	0.394(0.092)
29	0.480(0.038)	
30		0.145(0.079)
35	0.239(0.054)	0.0788(0.0540)
40	0.145(0.050)	0.0514(0.0350)
45	0.0890(0.0572)	0.0345(0.0240)
50	0.0596(0.0589)	0.0229(0.0392)
52	0.0510(0.0594)	
55	0.0406(0.0582)	
60	0.0285(0.0548)	
65		

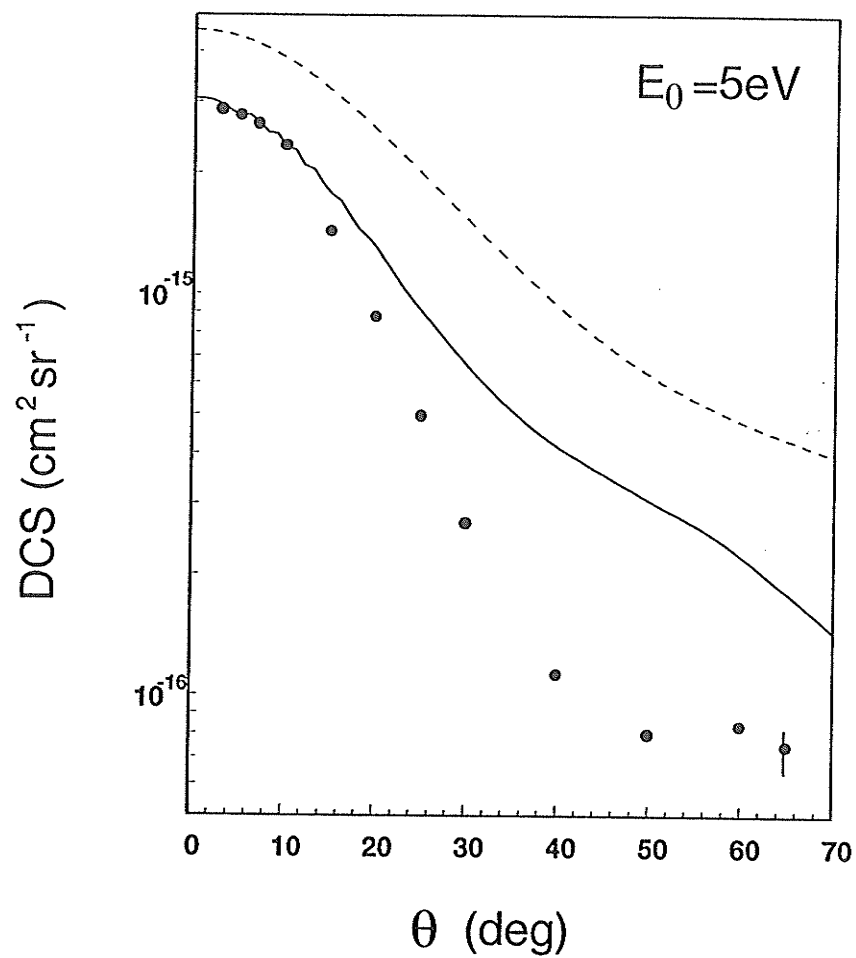


Figure 5.7. The ( $\dots 6s6p^1P_1$ ) differential cross section in Yb for an impact energy of 5eV. Experimental data (circles with error bars) have been normalized to the UDWA calculation (solid curve) of Clark et al. (Clark). Dashed curve represents the RDW calculation result of Srivastava et al. (Srivastava)

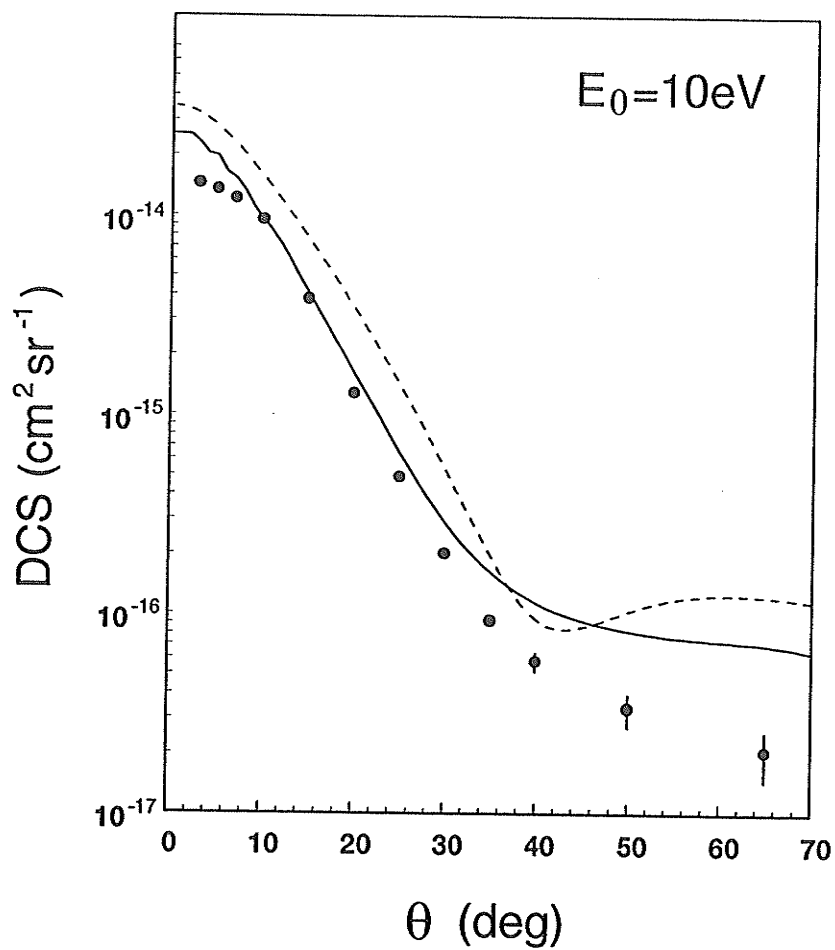


Figure 5.8. Same as Figure 5.7 except for impact energy of 10eV.

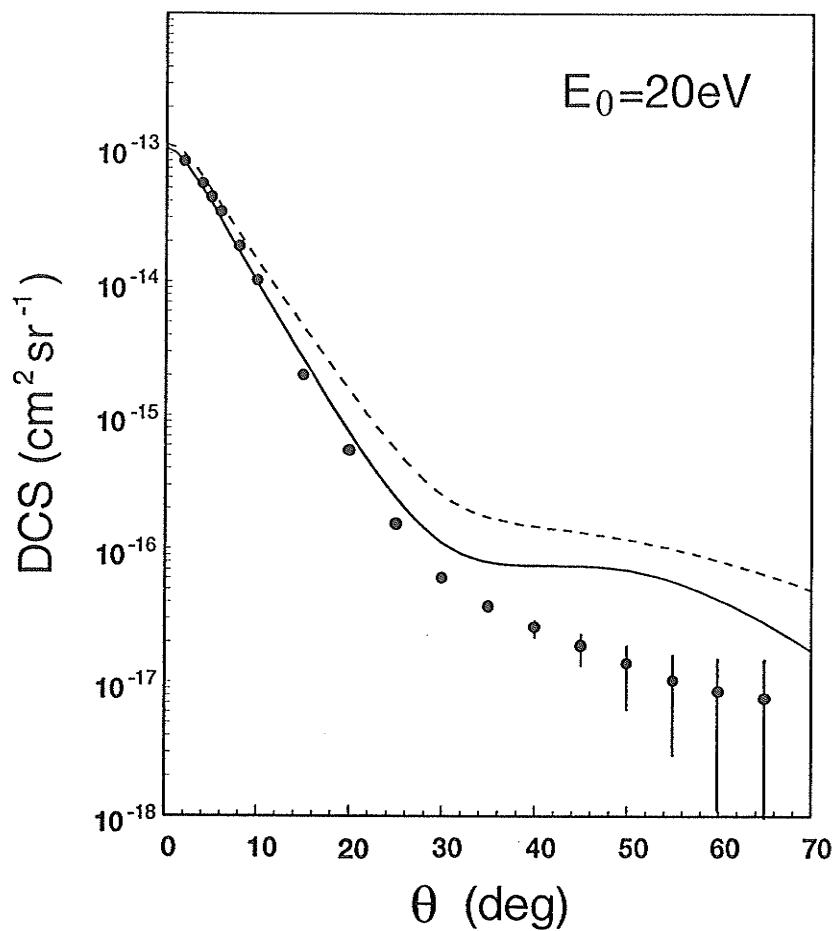


Figure 5.9. Same as Figure 5.7 except for impact energy of 40eV.

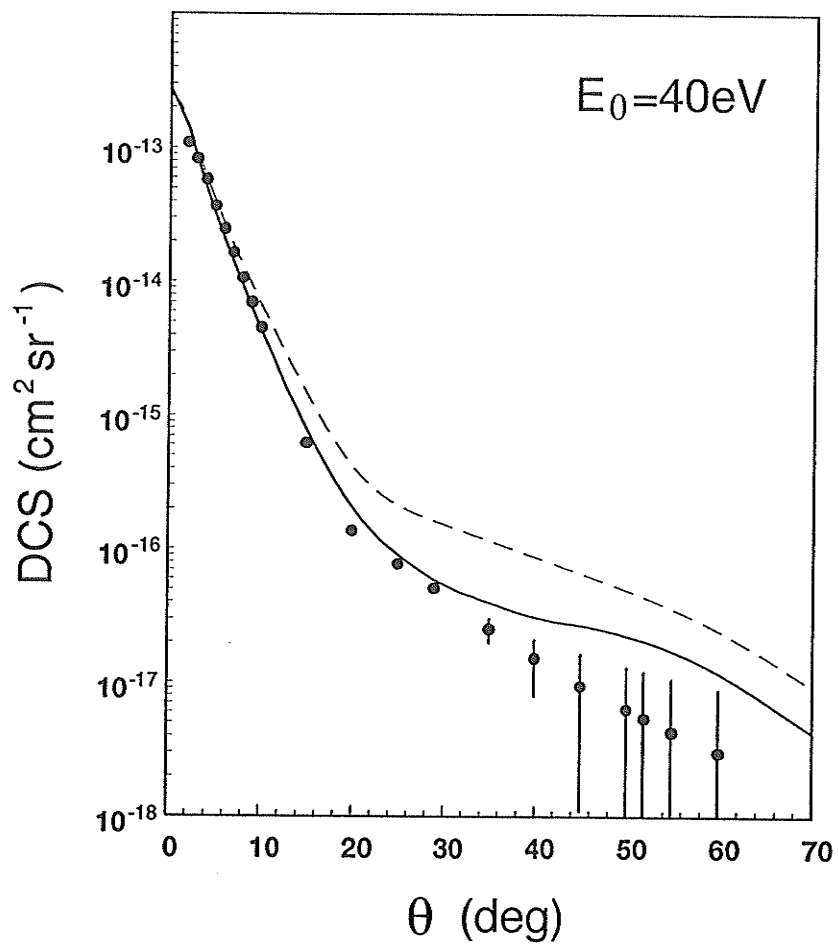


Figure 5.10. Same as Figure 5.7 except for impact energy of 40eV.

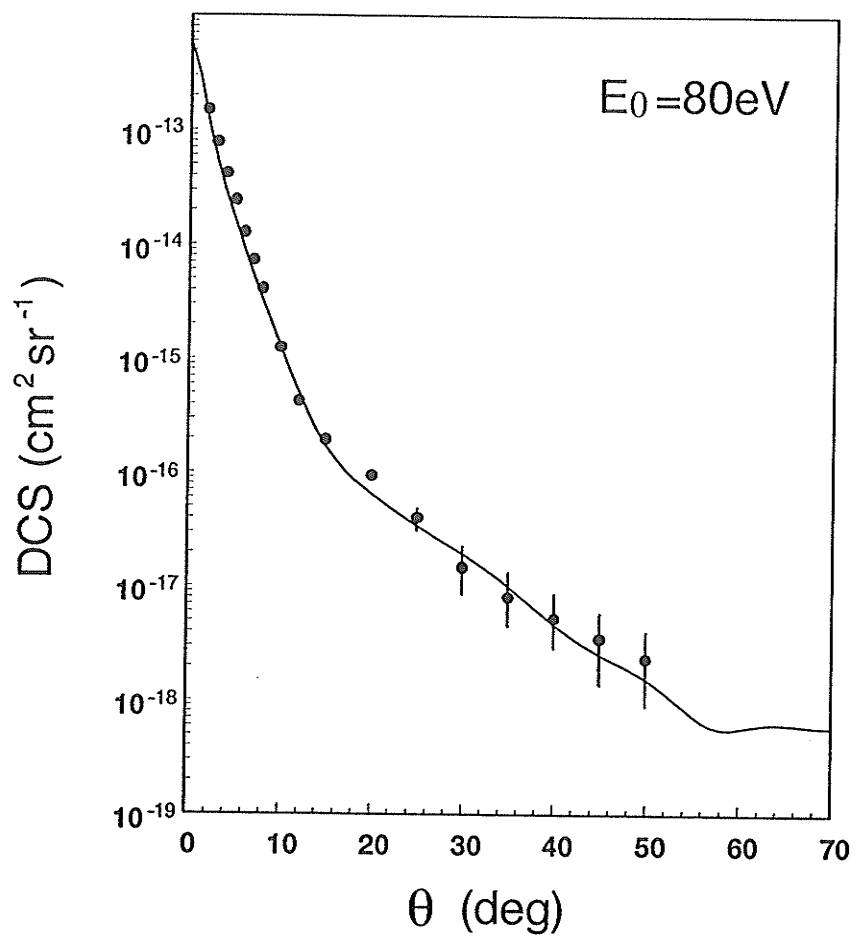


Figure 5.11. Same as Figure 5.7 except for impact energy of 80eV.

failure of both calculations to predict  $P_1^+$  and  $L_1^+$  in  $^{138}\text{Ba}$  ( $\dots 6s6p\ 6^1P_1$ ) at impact energy of 20eV.

Figure 5.8 - 5.10 exhibit good agreement between measured results and UDWA calculation results at higher impact energies of 10, 20, 40eV and at small scattering angles. But the UDWA calculation method seems to overestimate the DCS at large scattering angles. Compared with experimental results, UDWA calculation predicts deeper DCS minimum in magnitude at  $40^\circ$  for  $E_0 = 10\text{eV}$ ,  $30^\circ$  for  $E_0 = 20\text{eV}$ , and  $20^\circ$  for  $E_0 = 40^\circ$ . The same behavior was discussed by (Wang1994) in their work of DCS measurement in Ba ( $\dots 6s6p\ ^1P_1$ ) excitation, where the DWA method gave the calculated DCS to be as large as a factor of ten higher than the ones obtained in their measurement at large scattering angles and presented deeper DCS minima compared with measurement results. RDW calculation always predicts a higher DCS value than UDWA method does at all energies. But the discrepancy between two theories tends to diminish for higher impact energies. The same behavior was also demonstrated in the work by Wang et al (Wang1994). At  $E_0 = 80\text{eV}$ , the measured DCS is in excellent agreement with DCS calculated by UDWA method at all angles as shown in Figure 5.11. We attribute this to the better behavior of UDWA method at higher impact energies.

In summary, our experimental DCS show more forward peaking at higher impact energies, which reflects the general behavior of optically-allowed transitions. The agreement between experimental and theoretical DCS angular distributions is generally good but some deviations occur at large scattering angles. RDW calculation results agree with present results in shape but this method predicts higher DCS values than UDWA calculation in terms of magnitude. The extension of this type of experiments in Yb includes

the DCS measurements for  $^3P_1$  transition. Since  $^1S_0$  to  $^3P_1$  is a dipole-forbidden transition, it is interesting to see the angular behavior of its DCS in comparison with dipole-allowed  $^1S_0$  to  $^1P_1$  transition. This work would also complement our EICP measurements of ( $\dots 6s6p\ ^3P_1$ ) excitation in ytterbium.

#### **5.4 Polarization Dependent Energy Loss Spectra for Electron Scattering from Laser Excited Yb**

The electron spectrometer and metal vapor source are the same as what we used in Section 5.3 for DCS measurements. The high resolution gun was employed which can provide an electron beam with energy resolution less than 80meV and electron current of about 200nA. The laser beam was introduced to excite Yb to ( $\dots 6s6p\ ^6^3P_1$ ) level at  $\lambda = 555.6\text{nm}$  so that a considerable portion of ytterbium atoms were pumped to excited state. We are now interested in the further excitation of these atoms to higher energy level by electron inelastic collision.

A  $\lambda/4$  retardation plate rotator generates LHC, RHC and linearly polarized light alternatively at the interaction region (see Section 4.3). A four-quarter spectrum can be thus obtained which contains the energy loss spectra of laser excited atoms by LHC, RHC and linearly polarized light, and laser off spectrum, respectively.

A series of polarization dependent energy loss spectra were taken at impact energy  $E_0 = 20\text{eV}$  and scattering angle  $\theta = 10^\circ$ . Figure 5.12 shows the energy loss spectra for different polarization of excitation light and laser off spectrum with some features identified. We resorted to (Martin1978) to identify the features in the energy loss spectrum.

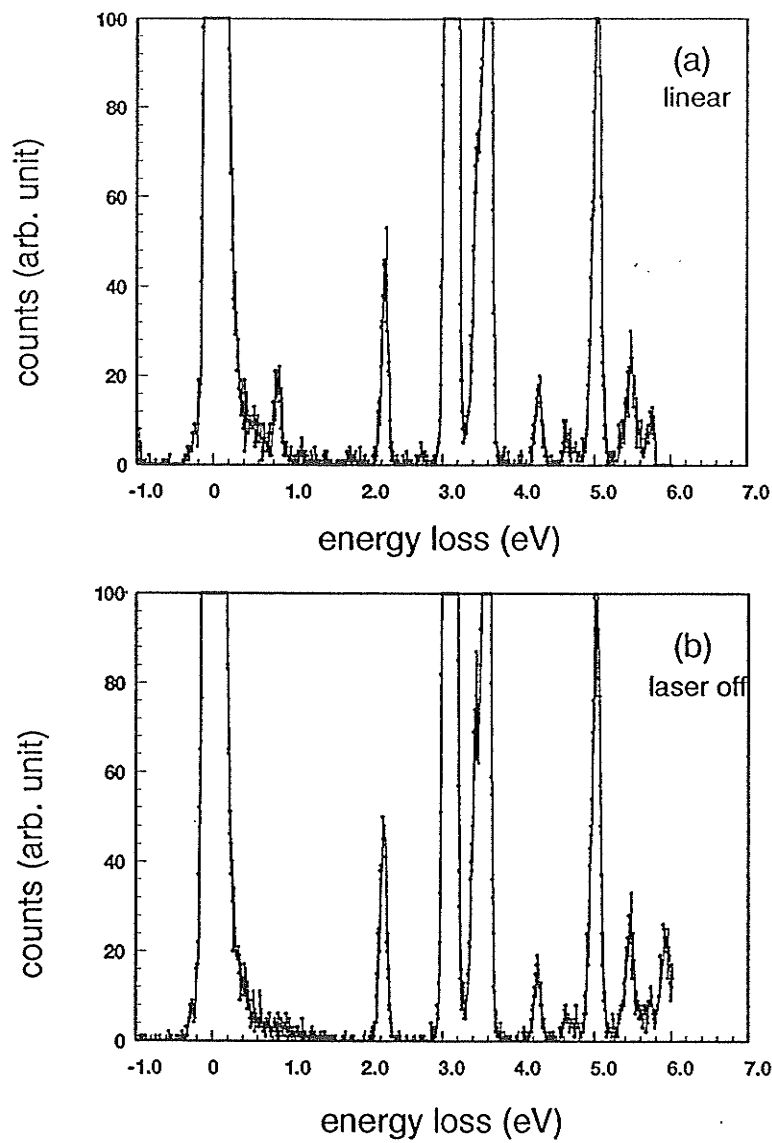
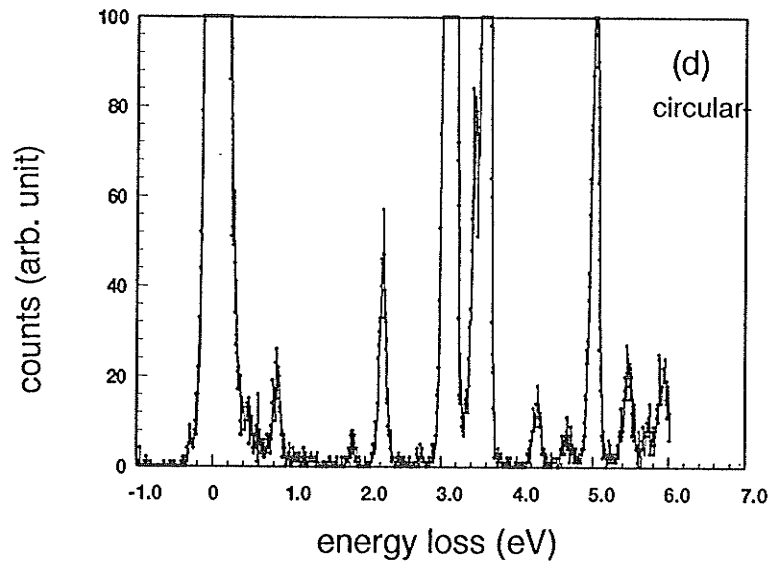
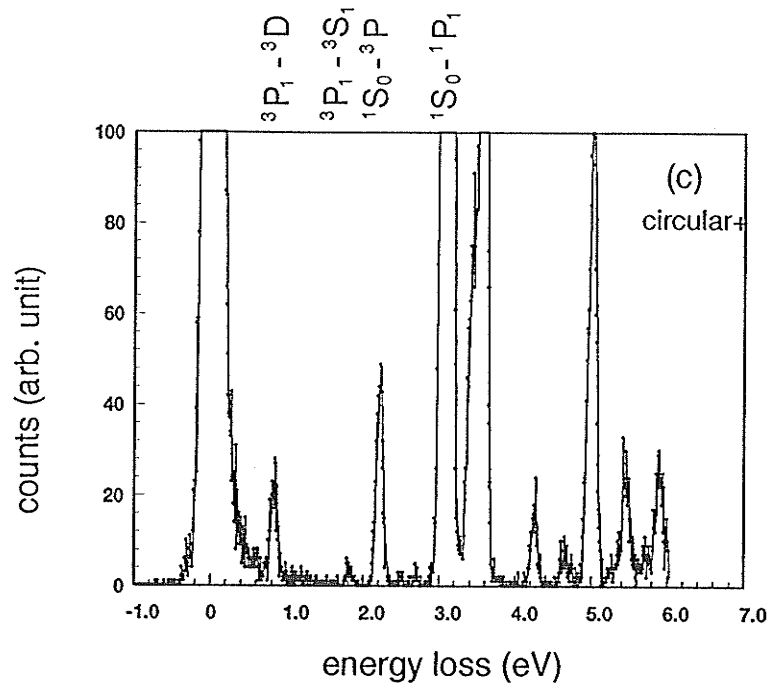


Figure 5.12. Energy loss spectra of ytterbium following laser pumping excitation to (...6s6p 3P1) level by different polarized light. Spectrum (a) results from linearly polarized light excitation, (c) and (d) result from circularly polarized light excitation. (b) is a laser-off spectrum. The identification of some features was made using Reference (Martin1978),



continuation of Figure 5.12

By comparing laser on and laser off spectra, we immediately realized that the features at energy loss of 0.83eV and 1.83eV originate in the electron collisional excitation from the excited state  $^3P_1$ , namely,  $^3P_1$  to  $^3D$  and  $^3P_1$  to  $^3S_1$  transitions. There seem to be some other features caused by laser excitation between energy loss of 2.40eV to 2.80eV, although it is very difficult to locate them due to limited energy resolution and weak signal. The laser polarization dependence is particularly obvious on  $^3P_1$  to  $^3S_1$  transition. When pumping light beam is introduced into the collision region, the atomic population of the ground state decreases. So does the scattering signal associated with ground state. We did not find any significant decrease in elastic and other inelastic features in these spectra. The reason may be that the dimension of laser beam is much smaller than that of the electron beam and metal vapor beam. Therefore the laser-atom interaction volume is only a small portion of the electron-atom interaction volume.

It is interesting to see such strong excited-state to excited state transition features. This allows us to carry out further research on this atom in the future. In particular, plans to measure excited-state to excited-state inelastic differential cross sections are underway.

## 5.5 Conclusion

Some preliminary investigations on  $^{174}\text{Yb}$  have been made with both superelastic-scattering technique and conventional inelastic-scattering cross-beam method. We have carried out the measurement of Stokes parameters  $P_1$ ,  $P_2$  and  $P_3$  at impact energy  $E_0 = 20\text{eV}$  and  $40\text{eV}$  using superelastic-scattering method. The experimental results are compared with DWA and RDW calculation results with qualitative agreement. Our results exhibit strong

characteristic of intercombination transition connecting the  $^3P_1$  state to the  $^1S_0$  state, which vigorously distinguishes itself from optically allowed transitions ( as we have seen in the case of Ba). This may indicate that the spin-orbit interaction plays an important role in this electron collisional transition which can induce the negative reflection symmetry of the charge cloud. In order to obtain the information about spin-orbit interaction, we need to employ a new laser beam geometry.

The measurement of differential cross sections in Yb yields the information about the angular behavior of  $^1P_1$  electron collisional excitation at different impact energies between 5eV to 80eV. The absolute DCS were determined by normalizing the measured integral cross section to the one from UDWA calculation. The comparison was then made between our experimental results and UDWA and RDW results. The agreement is generally good, particularly at small scattering angles and high impact energies. The DCS results exhibit forward peaking in the angular behavior at higher impact energies, which is the common angular behavior of the optical-allowed transitions.

The spectroscopic study of polarization dependent energy loss spectra in Yb gives us the information about electron scattering from laser-excited atom. The electron collisional excitations of  $^3P_1$  to  $^3D$  and  $^3P_1$  to  $^3S_1$  were identified and their dependence on laser light polarization was observed. This shows us that further research in the measurement for DCS between excited-state and excited-state is possible.

Ytterbium , as a heavy atom, provides considerable scientific interest for electron-scattering studies. We are particularly interested in the importance of relativistic effects during electron collisional excitation. New

efforts should be made for the further investigation on Yb toward this direction.

## CHAPTER 6

### OVERALL SUMMARY

In Chapter 4, we have shown the experimental results of EICP measurements for inelastic electron impact excitation of ( $\dots 6s6p\ 6^1P_1$ ) state in barium by means of time-inverse superelastic-scattering technique.  $P_l^+$ ,  $\gamma$  and  $L_{\perp}^+$  parameters have been intensively studied at various electron impact energies. We have extended scattering-angle coverage sufficiently in our experiment so that the angular behavior of these parameters shows pronounced structures which contain interesting physical meanings about the dynamic behavior of atomic charge cloud during collision. A comprehensive discussion about the behavior of  $P_l^+$ ,  $\gamma$  and  $L_{\perp}^+$  parameters has been given. Comparison of our experimental results with different distorted-wave and close-coupling calculations reveals generally satisfactory agreement. It has been pointed out that the angular behavior of these parameters exhibits some similarities to that of  $2^1P_1$  excitation in helium. Furthermore, the degree of coherence  $P^+$  has been calculated over the range of impact energies and scattering angles studied.  $P^+ = 1$  indicates that the ( $\dots 6s6p\ 6^1P_1$ ) excitation in Ba is fully coherent and the spin-dependent interaction is negligible in this regime. This conclusion verifies the predictions made by theoretical

calculation that barium  $^1P_1$  state is predominantly LS coupled and the total spin of the system is conserved during the collisional interaction.

The determination of magnetic sublevel partial differential cross sections for excitation of the Ba (...6s6p  $6^1P_1$ ) have also been presented in Chapter 4 based on the DCS measurements of Jensen et al and Wang et al in combination with our EICP measurement results of  $P_1^+$ ,  $\gamma$ ,  $L_\perp^+$  and  $P_1$ . The PDCS results have been extracted in collision frame and natural frame under the assumption that Ba  $6^1P_1$  level is a pure LS coupled singlet level. The results of our derived  $\lambda$  parameter and PDCS have been compared with those predicted by UDWA and RDW calculations with generally excellent agreement.

As a heavy, two-electron, close-shell atom, ytterbium provides a test ground for the importance of relativistic effects. We have used superelastic-scattering method to study the intercombination transitions connecting the  $^3P_1$  excited state to the  $^1S_0$  ground state in  $^{174}\text{Yb}$  at  $E_0 = 20\text{eV}$  and  $40\text{eV}$ . The Stokes parameters  $P_1$ ,  $P_2$  and  $P_3$  for electron impact excitation of (...6s6p  $^3P_1$ ) have been measured. We have seen that both RDW and DWA theories can qualitatively reproduce our results. We have noticed the different angular behavior of measured  $L_\perp^+$  and derived  $P_1^+$  for  $^1S_0$  to  $^3P_1$  transition in Yb in comparison with that in the Ba  $^1S_0$  to  $^1P_1$  transition. It has been pointed out that the origin of this dissimilarity in  $L_\perp^+$  and  $P_1^+$  for these two transitions may lie in the important role electron exchange processes play in the Yb  $^3P_1$  excitation. In the same chapter, we have discussed our DCS measurement for electron impact excitation of the (...6s6p  $^1S_0$  to  $^1P_1$ ) level in  $^{174}\text{Yb}$  using conventional cross-beam method. We have normalized our measured relative differential cross sections to the calculated DCS by UDWA theory. Both UDWA and RDW theories can predict the shape of DCS angular distribution

in a reasonable agreement with that of our measured results at small scattering angles. But some deviations occur at larger scattering angles. Finally, we have introduced our preliminary investigation on electron inelastic-scattering from laser excited  $^3P_1$  state in  $^{174}\text{Yb}$ .

Throughout the work accomplished in the electron scattering group of University of Manitoba, we have successfully demonstrated that laser-pumping (superelastic) technique, once feasible, is a more efficient means for the studies of electron impact excitation process in fine details. We have developed an electron scattering system for superelastic-scattering experiments to measure the electron impact coherence parameters in alkalis and alkaline-earth atoms. Great efforts have been made to elaborate the laser optical system, the electron spectrometer and data acquisition system. In particular, a high energy resolution gun has been designed and constructed which enable us to resolve most of the atomic electron transitions and some of the atomic fine structures.

The apparatus we have developed is sufficient to allow us to study relativistic effects (spin flip) in the electron collision process. The new schemes for superelastic-scattering experiments in this aspect include the studies of heavy atoms such as ytterbium by employing new geometries (possibly in-plane or  $45^\circ$  geometry) for pumping-laser beam direction, which will be a continuation of our previous work on Yb. Some further progresses have been made following the line of our study in Ba  $^1D_2$  to  $^1P_1$  transition including the EICP and DCS measurement using superelastic-scattering technique (Li1995c, Li1996). Differential cross sections for this transition have been measured by combining superelastic-scattering technique and constant residual energy method. Our study on electron scattering excitations between two excited states reveals a prospective research area in laser

spectroscopy. One possible experiment suitable to our current apparatus is the measurement of cross sections for these transitions.

The major obstacle to our experiments is the relatively low superelastic-scattering intensity which places limits on the effort to extend our measurement to large scattering angle. This may become a prominent problem if a high energy resolution electron source has to be used for an experiment. Radiation trapping effect plays a small, but unknown role in the measurements. The out-of-plane laser beam geometry has effectively limited the interaction region volume effect within small scattering angles and the modelling calculation for correction of this effect has been proven to be satisfactory. Nevertheless this effect does not possess physical meaning in nature and can severely deteriorate the EICP measurements at very small scattering angles. Since we do not perform any spin selection and analysis, our investigation on EICP only provides information about spin-averaged electron impact excitation process. For more complete studies of the excitation process, a spin-polarized electron source and a spin-sensitive electron detector must be employed.

In summary, the major contributions of our present work to the scientific community are: 1) We have verified the theoretical prediction that spin-dependent force is small for Ba  $^1S_0$  to  $^1P_1$  excitation and that Ba  $^1P_1$  state is predominantly LS coupled. 2) Our measurement on Yb is the first application of laser-pumping technique to the determination of EICP for excited level in which spin-dependent force may play a non-negligible role. One of the purposes of experimental investigation of EICP is to test theoretical calculations and to provide the guideline for the theorist to improve their approximation methods. The experimental results are of practical importance by themselves in the sense of providing data for other

scientific researches. We have noticed the potential applications of such knowledge to, for example, the design of metal vapour lasers (Leonard1976), the diagnosis of fusion plasmas (CIAMDA1987), and the understanding of processes occurring in supernova 1987A (McCray1989).

## REFERENCES

- (Andersen1979) N. Andersen, T. Andersen, J. O. Olsen, E. H. Pedersen, S. E. Nielsen, and J. S. Dalher, *Phys. Rev. Lett.*, 42 (1979) 1134
- (Andersen1982) N. Andersen and S, E. Nielsen, *Adv. At. Mol. Phys.*, 18 (1982) 265
- (Andersen1988) N. Andersen, J. W. Gallagher, and I. V. Hertel, *Phys. Rep.* 165 (1988) 1
- (Bartschat1987) K. Bartschat and D. H. Madison, *J. Phys. B* 20 (1987) 5839
- (Bedersen1969) B. Bederson, *Comments At. Mol. Phys.* 1 (1969) 41, 65
- (Bedersen1973) B. Bedersen, *Atomic Physics*, eds S. J. Smith and G. K. Walters, (Plenum Press, New York, 1973)
- (Bernius1988) M. T. Bernius, K. F. Man, and A. Chutjian, *Rev. Sci. Instrum.* 59 (1988) 2418
- (Bethe1957) H. A. Bethe and E. E. Salpeter, *Quantum Mechanics of One- and Two- Electron Atoms*, (Springer-Verlag, Berlin, 1957)
- (Bevington1969) P. R. Bevington, *Data Reduction and Error Analysis for the Physical Sciences*, (McGraw-Hill, New York, 1969)
- (Beyer) H. -J. Beyer, H. Hamdy, E. I. M. Zohny. K. R. Mahmoud. M. A. K. El-Fayoumin, H. Kleinpopen. J. Abdallah, Jr., R. E. H. Clark, and G. Csanak (unpublished)

- (Blum1979) K. Blum and H. Kleinpoppen, *Phys. Rep.*, 52 (1979) 203
- (Blum1980) K. Blum, F. J. da Paixao, and G. Csanak, *J. Phys.*, B13 (1980) L257
- (Blum1981) K. Blum, *Density Matrix Theory and Applications*, (Plenum Press, New York, 1981)
- (Born1926) M. Born, *Z. Phys.* 38 (1926) 803
- (Born1970) M. Born and E. Wolf, *Principle of Optics*, (Pergamon, New York, 1970)
- (Bridges1964) W. B. Bridges, *Appl. Phys. Lett.* 4 (1964) 128
- (Brinkmann1981) R. T. Brinkmann and S. Trajmar, *J. Phys. E* 14 (1981) 245
- (Brunger1989) M. J. Brunger, J. L. Riley, R. E. Scholten, and P. J. O. Teubner, *J. Phys. B* 22 (1989) 1431
- (Chutjian1979) A. Chutjian, *Rev. Sci. Instrum.* 50 (1979) 347
- (CIAMDA1987) CIAMDA 87, *An index to the literature on atomic and molecular collision data relevant to fusion research*, International Atomic Energy Agency, Vienna (1987)
- (Clark1979) D. L. Clark, M. E. Cage, D. A. Lewis, and G. W. Greenlees, *Phys. Rev. A* 20 (1979) 239
- (Clark) R. E. H. Clark and G. Csanak, private communication
- (Clark1989) R. E. H. Clark, J. Abdallah, Jr, G. Csanak and S. P. Kramer, *Phys. Rev. A* 40 (1989) 2935
- (Corr1990) J. J. Corr, P. J. M. van der Burgt, P. Plessis, M. A. Khakoo, P. Hammond, and J. W. McConkey, *J. Phys. B* 24 (1990) 1069

- (Csanak1992) B. Csanak, D. C. Cartwright, and S. Trajmar, *Phys. Rev.* A 45 (1992) 1625
- (Csanak1993) B. Csanak, D. C. Cartwright, and S. Trajmar, *Z. Phys. D* 25 (1993) 327
- (Csanak1971) G. Csanak, H. S. Taylor, and R. Yaris, *Phys. Rev.*, A3 (1971) 1322
- (Dahl1973) P. Dahl, *Introduction to Electron and Ion Optics*, (Academic Press, New York, 1973)
- (Danjo1993) A. Danjo, M. Zubek, and G. C. King, *Proceedings of the Eighteenth International Conference on the Physics of Electronic and Atomic Collisions*, Aarhus, Denmark, 1993, eds T. Andersen et al. (Aarhus University, Aarhus, Denmark, 1993), 170
- (da Paixao1980) F. J. da Paixao, N. T. Padial, G. Csanak, and K. Blum, *Phys. Rev. Lett.*, 45 (1980) 1164
- (da Paixao1984) F. J. da Paixao, N. T. Padial, and G. Csanak, *Phys. Rev.*, A 30 (1984) 1697
- (Eminyan1973) M. Eminyan, K. B. MacAdam, J. Slevin, and H. Kleinpoppen, *Phys. Rev. Lett.*, 31 (1973) 576
- (Eminyan1974) M. Eminyan, K. B. MacAdam, J. Slevin, and H. Kleinpoppen, *J. Phys. B: Atom. Mole. Phys.*, 7 (1974) 1519
- (Fabrikant1980) I. I. Fabricant, *J. Phys. B* 13 (1980) 603
- (Fabrikant1985) I. I. Fabricant, *Izv. Akad. Nauk Latv. SSR, Ser. Fiz. Tekh.* 6 (1985) 11
- (Fano1973) U. Fano and J. Macek, *Rev. Mod. Phys.*, 45 (1973) 553
- (Farrell1989) P. M. Farrell, C. J. Webb, W. R. MacGillivray, and M. C. Standage, *J. Phys. B* 27 (1989) L527
- (Grivet1965) P. Grivet, *Electron Optics*, (Pergamon, New York, 1965)

- (Hall1984) R. I. Hall and F. H. Read, *Electron-Molecule Collisions*, eds I. Shimamura and K. Takayanagi (Plenum, New York, 1984)
- (Hall1995) B. V. Hall, R. T. Sang, W. R. MacGillivray, and M. C. Standage, *Proceedings of the Nineteenth International Conference on the Physics of Electronic and Atomic Collisions*, Whistler, Canada, eds J. B. A. Mitchell, J. W. McConkey, and C. E. Brion (1995)
- (Hamdy1991) H. Hamdy, H. -J. Beyer, K. R. Mahmoud, E. I. M. Zohny, G. Hassan, and H. Kleinpoppen, *Proceedings of the Seventeenth International Conference on the Physics of Electronic and Atomic Collisions*, Brisbane, Australia, 1991, eds I. E. McCarthy et al. (North-Holland. Amsterdam, 1991), 132
- (Hamdy1993) H. Hamdy, H. -J. Beyer, M. A. K. El-Fayoumi, K. R. Mahmoud, E. I. M. Zohny, and H. Kleinpoppen, *Proceedings of the Eighteenth International Conference on the Physics of Electronic and Atomic Collisions*, Aarhus, Denmark, 1993, eds T. Andersen et al. (Aarhus University, Aarhus, Denmark, 1993)
- (Hanne1982) G. F. Hanne, Cz Szmytkowski, and M. van der Wiel, *J. Phys. B* 15 (1982) L109
- (Hanne1985) G. F. Hanne, V. Nickich, and M. Sohn, *J. Phys. B* 18 (1985) 2037
- (Hanne1988) G. F. Hanne, *Coherence in Atomic Collision Physics*, eds H. J. Beyer, K. Blum, and R. Hippler, (Plenum, New York, 1988), 41
- (Harting1976) E. Harting and F. H. Read, *Electrostatic Lenses*, (Elsevier Scientific Publishing Company, Inc., Amsterdam, 1976)
- (Henry1988) R. J. W. Henry and A. E. Kingston, *Advances in Atomic and Molecular Physics*, eds Sir D. Bates and B. Bederson, (Academic Press Inc, London, 1988), 267

- (Hecht1992) J. Hecht, *The Laser Guidebook*, (McGraw-Hill, Inc., New York, 1992)
- (Heddle1989) D. W. O. Heddle and J. W. Gallagher, *Rev. Mod. Phys.* 61 (1989) 221
- (Hertel1974) I. V. Hertel and W. Stoll, *J. Phys. B: Atom. Mole. Phys.*, 7 (1974) 570, and *J. Phys. B: Atom. Mole. Phys.*, 7 (1974) 583
- (Hertel1977) I. V. Hertel and W. Stoll, *Adv. At. Mol. Phys.*, 13 (1977) 113
- (Hummer1986) C. R. Hummer and D. J. Burns, *Phys. Rev. A* 33 (1986) 2995
- (Itikawa1986) Y. Itikawa, *Phys. Rep.* 143 (1986) 71
- (Jensen1978) S. Jensen, D. Register, and S. Trajmar, *J. Phys. B* 11 (1978) 2367
- (Kazakov1983) S. M. Kazakov and O. V. Khristoforov, *Opt. Spectrosc. (USSR)* 54 (1983) 443
- (King1972) G. C. M. King, A. Adams and F. H. Read, *J. Phys. B* 7 (1972) L254
- (Law1993) M. R. Law and P. J. O. Teubner, *Proceedings of the Eighteenth International Conference on the Physics of Electronic and Atomic Collisions*, Aarhus, Denmark, 1993, eds T. Andersen et al. (Aarhus University, Aarhus, Denmark, 1993), 150
- (Leonard1976) D. A. Leonard, *IEEE J. Quant. Elect.* 3 (1976) 380
- (Li1993) Y. Li, P. W. Zetner and S. Trajmar, *Phys. Rev. A* 48 (1993) 495
- (Li1994a) Y. Li and P. W. Zetner, *Phys. Rev. A* 49 (1994) 950
- (Li1994b) Y. Li and P. W. Zetner, *J. Phys. B* 27 (1994) L293

- (Li1994c) Y. Li, P. W. Zetner, and S. Trajmar, *J. Phys. B* 27 (1994) 4025
- (Li1995a) Y. Li and P. W. Zetner, *Proceedings of the Nineteenth International Conference on the Physics of Electronic and Atomic Collisions*, Whistler, Canada, eds J. B. A. Mitchell, J. W. McConkey, and C. E. Brion (1995) 231
- (Li1995b) Y. Li, P. V. Johnson, P. W. Zetner, G. Csanak, R. E. H. Clark, and J. Abdallah, Jr., *Proceedings of the Nineteenth International Conference on the Physics of Electronic and Atomic Collisions*, Whistler, Canada, eds J. B. A. Mitchell, J. W. McConkey, and C. E. Brion (1995) 473
- (Li1995c) Y. Li and P. W. Zetner, *J. Phys. B* 28 (1995) 5151
- (Li1996) Y. Li and P. W. Zetner, *J. Phys. B* 29 (1996) 1803
- (Lin1989) C. D. Lin, R. Shingal, A. Jain, and W. Fritsch, *Phys. Rev. A* 39 (1989) 4455
- (Macek1974) J. Macek and I. V. Hertel, *J. Phys. B: Atom. Mole. Phys.* 7 (1974) 2173
- (Madison1986) D. H. Madison, G. Csanak, and D. C. Cartwright, *J. Phys. B* 19 (1986) 3361
- (Machado1991) L. E. Machado, G. D. Meneses, G. Csanak, and D. C. Cartwright, *Proceedings of the Seventeenth International Conference on the Physics of Electronic and Atomic Collisions*, Brisbane, Australia, 1991, eds I. E. McCarthy et al. (North-Holland, Amsterdam, 1991), 127
- (Martin1978) W. C. Martin, R. Zalubas and L. Hagan, "Atomic Energy Levels - The Rare-Earth Elements", Nat. Stand. Ref. Data Ser., Nat.

- Bur. Stand. (U.S.), NSRDS-NBS 60, U. S. Govt. Printing Office,  
Washington (1978)
- (Martus1991) K. E. Martus, S. -H. Zheng, and K. Becker, *Phys. Rev. A*  
44 (1991) 1682
- (McDaniel1991) E. W. McDaniel, *Atomic Collisions*, (John Wiley & Sons,  
New York, 1991)
- (McClelland1987) J. J. McClelland, M. H. Kelley, and R. J. Celotta, *J. Phys.*  
B 20 (1987) L385
- (McGillivray1988) W. R. McGillivray and M. C. Standage, *Phys. Rep.* 168  
(1988) 1
- (McCray1989) R. A. McCray, *Invited paper of the Sixteenth  
International Conference on the Physics of Electronic and Atomic  
Collisions*, New York, U. S. A. (1989)
- (McLucas1982) C. W. McLucas, H. J. E. Wehr, W. R. McGillivray, and  
M. C. Standage, *J. Phys.* B 15 (1982) 1883
- (Meneses1990) G. D. Meneses, C. B. Pagan, and L. E. Machado. *Phys.*  
*Rev. A* 44 (1991) 4610
- (Mikosza1993) A. G. Mikosza, R. Hippler, J. B. Wang, and J. F.  
Williams, *Phys. Rev. Lett.* 71 (1993) 235
- (Moore1958) C. E. Moore, *Atomic Energy Levels as Derived from  
Analysis of Optical Spectra*, vol 3 (NBS Circular No 467)  
(Washington, DC: US Govt Printing Office)
- (Moore1983) J. H. Moore, C. C. Davis and M. A. Coplan, *Building  
Scientific Apparatus*, (Addison-Wesley Publishing Company, London,  
1983)
- (Murray1990) K. D. Murry, S. F. Gough, P. A. Neill, and A. Crowe, *J.*  
*Phys.* B 23 (1990) 2137

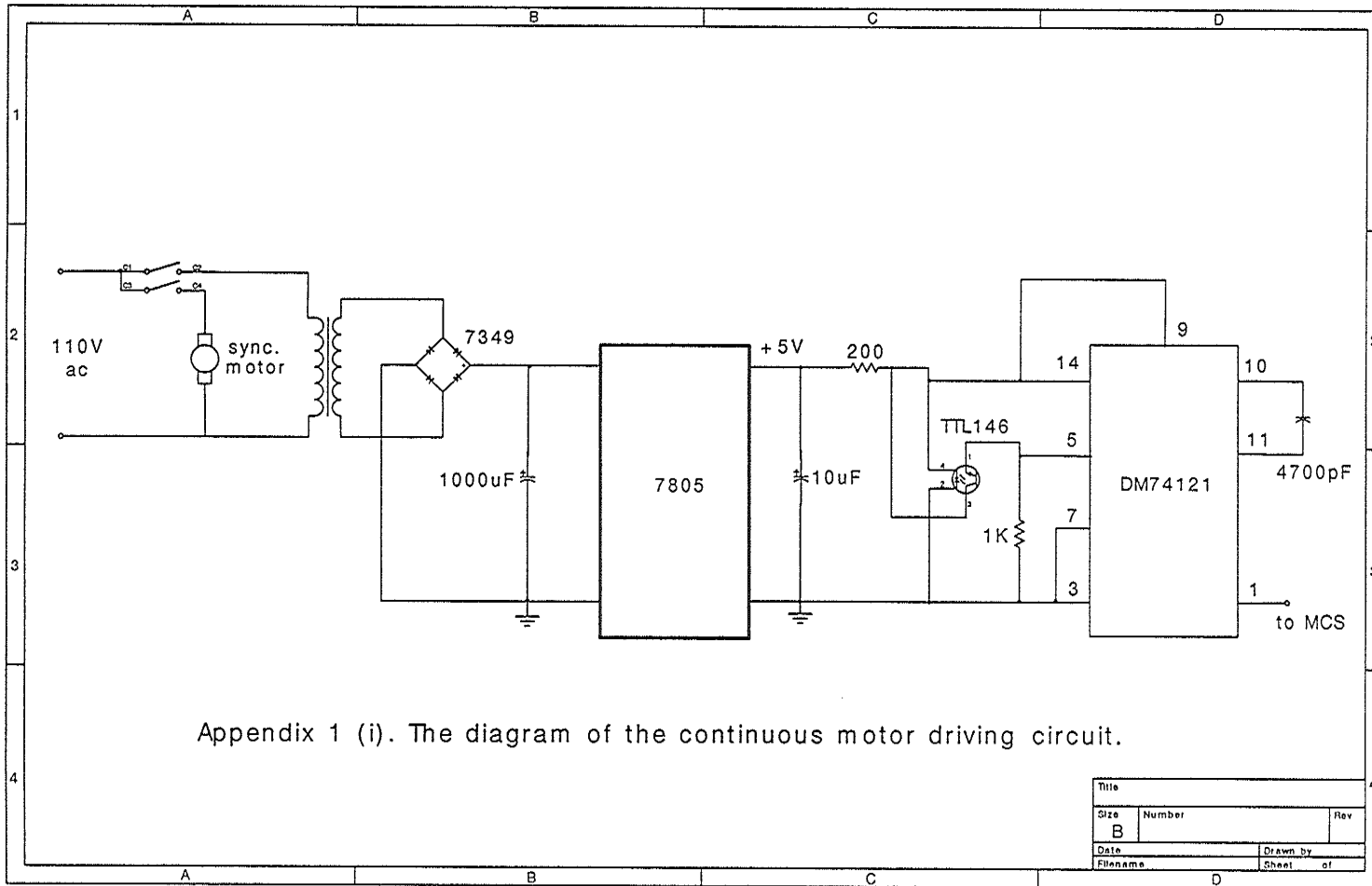
- (Percival1958) I. C. Percival and M. J. Seaton, *Phil. Trans. R. Soc. A* 251 (1958) 113
- (Pascual1993) R. Pascual, A. T. Masters, W. R. McGillivray, and M. C. Standage, *Proceedings of the Eighteenth International Conference on the Physics of Electronic and Atomic Collisions*, Aarhus, Denmark, 1993, eds T. Andersen et al. (Aarhus University, Aarhus, Denmark, 1993), 156
- (Ramsey1958) N. Ramsey, *Molecular Beams*, Oxford, Clarendon press, 1956
- (Register1983) D. F. Register, S. Trajmar, G. Csanak, S. W. Jensen, M. A. Fineman, and R. T. Poe, *Phys. Rev. A* 28 (1983) 151
- (Sang1994) R. T. Sang, P. M. Farrell, D. H. Madison, W. R. MacGillivray, and M. C. Standage, *J. Phys. B* 27 (1994) 1187
- (Scholten1988) R. E. Scholten, T. Andersen, and P. J. O. Teubner, *J. Phys. B* 21 (1988) L473
- (Shimon1981) L. L. Shimon, N. V. Golovchak, I. I. Garga, and I. V. Kurta, *Opt. Spectrosc. (USSR)* 50 (1981) 571
- (Sohn1992) M. Sohn and G. F. Hanne, *J. Phys. B* 25 (1992) 4627
- (Srivastava) R. Srivastava, R. P. McEachran, and A. D. Stauffer, private communication
- (Srivastava1992) R. Srivastava, T. Zuo, R. P. McEachran, and A. D. Stauffer, *J. Phys. B* 25 (1992) 3709
- (Srivastava1992b) R. Srivastava, T. Zuo, R. P. McEachran, and A. D. Stauffer, *J. Phys. B* 25 (1992) 1073, *J. Phys. B* 25 (1992) 2409
- (Srivastava1995) R. Srivastava, R. P. McEachran, and A. D. Stauffer, *J. Phys. B* 28 (1995) 885

- (Steph1980) N. C. Steph and D. E. Golden, *Phys. Rev. A* 21 (1980) 1848
- (Trajmar1968) S. Trajmar, J. K. Rice, and A. Kuppermann, *A Low-Energy, High-Resolution Electron Impact Spectrometer*, technical Memorandum 33-373, NASA, 1968
- (Valyi1977) *Atom and Ion Sources*, John Wiley & Sons, London, 1977
- (Walker1976) D. W. Walker, *Electron and Photon Interaction with Atoms*, eds H. Kleinpoppen and M. R. C. McDowell, (Plenum, New York, 1976), 203
- (Wang1994) S. Wang, S. Trajmar, and P. W. Zetner, *J. Phys. B* 27 (1994) 1613
- (Webb1985) C. J. Webb, W. R. McGillivray, and M. C. Standage, *J. Phys. B* 18 (1985) L259
- (Wedding1991) A. B. Wedding, A. G. Mikosza, and J. F. Williams, *J. Opt. Soc. Am. A* 8 (1991) 1729
- (Yariv1976) A. Yariv, *Introduction to Optical Electronics*, (Holt, Rinehart and Winston, New York, 1976)
- (Zagrebin1992) A. L. Zagrebin and M. G. Lednev, *Opt. Spectrosc. (USSR)* 72 (1992) 289
- (Zetner1986) P. W. Zetner, W. B. Westerveld, M. C. Standage, *J. Phys. B* 19 (1986) 4205
- (Zetner1989) P. W. Zetner, S. Trajmar, G. Csanak, and R. E. H. Clark, *Phys. Rev. A* 39 (1989) 6022
- (Zetner1990) P. W. Zetner, S. Trajmar, and G. Csanak, *Phys. Rev. A* 41 (1990) 5980
- (Zetner1992) P. W. Zetner, Y. Li, and S. Trajmar, *J. Phys. B* 25 (1992) 3187

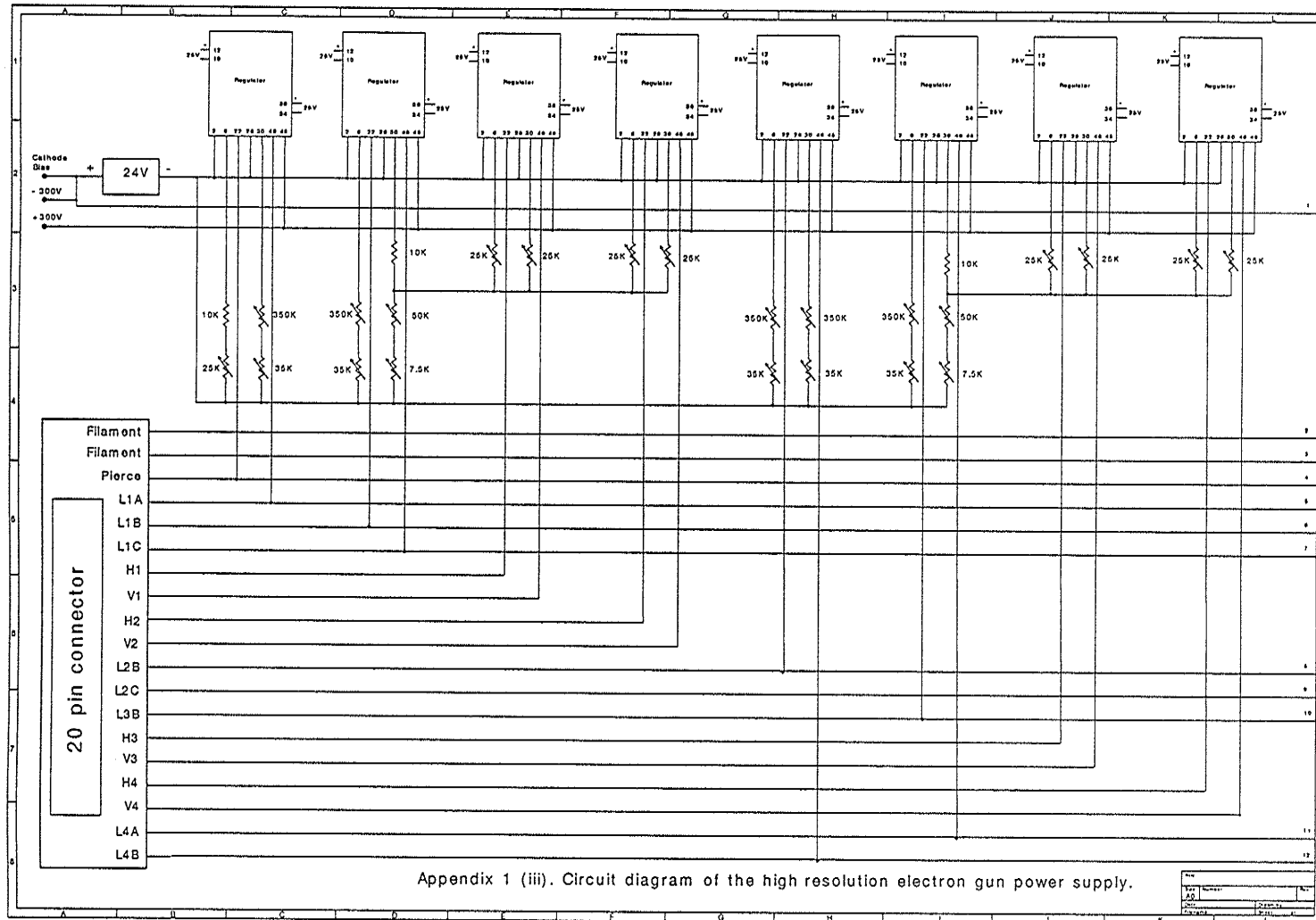
- (Zohny1990) E. I. M. Zohny, M. A. K. El-Fayoumi, H. Hamdy, H. -J. Beyer, Y. A. Eid, F. Shahin, and H. Kleinpoppen, *Proceedings of the Sixteenth International Conference on the Physics of Electronic and Atomic Collisions*, New York, 1989, eds A. Dalgarno, R. S. Freund, M. S. Lubell, and T. B. Lucatorto (AIP, New York, 1990), 173
- (Zuo1991) T Zuo, R. P. McEachran, and A. D. Stauffer, *J. Phys. B* 24 (1991) 2853
- (Zuo1992) T. Zuo, R. P. McEachran, and A. D. Stauffer, *J. Phys. B* 25 (1992) 3393

**APPENDIX 1**

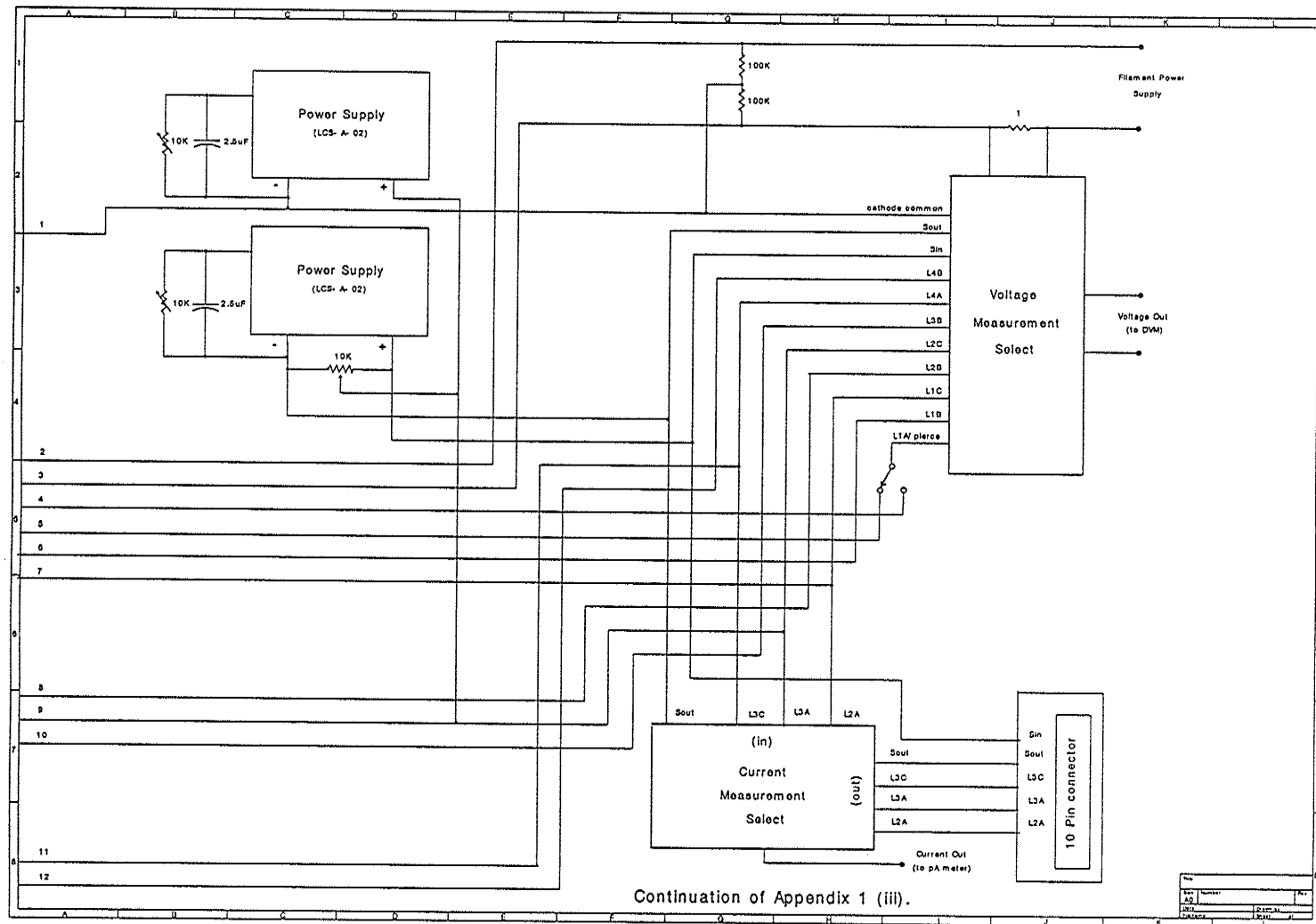
**CIRCUIT DIAGRAMS**





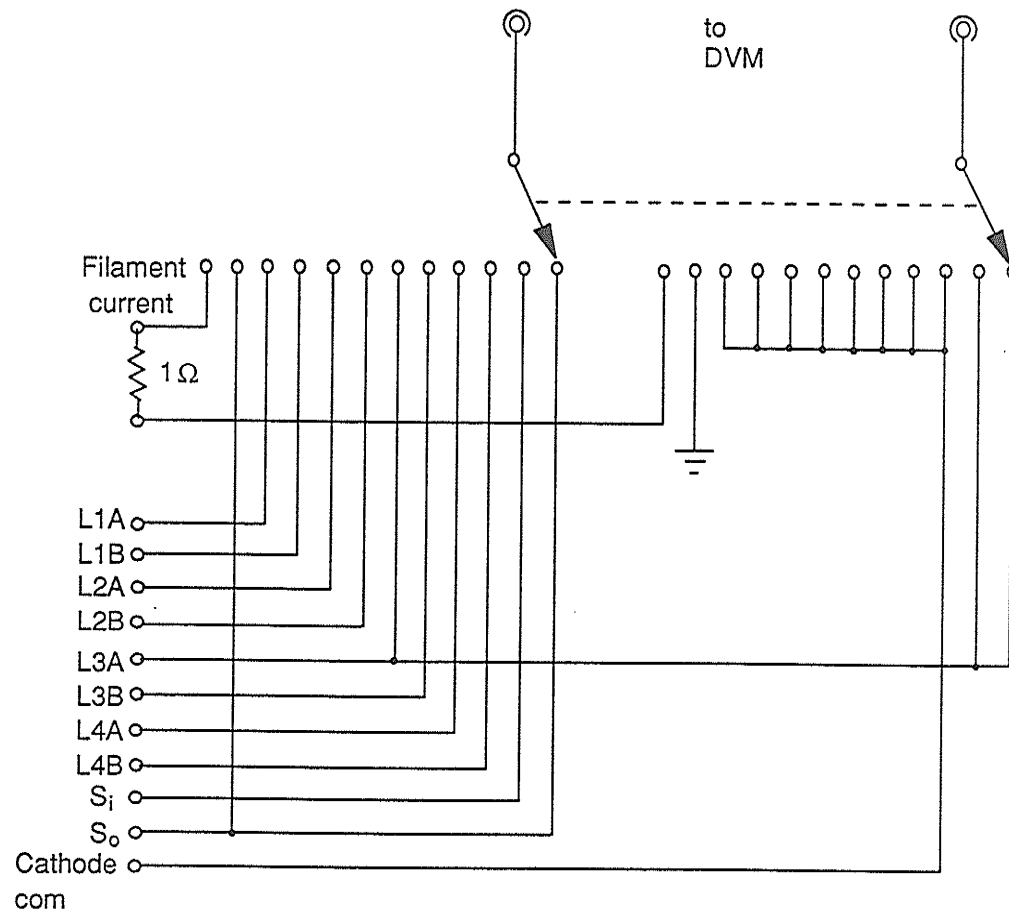


Rev	1
Date	1964
By	...
Checked	...
Approved	...

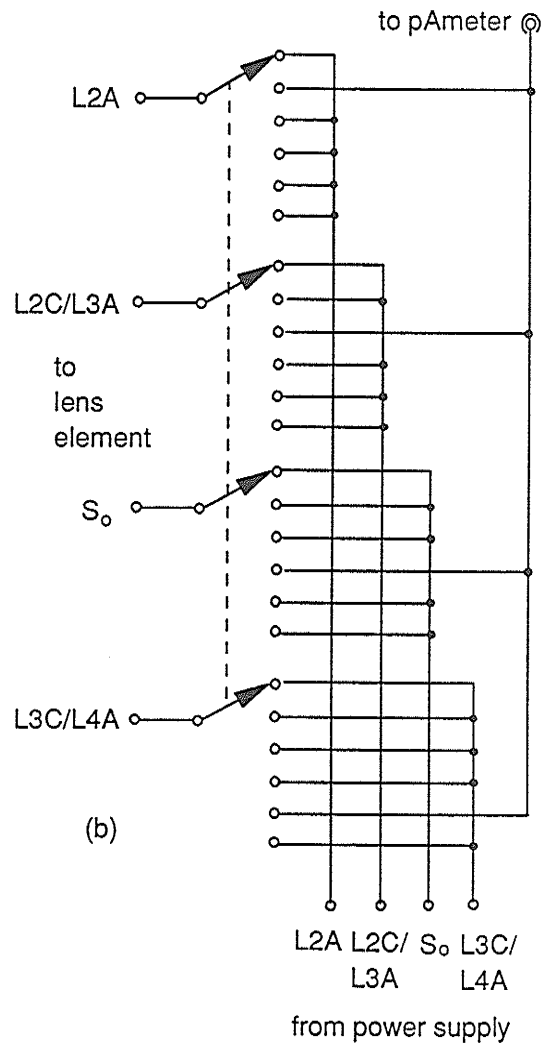


Continuation of Appendix 1 (iii).

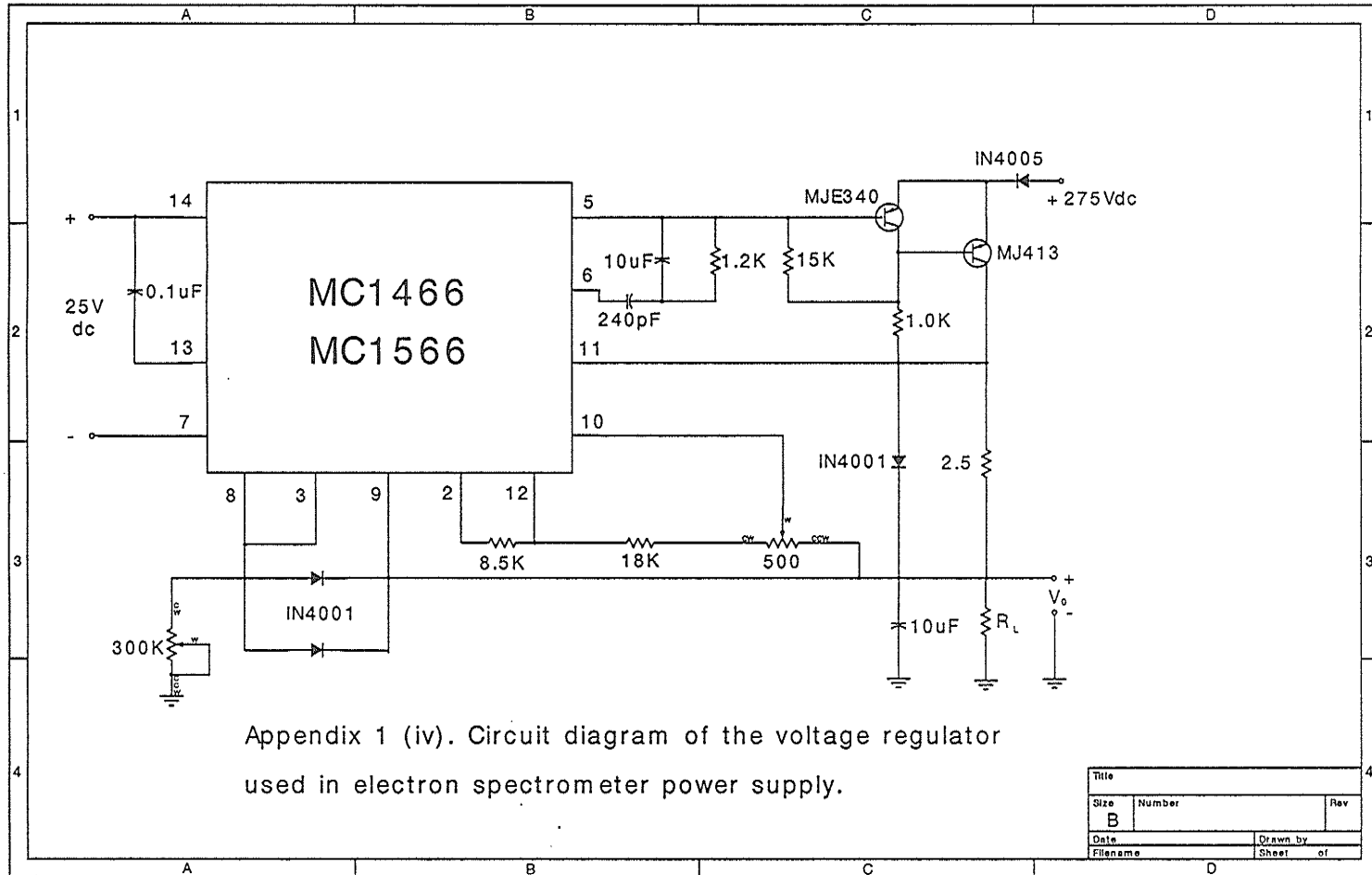
Rev	Number	Date
1		
2		
3		
4		
5		
6		
7		
8		
9		
10		
11		
12		



Continuation of Appendix 1 (iii). Voltage measurement select switch of the high resolution gun.

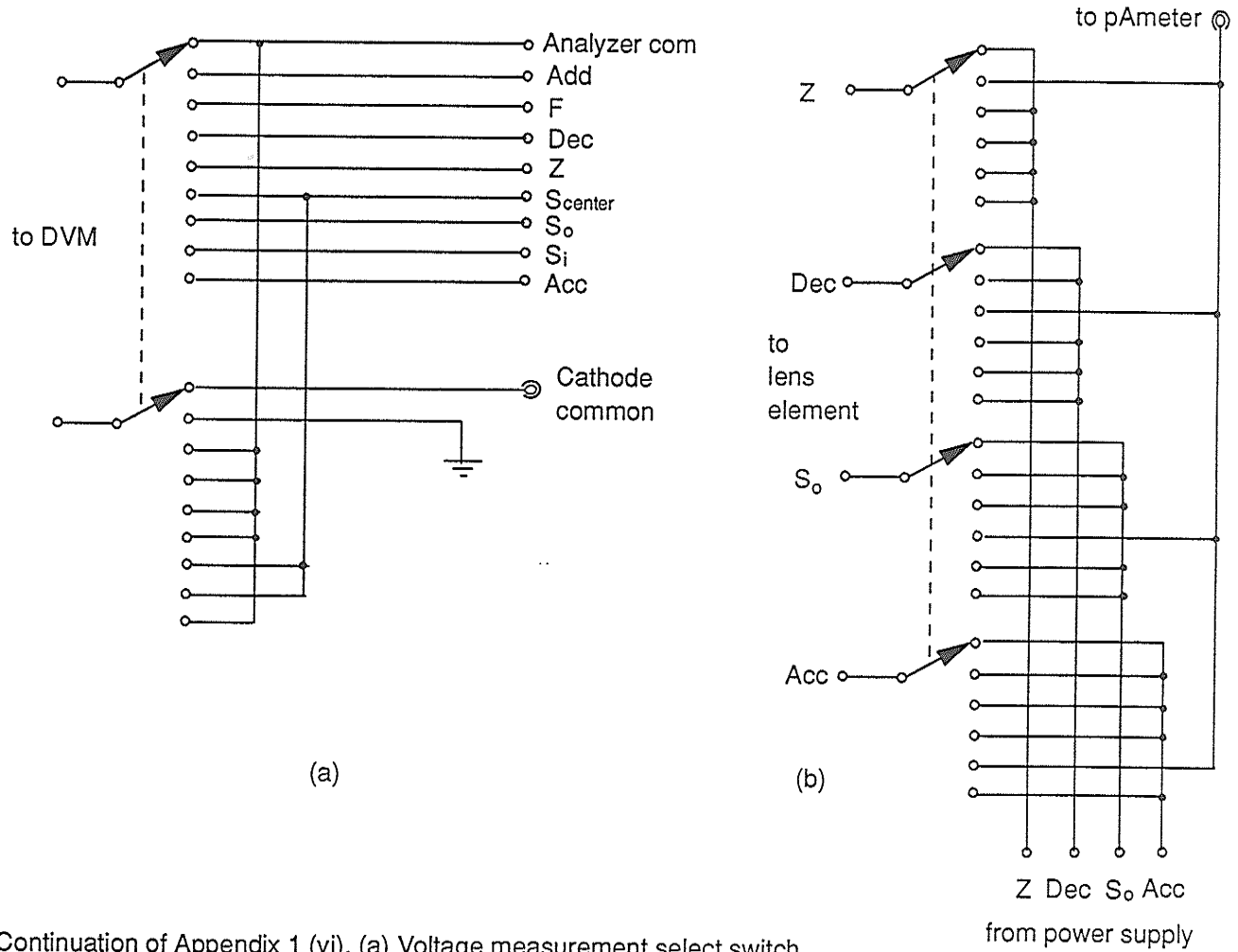


Continuation of Appendix 1 (iii). Current measurement select switch of the high resolution gun.

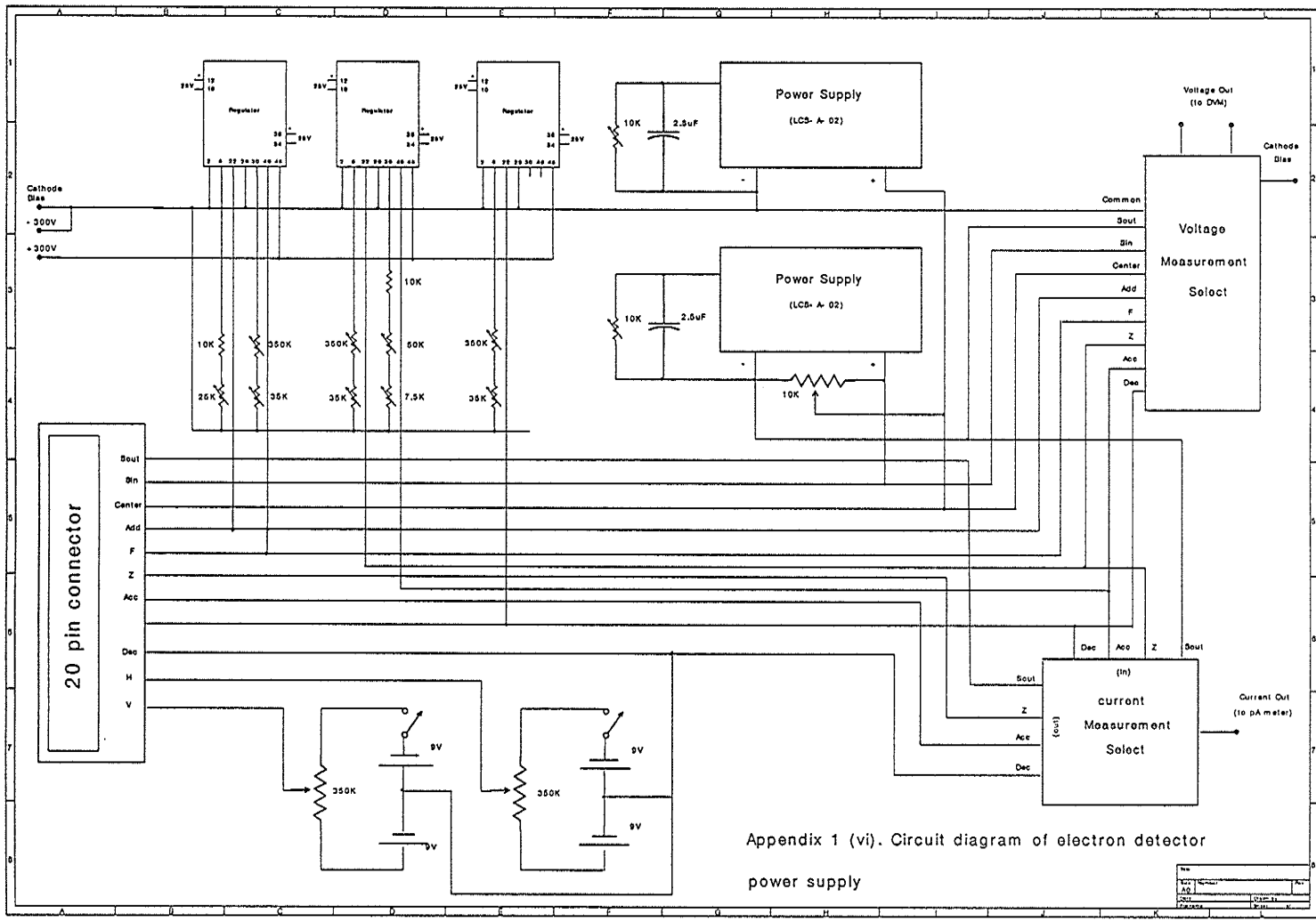


Appendix 1 (iv). Circuit diagram of the voltage regulator used in electron spectrometer power supply.

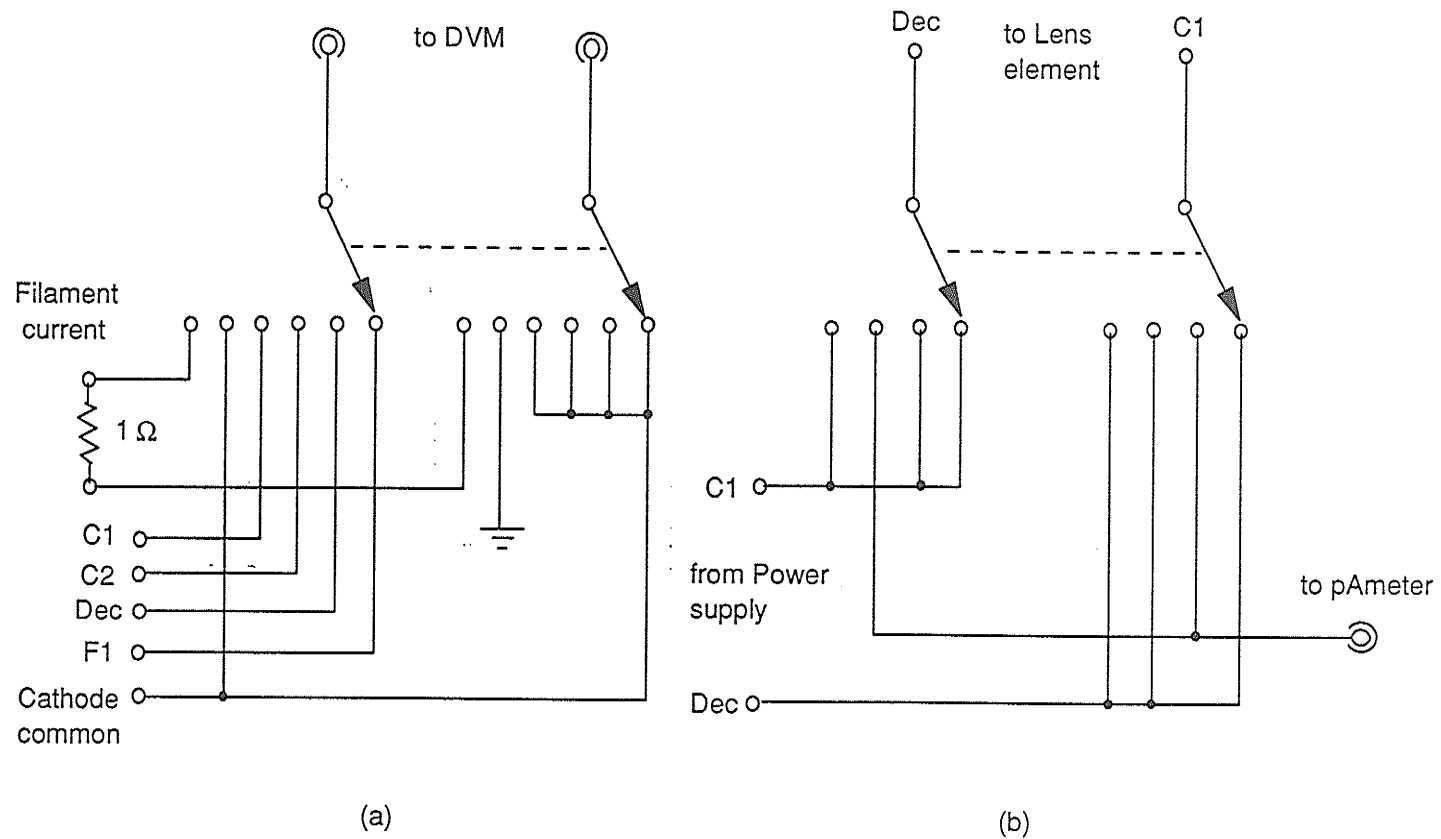
Title		
Size	Number	Rev
B		
Date	Drawn by	
Filename	Sheet of	



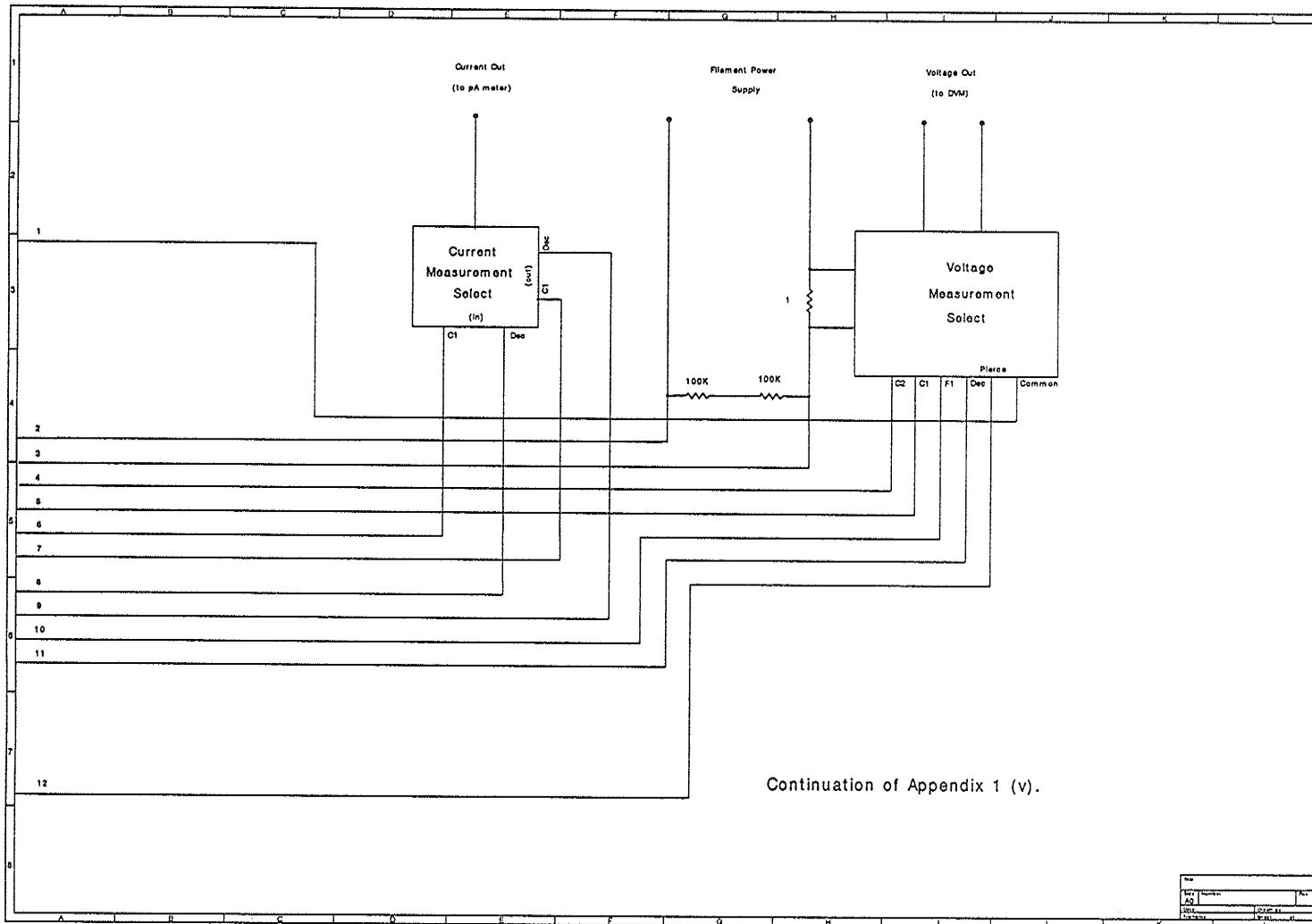
Continuation of Appendix 1 (vi). (a) Voltage measurement select switch.  
 (b) Current measurement select switch.



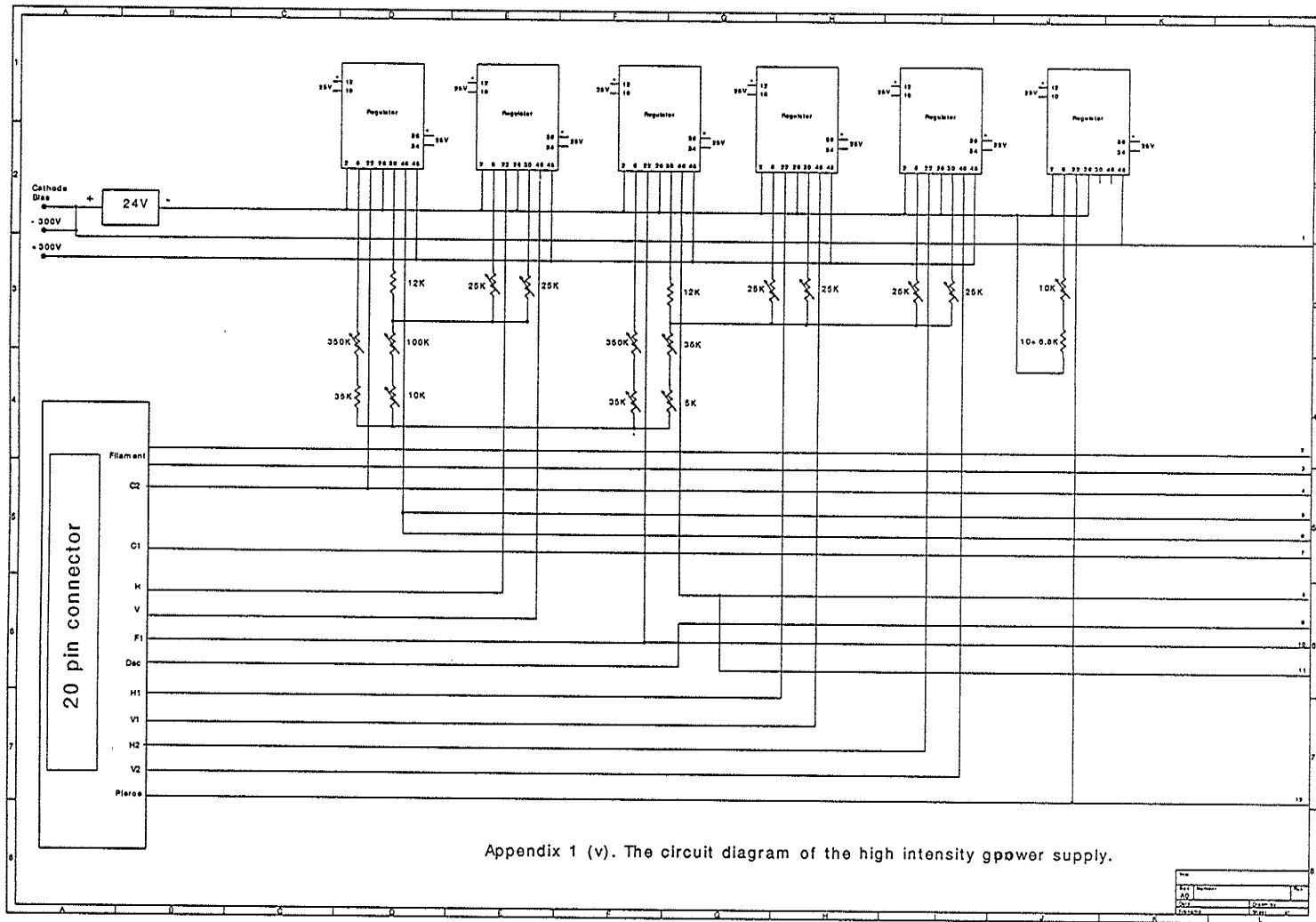
Appendix 1 (vi). Circuit diagram of electron detector power supply



Continuation of Appendix 1 (v). (a) Voltage measurement select switch.  
 (b) Current measurement select switch.



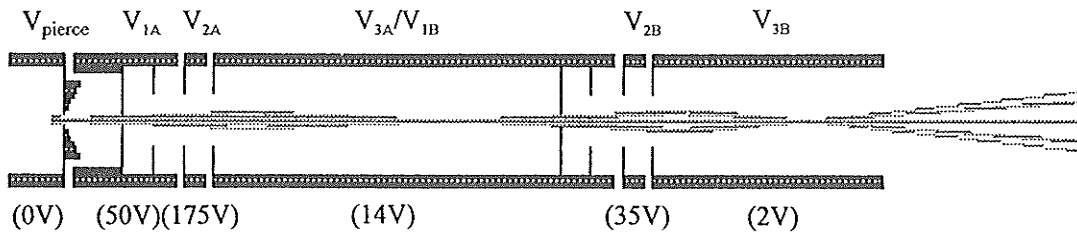
Rev	
App	
Proj	
Drawn	
Checked	
DATE	



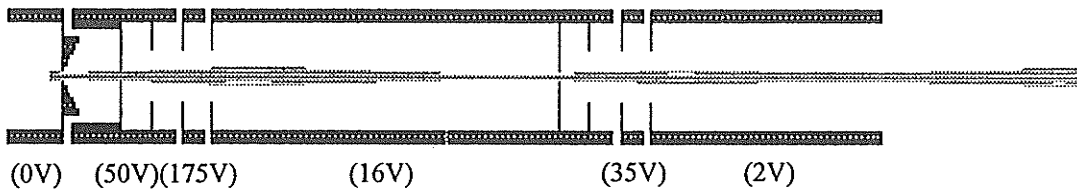
Appendix 1 (v). The circuit diagram of the high intensity power supply.

## **APPENDIX 2**

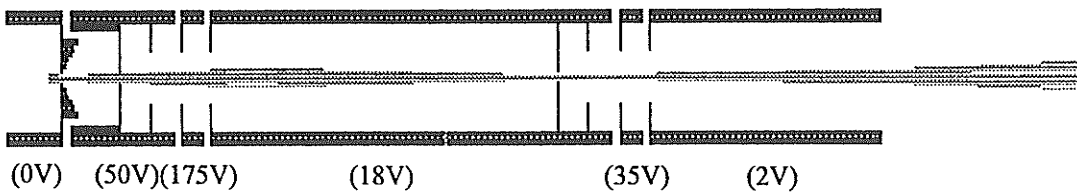
# **ELECTRON OPTICS SIMULATION**



(a)

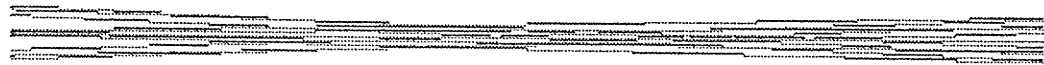
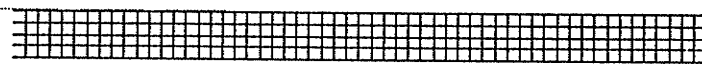
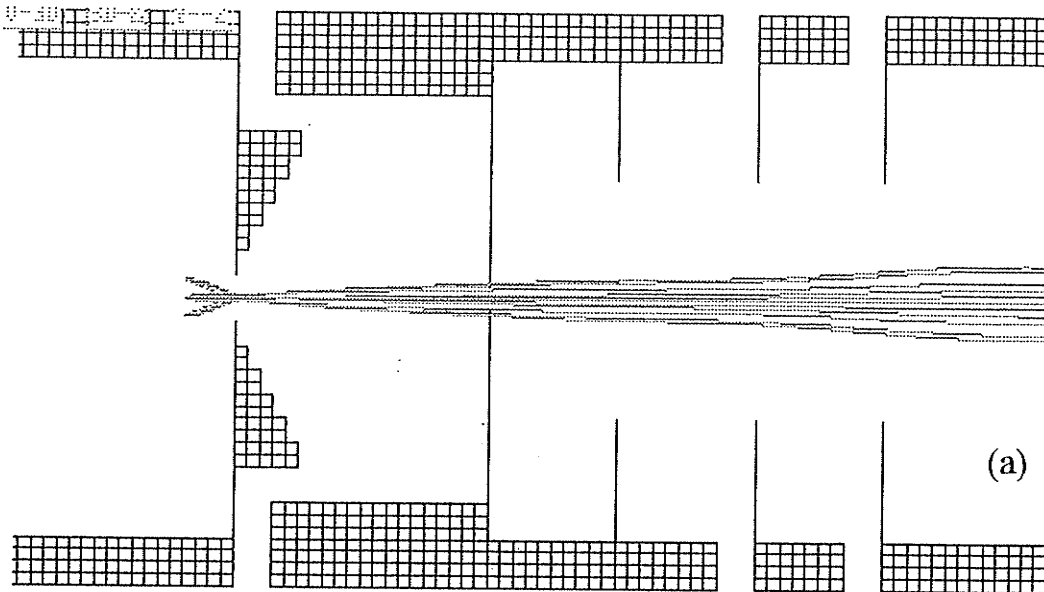


(b)

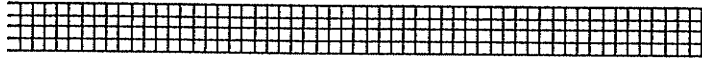


(c)

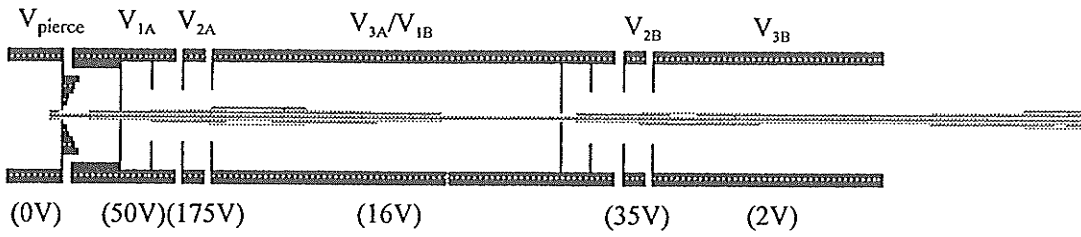
Appendix 2 (i). The dependence of electron trajectory on different lens potential  $V_{3A}/V_{1B}$  — the most sensitive potential in the entrance lens stack. The size of the object is chosen to be 0.060in in diameter and the distance between the filament tip and the pierce element (d) is 0.060in. (a)  $V_{3A} = 14V$ , (b)  $V_{3A} = 16V$ , and (c)  $V_{3A} = 18V$ .



(b)

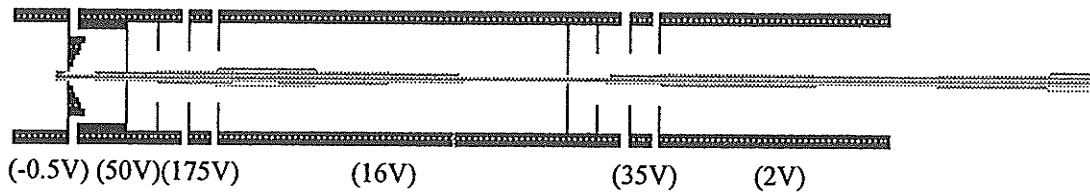


Appendix 2 (ii). The details of electron rays in the filament-Pierce-Wehnelt extraction diode region (a) and at the end of the entrance lens stack (b).

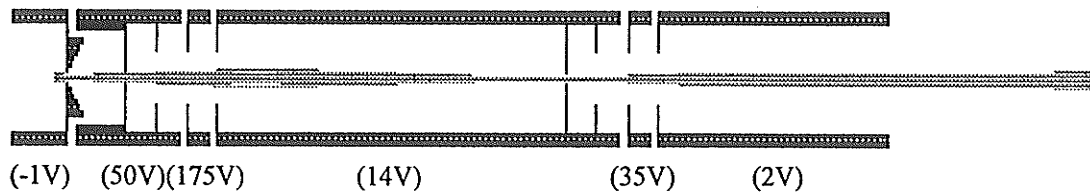


$d = 0.060\text{in}$

(a)

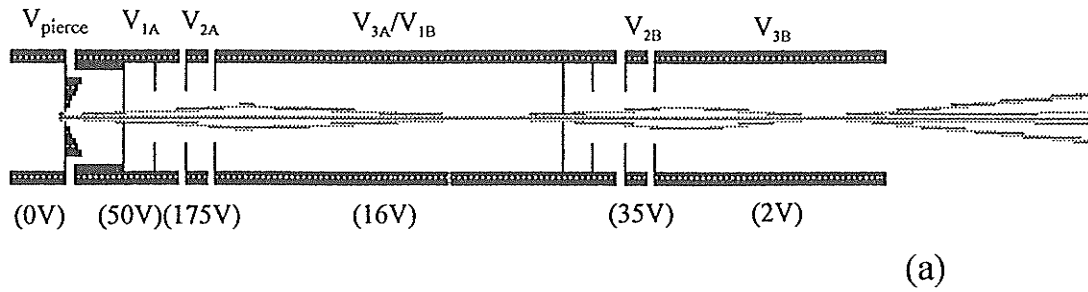


(b)

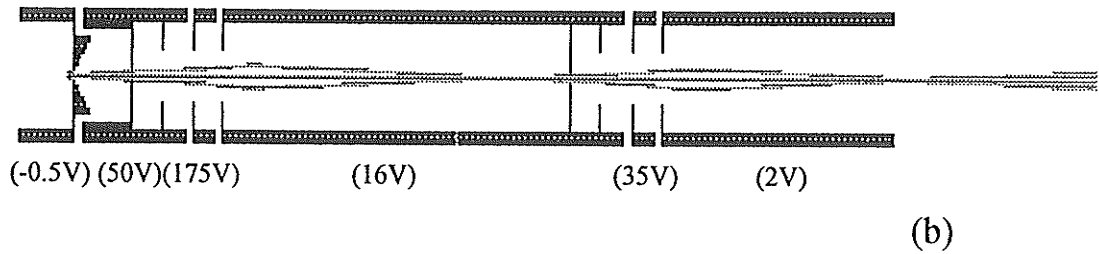


(c)

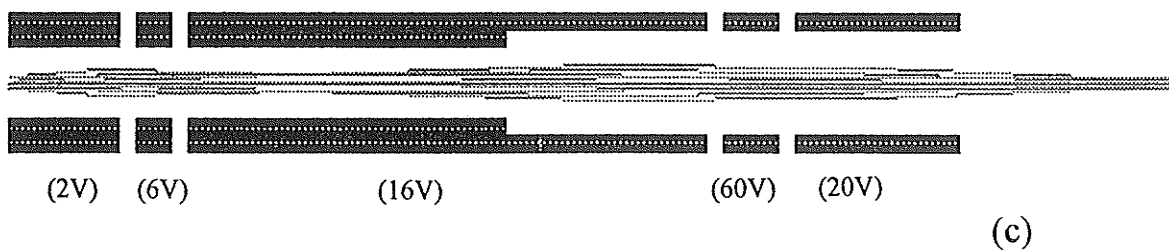
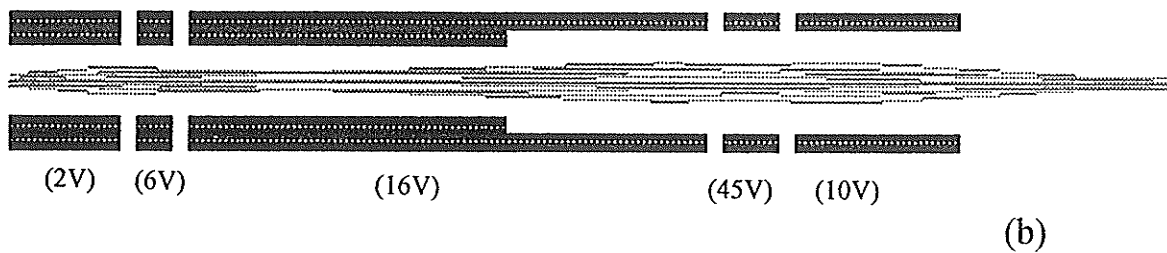
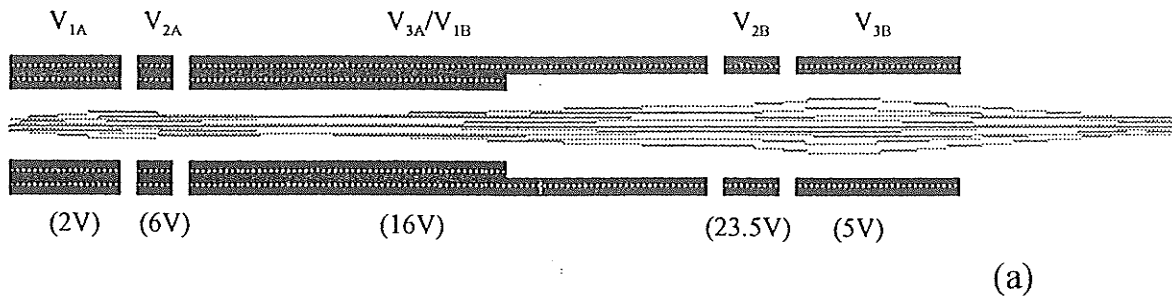
Appendix 2 (iii). The influence of the pierce element potential on the electron beam trajectory. (a)  $V_{\text{pierce}} = 0\text{V}$ , (b)  $V_{\text{pierce}} = -0.5\text{V}$ , and (c)  $V_{\text{pierce}} = -1\text{V}$ .



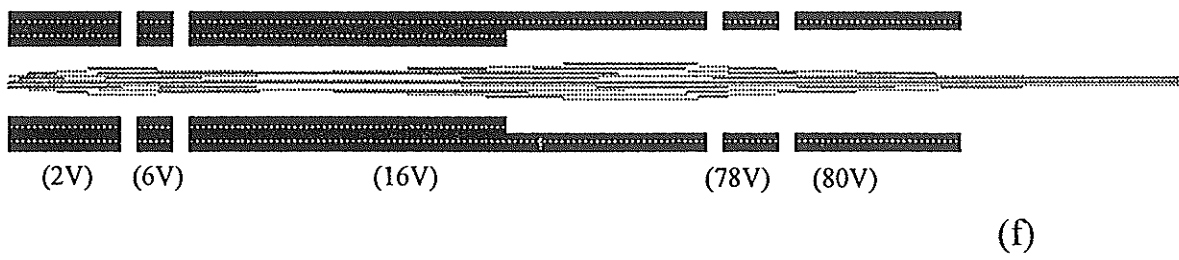
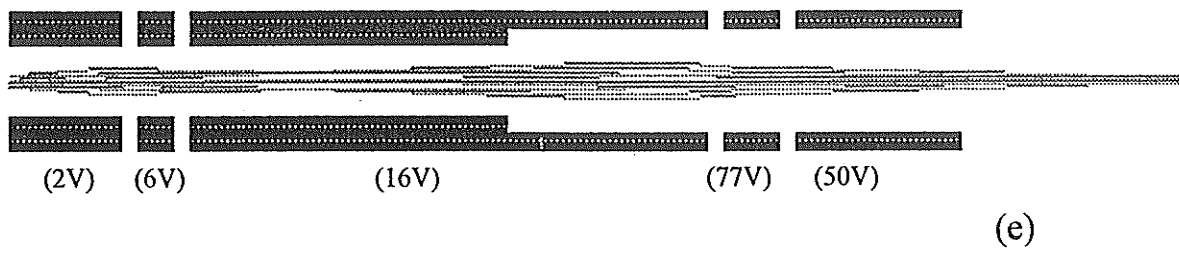
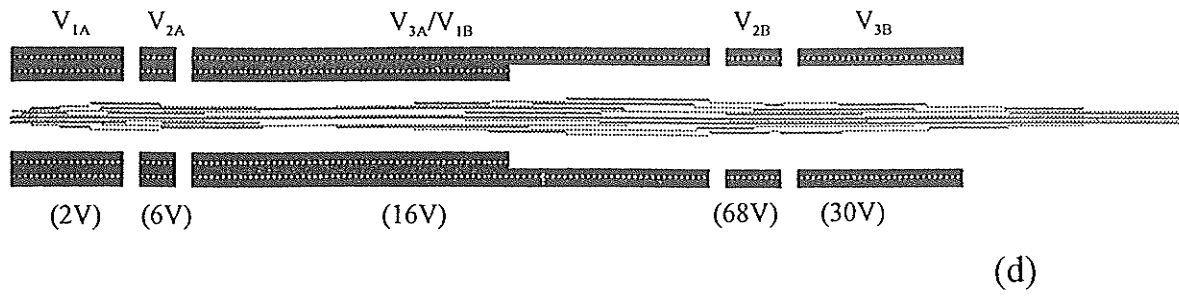
$d = 0.030\text{in}$



Appendix 2 (iv) An applied potential on the pierce element can be used to compensate the location change of the beam cross-over caused by displacement of the filament in order to bring the cross-over of the electron beam back to the end of the entrance lens stack. The distance between the filament tip and the pierce element ( $d$ ) is 0.030in.



Appendix 2 (v). By adjusting only one lens potential ( $V_{2B}$ ), the cross-over of the electron beam can be located at the interaction center (1.5in away from the end of the exit lens stack) for the electron beam with a wide range of kinetic energies. In practice,  $V_{3A}/V_{1B}$  may also be adjusted.



## **APPENDIX 3**

# **DATA ACQUISITION PROGRAMS**

This Appendix includes the original programs for data acquisition. The programs with extension ".TXT" are command files that can run in MCS emulator environment. The Quick Basic programs (with extension ".BAS") have been compiled and can be execute by MCS command files. The detailed descriptions about the functions of each program or subroutine are given in the header information area.

## RAMP.TXT

```
SET_PRESET_COUNT 999999999
SET_PRESET_LENGTH 4096
START
RUN "RMAIN.EXE"
STOP
STOP
□
```

## RMAIN.BAS

```
DIM CNT%(720)
DECLARE SUB Normalize (PASSCNT%, NRAMP%, RLT%, SCALE&)
DECLARE SUB Skip (NUMCHAN%)
DECLARE SUB Display (BIN&, RCT%, COUNTS&, PASSCNT%, I%, BINWIDTH%, SCALE&, XNUM%, YNUM%)
DECLARE SUB PlotChan (PASSCNT%, CHANNEL%, COUNTS&, BINWIDTH%, SCALE&, VALUEX%, VALUEY%)
DECLARE SUB Getchan (CHAN%, CONTENTS&)
DECLARE SUB Senddata (RCT%, CH%)
DECLARE SUB Setclock (DWELL%)
DECLARE SUB CavWait ()
DEFINT A-Z
CONST MBASE = &H2A0 ' address of I/O port used by PCL I/O card
*****
' RMAIN.BAS version 1991
' This program is for generating a ramp and outputting it from I/O port, while
' gets data from MCS and displays it on the monitor. It can also control I/O to
' output Start Out and Channel Advance Out for MCS. Associating with RSET.EXE,
' user can set ramps with different parameters.
*****
KEY(1) ON ' set F1 key to stop program
ON KEY(1) GOSUB Halt
KEY(2) ON
ON KEY(2) GOSUB Fastscan
KEY(3) ON
ON KEY(3) GOSUB Suspend
KEY(4) ON
ON KEY(4) GOSUB Stopend
ON ERROR GOTO ErrorRoutine
*****
SHELL "MS C80 -NONRESIDENT"
'#####
LOCKMD = 0
OPEN "RMAIN.DAT" FOR INPUT AS #1 'get parameters from RSET
INPUT #1, NPASS, DWELL, RLT, RLTOLD, RLTNEW, JCH, MODE, JCT, RHT, JPERC, RPERC, NRAMP, LOCKMD
CLOSE #1
HDW = NRAMP * RLT
RSTEP! = RLTOLD / RHT
BINWIDTH = HDW \ 620: IF BINWIDTH = 0 THEN BINWIDTH = 1
IF BINWIDTH * HDW > 620 THEN BINWIDTH = BINWIDTH + 1
FOR I = 1 TO 620 'load initial values to array
CNT%(I) = 190
NEXT I
CALL Setclock(DWELL) 'set timers
4 FOR PASSCNT = 1 TO NPASS
5 SCREEN 2: CLS 'set graphics screen
LOCATE 25, 70: PRINT "CH"; HDW
LOCATE 4, 60: PRINT "PASS COUNT: "; PASSCNT'print pass count in upper right corner
6 LINE (0, 20)-(620, 190), , B 'draw box
LOCATE 2, 5
PRINT "[F1=HALT] [F2=FAST SCAN] [F3=SUSPEND] [F4=STOP AT END] [S=SINGLE]"
SUSPMK = 0
OUT MBASE + 2, 1 'send start pulse to mcs
```

```

OUT MBASE + 2, 0
I = 0: BIN& = 0
*****
FOR RAMP = 1 TO NRAMP
FOR RCT = 1 TO JCH - 1
16 CALL Senddata(RCT / RSTEP!, MODE) 'step-ramp voltage in channel 0
CavWait 'wait for channel advance clock
IF SUSPMK = 1 THEN GOSUB Suspend
OUT &H2A2, 2 'send channel advance pulse
OUT &H2A2, 0
CHAN = (RAMP - 1) * RLT + RCT
24 CALL Getchan(CHAN, COUNTS&) 'read contents of channel RCT
25 CALL Display(BIN&, CHAN, COUNTS&, PASSCNT, I, BINWIDTH, SCALE&, XNUM, YNUM)
CNT%(XNUM) = YNUM
NEXT RCT
FOR RCT = JCH - 1 TO RLT 'generate jump
27 CALL Senddata((RCT - JCH) / RSTEP! + JCT, MODE) 'send data to DAC
28 CavWait 'wait for channel advance pulse
IF SUSPMK = 1 THEN GOSUB Suspend
OUT &H2A2, 2
OUT &H2A2, 0
CHAN = (RAMP - 1) * RLT + RCT
29 CALL Getchan(CHAN, COUNTS&)
30 CALL Display(BIN&, CHAN, COUNTS&, PASSCNT, I, BINWIDTH, SCALE&, XNUM, YNUM)
CNT%(XNUM) = YNUM 'send Y coordinates to arrays
NEXT RCT
CALL Senddata(0, MODE) 'reset DAC
OUT &H2A2, 4 'reset external device
OUT &H2A2, 0
DO UNTIL INP(&H2A1) AND 4 'wait for ready signal from ext. dev.
LOOP
NEXT RAMP
31 CALL Normalize(PASSCNT, NRAMP, RLT, SCALE&) 'find new scale
32 CALL Skip(4096 - NRAMP * RLT) 'scan past any unused channels
IF SUSPMK = 2 THEN EXIT FOR 'stop at end of pass if switch
NEXT PASSCNT
#####
IF MODE = 1 THEN 'voltage locking
LOCATE 2, 5: PRINT "LOCK ANY INTERESTING ENERGY LOSS? (Y/N) "
DO: V$ = INKEY$
IF V$ = "N" OR V$ = "n" THEN GOTO NLC
IF V$ = "Y" OR V$ = "y" THEN LOCKMD = 1: EXIT DO
LOOP
END IF
IF MODE = 0 AND LOCKMD = 1 THEN
LOCATE 2, 5: PRINT "RESET ENERGY LOSS RAMP TO ZERO? (Y/N) 'reset locked voltage "
DO: V$ = INKEY$
IF V$ = "N" OR V$ = "n" THEN GOTO NLC
IF V$ = "Y" OR V$ = "y" THEN CALL Senddata(0, 1): LOCKMD = 0: GOTO NLC
LOOP
END IF
IF MODE = 0 AND LOCKMD = 0 THEN
LOCATE 2, 5: PRINT "PRESS [ESC] TO RETURN MCS. "
DO
V$ = INKEY$
IF V$ = CHR$(27) THEN GOTO NLC
LOOP
END IF
X0 = 0: Y0 = 40: X00 = 0
LOCATE 2, 5
PRINT "[USE ARROWS TO MOVE CURSOR] [L=LOCK] [ESC=QUIT] [<,>=FINE ADJUST]"
DO
LINE (X0 + 10, 21)-(X0 + 10, CNT%(X0 + 10) - 1)
LINE (X0 + 10, CNT%(X0 + 10) + 1)-(X0 + 10, 189)
V$ = INKEY$

```

```

IF V$ = CHR$(0) + CHR$(77) THEN GOSUB RIGHT
IF V$ = CHR$(0) + CHR$(75) THEN GOSUB LEFT
IF V$ = CHR$(60) THEN GOSUB FINELT
IF V$ = CHR$(62) THEN GOSUB FINERT
IF V$ = "L" OR V$ = "I" THEN GOSUB LC
LOOP UNTIL V$ = CHR$(27)
*****
NLC:
OPEN "RMAIN.DAT" FOR OUTPUT AS #1 ' keep lock mode in file
WRITE #1, NPASS, DWELL, RLT, RLTOLD, RLTNEW, JCH, MODE, JCT, RHT, JPERC, RPERC, NRAMP, LOCKMD
CLOSE #1
END
'
Halt:
SHELL "MS C80 -NONRESIDENT" ' switch to ega
CALL Senddata(0, MODE)
SCREEN 0: END
RETURN
'
Fastscan: 'advance mcs to end of scan and start new pass
Skip (HDW - CHAN)
RCT = RLT
RAMP = NRAMP
RETURN
'
ErrorRoutine:
IF ERR = 53 THEN 'file not found
PRINT "Data file not found. No default values available."
RESUME NEXT 'return to Init
ELSE
IF ERR = 52 THEN RESUME NEXT 'return to Init
SHELL "MS C80 -NONRESIDENT"
SCREEN 0: PRINT "ERROR "; ERR: PRINT " IN LINE "; ERL
INPUT A
END IF
END
RETURN
'
Suspend: 'suspend the program and execute single advance
SUSPMK = 1
DO
SNG$ = INKEY$
IF SNG$ = "S" OR SNG$ = "s" THEN
CavWait
RETURN
END IF
LOOP UNTIL SNG$ = CHR$(27)
CavWait
SUSPMK = 0
RETURN
'
Stopend:
SUSPMK = 2
RETURN
'
RIGHT: 'cursor adjustment for locking
LINE (X0 + 10, 21)-(X0 + 10, CNT%(X0 + 10) - 1), 0
LINE (X0 + 10, CNT%(X0 + 10) + 1)-(X0 + 10, 189), 0
X0 = X0 + 3: X00 = X0 * BINWIDTH
IF X0 > (HDW \ BINWIDTH - 8) THEN X0 = HDW \ BINWIDTH - 8
RETURN
'
LEFT:
LINE (X0 + 10, 21)-(X0 + 10, CNT%(X0 + 10) - 1), 0
LINE (X0 + 10, CNT%(X0 + 10) + 1)-(X0 + 10, 189), 0

```

```

X0 = X0 - 3: X00 = X0 * BINWIDTH
IF X0 < -3 THEN X0 = -3
RETURN

FINELT:      'fine adjustment
LINE (X0 + 10, 21)-(X0 + 10, CNT%(X0 + 10) - 1), 0
LINE (X0 + 10, CNT%(X0 + 10) + 1)-(X0 + 10, 189), 0
X00 = X00 - 1: X0 = X00 \ BINWIDTH
IF X0 < -3 THEN X0 = -3
IF X0 > HDW \ BINWIDTH - 8 THEN X0 = HDW \ BINWIDTH - 8
RETURN

FINERT:
LINE (X0 + 10, 21)-(X0 + 10, CNT%(X0 + 10) - 1), 0
LINE (X0 + 10, CNT%(X0 + 10) + 1)-(X0 + 10, 189), 0
X00 = X00 + 1: X0 = X00 \ BINWIDTH
IF X0 > HDW \ BINWIDTH - 8 THEN X0 = HDW \ BINWIDTH - 8
IF X0 < -3 THEN X0 = -3
RETURN

LC:
X1 = RLT * (X00 / RLT - X00 \ RLT)
IF X1 < JCH THEN
    LCHT = X1 / RSTEP!
ELSE
    LCHT = (X1 - JCH) / RSTEP! + JCT
END IF
CALL Senddata(LCHT, MODE) 'lock voltage corresponding to LCHT
RETURN

*****
:
:
:
SUB CavWait STATIC
    CONST MBASE = &H2A0
    CAV = 1
    WHILE CAV
        VALUE = INP(MBASE)
        CAV = (VALUE AND 2) / 2
    WEND
    WHILE CAV = 0
        VALUE = INP(MBASE)
        CAV = (VALUE AND 2) / 2
    WEND
END SUB

*****
SUB Display (BIN&, RCT, COUNTS&, PASSCNT, I, BINWIDTH, SCALE&, XNUM, YNUM) STATIC
    BIN& = BIN& + COUNTS&      ' bin data in 5 channels
    IF I = BINWIDTH - 1 THEN
        CALL PlotChan(PASSCNT, RCT, BIN& / (BINWIDTH), BINWIDTH, SCALE&, VALUEX, VALUEY) ' plot binned data
        I = 0: BIN& = 0: XNUM = VALUEX: YNUM = VALUEY
    ELSE
        I = I + 1
    END IF
END SUB

*****
SUB Getchan (CHAN, CONTENTS&) STATIC
    ' this subroutine returns the contents in decimal of mcs
    '      channel number CHAN
    DEF SEG = &HD000
    CONTENTS& = PEEK(4 * (CHAN - 1) + 2)
    CONTENTS& = CONTENTS& * 65536 + PEEK(4 * (CHAN - 1)) + 256 * PEEK(4 * (CHAN - 1) + 1)
    DEF SEG
END SUB

```

```

*****
SUB Normalize (PASSCNT, NUMRAMP, RLT, SCALE&) STATIC
' this subroutine finds the maximum number of counts in the
' spectrum and adjusts the display so the next pass will be on scale
COUNTSMAX& = 0: SUMSCALE& = 0
FOR CHANNEL = 1 TO 4000
CALL Getchan(CHANNEL, COUNTS&)
IF COUNTS& > COUNTSMAX& THEN COUNTSMAX& = COUNTS&
NEXT
SCALE& = 1.5 * COUNTSMAX&
END SUB

```

```

*****
SUB PlotChan (PASSCNT, CHANNEL, COUNTS&, BINWIDTH, SCALE&, VALUEX, VALUEY) STATIC
IF COUNTS& <= 1 THEN COUNTS& = 1
IF COUNTS& >= 1.18E+08 THEN COUNTS& = 1.18E+08
U0 = CHANNEL \ BINWIDTH + 10: V0 = 188 - 10 * LOG(COUNTS&)
IF V0 < 20 THEN V0 = 20
PSET (U0, V0)
VALUEX = U0: VALUEY = V0
LOCATE 1, 1
END SUB

```

```

*****
SUB Senddata (RCT%, CH%) STATIC
' this subroutine places the number RCT% (0-4096) on the
' data lines to the Kepco programmer, for the output channel CH%,
' and sends a 5 us strobe pulse
CONST MBASE = &H2A0
'
MSB = INT(RCT / 256) 'upper 4 bits of RCT
LSB = RCT - 256 * MSB 'lower 8 bits
'
OUT &H2A0, LSB
OUT &H2A1, MSB + 16 * CH
'
FCP = 1
WHILE FCP
FCP = INP(&H2A0) AND 1 'wait for fcp% to
WEND 'go low
' (fcp is 1st bit in port 0)
WHILE FCP = 0
' wait for fcp to
FCP = INP(&H2A0) AND 1 'go high
WEND
OUT &H2A1, MSB + 16 * CH 'send 0 to strobe
WHILE FCP
FCP = INP(&H2A0) AND 1 'wait for fcp low
WEND
OUT &H2A1, MSB + 32 + 16 * CH 'send 1 to strobe
END SUB

```

```

*****
' This subroutine sets the rates and modes for clocks 0 and 1
' on the digital I/O card
SUB Setclock (DWELL)
CONST MBASE% = &H2A0 'set timer 0
OUT MBASE% + 7, &H16 'for 5 us square wave
OUT MBASE% + 4, 5 ' (FCP)
'
OUT MBASE% + 7, &H76 'set timer 1
' for selected
' square wave (CAV)
N = DWELL * 10 'find n to load divide-by-n counter
LSB = N AND &HFF
MSB = (N AND &HFF00) / 256

```

```
OUT MBASE% + 5, LSB  
OUT MBASE% + 5, MSB
```

```
END SUB
```

```
SUB Skip (NUMCHAN%)
```

```
*****
```

```
' this subroutine advances the mcs ahead by NUMCHAN channels
```

```
FOR I = 1 TO NUMCHAN
```

```
OUT &H2A2, 2
```

```
OUT &H2A2, 0
```

```
NEXT
```

```
END SUB
```

## DATSAVE.TXT

```
SET_MCB 1
FILL_BUFFER
SET_MCB 0
SAVE "BUFFILE.MCS"
RUN "DATSAV.EXE"
SET_MCB 1
□
```

## DATSAV.BAS

```
*****
' DATSAV.BAS version 1991
' This program is for saving data as random disk file. With single save mode,
' user can input four items of description and a changed value. With repetitive
' save mode, only changed value is required. The program obtains data file from
' buffer file and save it as filename created from date and index number.
*****
ON ERROR GOTO ERRORRT
DIM TR$(65)
RETRY: OPEN "FILDESC.MCS" FOR RANDOM AS #1 LEN = 225
FIELD #1, 1 AS MD$, 8 AS IND$, 8 AS DS$, 50 AS AS$, 50 AS D1$, 50 AS D2$, 50 AS D3$, 8 AS CVL$
GET #1
MODE$ = MD$
INDEX$ = IND$: INDEX = VAL(IND$)
D0$ = DS$
CHG$ = AS$
DESC1$ = D1$
DESC2$ = D2$
DESC3$ = D3$
CHG = VAL(CVL$)
FIELD #1, 58 AS CHGSUM$, 167 AS DUMMY$
GET #1
CHGDESC$ = CHGSUM$
CLOSE #1
FOR I = 1 TO 50
  V$ = MID$(CHG$, I, 1)
  IF V$ <> " " THEN STRLN = I: EXIT FOR
NEXT I
CHG$ = RIGHT$(CHG$, 51 - STRLN)
MODE = VAL(MODE$)
SELECT CASE MODE
  CASE 0
    GOSUB SNGL
  CASE 1
    GOSUB REPT
END SELECT
OPEN "BUFFILE.MCS" FOR RANDOM AS #1 LEN = 256
FIELD #1, 256 AS TRANSFER$
FOR I = 1 TO 65
  GET #1
  TR$(I) = TRANSFER$
NEXT I
CLOSE #1
IF INDEX > 9 THEN
  NAME$ = "A:" + LEFT$(D0$, 6) + RIGHT$(STR$(INDEX), 2) + ".MCS"
  ' NAME$ = "A:" + LEFT$(D0$, 2) + MID$(D0$, 4, 2) + RIGHT$(D0$, 2) + RIGHT$(STR$(INDEX), 2) + ".MCS"
ELSE
  NAME$ = "A:" + LEFT$(D0$, 6) + "0" + RIGHT$(STR$(INDEX), 1) + ".MCS"
  ' NAME$ = "A:" + LEFT$(D0$, 2) + MID$(D0$, 4, 2) + RIGHT$(D0$, 2) + "0" + RIGHT$(STR$(INDEX), 1) + ".MCS"
END IF
SHELL "CHECK.BAT"
```

```

OPEN "CHFILE.DAT" FOR INPUT AS #1
INPUT #1, CHECK$
CHECK = VAL(MID$(CHECK$, 14, 8))
CLOSE #1
IF CHECK < 34000 THEN
CLS : LOCATE 5, 10
PRINT "DATA DISKETTE IS FULL, CHANGE A NEW ONE, WHEN READY PRESS ESC"
DO: V$ = INKEY$
LOOP UNTIL V$ = CHR$(27)
END IF
OPEN "RMAIN.DAT" FOR INPUT AS #1
INPUT #1, DUM1, DUM2, RLT, DUM4, DUM5, DUM6, DUM7, DUM8, DUM9, DUM10, DUM11, NRAMP, DUM13
RANGE$ = STR$(RLT * NRAMP)
CLOSE #1
OPEN NAMES FOR RANDOM AS #1 LEN = 256
BYTENUM = LOF(1)
IF BYTENUM > 10000 THEN GOTO OVERWRT
CONT: FIELD #1, 256 AS TRANSFER$
FOR I = 1 TO 65
LSET TRANSFER$ = TR$(I)
PUT #1
NEXT I
LOCK #1, 1 TO 65
FIELD #1, 1 AS MD$, 8 AS IND$, 8 AS D$, 50 AS A$, 50 AS D1$, 50 AS D2$, 50 AS D3$, 8 AS R$, 31 AS DUMMYS
LSET MD$ = MODE$
RSET IND$ = STR$(INDEX)
LSET D$ = D0$
LSET A$ = CHGDESC$
LSET D1$ = DESC1$
LSET D2$ = DESC2$
LSET D3$ = DESC3$
RSET R$ = RANGE$
PUT #1
CLOSE #1
END

```

```

##### SUBROUTINE #####
SNGL:
CLS
FOR I = 3 TO 21
LOCATE I, 5
PRINT CHR$(176)
LOCATE I, 75
PRINT CHR$(176)
NEXT
FOR I = 5 TO 75
LOCATE 3, I: PRINT CHR$(176)
LOCATE 21, I: PRINT CHR$(176)
NEXT
LOCATE 3, 30
PRINT " SINGLE SAVE MODE "
RETRY1: LOCATE 5, 13
PRINT "DATE (mmdyy)"; : INPUT D0$
IF VAL(LEFT$(D0$, 2)) > 12 OR VAL(LEFT$(D0$, 2)) < 1 THEN GOTO RETRY1
IF VAL(MID$(D0$, 3, 2)) > 31 OR VAL(MID$(D0$, 3, 2)) < 1 THEN GOTO RETRY1
' IF MID$(D0$, 3, 1) < "." OR MID$(D0$, 6, 1) < "-" THEN GOTO RETRY1
IF LEN(D0$) < 6 THEN GOTO RETRY1
RETRY2: LOCATE 7, 13
PRINT "INDEX NUMBER (LESS THAN 100)"; : INPUT INDEX
IF INDEX > 99 OR INDEX < 0 THEN GOTO RETRY2
LOCATE 9, 13
PRINT "4 ITEMS TO DESCRIBE THE EXPERIMENT (LESS THAN 50 CHARACTERS)"
LOCATE 11, 13
INPUT "1: "; CHGDESC$
LOCATE 13, 13
INPUT "2: "; DESC1$
LOCATE 15, 13

```

```
INPUT "3: "; DESC2$
LOCATE 17, 13
INPUT "4: "; DESC3$
RETURN
```

```
REPT:
CLS
INDEX = INDEX + 1
IF INDEX > 99 THEN GOTO ERRORRT:
FOR I = 5 TO 9
  LOCATE I, 10
  PRINT CHR$(176)
  LOCATE I, 70
  PRINT CHR$(176)
NEXT
FOR I = 10 TO 70
  LOCATE 5, I
  PRINT CHR$(176)
  LOCATE 9, I
  PRINT CHR$(176)
NEXT
LOCATE 5, 30
PRINT " REPETITIVE SAVE MODE "
LOCATE 7, 20
PRINT "INPUT "; CHG$; : INPUT CHG
OPEN "FILDESC.MCS" FOR RANDOM AS #1 LEN = 9
FIELD #1, 1 AS MD$, 8 AS INDS
LSET MD$ = "1"
RSET INDS = STR$(INDEX)
PUT #1
CLOSE #1
CHGDESC$ = CHG$ + "=" + STR$(CHG)
RETURN
```

```
OVERWRT:
CLS
LOCATE 5, 5
PRINT "THE DATA FILE ["; NAME$; "] ALREADY EXISTS, OVERWRITE OR NOT? (Y/N)"
DO: V$ = INKEY$
IF V$ = "Y" OR V$ = "y" THEN GOTO CONT
IF V$ = "N" OR V$ = "n" THEN CLOSE #1: GOTO RETRY
LOOP
ERRORRT:
BEEP
IF ERR = 71 THEN
  PRINT "DISK NOT READY"
  RESUME NEXT
END IF
IF ERR = 11 THEN
  PRINT "DIVISION BY ZERO"
  RESUME NEXT
END IF
IF ERR = 61 THEN
  PRINT "DISK IS FULL"
  RESUME NEXT
END IF
LOCATE 25, 5
PRINT "          ERROR HAPPENS, RUN AGAIN"
FOR I = 1 TO 8000: NEXT
END
```

## REPSAVE.TXT

```
set_mcb 1
fill_buffer
set_mcb 0
save "buffile.mcs"
run "repsav.exe"
set_mcb 1
□
```

## REPSAV1.BAS

```
*****
' REPSAV1.BAS version 1995
' Modified from REPSAV.BAS in order to display the date and index
' This program has the functions of executing repetitive save and changing
'save mode. For repetitive save, user can input four items of description
'and a changed value. User can also flip switch code to change save mode.
'Then it keeps the descriptions and switch code on a temporary file.
*****
ON ERROR GOTO ERRORT
CLS
OPEN "FILDESC.MCS" FOR RANDOM AS #1 LEN = 17
FIELD #1, 1 AS MD$, 8 AS IND$, 8 AS D$
GET #1
mode = VAL(MD$)
INDEX$ = IND$
D0$ = D$
CLOSE #1
SELECT CASE mode
CASE 0
GOSUB REPT
CASE 1
GOSUB SELT
END SELECT
END

##### SUBROUTINE #####

SELT:
FOR I = 10 TO 70
LOCATE 3, I
PRINT CHR$(176)
LOCATE 17, 1
PRINT CHR$(176)
NEXT
FOR I = 3 TO 17
LOCATE I, 10: PRINT CHR$(176)
LOCATE I, 70: PRINT CHR$(176)
NEXT
LOCATE 5, 21
PRINT "The last date: ", D0$, "The last index: ", RIGHT$(INDEX$, 3)
LOCATE 9, 21
PRINT "1. CHANGE TO SINGLE MODE"
LOCATE 11, 21
PRINT "2. KEEP REPETITIVE MODE"
LOCATE 13, 21
PRINT "3. QUIT"
DO: V$ = INKEY$
IF V$ = "1" THEN
GOSUB SNGL: EXIT DO
END IF
IF V$ = "2" THEN
```

```

GOSUB REPT: EXIT DO
END IF
LOOP UNTIL V$ = "3"
RETURN

SNGL:
OPEN "FILDESC.MCS" FOR RANDOM AS #1 LEN = 1
FIELD #1, 1 AS mode$
LSET mode$ = "0"
PUT #1
CLOSE #1
RETURN

REPT:
RETRY: CLS
FOR I = 3 TO 23
  LOCATE I, 5: PRINT CHR$(176)
  LOCATE I, 75: PRINT CHR$(176)
NEXT
FOR I = 5 TO 75
  LOCATE 3, I: PRINT CHR$(176)
  LOCATE 23, I: PRINT CHR$(176)
NEXT
LOCATE 3, 29: PRINT " REPETITIVE SAVE MODE "
LOCATE 5, 10
PRINT "The last date: "; D0$, "The last index: "; RIGHTS(INDEX$, 3)

LOCATE 7, 10
PRINT "DATE (mmddyy)"; : INPUT D0$
IF VAL(LEFT$(D0$, 2)) > 12 OR VAL(LEFT$(D0$, 2)) < 1 THEN GOTO RETRY
IF VAL(MID$(D0$, 3, 2)) > 31 OR VAL(MID$(D0$, 3, 2)) < 1 THEN GOTO RETRY
IF MID$(D0$, 3, 1) <> "-" THEN GOTO RETRY
IF MID$(D0$, 6, 1) <> "-" THEN GOTO RETRY
LOCATE 7, 40: INPUT "INDEX NUMBER"; INDEX$
LOCATE 9, 10
PRINT "CHANGED PARAMETER (LESS THAN 50 CHARACTERS)"
LOCATE 11, 10: INPUT CHG$
LOCATE 13, 10
PRINT "CHANGED VALUE "; CHG$, "=: "; INPUT CHG
LOCATE 15, 10
PRINT "3 ITEMS TO DESCRIBE THE EXPERIMENT (LESS THAN 50 CHARACTERS EACH)"
LOCATE 17, 10: INPUT "1: "; DESC1$
LOCATE 19, 10: INPUT "2: "; DESC2$
LOCATE 21, 10: INPUT "3: "; DESC3$
OPEN "FILDESC.MCS" FOR RANDOM AS #1 LEN = 225
FIELD #1; 1 AS mode$, 8 AS INDS$, 8 AS D$, 50 AS a$, 50 AS D1$, 50 AS D2$, 50 AS D3$, 8 AS CVL$
LSET mode$ = "1"
RSET INDS$ = INDEX$
LSET D$ = D0$
RSET a$ = CHG$
LSET D1$ = DESC1$
LSET D2$ = DESC2$
LSET D3$ = DESC3$
LSET CVL$ = STR$(CHG)
PUT #1
FIELD #1, 58 AS CHGSUM$, 167 AS DUMMY$
LSET CHGSUM$ = CHG$ + "=" + STR$(CHG)
PUT #1
CLOSE #1
RUN "SAVROUTN.EXE"
RETURN

ERROUT: LOCATE 25, 5
PRINT "      ERROR HAPPENS, RUN AGAIN.
FOR I = 1 TO 8000: NEXT
END

```

## RSET.TXT

```
SET_PRESET_COUNT 999999999
SET_PRESET_LENGTH 4096
START
RUN "RSET.EXE"
STOP
STOP
□
```

## RSET.BAS

```
*****
DEFINT A-Z
' RSET.BAS Version 1991
' This program prompts user to select ramp modes and initial parameters for the ramp. It can also save the inputted parameters in a
' data file and run RAMP.EXE. In the case that ramp along with jump is too high, it will shorten the ramp length so that the
' maximum output from DAC is 10Volts.
*****
RETRY0:
SCREEN 0: CLS
RCT = 0
MODE = 1
CH = 0
OPEN "RMAIN.DAT" FOR INPUT AS #1 'get previous parameters
INPUT #1, NPASS, DWELL, RLT, RLTOLD, RLTNEW, JCH, MODE, JCT, RHT, JPERC, RPERC, NRAMP, LOCKMD' read
default settings
CLOSE #1
LOCATE 5, 5
PRINT " ----- MODE SELECTION -----"
LOCATE 7, 5
PRINT " 1. ENERGY LOSS SWEEP."
LOCATE 9, 5
PRINT " 2. IMPACT ENERGY SWEEP."
LOCATE 11, 5
PRINT " 3. QUIT"
DO
  VS = INKEY$
  IF VS = "1" THEN MODE = 1: GOTO INIT
  IF VS = "2" THEN MODE = 0: GOTO INIT
LOOP UNTIL VS = "3"
GOTO QUIT

INIT: CLS : LOCATE 5, 5
PRINT "NUMBER OF PASSES["; NPASS; "]: INPUT NPASS$
IF NPASS$ <> "" THEN NPASS = VAL(NPASS$)
LOCATE 7, 5
PRINT "DWELL TIME (in milliseconds) ["; DWELL; "]: INPUT DWELLS$
IF DWELLS$ <> "" THEN DWELL = VAL(DWELLS$)
RETRY:
LOCATE 9, 5
PRINT "RAMP LENGTH (channels) ["; RLTOLD; "]: INPUT RLT$
IF RLT$ <> "" THEN
  RLT = VAL(RLT$)
  ELSE RLT = RLTOLD 'if input new value then perserve old value
END IF
IF RLT = 0 THEN
  LOCATE 9, 40
  PRINT "RAMP LENGTH CAN'T BE ZERO": GOTO RETRY
END IF
HDW = 4096
NUMRAMP = HDW \ RLT
IF NUMRAMP = 0 THEN
```

```

LOCATE 9, 40
PRINT "RAMP TOO LONG      ": GOTO RETRY
END IF
LOCATE 11, 5
PRINT "RAMP HEIGHT (PERCENT FULL SCALE): ["; RPERC; "]": INPUT RPERC$
IF RPERC$ <> "" THEN RPERC = VAL(RPERC$)
RENUM: LOCATE 13, 5
PRINT "NUMBER OF RAMPS: ["; NRAMP; "]": INPUT NRAMP$
IF NRAMP$ <> "" THEN NRAMP = VAL(NRAMP$)
IF NRAMP > NUMRAMP THEN
  LOCATE 13, 40: PRINT "THE MAXIMUM RAMP NUMBER IS"; NUMRAMP
  GOTO RENUM
END IF
IF NRAMP = 0 THEN
  LOCATE 13, 40: PRINT "THE RAMP NUMBER CAN'T BE ZERO"
  GOTO RENUM
END IF
LOCATE 15, 5
PRINT " JUMP CHANNEL: ["; JCH; "]": INPUT JCH$
IF JCH$ <> "" THEN JCH = VAL(JCH$)
IF JCH >= RLT THEN JCH = RLT: GOTO RETRY1
LOCATE 17, 5
PRINT "JUMP HEIGHT (PERCENT FULL SCALE): ["; JPERC; "]": INPUT JPERC$
IF JPERC$ <> "" THEN JPERC = VAL(JPERC$)
RETRY1: JCT = JPERC * 40.96
RHT = RPERC * 40.96
IF (RLTOLD / RHT) * (4095 - JCT) + JCH <> RLTNEW THEN
  RLTOLD = RLT
  RLTNEW = (RLTOLD / RHT) * (4095 - JCT) + JCH - 1
END IF
IF RLTNEW < RLT THEN
  RLT = RLTNEW: LOCATE 19, 5: PRINT "WARNING:RAMP LENGTH TOO LARGE, SHORTEN TO"; RLT; "CHANNELS"
END IF
LOCATE 21, 5
PRINT "PROCEED TO RAMP (SPACE BAR) OR RE-ENTER PARAMETERS (ESC)"
DO: Z$ = INKEY$
IF Z$ = CHR$(27) THEN GOTO RETRY0
IF Z$ = " " THEN GOTO JHET
LOOP
JHET: OPEN "RMAIN.DAT" FOR OUTPUT AS #1
WRITE #1, NPASS, DWELL, RLT, RLTOLD, RLTNEW, JCH, MODE, JCT, RHT, JPERC, RPERC, NRAMP, LOCKMD
CLOSE #1
RUN "RMAIN.EXE"
QUIT: END

```

## ERASE

clear  
fill\_buffer

## PLOT.TXT

run "PLOT.EXE" ?

## RECCOM.TXT

SET\_MCB 0  
RECALL "BUFFILE.MCS"  
SET\_MCB 1  
RESTORE

## RECALL.TXT

```
SET_MCB 0  
RUN "RECALL.EXE"  
RECALL "BUFFILE.MCS"  
SET_MCB 1  
RESTORE  
□
```

## RECALL.BAS

CORRUPT FILE